Confronting models with cosmic perturbations: Cosmological perturbations in earliest and latest stages

Wessel Valkenburg

LAPTH-Thèse-1346/09
Juillet 2009

THÈSE

présentée pour obtenir le grade de
DOCTEUR EN PHYSIQUE DE L'UNIVERSITÉ DE SAVOIE

par
Wessel Valkenburg

Sujet :

Confronting models with cosmic perturbations

Cosmological perturbations in earliest and latest stages

Soutenue le 6 Juillet 2009 après avis des rapporteurs :

Prof. Juan García-Bellido	Rapporteur
Prof. Glenn Starkman	Rapporteur

devant la Commision d'examen composèe de :

Prof. Edward Kolb	Président
Prof. Juan García-Bellido	Rapporteur
Prof. Glenn Starkman	Rapporteur
Dr. Julien Lesgourgues	Directeur de Thèse
Prof. Pierre Salati	Co-directeur de Thèse
Prof. Andrew Liddle	
Dr. Antonio Riotto	

'At the age of six I wanted to be a cook. At seven I wanted to be Napoleon. And my ambition has been growing steadily ever since.'

- Salvador Dali -

Contents

Preface

This thesis is the result of close to three years of research at the Laboratoire d'Annecy-Le-Vieux de Physique Théorique, under supervision of Julien Lesgourgues, sometimes closely, sometimes distantly. My research in this time focussed on a variety of topics. Even though these topics at first sight might seem unrelated, they share one fundamental connection: cosmic perturbations.

Cosmic perturbations describe the fact that the universe is not filled by an exactly homogeneous fluid. Matter is in galaxies and clusters, with voids between them. The cosmos does not only show perturbations in the form of clustered matter (large scale structure, LSS), it also shows perturbations in the photon fluid that still fills the universe today, the cosmic microwave background (CMB). These together are the cosmic perturbations.

The universe is expanding. It is likely that it has been expanding for quite a while, even if we go all the way back to the point where all matter in the universe was densely packed together to form a plasma with a high temperature, possibly up to $T \sim 10^{15}$ GeV ($T \sim 10^{10}$ °C). And what happened before then? The quest of cosmology is to understand the evolution of the universe, and to understand this evolution back to ever earlier times. Even if there is an absolute zero of time in our universe, *i.e.*, a singularity in space time in which the spatial volume of our universe was zero and the temperature of its contents infinite, the quest could continue beyond that point, in order to find out how and inside what 'space time' that singularity was created in the first place.

As our knowledge is finite, we can only measure back in cosmic time up to a finite distance. Beyond that point we can only fantasise. Therefore, any description of the universe starts out at some level at which initial conditions are defined. They can be drawn from a set of possible initial conditions. Or they can be god-given, as some people like to have their minds eased. Some others prefer to use drugs.[1] Cosmologists tend to try to be modest, and describe our universe as 'not so special'. This implies that the universe could have had a range of initial conditions, from which our present universe is just one not so special drawing. But then the question is: how can one determine a measure for naturalness on a set of initial conditions? The answer is: one cannot. We can guess, though. We can guess within certain theoretical frameworks. Still, at some point something has to be taken for granted and the question about it must be postponed to later times, as asking questions beyond that point will lead to only a higher level at

[1] Some do both.

which one has to take things for granted. If that is not satisfying, one must go to an even higher level in the explanations and take some things for granted. In daily life we take for granted that gravity, on human scales, describes an attractive force between massive bodies. In theoretical physics, we take for granted that everything is described by symmetries. And within that framework, we can define what would be a natural range for, let us say, particle couplings.

This is where we get back to cosmic perturbations. Where did they come from? What specified their initial conditions? If the universe started out at a temperature of 10^{15} GeV, and if it were the true 'start' of the universe, then the most likely state of the universe would be nice and smooth and homogeneous. If it were not, then some information, some order in the chaos, would have been put in by hand, which would make our universe special and not so modest.[2] Remember that the judgement about naturalness is a matter of taste. So if it were smooth and homogeneous, the only spatial fluctuations in the density of energy would be thermal of nature. With only thermal fluctuations, the universe would probably have looked smooth and homogeneous today [160]. It is not. Matter is in galaxies and clusters, with voids between them. The cosmos shows perturbations, beyond thermal fluctuations at $T \sim 10^{15}$ GeV (back till that temperature of the universe, temperature can be used as a time parameter).

There is more information in the cosmic perturbations than just the fact that they exist. They show a certain correlation of perturbations on very large scales. This implies that two opposite ends of the universe as far as we can observe it, know about each other. The universe therefore seems older than one naively might have expected. The cosmic perturbations give a plethora of information about the universe, as they have a certain, not random, distribution. The shape of this distribution tells us about the universe at its earliest stages, and about the evolution of the universe between then and now.

This thesis consists of three parts. In the first part, we will briefly and roughly go through the foundations of cosmic perturbations necessary for understanding Parts II and III. I write roughly, as many books are and can be written about cosmic perturbations, as it is a large and lively topic, evolving today, and in this thesis we can only devote a part of the thesis to its introduction.

In Part II, we will consider new work on the initial conditions of the universe at $T \sim 10^{15}$ GeV. These in fact are most likely not randomly chosen initial conditions, but the natural consequence of inflation, as described in Part I. Part II focuses on a certain class of constraints on inflation that can be obtained from the observations of cosmic perturbations. We will show that numerical calculations shed new light on the shape of the inflaton potential in Chapters 3 and 4, with the inflaton being the particle that drives cosmic inflation. A thorough comparison of different

[2] In thermodynamics, we take for granted that entropy is ever increasing. If we would take as an initial condition that the hot particles are randomly spread over a volume, and they are so hot that we can ignore gravitational forces, then there are many more states with the particles homogeneously spread over the volume, than there are states with the particles clumped together. On top of that, all the states of lower entropy, with the particles in clumps, would be more likely to evolve towards the homogeneous state of higher entropy than to another low-entropy state. In all ways, the homogeneous distribution is the favoured state.

methods is made in Chapter 5. The last chapter of Part II, Chapter 6, deals with the inevitable choices that must be made when performing statistical analyses on cosmic data, and shows that different choices will lead to different bounds on the same parameters. This chapter is a nice example of a discussion about the taste involved in determining a definition of naturalness. Part II represents scientific work, published in Refs. [14, 103, 149, 150, 265, 267].

In Part III we will see two examples of the information cosmic perturbations can give us about the evolution of the universe after $T \sim 10^{15}$ GeV. In Chapter 7 we show that cosmic perturbations can be used to constrain the mass of neutrinos, by means of their possible role in the evolution of the universe and its perturbations. Finally, in Chapter 8 we show that cosmic perturbations can be used to rule out certain theories trying to explain the apparent acceleration of the expansion of the universe today. Part III represents scientific work published in Refs. [151, 266].

Numerical simulations were performed on the MUST cluster at LAPP (CNRS & Université de Savoie).

Part I

Some of the foundations of modern cosmology

Chapter 1

The basics of inflation

In this chapter I will give an introduction to the physics of cosmic inflation. The aim is to provide the reader with the level of understanding necessary to read Part II. I will motivate cosmic inflation by going through the initial conditions that are needed for the Hot Big Bang in order to lead to today's observations. Then I will overview different classes of inflationary models existing in the literature. Most of this chapter is inspired on Refs. [66, 71, 114, 133, 154, 221].

1.1 Anisotropy, expansion and its implications

Today we observe a close to anisotropic, down to $\mathcal{O}(10^{-5})$, Cosmic Microwave Background radiation (CMB). If we assume that we are not in a special place in the universe (the Copernican Principle), this implies that the universe looks about the same everywhere on large enough scales (the cosmological principle). At the time of last scattering of the CMB-photons, the universe was therefore close to anisotropic and homogeneous. Such a universe is well-described by the Friedmann-Lemaître-Robertson-Walker metric,

$$ds^2 = a(\tau)^2 \left(-d\tau^2 + \frac{dr^2}{1 - Kr^2} + d\Omega^2 \right), \tag{1.1}$$

with conformal time τ. With a sufficiently large positive energy density, such a spacetime is expanding, $H \equiv \frac{a'}{a^2} > 0$, with $a' = \partial_\tau a$.

Causality

In expanding spacetimes there is an upper limit on the comoving distance between two points in space that are within each others past light cone at any given time, even though physical distances go to zero for $a \to 0$. The particle horizon is the distance traveled by a photon from time zero on,

$$d_{\mathrm{H}} = a(\tau) \int_0^\tau d\tau. \tag{1.2}$$

In a purely matter dominated universe, this horizon is equal to twice the Hubble radius, $R_{\rm H} = H^{-1}$. In such a universe, the Hubble radius evolves as $R_{\rm H} = R_{\rm H}(t_0)\left(\frac{a}{a_0}\right)^{3/2}$.

So, the CMB looks about the same in any direction. But have all points on the sphere, from which the photons last scattered towards us, ever been in causal contact?

The temperature (or redshift) at which the photons decoupled from the plasma is determined by the time at which the expansion time of the universe, H^{-1}, overtook the scattering rate of photons, at that time dominated by Thomson scattering, $\Gamma_{\rm T} = \sigma_{\rm T} n_{\rm e}$. That is, when the typical distance between two scatters is as large as the typical time it takes that same distance to grow by a factor of two, the probability for a photon to scatter in that time is equal to a half. Beyond that point in time, the probability for a photon to get scattered once more before traveling to the observer goes to zero quickly. The Thomson scattering rate is determined by the number density of free electrons, in its turn determined by the baryon density and the ionisation fraction, itself determined by the baryon and matter densities. Altogether two numbers determine the temperature of photon decoupling: $\Omega_{\rm b}$ and Ω_k[1], if we assume that the universe is as good as purely matter dominated at that epoch. Today's temperature of the CMB-spectrum is measured by the FIRAS instrument on the COBE satellite, and is $T_0 = 2.725 \pm 0.002$ K [183, 184]. This means that for a typical value of $\Omega_{\rm b} \sim 0.02$, we have roughly $z_{\rm dec} = 1100$.

This implies that at decoupling, the horizon was $d_{\rm H}(\tau_{\rm dec}) \simeq 1101^{-3/2} d_{\rm H}(\tau_0) \sim \mathcal{O}(10^{-5}) d_{\rm H}(\tau_0)$. If we combine this with an estimate of the Hubble factor today, by means of observing type Ia supernovae and calibrating by means of variable Cepheids, $H_0 = 62.3 \pm 6.3$ [227], and we assume that today's particle horizon indeed corresponds to $2R_{\rm H}$, then the horizon at decoupling corresponds to an angle of roughly one degree on the last scattering surface we observe.

The horizon estimate used in the previous lines, is the maximum particle horizon in a matter dominated universe. Is there any possibility that the big bang happened longer ago, during the preceding radiation era? Let us define the big bang as the moment when the particle horizon was zero. This is simply saying that the first event in our past light cone happened at the big bang. This does not necessarily mean that the scale factor had to be zero at the big bang. In a purely matter dominated universe, the particle horizon is $d_{\rm H} = a(\tau)(\tau - \tau_{\rm BB})$. Then the scale factor at the big bang (and thereby the temperature of the plasma, by $T \propto a^{-1}$) can be written as a function of the particle horizon today, using $a_{\rm mat} = (\tau/\tau_0)^2$, such that $a_{\rm BB} = a_0(1 - d_{\rm H_0}/\frac{2}{H_0})$. For $a_0 = 1$ and with $\tau_{\rm BB} = 0$, the conformal time at an infinite-temperature big bang, we retrieve $d_{\rm H} = 2/H_0$. For the moment, the subscript '$_0$' denotes any hypothetical 'today'. This means that in a matter dominated universe, the largest age and thereby the largest particle horizon the universe can possibly have, is limited by $2/H_0$. If before the matter dominated epoch, there was an era of radiation domination starting form the big

[1] $\Omega_k \equiv \frac{K}{a^2H^2} = 1 - \Omega_{tot}$

bang on, and the matter-radiation equality occurred at $a = a_{\rm eq}$, the particle horizon becomes $d_{\rm H_0} = \frac{2}{H_0}\left[1 - \frac{1}{2}\sqrt{\frac{a_{\rm eq}}{a_0}}\left(1 + \frac{a_{\rm BB}}{a_{\rm eq}}\right)\right]$. This means that the radiation era cannot help to increase today's maximal particle horizon, since even for a big bang at infinite temperature ($a_{\rm BB} = 0$) we have at most $d_{\rm H_0} = \frac{2}{H_0}$.

The answer to the question if the origins of CMB photons we observe in all directions have ever been in causal contact, is 'no, if the content of the universe has always been dominated by matter or radiation'. Then why is the temperature the same in all directions, up to one part in 10^5? Moreover, why is the deviation from the average temperature not random, but why does it have a non-zero two-point correlation over all angular scales? This is the horizon problem.

Flatness

The spatial curvature of the universe today is best constrained by the angular scale of certain length scales at the decoupling of the CMB-photons. The temperature of the CMB-photons has a non-zero two-point correlation function. The spectrum of this two-point correlation function has peaks at wave number $k_n = n\pi/r_{\rm s}$, with $r_{\rm s}$ the sound horizon at the recombination of electrons and protons (and a small fraction of ions), just before the decoupling of the photons. What follows is a qualitative explanation.

The reason for the relation between the wave number of the peaks and the sound horizon at recombination, is that the photon-baryon fluid oscillates in the small gravitational potential fluctuations that are part of the initial conditions. Consider fluctuations at only one wavelength. From the time at which the initial conditions are set on, the fluid starts falling in the potential wells, up till the moment where the pressure takes over and pushes the fluid out again. The fluid bounces back to its initial state, and even passes beyond it, because the initial conditions include a non-zero pressure, who's distribution is related to the distribution of energy density. Hence, there are two extrema at which an observer sees a maximal enhancement of the correlation in the fluid: when the fluid is maximally compressed in the wells (and there is maximal rarefaction on the potential hills) and when the fluid experiences maximal rarefaction in the wells (and maximal compression at the hills). In the intermittent state, corresponding to almost the initial condition, there is still correlation, only it is not enhanced by the gravitational compression. Now, the longest wavelength at which this enhancement due to compression is at its maximum, corresponds to the maximum distance a pressure wave (sound wave) can have traveled from the initial conditions until recombination. This length obviously is the sound horizon. If you consider a wave length larger than the sound horizon, you may still expect a compression in the potential wells (and rarefaction on the hills), enhancing the correlation at that scale. However, the compression and rarefaction will not be at their maximum yet, as the information about the pressure (heating dense areas and cooling dilute areas) has not traveled over the whole wavelength yet. The correlation will be less enhanced. Indeed the first peak in the CMB is a smooth function, not a step-function at exactly the sound horizon.

The angle θ at which the sound horizon is observed in the CMB, is roughly set by $\theta = r_{\rm s}/D_{\rm A}(z_{\rm dec})$, with $D_{\rm A}$ the angular diameter distance,

$$D_{\rm A}(z_{\rm dec}) = \frac{a_0}{z_{\rm dec}+1}\frac{\chi_k}{H_0 a_0}\int_0^{z_{\rm dec}} \frac{dz}{\sqrt{\Omega_{\rm rad}(z+1)^4 + \Omega_{\rm m}(z+1)^3 + \Omega_\Lambda + \Omega_k(z+1)^2}}, \tag{1.3}$$

$$\chi_k(r) = \begin{cases} r & \text{for} \quad k=0 \\ \frac{1}{\sqrt{k}}\sin\sqrt{k}r & \text{for} \quad k>0 \\ \frac{1}{\sqrt{-k}}\sinh\sqrt{-k}r & \text{for} \quad k<0. \end{cases} \tag{1.4}$$

The sound speed until the time of decoupling is determined by the baryon density and the photon density. The temperature of the CMB today is measured up to high accuracy, leaving only the baryon density as an unknown parameter. The baryon density at the same time sets the redshift to decoupling. The angular diameter distance is mostly dependent on curvature k and H_0, the Hubble factor today. Here again, if one takes into account the local observations of H_0, Ω_k and $\Omega_{\rm b}$ are left as the parameters determining the angular size of the first peak in the CMB power spectrum.

Along the same lines of reasoning about the relation between the position of the first peak and the sound horizon, the second and third peak in the CMB-power spectrum are higher harmonics of the sound horizon. The second peak corresponds to the wavelength of perturbations that have compressed and relaxed exactly once, the third peak corresponds to the wavelength of perturbations that have compressed, relaxed and compressed once again. Now, if the baryon density would be increased, this would increase the gravitational mass in a potential well during its compressed phase in the oscillation. It looks like a forced oscillator, i.e., an oscillator with a constant force away from its (otherwise) equilibrium position, such that excursions are not symmetric in different directions. Hence, the compressions will have a higher density, but the rarefaction will be less pronounced. Therefore, increasing the baryon density means amplifying the first and third peaks (all odd peaks), and damping the second peak (and all other even peaks). This dependence on the ratio of the amplitudes of the peaks makes $\Omega_{\rm b}$ an easily constrained parameter.

Altogether, the current constraints on $\Omega_{\rm b}$ and Ω_k from WMAP are [70, 134] $-0.0178 < \Omega_k < 0.00066$ and $\Omega_{\rm b}h^2 = 0.02273 \pm 0.062$, with $h \equiv H_0/(100$ km s^{-1} Mpc$^{-1})$, both at 95% confidence level (CL). It is important to realize that these numbers were obtained under the 'Hubble prior' of $H_0 = 72 \pm 8$ km s^{-1} Mpc^{-1} [82], taking the locally observed H_0 to be equal to the global H_0.

Now why is this whole story about the global curvature interesting? Let $\hat{\Omega}_k(t)$ be the curvature content at any time t, and $\Omega_k \equiv \hat{\Omega}_k(t_0)$. During matter domination $\hat{\Omega}_k \propto a = 1/(1+z)$, such that if $\hat{\Omega}_k(t_0) = \mathcal{O}(10^{-2})$, this implies $\hat{\Omega}_k(t_{\rm dec}) = \mathcal{O}(10^{-5})$. During radiation domination $\hat{\Omega}_k \propto a^2$. Then if we take the matter-radiation equality to be at $z_{\rm eq} \sim 3200$ and $T_{\rm eq} = 75$ eV (more on this number later), and the radiation era to start out at a temperature of

$T_{\rm reheating} = 10^8$ GeV (this number is based on theoretical constraints), we find that $\hat{\Omega}_k(t_{\rm reheating}) = \mathcal{O}(10^{-36})$.

Unless $\hat{\Omega}_k = 0$, there is no reason why $\hat{\Omega}_k(t_{\rm reheating})$ should be so close to zero. This is the flatness problem.

A note on matter-radiation equality

Above we assumed $z_{\rm eq} \sim 3200$. This number is determined by Ω_γ and $\Omega_{\rm m}$ today and the number of neutrino species.. The CMB-temperature is measured up to high accuracy, such that $\Omega_\gamma h^2$ can be considered a known practically fixed number. $\Omega_{\rm m}$ is only poorly constrained by the CMB alone. What does constrain $\Omega_{\rm m}$ more tightly, is to combine CMB observations with those of the matter power spectrum, the two point correlation on the observed distribution of galaxies. If one postulates a presence of a close to scale invariant super Hubble spectrum of frozen energy perturbations, these perturbations will enter the Hubble horizon one by one, and start evolving according to the contents of the observable universe. During radiation domination, the amplitude of matter density perturbations grow as $\delta \propto \ln a$. On top of that, the density perturbations in the baryon component of the matter have a shrinking component, which shrinks as $\delta_{\rm baryon} \propto a^{-2}$. During matter domination they grow as $\delta \propto a$. Hence, small scale modes that enter the horizon during radiation equality, will grow as $\propto \ln a$ until matter domination. Modes that enter after the transition to matter domination, will only experience the growth $\propto a$. Therefore, the mode that enters at matter-radiation equality marks a change in slope in the matter power spectrum. The larger $\Omega_{\rm m}$ today, the later the equality will have taken place, hence the larger the scale that corresponds to the horizon size at equality (the scale of change in slope). The knee in the spectrum has been observed.

The CMB on its own also is capable of constraining Ω_m, since the photon decoupling takes place when the radiation density is not yet negligible. We will see in the next chapter, that during matter domination, the linearly perturbed gravitational potential remains constant. During radiation domination, it does change. Depending on how close to matter-radiation equality the photon decoupling took place, the gravitational potentials will still be changing. If a photon passes through a changing gravitational potential, is gains or looses energy if the potential shallows of deepens. Hence, the CMB anisotropy contains a contribution due to this effect, the magnitude of which determines how long after the matter-radiation equality the photon decoupling took place.

When one for example considers only SDSS Luminous Red Galaxies (LRG), data release 4 (DR4) [255] and the WMAP 3yr data release, one finds that $\Omega_{\rm m}h^2 = 0.12 \pm 0.005$ and 68% CL (when a tilt of the primordial spectrum and its running are allowed to vary) [255]. In such a case, $z_{\rm eq} \simeq 2500$. Note that this number changes from data set to data set, and the strongest constraints are obtained by combining sets. The number quoted here is more for illustrative purposes. The time dependence of matter perturbations is reviewed more thoroughly in Chapter 2.

The age of the universe

A problem closely related to the flatness problem is the oldness of the universe. Qualitatively it is as follows. If initially Ω_k had been of order unity, then if the universe were closed, the universe would have recollapsed within less than a second after the Planck time, or if the universe were open, its expansion would have been curvature dominated rapidly, cooling the photons down to the observed temperature of $2.726K$ within less than a second. Our solar system itself has an age of probably $\mathcal{O}(10^{10})$ years. So, independent of the observed curvature in the CMB-spectrum, the initial curvature must have been fine tuned already to let the universe reach the age and temperature it has right now.

Cosmic relics

As the universe cools down continuously, when it is matter or radiation dominated, spontaneous symmetry breakings may occur. Given the limited size of the Hubble radius, this can lead to topological defects. The Hubble radius grows with time, in a radiation or matter dominated universe. If we remember that the Hubble radius at decoupling already had a size that we observe today under an angle of about one degree, this means that for any theory predicting topological defects, we should observe numerous topological defects. We do not observe any. But if it is natural for these defects, or any other troublesome relic for that matter, to occur at some temperature, some dynamical mechanism must have diluted the relic density such that we should of the order of one defect per Hubble volume today.

1.2 Inflation to the rescue

Curvature

The evolution of the curvature is set by $\hat{\Omega}_k \equiv \frac{k}{a^2H^2} = 1-\Omega_{\rm tot}$. $\Omega_{\rm tot}$ is determined by the energy content of the universe, by definition normalised to the critical energy density for which the universe is exactly flat, $k = 0$. The dependence of the Hubble factor on the scale factor, is given by the Friedmann equations,

$$H^2 \equiv \left(\frac{\dot{a}}{a}\right)^2 = \frac{1}{3}\rho + \frac{\Lambda}{3}, \tag{1.5}$$

$$\frac{\ddot{a}}{a} = -\frac{4}{3}(\rho + 3p) + \frac{\Lambda}{3}, \tag{1.6}$$

where $\dot{a} \equiv \partial_t a$, with cosmic time t defined by $dt = a\, d\tau$. Let us ignore the cosmological constant Λ for now. Hence, if the universe is radiation dominated and has a small curvature term, we have $\rho_{\rm rad} \propto a^{-4}$, $H \propto a^{-2}$ and $\hat{\Omega}_k \propto a^2$. If we replace the radiation by non-relativistic matter, we have $\rho_{\rm mat} \propto a^{-3}$, $H \propto a^{-3/2}$ and $\hat{\Omega}_k \propto a$. If the universe is curvature dominated, we have $\rho_{\rm k} \propto a^{-2}$, $H \propto a^{-1}$ and $\hat{\Omega}_k \propto$ constant. So, if we want to drive $|\Omega_k|$ to zero dynamically, the universe must have a content such that $H \propto a^n$ and $\rho \propto a^{2n}$, with $n > -1$.

Horizon

If we restrict ourselves to a monotonically growing scale factor with time, and take the ansatz $a_{\rm inf} = a_{\rm end}\left(\frac{t}{t_{\rm end}}\right)^m$, with $a_{\rm end}$ and $t_{\rm end}$ denoting the scale factor and time at the end of the epoch of which this scale factor is the proper description, we find that the contribution of that epoch to the particle horizon today is,

$$\begin{aligned} d_{\rm H,inf} &= a_0 \int_{a_{\rm ini}}^{a_{\rm end}} \frac{da}{a^2 H} \\ &= \frac{t_{\rm end} a_0}{a_{\rm end}^{\frac{1}{m}}} \int_{a_{\rm ini}}^{a_{\rm end}} a^{\frac{1}{m}-2} da \\ &= \frac{t_{\rm end} a_0}{a_{\rm end}^{\frac{1}{m}}} \frac{m}{1-m}\left(a_{\rm end}^{\frac{1}{m}-1} - a_{\rm ini}^{\frac{1}{m}-1}\right), \end{aligned} \tag{1.7}$$

using $H \equiv \frac{\partial_\tau a}{a^2} \equiv \frac{\dot{a}}{a}$ and using cosmic time t, defined by $dt = a\, d\tau$. In this equation, $t_{\rm end}$ will be defined as some combination of H_0, a_0, $a_{\rm eq}$ and $a_{\rm end}$. For $m < 1$, we find that

$$\lim_{m\uparrow 1} \frac{a_{\rm end}^{\frac{1}{m}-1} - a_{\rm ini}^{\frac{1}{m}-1}}{1-m} = \log\frac{a_{\rm end}}{a_{\rm ini}}. \tag{1.8}$$

Hence, for $m > 1$, a configuration with m very close to one and $a_{\rm ini}$ very close to zero, could solve the horizon problem. Taking m to be very close to one would be fine tuning though. For $m > 1$, the particle horizon remains positive (since $a_{\rm ini} < a_{\rm end}$), and $\lim_{a_{\rm ini}\to 0} d_{\rm H} = \infty$.

In our ansatz of $a \propto t^m$, we have $H \propto a^{-\frac{1}{m}}$. If we want the same epoch to drive spatial curvature to zero, we have $\frac{1}{m} < 1$, such that the flatness problem and the horizon problem can be solved simultaneously if $m > 1$. If $m > 1$, we have $\ddot{a} > 0$, in other words, the expansion accelerates. This explains the name of this epoch: *Inflation*. Note that the condition of accelerated expansion can also be written as $-\dot{H}/H^2 < 1$.

Relics

If two objects are more than the Hubble radius separated from each other, they can not communicate from that moment on, unless the Hubble radius changes significantly in the mean time. The reasoning for this looks like the reasoning about the decoupling of photons, above. The Hubble radius corresponds to the time it takes for the scale factor to double in size. Hence, if any form of information travels along the distance that corresponds to the Hubble radius at a given moment, let us call that distance L, the object that initially was at one Hubble radius from the source of information (distance L), will be at a distance $2L$ from the source. The information cannot get beyond half way between the two objects. Objects outside each others particle horizon can never have communicated, objects more than the

Hubble radius removed from each other, cannot communicate at that moment. During inflation, the comoving Hubble radius decreases. That is, $R_{\rm H}/a = 1/aH$, and $\partial_t 1/aH = -\ddot{a}/\dot{a}^2 < 0$.

Let us consider topological defects. When these form, in most cases the number of relics that forms is of the order of one per Hubble volume. This is simply because in a spontaneous symmetry breaking, the maximum distance over which a field can communicate and fall into the same non-symmetric state along that distance, is set by the Hubble radius. If before inflation these defects formed, and at the beginning of inflation the number of defects is one per Hubble radius, then inflation will decrease the comoving Hubble volume such that the number of defects per Hubble volume becomes much less than one. After inflation the comoving Hubble radius grows again, such that today the number of defects can again be of the order of one per Hubble volume, and the defects cannot dominate the evolution of the universe, as is in agreement with observations.

Duration of inflation

Let us first consider the horizon problem. The largest scale at which we observe correlations that indicate causal contact, is the distance to the last scattering surface of the CMB photons. Let us make a rough estimate of the comoving distance to the last-scattering surface. For now, we assume that the universe today is matter dominated, and the last scattering took place during matter domination, at a redshift of $z \simeq 1100$. During matter domination we have $a_{\rm mat} = a_0 \left(\frac{\tau}{\tau_0}\right)^2$, $H = \frac{2\tau_0^2}{a_0 \tau^3}$, such that $\tau_0 = \frac{2}{H_0}$ and $\tau_{\rm dec} = \sqrt{\frac{1}{1100}}\tau_0$. Then the comoving distance to the last-scattering surface is set by $\Delta\tau = \tau_0 \left(1 - \sqrt{\frac{1}{1100}}\right) \simeq \tau_0 = \frac{2}{H_0}$. This is the distance from us, observers, to the surface. We see correlations in opposing points, hence the distance over which points in space seem to have been in causal contact is at least equal to $\frac{4}{H_0}$. This means that the comoving particle horizon at last scattering must be at least $\frac{4}{H_0}$. As the comoving particle horizon grow with τ, this implies that the comoving particle horizon today is about $\frac{4}{H_0} + \Delta\tau \simeq \frac{6}{H_0}$.

If we want causal contact to have extended up to this comoving scale at the beginning of inflation, this implies that the comoving Hubble radius at the beginning of inflation was at least equal to today's comoving particle horizon. The decrease of the comoving Hubble radius during inflation must compensate the growth of the comoving Hubble radius after inflation. Hence,

$$
\begin{aligned}
a_{\rm ini} H_{\rm ini} &= \frac{H_0}{6} \\
a_{\rm end} H_{\rm end} &= a_{\rm end} H_0 \left(\frac{a_0}{a_{\rm eq}}\right)^{\frac{3}{2}} \left(\frac{a_{\rm eq}}{a_{\rm end}}\right)^2 \\
\frac{a_{\rm end} H_{\rm end}}{a_{\rm ini} H_{\rm ini}} &= 6 \frac{a_{\rm eq}^2}{a_{\rm end}} \left(\frac{a_0}{a_{\rm eq}}\right)^{\frac{3}{2}}
\end{aligned}
\tag{1.9}
$$

The temperature of the CMB photons today is $T_0 = \mathcal{O}(10^{-13})$ GeV. If the radiation era started out at a temperature of 10^{15} GeV, we find that the scale factor must grow by a factor,

$$\log \frac{a_{\rm end}}{a_{\rm ini}} = 62 + \log \frac{T_{\rm end}}{10^{15}{\rm GeV}}, \tag{1.10}$$

for a typical value of $a_{\rm eq}$ and if we assume that the Hubble parameter does not change significantly during inflation, which is a reasonable assumption, as we will see later on. Hence, in order to solve the horizon problem, inflation must last at least for about 60 *e-foldings*, although this number depends on the reheating temperature, the temperature at which the radiation era starts.

Concerning cosmic relics, the condition to prevent cosmic relic domination is the same as the condition to solve the horizon problem: if one relic formed per Hubble volume at the onset of inflation, a duration of inflation of $62+\log \frac{T_{\rm end}}{10^{15}{\rm GeV}}$ e-foldings ensures us that today we will not observe more than one relic in our Hubble volume.

Remember that $\hat{\Omega}_k \equiv \frac{k}{a^2H^2}$. At the beginning of inflation, $\hat{\Omega}_k$ cannot be too large, otherwise inflation would never start. If $\hat{\Omega}_k = 1$, it would stay so forever. Hence, $|\hat{\Omega}_k|_{\rm ini} < 1$ is a firm upper bound. This means that at the end of inflation, $|\hat{\Omega}_k|_{\rm end} < \left(\frac{a_{\rm ini}H_{\rm ini}}{a_{\rm end}H_{\rm end}}\right)^2$, such that today $\Omega_k = |\hat{\Omega}_k|_{\rm end}\left(\frac{a_{\rm end}H_{\rm end}}{a_0H_0}\right)^2 < \left(\frac{a_{\rm ini}H_{\rm ini}}{a_0H_0}\right)^2$. In order to match the observations, $\Omega_k = \mathcal{O}(10^{-2})$, this gives $a_{\rm ini}H_{\rm ini} < \frac{H_0}{10}$. This upper bound adds the small difference of $\log 10/6$ to the needed number of e-foldings, such that is it fair to say that solving the horizon problem, the relic problem and the flatness problem, all leads to the same minimal number of e-foldings, set by the reheating temperature.

1.3 The simplest model of inflation

The definition of inflation is a period of accelerated expansion. The acceleration is given by Eq. (1.6), which we repeat here,

$$\frac{\ddot{a}}{a} = -\frac{4}{3}(\rho + 3p) + \frac{\Lambda}{3}. \tag{1.11}$$

Hence the expansion accelerates in the case of domination by a positive cosmological constant Λ (de Sitter inflation), or by a matter for which $3p < -\rho$.

The simplest field that is capable of having negative pressure, is the scalar field, with

$$\rho = \frac{1}{2}\dot{\phi}^2 + V(\phi), \tag{1.12}$$

$$p = \frac{1}{2}\dot{\phi}^2 - V(\phi). \tag{1.13}$$

As soon as the energy density of the scalar field is dominated by its potential energy, or more exact, if $V(\phi) > \dot{\phi}^2$, we have $p/\rho < -1/3$.

The equation of motion of a scalar field in an FLRW spacetime is

$$\ddot{\phi} + 3H\dot{\phi} + \frac{dV(\phi)}{d\phi} = 0. \tag{1.14}$$

If we assume spatial flatness, which is a good approximation shortly after the onset of inflation, the Friedmann equation becomes,

$$H^2 = \frac{1}{3M_{\rm P}^2}\left(\frac{1}{2}\dot{\phi}^2 + V(\phi)\right). \tag{1.15}$$

Together these can be rewritten to,

$$\dot{\phi} = -2M_{\rm P}^2 H'(\phi), \tag{1.16}$$

$$-\frac{V(\phi)}{2M_{\rm P}^4} = H'(\phi)^2 - \frac{3}{2M_{\rm P}^2}H^2(\phi), \tag{1.17}$$

if one assumes that ϕ changes monotonically in time, since a division by $\dot{\phi}$ appeared in this derivation and ϕ could not be used as a time parameter if it were not monotonic.

If ϕ rolls downhill, then $\partial_\phi V(\phi)/\dot{\phi} < 0$. Hence $3H\dot{\phi}$ is a friction term, and for any choice of initial conditions sufficiently remote from the minimum of the potential, the scalar field has an attractor solution where $\ddot{\phi} \sim 0$.

There is a plethora of inflationary models. To begin with, there is a large range of single scalar-field potentials, some more motivated by particle physics (super symmetry) than others. Then there is hybrid inflation, in which inflation is driven by one scalar field, but ends in an interplay of the driving field and a second scalar field. In multiple inflation, inflation is driven by possibly two or more fields. There are modified gravity theories, in which the Einstein-Hilbert action, describing General Relativity, is no longer the correct description at high energies. String theory provides a zoo of scenarios that can drive inflation as well. In this chapter, which is meant to support the first part of this thesis, the only goal is to give a basic understanding of inflation. The different chapters following this introduction, are about relating observables to constraints on inflation. The ultimate goal is to perform a model selection, and let the data tell us which is the true model of inflation. We will see however, that current data constrain the shape of the potential, but do hardly discriminate between different models. The focus will be on the best way to constrain the potential, and not necessarily on the actual constraints. Therefore, as most of the mentioned models are capable of explaining the observations, we will not discuss each of them separately, and we suffice with the example of single-field inflation. In the next section, we will discuss how to relate the observations to the shape of the potential, in the case of a single scalar field.

1.4 Quantum fluctuations and the spectrum of primordial perturbations

During inflation, the inflaton is the dominating energy content of the universe. This means that fluctuations in the scalar field imply fluctuations in the metric. This has some consequences. One consequence is that the fluctuations in the scalar field cannot be computed as if the scalar field were in a homogeneous background, but are computed taking into account the coupling to the Einstein equations (through the stress-energy tensor). Another consequence is that the mapping of small perturbations to a background coordinate system is not unique. Perturbations are defined with respect to an average. This average is associated to some background metric. The perturbed quantities are the physical quantities, and a coordinate transformation will only change the mapping, but not the physical quantities. However, the coordinate transformation will change the definition of the average background quantity, as the average is performed over equal-time hypersurfaces, and time may be redefined by the coordinate transformation. One can imagine that in one choice of coordinates there are no perturbations, and that under a small coordinate transformation perturbations emerge. As there are four dimensions in General Relativity, there are four coordinates to transform, hence four degrees of freedom defining the gauge transformation. A 4×4 symmetric tensor has ten degrees of freedom. As four of those can be set to zero by some gauge transformation, only six physical degrees of freedom remain for the perturbations in the metric. The safest is to perform calculations on gauge invariant variables, which will correspond to the only physical degrees of freedom. The derivation of gauge invariant perturbation variables is rather lengthy, so we only quote the result here.

The six degrees of freedom in the metric can be split into two scalar, two vector and two tensor degrees of freedom. The equations of motion for the vector degrees of freedom only allow for decaying solutions. From generic initial conditions, we do not expect the vector perturbations to be of different magnitude than the scalar and tensor perturbations, hence we expect them to play no significant role, and we will ignore them. The tensor perturbations are gauge invariant on their own.

Next we will closely follow Chapter 14 in Ref. [154], to come to the definition of the gauge invariant scalar curvature perturbation. Let us start with the most generic perturbation of the FLRW-metric,

$$ds^2 = a^2(\tau)\left[-(1+2A)d\tau^2 - B_i d\tau dx^i + [(1+2\psi)\delta_{ij} + 2E_{ij}]dx^i dx^j\right]. \quad (1.18)$$

These perturbations contain 10 degrees of freedom. Those degrees can be de-

composed in their scalar (^{S}), vector (^{V}) and tensor (^{T}) contributions by,

$$A = A^S, \tag{1.19}$$

$$\psi = \psi^S \tag{1.20}$$

$$B_i^S = -\frac{ik_i}{k}B, \tag{1.21}$$

$$E_{ij}^S = \left(-\frac{k_i k_j}{k^2} + \frac{1}{3}\delta_{ij}\right)E, \tag{1.22}$$

$$B_i^V = B_i^V, \qquad \text{with } k_i B_i^V = 0, \tag{1.23}$$

$$E_{ij}^V = -\frac{i}{2k}(k_i E_j + k_j E_i), \tag{1.24}$$

$$E_{ij}^T = \frac{h_{ij}^T}{a^2}. \tag{1.25}$$

A gauge invariant quantity describing the scalar perturbations is then,

$$\mathcal{R} = \psi - H\frac{\delta\phi}{\dot{\phi}}, \tag{1.26}$$

which is the comoving curvature perturbation, or the spatial curvature perturbation on the hypersurface of constant time, $\mathcal{R} = \psi_{\rm com}$. In a comoving slicing, that is, in a gauge with $\delta\tau = 0$, the spatial slicing is such that it is orthogonal to the world lines of comoving (free falling) observers. For a comoving observer, the expansion is isotropic (if we assume no vorticity), hence these observers do not observe an energy flux. Thus, $\delta\tau = 0$ implies $\delta\phi_{\rm com} = 0$. Under any gauge transformation that only affects the time variable, *e.g.* to change to a comoving slicing, $\psi \to \psi + \frac{a'}{a}\delta\tau$ and $\delta\phi \to \delta\phi + \phi'\delta\tau$. Hence, to transform to comoving slicing, from any gauge, we need $\delta\tau = \delta\phi/\phi'$. Therefore, in any gauge, Eq. (1.26) corresponds to the curvature perturbation on comoving hypersurfaces, and it is gauge invariant.

In case of isotropy in some quantity χ, its two-point correlation function is a function of distance,

$$\langle\chi(\vec{x})\chi^*(\vec{x}+\vec{r})\rangle = f_\chi(r), \tag{1.27}$$

where $\langle\ldots\rangle$ denotes averaging over $\vec{x}$ and $r = |\vec{r}|$. Substituting $\chi(\vec{x}) \to \int \frac{d^3k}{(2\pi)^3}\chi_k \exp(i\vec{k}\vec{x})$, we can define the power spectrum P_χ of the two-point correlation function f_χ by

$$\begin{aligned} f_\chi(r) &= \int \frac{k^2 dk}{2\pi^2} e^{-ikr}\,|\chi_k|^2 \\ &= \int d\ln k\; P_\chi(k) e^{-ikr}, \end{aligned} \tag{1.28}$$

$$P_\chi(k) = \frac{k^3}{2\pi^2}\,|\chi_k|^2\,. \tag{1.29}$$

This is the classical definition. In the case of quantum fields, the definition of $\langle \ldots \rangle$ changes to taking the expectation value $\langle 0| \ldots |0\rangle$, with $|0\rangle$ the vacuum state. If the Fourier transform is appropriately written in terms of creation and annihilation operators, the result is identical, with χ_k the mode function of field $\chi(\vec{x})$.

The equation of motion for the scalar and tensor perturbations is,

$$\mu''_{S,T} + \left[k^2 - \frac{z''_{S,T}}{z_{S,T}} \right] \mu_{S,T} = 0, \tag{1.30}$$

with $\mu_S = 2z_S\mathcal{R}$, $\mu_T \equiv z_T h$, $z_S \equiv a\sqrt{2 - aa''/a'^2}$ and $z_T = a$. Both tensor degrees of freedom are represented by h, although in principle h should cary a label defining both degrees of freedom. The power spectra of perturbations then are given by,

$$\mathcal{P}_\mathcal{R} = \frac{k^3}{8\pi^2} \left| \frac{\mu_S}{z_S} \right|^2, \tag{1.31}$$

$$\mathcal{P}_h = \frac{2k^3}{\pi^2} \left| \frac{\mu_T}{z_T} \right|^2, \tag{1.32}$$

where both degrees of freedom in the tensor perturbations have been taken into account. The initial conditions for Eq. (1.30) are,

$$\lim_{k/aH \to \infty} \mu_{S,T}(\tau) = \frac{4\sqrt{\pi}}{m_\mathrm{P}} \frac{e^{-ik(\tau - \tau_i)}}{\sqrt{2k}}, \tag{1.33}$$

which is the Bunch-Davies vacuum (see Appendix A). Very briefly, the past time vacuum state is chosen at a time that the modes of comoving wavenumber k were so deep in ultra violet, that the field was practically a massless field that did not feel the expansion and seemingly observed a Minkowsky metric.

The equations of motion for the perturbations, Eq (1.30), can in most cases not be solved analytically. We can however take a closer look and give rough estimates of the evolution of the mode functions during inflation. The quantity that dominates the oscillation frequency, is determined by the ratio $k^2 z_{S,T}/z''_{S,T}$. Let us first consider the tensors. If we come back to our earlier definition of inflation, that $\ddot{a} > 0$, and we stick to the postulate $a \propto t^m$, with $m > 1$, then we have $a(k/a - a''/a^2) = a(k/a - (aH^2 + \ddot{a}))$. Now $aH^2 \propto t^{m-1}$, which is a growing function of time. Therefore, as k/a decreases in time and a''/a^2 increases in time, for any k and a sufficiently long period of inflation, the equation of motion will eventually be dominated by the term a''/a. This implies that at early times $\mu''_T + k^2\mu_T = 0$, and at late times $\mu''_T - \frac{z''_T}{z_T}\mu_T = 0$. The late time solution implies $\mu_T \propto z_T$, such that at late times $\mathcal{P}_h \propto$ constant.

For scalar perturbations, $z''_S/z_S \propto t^{3m-2}$, which is also a growing function of time. Therefore, the same reasoning goes for the scalar perturbations, that at late time $\mathcal{P}_\mathcal{R} \propto$ constant.

This rough estimate has important consequences. During inflation, quantum fluctuations that occur at small scales, at which they have significant amplitude

(the far ultra violet), get blown up to cosmological scales. Normally, quantum fluctuations would decorrelate, such that at large scales the correlation is absent. During inflation, the modes get stretched beyond the Hubble radius, where there is no more communication along the size of the mode, and the decorrelation stops. At that moment the modes freeze in to remain constant curvature and tensor perturbations. This is the source for the primordial spectrum of density perturbations, which shows a non-zero two point correlation function on scales that are larger than the Hubble radius today.

Quantum to classical transition

So far, we learned that the scalar field during inflaton creates quantum fluctuations on super-Hubble scales, that remain of constant amplitude in time. As they are quantum fluctuations, they should be properly described in terms of the full wave function of the universe. This implies that we could perform a diffraction experiment [127], that would reveal the quantum nature of the perturbations in the form of an interference spectrum that would not exist if the scalar field could be described classically.

It may be helpful to make the analogy to a double-slit experiment with an incident electron beam. On a detection screen behind the double slit, we would observe an interference pattern, showing that the electron, once it passes the double slit, is described by a coherent superposition of two states, namely the state that went through slit A and the state that went through slit B. Because of the coherence, *i.e.*, both states are in phase, the states amplify and suppress the amplitude of the wave-function of the electron on the detection screen, increasing and decreasing the chance to detect the electron at a certain point on the screen. In a classical description, the electron definitely passed either slit A or slit B, but would not obey any interference pattern when hitting the detection screen. Classically, 50% of the electrons passes through slit A, 50% passes through slit B. The quantum and classical descriptions will agree, if the superposed states loose their coherence. This could be caused for example by some state-dependent interaction somewhere near the passage of the slit. The state that suffers the interaction, will change of phase, for example simply by being delayed on its way to the detection screen. In the case of a large number of electrons, the phase difference averages out in such a way the on average there is no interference pattern. Hence, if because of some interaction on the way, the coherence is lost, the evolution of the beam of electrons is described by means of classic stochastic variables: each electron has a 50% chance of passing through slit A, and a 50% chance of passing through slit B. This is the process of decoherence.

If the scalar field remains a coherent superposition of states up till today, then its state at some remote distance remains undetermined until the moment that we make a measurement. That means it is not possible to classically describe the evolution of matter perturbations, and we would need to evaluate the full wave function of the universe in order to say anything about structure formation between inflation and today. Clearly, structures are deterministically observed.

They are observed as having grown from primordial perturbations that are described by classical stochastic variables. The same goes for the anisotropies in the CMB. Hence, somewhere the process of decoherence must have taken place, and moreover, the quantum fluctuations must have translated to classical stochastic variables. And in fact, so it happened.

A full explanation of the process of the quantum-to-classical transition of the scalar field perturbations on super-Hubble scales, would be too detailed and lengthy to put here. See for example Refs [127, 195, 209]. Even though we do not give the proof of this transition here, we are on the safe side. If the scalar perturbations would not go classical on super-Hubble scales during inflation, they would still do so during reheating. The coherent modes of the scalar field would interact with a zoo of particles. These interactions are most likely to be state dependent, hence having the standard scenario of decoherence as a consequence.

Slow-Roll Approximation

The amplitude of a certain mode at the time it freezes in, is related to the Hubble factor at the time of freeze in. In the line of the intuitive explanation above: if the Hubble factor is larger, the Hubble radius is smaller, and the decohering stops at an earlier stage, hence at a larger amplitude of the mode.

As mentioned before, the evolution of the scalar field and the perturbation equations can usually not be solved analytically. In the following chapters the focus will lay on numerical (as good as exact) calculations, compared to existing analytical approximations. As the approximations do give insight in the dynamics of inflation, I will briefly mention the results of the Slow-Roll approximation, without derivations.

The Slow-Roll approximation consists in demanding that all derivatives of the inflaton potential remain small during inflation. There are different choices of parameters on the market, but here I will give the Hubble-flow parameterisation, as in Ref. [145]. If we take the number of e-foldings, $N = \log a/a_{\rm ini}$, as a time parameter, we can define,

$$\epsilon_0 \equiv \frac{H(N_{\rm ini})}{H(N)}, \tag{1.34}$$

$$\epsilon_n \equiv \frac{d\ln\epsilon_{n-1}}{dN}, \qquad \text{with } n \geq 1. \tag{1.35}$$

In this case $\epsilon_1 = -\frac{\dot{H}}{H^2}$, and by definition during inflation $\epsilon_1 < 1$. The Slow-Roll approximation in this parameterisation consists in demanding $\epsilon_n \ll 1$, for all n.

One can find relations between the scalar field potential $V(\phi)$ and ϵ_n,

$$H^2 \simeq \frac{8\pi}{3m_{\rm P}^2}V, \tag{1.36}$$

$$\epsilon_1 \simeq \frac{m_{\rm P}^2}{16\pi}\left(\frac{\partial_\phi V}{V}\right)^2, \tag{1.37}$$

$$\epsilon_2 \simeq \frac{m_{\rm P}^2}{4\pi}\left[\left(\frac{\partial_\phi V}{V}\right)^2 - \frac{\partial_\phi^2 V}{V}\right], \tag{1.38}$$

$$\epsilon_2\epsilon_3 \simeq \frac{m_{\rm P}^4}{32\pi^2}\left[\frac{\partial_\phi^3 V \partial_\phi V}{V^2} - 3\frac{\partial_\phi^2 V}{V}\left(\frac{\partial_\phi V}{V}\right)^2 + 2\left(\frac{\partial_\phi^2 V}{V}\right)^4\right]. \tag{1.39}$$

Then to lowest order

$$\mathcal{P}_{\mathcal{R}0}(k_*) = \frac{H^2}{\pi\epsilon_1 m_{\rm P}^2}, \tag{1.40}$$

$$\mathcal{P}_{h0}(k_*) = \frac{16H^2}{\pi m_{\rm P}^2}, \tag{1.41}$$

where H and ϵ_1 are evaluated at $k_* = aH$, with k_* a free to choose pivot scale. To next order we have,

$$\log\frac{\mathcal{P}(k)}{\mathcal{P}_0(k_*)} = b_0(\epsilon_n) + b_1(\epsilon_n)\log\frac{k}{k_*} + \frac{b_2(\epsilon_n)}{2}\log^2\frac{k}{k_*} + \ldots \tag{1.42}$$

Here for scalar perturbations $b_1 = n_S - 1$ is the tilt of the spectrum, $b_2 = \alpha_S$ is the running of the spectrum, and similarly for tensor perturbations $b_1 = n_T$, $b_2 = \alpha_T$.

What can we observe?

Now that we have seen how the scalar potential relates to the curvature perturbations, it is interesting to note that the absolute scale of inflation, H, can only be determined if the amplitudes of both the scalar and the tensor perturbations are observed. Up till today, the tensor spectrum has not been observed yet, although the observations still allow for a non-zero tensor spectrum. By only observing the scalar spectrum, we can constrain somewhat the shape of the inflaton potential, but even the shape remains degenerate.

1.5 Reheating

After inflation ends, when the acceleration stops and the inflaton field's energy is no longer dominated by potential energy, the universe might look very empty and cold, as everything diluted away. This picture seems far from the high temperature of the beginning of the radiation era.

We will give an intuitive explanation as in Ref. [154]. At the end of inflation, the inflaton reaches the minimum of its potential. As the inflaton will have kinetic energy, it will oscillate around this minimum. During these oscillations the inflaton will decay into other particles, eventually into dark matter and standard-model particles. At a first glance, one may wonder why the inflaton did not decay before and stop inflation to early. Even if the inflaton is very unstable, that is, it has a very short lifetime, the Hubble time during inflation, H_I^{-1}, will be even shorter. Hence, the chance per Hubble volume that the inflaton will decay before the end of inflation is negligibly small. If inflation were the very first epoch in the life of the universe, than the age of the universe is directly proportional to the Hubble time, and the inflaton will have been too young to decay earlier.

When the inflaton is near the minimum of its potential, and this potential can be approximated by $V(\phi) \propto \phi^2$, than the average energy density $\bar{\rho} = \left\langle \dot{\phi}^2 \right\rangle$ obeys the equation,

$$\dot{\bar{\rho}} + 3H\bar{\rho} = 0, \tag{1.43}$$

which has the solution $\bar{\rho} \propto a^{-3}$, which means that the amplitude of the oscillations of the inflaton in its potential decreases. As during non-relativistic matter domination, the Hubble time will increase, and this period lasts just until the Hubble time meets the decay time of the inflaton.

In general there are two possibilities for the rate of the decay. The inflaton either decays into bosons and fermions or into fermions alone. In the first case, there is no mechanism that prevents the decay, and the inflaton will decay almost instantaneously into bosons, which is often referred to as *preheating*. The bosons will start interacting with each other and will soon thermalise the universe, the process of *reheating*. If the inflaton decays into fermions only, Pauli's exclusion principle will provide a break on the decay-rate. The only implication is that reheating will take more time to complete.

A whole lot more can be said about reheating, but for the rest of this thesis it suffices to accept that a mechanism for reheating exists. If the mechanism of reheating leaves any imprint in the shape of cosmic perturbations, it can only be on scales close to or smaller than the Hubble radius at the time of reheating, which is a scale that today is too small to observe. That reheating does not interfere with the super Hubble perturbations can be understood as follows. In principle the reheating temperature will be equal everywhere, as the inflaton rolled down the same potential everywhere. But, as the inflaton suffered quantum fluctuations, it will not reach the minimum everywhere at the *same time*. Hence, some regions will have reheated slightly earlier than others, and started cooling down slightly earlier, exactly in correspondence with the super Hubble energy perturbations. This is exactly how the super-hubble quantum fluctuations are translated in temperature correlations on super-hubble scales. Obviously, reheating can completely redefine the sub-hubble perturbation spectrum, which however is a scale that is too small to observe today.

This intuitive explanation is gauge dependent. We could give the same reasoning in a synchronous picture: the inflation will reach the minimum at the same

time everywhere, but with a slightly different kinetic energy, or, in other words with a difference in expansion history, hence a larger or smaller volume to fill with the same amount of energy, in accordance with the super Hubble perturbations.

1.6 Difficulties for inflation

Until so far, it looks as if inflation is the perfect son in law. It does have its caveats though. Let us briefly mention a few, following Ref. [28]. First of all, one can argue that in order to fit the data, the parameters describing the inflaton potential impose a strange relation between the different derivatives of the inflaton potential. For example, if the amplitude of perturbations is $\mathcal{O}(10^{-5})$, then Eqs. (1.36–1.42) show that only potentials with a specific relation between the different derivatives of the potential, will provide the spectrum that is observed. In other words, if the whole space of potentials would be equally natural, then the class of potentials that provides the right spectrum is a fine-tuned subclass. This, however, is a difficult discussion, as it is about what is natural and what is not. Does the smooth spectrum have to be a natural outcome of any inflation model, or could we have had a universe with any spectrum, and do we happen to be in the one with a smooth spectrum resulting from that small corner of parameter space?

A more interesting problem, is the trans-planckian problem. Inflation blows small scale quantum fluctuations up to large scale classically observable perturbations. If inflation starts out early enough, and there is no empirical or theoretical reason why this should not be the case, the same growth of scales is important for length scales that initially are below the Planck length. This means that scales about which we do not understand the physics at all, have their impact on observable scales. This could significantly alter the observations, yet we ignore this effect so far.

A similar problem is the fact that the potential energy of the inflaton for many models is of the order $\sim 10^{16}$ GeV. This scale is close to energy scales for which we expect quantum-gravity effects to become relevant, such that it is unclear wether we can stick to the simple effective Einstein-Hilbert action for gravity.

These problems have in common that they point out relations between inflation and areas of physics that are unknown. This is for sure a potential caveat to keep in mind, but they are not strong enough to rule out inflation. They simply mean that inflation might be different from what we think, or it might be just what we think it is.

Also, not all observations seem to agree with inflationary predictions. It has been pointed out that the angular correlation in the CMB on large scales $>$60 degrees, resides inside our galaxy. If the source of this correlation is to be sought in the galaxy, this means that the large angle correlation on cosmological scales is absent [53]. This is in disagreement with generic predictions of inflation, in which one expects correlations on all scales. An implication could be that inflation started out just at the right moment, to last exactly enough e-folds such that we observe no curvature, no cosmic relics, and just enough large scale correlations. This remains to be investigated further, though.

Chapter 2

From the primordial spectrum to observations

In this chapter we will make the link from the inflationary perturbations to two observables today: the power spectrum of the CMB and the power spectrum of the large scale structure distribution. Also most of this chapter is inspired on Refs. [66, 71, 114, 133, 154, 221].

2.1 The initial conditions from inflation

In Chapter 1 we saw that the map from an averaged background metric to the perturbed physical metric suffers from a gauge dependence. Calculations are most safely performed in gauge-invariant variables or in a specified gauge. I repeat here the perturbed metric, (1.18),

$$ds^2 = a^2(\tau)\left[-(1+2A)d\tau^2 - B_i d\tau dx^i + [(1+2\psi)\delta_{ij} + 2E_{ij}]dx^i dx^j\right]. \quad (2.1)$$

Let us focus on scalar perturbations. The two gauge-invariant quantities describing scalar perturbations are the Bardeen potentials,[11], in Fourier-space,

$$\Psi = A - aHk^{-1}\sigma - k^{-1}\sigma' \quad (2.2)$$

$$\Phi = -\frac{4k^2}{a^2}{}^{(3)}R + Hk^{-1}\sigma, \quad (2.3)$$

for $\hat{\Omega}_k \simeq 0$ and with $\sigma = k^{-1}E_T' - \frac{B}{2}$, the scalar potential for the shear of the hypersurface of constant time (the comoving hypersurface) and ${}^{(3)}R$ the Ricci scalar in the three spatial dimensions, defined on the spatial part of the metric $g_{\rm ij}$. In the newtonian / longitudinal gauge, the Bardeen potentials correspond to the newtonian potentials, $ds^2 = a(\tau)^2\left[-(1+2\Psi)d\tau^2 + (1-2\Phi)\delta_{ij}dx^i dx^j\right]$. Besides, if anisotropic stress is absent, we have $\Phi = \Psi$, which is the case for adiabatic perturbations if neutrinos van be ignored. There is an important re-

lation between the Bardeen potentials and the comoving curvature perturbation $\mathcal{R} \equiv -\frac{4k^2}{a^2}\,{}^{(3)}R_{\rm comoving}$,

$$-\mathcal{R} = \frac{2}{3(1+w)}\left[\Psi + \frac{\dot{\Phi}}{aH}\right] + \Phi. \tag{2.4}$$

Here $w \equiv \bar{P}/\bar{\rho}$, not necessarily a constant, from the unperturbed background stress-energy tensor $T_{00}/a^2 = -\rho\eta_{00}$, $T_{ij}/a^2 = P\eta_{ij}$, with the Minkowsky metric $\eta_{\mu\nu}$. Hence, if $\Phi = \Psi$ and w and Φ are constant, $\mathcal{R} =$ constant $\times\,\Psi$. This is the case on super-hubble scales during radiation or matter domination. All observable scales today were super-hubble at the end of inflation, hence the initial conditions are conveniently set as a constant super-hubble spectrum at the end of inflation, and the evolution in time of any mode in Ψ only becomes important close to re-entering the Hubble radius. For example, on super-hubble scales we have,

$$P_\Psi = \frac{4}{9}P_\mathcal{R}, \qquad \text{for } \tfrac{k}{aH} \ll 1, \qquad w = \frac{1}{3}, \qquad \text{Radiation era,} \tag{2.5}$$

$$P_\Psi = \frac{9}{25}P_\mathcal{R}, \qquad \text{for } \tfrac{k}{aH} \ll 1, \qquad w = 0, \qquad \text{Matter era.} \tag{2.6}$$

$$\tag{2.7}$$

2.2 The Bardeen equation

We gave the definition of the Bardeen potentials, but to derive their evolution, we need to know the energy contents of the universe. To come to the one equation that describes the evolution of the gravitational potential, we first need to define all matter perturbations. Remember that in a homogeneous isotropic background we have $T^\nu_\mu = \text{diag}(-\bar{\rho}, \bar{P}, \bar{P}, \bar{P})$. The most general perturbations can be parameterised as,

$$T^0_0 = -\bar{\rho}(1+\delta), \tag{2.8}$$

$$T^0_j = (\bar{\rho} + \bar{P})(v_j - B_j), \tag{2.9}$$

$$T^j_0 = -(\bar{\rho} + \bar{P})v^j, \tag{2.10}$$

$$T^i_j = \bar{P}\left[(1+\pi_L)\delta^i_j + \Pi^i_j\right]. \tag{2.11}$$

Here δ is the over density, π_L is the isotropic pressure perturbation, v_j represents the energy flux which is the time like eigenvector of T^ν_μ with eigenvalue $\rho = \bar{\rho}(1+\delta)$, B_j is the previously defined metric perturbation, and Π^i_j is the traceless part of the stress tensor, called the anisotropic stress tensor, and can be further decomposed as,

$$\Pi^i_j = \Pi\epsilon^{(S)i}_j + \Pi^{(V)}\epsilon^{(V)i}_j + \Pi^{(T)}\epsilon^{(T)i}_j, \tag{2.12}$$

in its scalar, vector and tensor contributions. Here the $\epsilon^{(S,V,T)}$ are normal projection tensors representing the respective contributions. All $\Pi^{(S,T,V)}$ are gauge invariant by themselves. Other gauge invariant quantities are

$$V \equiv v - \frac{1}{k}\psi', \tag{2.13}$$

$$D_s \equiv \delta + 3(1+w)aH\left(\frac{\psi'}{k^2} - \frac{B}{k}\right), \tag{2.14}$$

$$D \equiv D_s + 3(1+w)\frac{aH}{k}V, \tag{2.15}$$

$$D_g \equiv D_s - 3(1+w)\Phi, \tag{2.16}$$

$$V^V \equiv v^V - \frac{E_V'}{k}, \tag{2.17}$$

$$\Omega \equiv V^V - B^V, \tag{2.18}$$

$$\sigma^V = \Omega - V^V. \tag{2.19}$$

Here we used $v_i = v\epsilon_i^S + v_i^V$ and $B_i^V = B^V\epsilon_i^V$. The Einstein equations describing the metric perturbations contain a number of constraint equations and a number of dynamical equations. Let us focus on the scalar part. The constraint equations read,

$$4\pi G_N a^2 \rho D = -(k^2 - 3K)\Phi, \tag{2.20}$$

$$4\pi G_N a^2(\rho + P)V = k(aH\Psi + \dot{\Phi}). \tag{2.21}$$

The dynamical equations can be recast as the Bardeen equation, where energy conservation has been used,

$$\Phi'' + 3aH(1+c_s^2)\Phi' + \left[3(c_s^2 - w)a^2H^2 - (2 + 3w + 3c_s^2)K + c_s^2k^2\right]\Phi \tag{2.22}$$

$$= \frac{8\pi G_N a^2 P}{k^2}\left[aH\Pi' + \{2(aH)' + 3a^2H^2(1 - c_s^2/w)\}\Pi - \frac{1}{3}k^2\Pi + k^2\Gamma\right], \tag{2.23}$$

where $\Gamma = \pi_L - \frac{c_s^2}{w}\delta$ is proportional to the entropy flux of the perturbations. As mentioned before, $\Gamma = 0$ characterises adiabatic perturbations. The sound speed c_s is defined as $c_s = \frac{\dot{P}}{\dot{\rho}} = \frac{P'}{\rho'}$. Hence, for a pressureless matter, e.g. dust, we have $c_s = w = 0$, such that in a spatially flat and isotropic matter dominated era we have

$$\Phi'' + \frac{6}{\tau}\Phi' = 0, \qquad \text{Matter era}, \tag{2.24}$$

with the general solution $\Phi = \Phi_0 + \frac{\Phi_1}{\tau^5}$. In other words, during the matter era, the linear potential perturbations remain constant, with the decaying term rapidly vanishing.

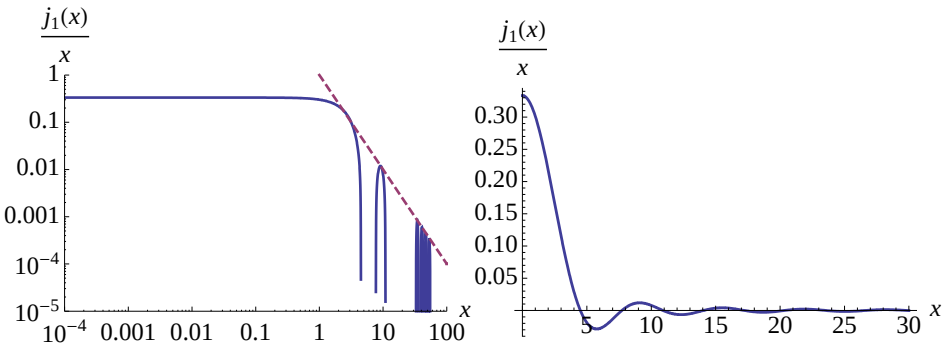

Figure 2.1: The evolution of the Bardeen potential during the radiation era, in arbitrary dimensions, with the $x = c_s k\tau$. A Hubble-radius sized mode corresponds to $x \sim 1$. *Left:* In Log-Log scale the absence of evolution on super-Hubble scales is visible. *Left and right:* The potential oscillates on sub-Hubble scales, with an amplitude decreasing $\propto x^{-2} \propto a(\tau)^{-2}$ (purple dashed line).

In a pure and isotropic radiation fluid, we have $w = \frac{1}{3}$, hence $c_s^2 = w$, and

$$\Psi'' + \frac{4}{\tau}\Psi' + \frac{k^2}{3}\Psi = 0, \qquad \text{Radiation era,} \tag{2.25}$$

which has the general solution $\Psi = \frac{1}{\tau}\left[C_1 j_1(c_s k\tau) + C_2 y_1(c_s k\tau)\right]$, with constants $C_{1,2}$ and the Bessel functions $j_n = \sqrt{\frac{\pi}{2x}} J_{n+\frac{1}{2}}(x)$ and $y_n = \sqrt{\frac{\pi}{2x}} Y_{n+\frac{1}{2}}(x)$. For super hubble scales, *i.e.* $k\tau \ll 1$, we have $\Psi(c_s k\tau) \simeq \frac{1}{3}C_1 + C_2 x^{-3}$, such that for all modes that were super hubble for sufficiently long times (which is the case for observable length scales), we have $\Psi = \frac{C_1}{x} j_1(x) = C_1\left(x^{-3}\sin(x) - x^{-2}\cos(x)\right)$, where $x = c_s k\tau$. Hence, also during radiation era, super-Hubble modes in the Bardeen potentials remain constant, however on sub-Hubble scales they start oscillating and diluting as $\propto a^{-2}$, as is shown in Figure 2.1. These oscillations are the acoustic oscillations of the radiation fluid, which are responsible for the acoustic peaks we observe in the CMB power spectrum.

2.3 Matter power spectrum

In the previous chapter we briefly introduced the power spectrum. The reason that we are interested in power spectra, is that they provide all the statistically interesting information about distributions, of *e.g.* matter of photons. In a sense, the power spectrum contains the information about the common origin of different points on the sky. When considering the origin of the universe, one will always look for similarities in different directions, or, correlations. The presence or absence of the correlations tells about certain properties of the initial state that was or was not shared by different regions. Let us continue to see how the power spectrum of the matter perturbations comes about from the perturbed metric.

On scales that are much smaller than the Hubble radius, the perturbations of the metric become very small in comparison with the perturbations in the stress-

energy tensor. This has the consequence that the difference between $\{D_{(}.), V\}$ and $\{\delta, v\}$ becomes very small. In other words, the gauge dependence of energy and velocity measures becomes negligible. This can also be seen by realising that sub-Hubble means $k/a > H$ in Eqs. (2.13–2.19). The implication is that on sub-Hubble scales we can simply treat $a(\tau)^2\Psi$ as the newtonian potential $a(\tau)^2\psi$. Then Poisson's equation relates the potential to an over-density,

$$\nabla^2\psi = 4\pi G_N \delta\rho, \tag{2.26}$$

or in momentum space

$$-\frac{k^2}{a(\tau)^2}\psi = 4\pi G_N \delta\rho. \tag{2.27}$$

Let us focus on the time behaviour and write $\delta_\rho = \delta\rho/\rho$ and $\rho \propto \rho_0 a(\tau)^{-3}$, such that we find $\delta_\rho \propto a(\tau)\psi$. Hence, $\mathcal{P}_\rho \propto a(\tau)^2\mathcal{P}_\Psi \propto a(\tau)^2\mathcal{P}_\mathcal{R}$. During radiation era, the power spectrum on sub-Hubble scales decreases as $P_\rho \propto a(\tau)^{-2}$, and during matter era grows as $P_\rho \propto a(\tau)$.

To make a translation to the matter power spectrum is slightly more complicated. During the radiation era, $\mathcal{P}_\rho$ describes the perturbations in the dominating energy density component, the photons (and neutrinos). The evolution of the non-relativistic matter is then determined by its behaviour in following the gravitational potential set by the photons, who themselves are not self-gravitating, as their pressure counteracts the gravity. It turns out that the perturbations in the matter grow as $\delta_m \propto \ln a$ during radiation domination. During matter domination they are the dominating energy, hence $\delta_m \propto \delta_\rho \propto a(\tau)^{-2}$.

Modes that re-enter the Hubble radius during radiation era start growing $\propto \ln a$. Modes that enter during matter era, will only experience growth, the smaller modes experiencing the growth earlier as they enter earlier. Along this reasoning, the matter power spectrum must have a change in slope, corresponding to the modes that re-entered the Hubble radius during the matter-to-radiation equality. This is evident in Figure 2.2.

Note that in this reasoning we ignore the fact the the radiation-to-matter transition is gradual, which does have consequences that cannot be ignored (e.g., for a period the matter perturbations will grow logarithmically). Still, this gives a rough but good understanding of the matter power spectrum.

2.4 Temperature anisotropies

With the information at hand, we can already give an estimate of the temperature anisotropies of the CMB. So far we focused on the gravitational evolution of the universe, although in principle the quantities describing the evolution of the radiation-matter mixture in the universe have been defined. Assuming that the evolution is known, and that photons decouple from other matter instantaneously,

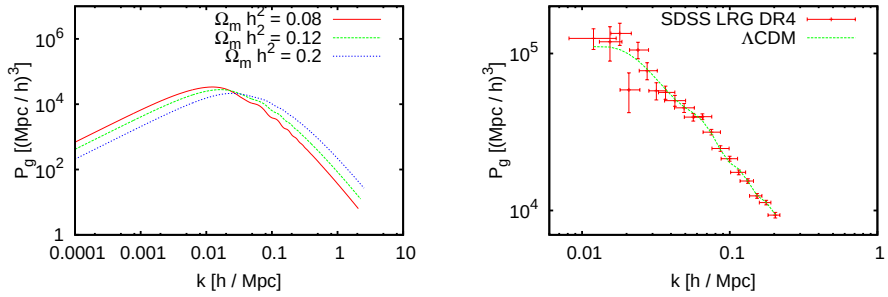

Figure 2.2: *Left:* The matter power spectrum for different values of $\Omega_m h^2$, with $h = H_0/(100 \text{ km s}^{-1}\text{Mpc}^{-1}) = 0.7$, with a scale invariant super Hubble spectrum. *Right:* The best-fit curve for the ΛCDM model in a combined analysis with WMAP 5-yr data and the SDSS LRG DR4 galaxy power spectrum, versus that observed spectrum. All theoretical spectra are calculated using CAMB.

the energy change of a photon between decoupling and detection is defined by,

$$\frac{E_f}{E_i}^{(S)} = \frac{T_0}{T_{\text{dec}}}\left(1 - \left[\tfrac{1}{4}D_g^{(r)} + V_j^{(b)}n^j + \Psi + \Phi\right]_i^f + \int_i^f \left(\Psi' + \Phi'\right) d\tau\right). \quad (2.28)$$

Here $D_g^{(r)}$ denotes the density perturbation in the radiation fluid, $V_j^{(b)}$ denotes the peculiar velocity of the baryonic matter component (emitter and observer), and n^j is the tangent to the photon geodesic at emission / detection. The superscript $^{(S)}$ is to remind the reader that so far we only consider scalar contributions to the anisotropy. If we translate this to the observed temperature anisotropy at our position, we see that all final quantities are the same in all directions, except for $V_j^{(b)}n^j$, such that all final quantities only contribute to the monopole (hence are absorbed in T_0). The term $V_j^{(b)}n^j\Big|^f$ only contributes to the dipole caused by our motion, and is in fact the largest contributor to the dipole. The observed temperature anisotropy for the quadrupole and higher terms is therefore determined by,

$$\frac{\Delta T(\vec{n})}{T}^{(S)} = \left[\tfrac{1}{4}D_g^{(r)} + V_j^{(b)}n^j + \Psi + \Phi\right](t_{\text{dec}}, \vec{x}_{\text{dec}}) + \int_i^f \left(\dot{\Psi} + \dot{\Phi}\right) dt, \quad (2.29)$$

where $\vec{n}$ denotes the direction from which the observer observes the photon ($\vec{n} = n^j|_f$).

If the initial conditions are adiabatic, such that $\Gamma = 0$ and if $\Phi = \Psi$, the first

part of the contribution translates into,

$$\left.\frac{\Delta T(\vec{n})}{T}^{(S)}\right|_{\rm OSW} \equiv \left[\tfrac{1}{4}D_g^{(r)} + V_j^{(b)}n^j + \Psi + \Phi\right](t_{\rm dec}, \vec{x}_{\rm dec}) \tag{2.30}$$

$$= \frac{1}{3}\Psi(t_{\rm dec}, \vec{x}_{\rm dec}) \qquad \text{[ADIABATIC]}, \tag{2.31}$$

on large angular scales, where it is important to realise that the initial conditions are described by adiabatic perturbations, but the evolution on sub-hubble scales does not necessarily stay adiabatic. If the initial conditions are isocurvature, such that $\Psi = \Phi = 0$, the first part of the contribution translates into,

$$\left.\frac{\Delta T(\vec{n})}{T}^{(S)}\right|_{\rm OSW} = 2\Psi(t_{\rm dec}, \vec{x}_{\rm dec}) \qquad \text{[ISOCURVATURE]}, \tag{2.32}$$

again on large angular scales. In these lines, OSW stands for the ordinary Sachs-Wolfe effect, after the first people to derive it. The second term,

$$\left.\frac{\Delta T(\vec{n})}{T}^{(S)}\right|_{\rm ISW} \equiv \int_i^f \left(\dot{\Psi} + \dot{\Phi}\right) dt, \tag{2.33}$$

is the integrated Sachs-Wolfe effect (ISW). The ISW-effect describes the energy gained or lost by a photon due to changing gravitational potentials on its path to the observer. Simply put, if a potential shallows while the photon already entered, the photon gained more energy by falling in than it will loose by climbing out again. It is this effect that can give the CMB the power to distinguish between universes with Dark Energy, massive neutrino's or strong inhomogeneities, as we will see in Part III of this thesis.

As mentioned before, vector perturbations only have decaying solutions and usually can be safely ignored. Tensor perturbations decay on sub-Hubble scales, but in super-Hubble scales are constant. Hence tensor perturbations do contribute to the temperature anisotropy. Without going into further detail, we give their resulting contribution here,

$$\frac{\Delta T(\vec{n})}{T}^{(T)} \equiv \int_i^f \dot{E}_{ij}n^i n^j dt. \tag{2.34}$$

2.4.1 Some ignored but known effects

So far we have only considered the Einstein equations and the rough approximation of describing everything as perfect fluids. We ignored the Boltzmann equations, thereby not paying attention to the differences between photons and baryons and dark matter particles. The difference in mean free path of photons and mean free path of massive particles, leads to diffusion damping. Around decoupling, which is not instantaneous in reality, the period during which the coupling between photons

and baryons is not perfect induces damping of perturbations at a larger range of scales, this is the Silk damping.

The Universe reionises at low redshift ($z \sim 6 - 10$), after which point the photons will interact again with matter, mostly leading to polarisation of the photon fluid. Besides, CMB photons cross galaxies and interact with high-energy electrons on these galaxies, the Sunyaev-Zel'dovich effect.

Besides polarisation, these effects go into too much detail to discuss in this brief overview.

2.4.2 The power spectrum

The CMB in approximation left from a two-dimensional sphere at a distance $r_{\rm dec}$ from the observer. Its power spectrum is therefore best described in terms of spherical harmonics, the spherical counterpart of the Fourier transformation, taking into account the curvature on a sphere.

The power spectrum of an autocorrelation function for a quantity X is defined in general as,

$$a^X_{lm} \equiv \int_0^{2\pi} d\phi \int_0^{\pi} d\theta \; \frac{X(\theta,\phi) - \bar{X}}{\bar{X}} \; Y_{lm}(\theta,\phi) \tag{2.35}$$

$$C^{XX}_l \equiv \frac{1}{2l+1} \sum_{m=-1}^{m=l} \left|a^X_{lm}\right|^2, \tag{2.36}$$

with Y_{lm} being the spherical harmonics, and we take
$\vec{n} = (\cos\phi \sin\theta, \sin\phi \sin\theta, \cos\theta)$. The temperature-temperature correlation, taking into account the different damping effects, is shown in Figure 2.3.

2.5 CMB Polarisation

Although in this thesis we do not deal with the polarisation of the CMB, a future detection of certain modes of polarisation would strongly narrow down the allowed parameter space for inflation. We have seen that a detection of tensors is necessary in order to determine the scale of inflation, in its turn crucial for selecting models. If one could never measure this scale, one might argue that there is no more use in continuing the investigation of inflation, as it would become a 'theory of everything'. Hence, even though there is no direct relation to the following chapters, an introduction to CMB polarisation is inevitable for the motivation for considering inflation on the whole.

As mentioned in Chapter 1, the scattering process that dominates the coupling between photons and massive matter around the time of decoupling, is Thomson scattering. The classical explanation of Thomson scattering is that an electron is accelerated in the oscillating electric field of an incident electromagnetic wave. The acceleration causes the electron in its turn to emit radiation, as the vibration of the electron changes its electric field in an oscillating fashion. Speaking strictly

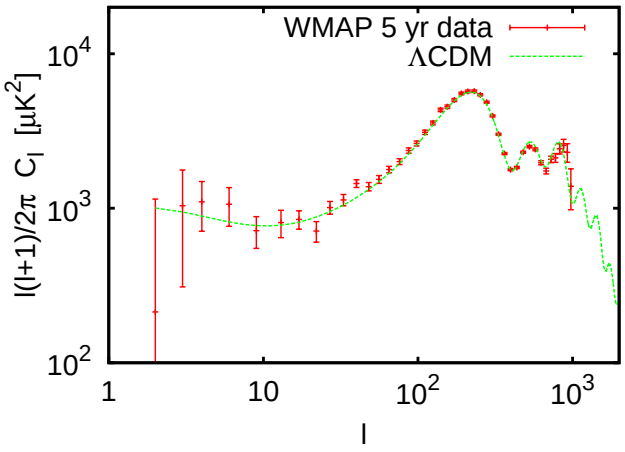

Figure 2.3: The power spectrum of the temperature auto-correlation, in terms of multipoles l. The binned data is the five-year data release from WMAP (in red). The theoretical spectrum represents a ΛCDM model, and is calculated using CAMB.

classically, the electric amplitude of the wave observed at some vector $\vec{n}$ from the electron, is determined by the component of the electric amplitude of the incident wave in the plane perpendicular to the vector describing the direction of the outgoing wave. If the electric field in the incoming wave is orthogonal to the plane of scattering, the outgoing wave will have the same electric field. This is illustrated in Figure 2.4.

Let us turn this classical description into a quantum mechanical picture, albeit still intuitive. Individual photons are described by an electric and a magnetic field, oscillating perpendicular to each other, both perpendicular to the direction of propagation of the photon. If the electron is non-relativistic (which is a condition for Thomson scattering, otherwise we would need the more general description of Compton scattering), the electron will not gain energy from the photon and will scatter the photon in a somewhat random direction. If we remember the classical picture of the electron vibrating along the oscillating electric field of the photon, from Figure 2.4 we can understand that most photons will be scattered in directions that preserve the direction of the electric field of the incoming photon. Or, photons scattered in the direction of the observer will originally mostly have had an electric component perpendicular to the plane of scattering.

Now we come to the point of polarisation of radiation, *i.e.*, a correlation between the individual polarisations in a group of photons. We understand that only photons with a polarisation perpendicular to the plane of scattering are scattered towards the observer. If, from the point of view of the electron, photons come from all directions with random polarisation, the observer will still see random polarisation in the scattered photons. If the electron sees a dipole in the incoming radiation, the observer will still see random polarisation, as photons from left and right of the electron (imaging the dipole to be oriented as such) average each

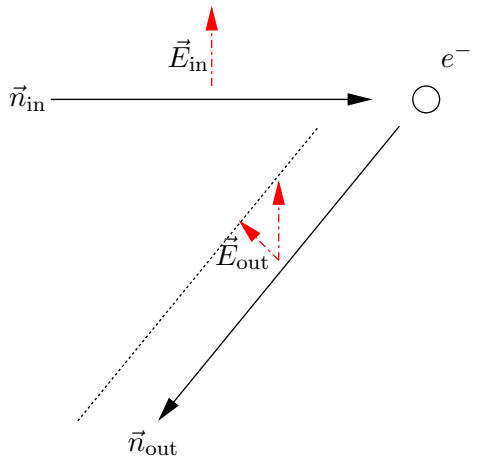

Figure 2.4: A two dimensional sketch of the change of electric field under a scattering on an electron. The electric component of the outgoing wave $\vec{E}_{\rm out} \propto \vec{n}_{\rm out} \cdot \vec{E}_{\rm in}$.

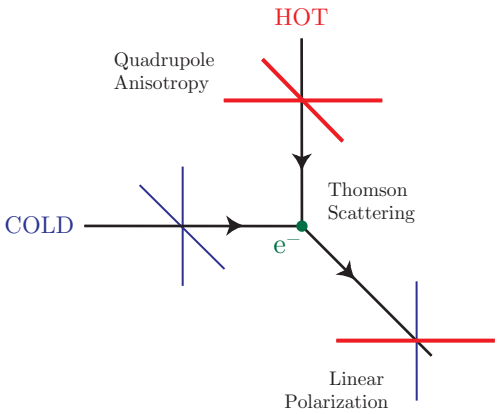

Figure 2.5: After scattering, there will only be a correlation in the polarization of the photons if the electron sees a quadrupole temperature anisotropy. Figure taken from Ref. [14].

other out when ending up in the beam towards the observer. If the electron observes a quadrupole, *e.g.*, more photons coming in from top and bottom and less from left and right, the observer will see a preferred polarisation in the photons, namely a preference for polarisation perpendicular to the plane of scattering of the photons that fell in from top and bottom on the electron. Hence, if there was a temperature quadrupole in the photon fluid at the time of last scattering, we will observe polarisation of the photon fluid today.

For the mathematical description of the polarisation we will closely follow Ref. [14]. The polarisation anisotropy can be described by a 2×2 intensity matrix, $I_{ij}(\hat{n})$, with $\hat{n}$ a direction on the sky. The matrix I_{ij} is defined with respect to orthonormal vectors perpendicular to $\hat{n}$.The linear polarisation is described by the Stokes parameters $Q = \frac{1}{4}(I_{11} - I_{22})$, $U = \frac{1}{2}I_{12}\cos\Delta$ and $V = \frac{1}{2}I_{12}\sin\Delta$. Here Δ denotes a phase difference between oscillations of the electric field along the components $\hat{e}_1$ and $\hat{e}_2$. In nature we do not expect such a phase difference, which would correspond to a circular polarisation component, so we continue with $\Delta = 0$. The temperature anisotropy in terms of I_{ij} is $T = \frac{1}{2}(I_{11} + I_{22})$. The temperature anisotropy describes the field strength of the radiation field, which is independent of a rotation of the $\{\hat{e}_1, \hat{e}_2\}$-basis. Therefore we could describe the temperature anisotropy in terms of a spin-0 spherical harmonics expansions in Eq. (2.36). The parameters Q and U transform as tensors, hence must be expanded using tensor spherical harmonics,

$$Q(\hat{n}) \pm iU(\hat{n}) = \sum_{l=2}^{\infty}\sum_{m=-l}^{m=l} a^{(\pm 2)}\ {}_{\pm 2}Y_{lm}(\hat{n}). \tag{2.37}$$

The $a^{(\pm 2)}$ can be linearly combined to a component that is invariant under a parity transformation $\hat{n} \to \hat{n}' = -\hat{n}$ and a component that keeps the dependence: $e_{lm} = \frac{1}{2}(a^{(2)} + a^{(-2)})$ and $b_{lm} = \frac{1}{2}(a^{(2)} - a^{(-2)})$, such that under $\hat{n} \to \hat{n}' = -\hat{n}$ we have $e_{lm} \to e_{lm}$ and $b_{lm} \to -b_{lm}$. In this basis, the polarisation field takes the form of two spin-0 expansions,

$$E(\hat{n}) = \sum_{l,m} e_{lm}Y_{lm}(\hat{n}), \tag{2.38}$$

$$B(\hat{n}) = \sum_{l,m} b_{lm}Y_{lm}(\hat{n}), \tag{2.39}$$

$$\tag{2.40}$$

The field $E(\hat{n})$ is curl-free, and the field $B(\hat{n})$ is divergence free. Examples of the E-mode and B-mode polarisation are given in Figure 2.6.

The notion of curl- or divergence-free modes has important consequences. Remember that we decomposed the metric perturbations in curl-free modes and divergence-free modes in order to distinguish between scalar, vector and tensor contributions. Therefore, the B-modes can not be produced at first order by scalar perturbations. Simply put, the scalar perturbations of the metric cannot

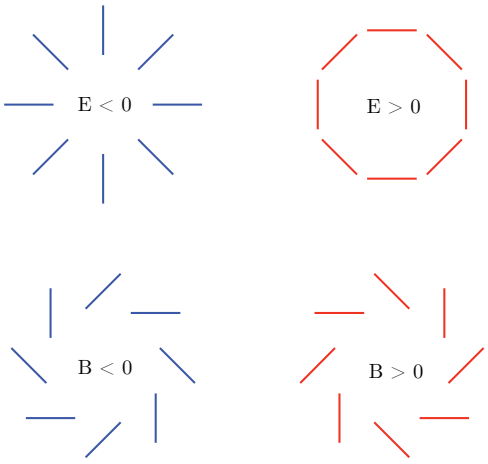

Figure 2.6: The E-modes are curl-free, the B-modes are divergence free, but have a 'handedness'. Figure taken from Ref. [14].

have a 'handedness', and therefore will not give observably correlated B-mode polarisation beyond an expectable random noise. The other way around, tensor perturbations in the metric will give both E- and B-mode polarisation.

As with temperature anisotropies, anisotropy in E-mode polarisation will constrain cosmological parameters because they give a direct look at the (local) temperature quadrupole at decoupling, but they cannot break the degeneracy between scalar and tensor perturbations. B-modes can. That is why one of the points of focus of near future CMB-experiments is to observe a non-zero B-mode polarisation in the CMB. If this possible smoking gun of inflation would not exist, one should ask wether inflation is worth considering at all. Of course, care has to be taken of possible foregrounds of gravitational waves [83, 84, 96, 135]

2.6 Non-Gaussianity

When discussing inflation in Chapter 1, we assumed that inflation could be described by a single, free scalar field. We assumed that the initial conditions for the quantum fluctuations were given by the Bunch-Davies vacuum in the far ultraviolet. From these assumptions it follows that the inflaton fluctuations are drawn from a Gaussian distribution, and the linear perturbations in the gravitational potential at the time of decoupling are still Gaussian. The following description is along the lines of Ref. [134].

A lot of attention nowadays is being paid to the possibility of the cosmic perturbations being slightly non-Gaussian. Although the rest of this thesis does not deal with non-gaussianities, it is worth mentioning here just like polarisation in the previous section, because a detection of non-gaussianity would have strong consequences for inflation.

If perturbations in the inflaton field are strictly Gaussian, the perturbations

in the gravitational potential at decoupling is correctly described by linear perturbation theory, $\Phi = \Phi_{\rm L}$. If it is not, its deviation from the linear theory is parametrized by $f_{\rm NL}$,

$$\Phi = \Phi_{\rm L} + f_{\rm NL}\Phi_{\rm L}^2. \tag{2.41}$$

We already observe that $\Phi \sim \mathcal{O}(10^{-5})$, so corrections to the linear potential are smaller then $\Phi_{\rm L}$ by a factor $10^{-5} f_{\rm NL}$. Observations today constrain $f_{\rm NL} < 10^2$, hence the corrections to the linear potential are less than 0.1%. Yet, from higher order corrections to the potential from a free single scalar field, we expect corrections only of order $f_{\rm NL} \sim \mathcal{O}(10^{-2})$. Therefore, measuring $f_{\rm NL} \sim \mathcal{O}(10^2)$ would imply that either (a) the inflaton is not a single scalar field, or (b) the relation between the inflaton ϕ and the curvature $\mathcal{R}$ is non-linear, or (c) the initial conditions for the scalar-field quantum fluctuations are not properly described by the Bunch-Davies vacuum.

Part II

Constraints from primordial perturbations

Chapter 3

The inflaton potential: probing $V(\phi)$

In this chapter, we will use two data sets of different observables at the same time, to constrain the shape of the inflaton potential. We combine an observation of the CMB from the third year data release of WMAP with the Luminous Red Galaxy power spectrum from the fourth data release of SDSS. As explained in chapters 1 and 2, the observed correlation functions of the CMB and the LSS are directly related to the shape of the primordial power spectra $\mathcal{P}_{\mathcal{R}}$ and $\mathcal{P}_h$, present on super-Hubble scales at the beginning of the radiation era. The primordial power spectrum in its turn, is directly related to the expansion history during inflation, since there is a relation between the Hubble radius at a given moment and the amplitude of the modes that exit the Hubble radius at that time. Previous similar analyses in the literature, usually first found constraints on the parameters describing the primordial power spectrum, and then theoretically inferred bounds on the inflaton potential. In this chapter, we will not make that intermediate step: we numerically calculate the theoretical observables today directly from a number of parameters describing the inflaton potential, and compare those to the actually observed quantities. By removing the intermediate step, we obtain more accurate constraints on the inflaton potential than others did before us.

The parameters we use to describe the inflationary history are the lowest order parameters in a Taylor expansion of the potential, (varying from two to four derivatives of the potential with respect to the scalar field ϕ), hence describing the potential as a Taylor expansion, and the initial velocity of the scalar field $\dot{\phi}$. We take the value of the scalar field at which we perform the Taylor expansion to be corresponding to the middle of the range in momentum space over which the observed spectra extend.

In this study, we are only interested in how far we can constrain the inflaton potential within the range of observable modes, and we shall not extrapolate the inflaton potential all the way to the end of inflation, thereby minimising the theoretical prior on the shape of the potential.

3.1 Introduction

Cosmological inflation is known to be a successful paradigm providing self-consistent initial conditions to the standard cosmological scenario [99, 112, 161, 163, 228, 244] and explaining the generation of primordial cosmological perturbations [1, 12, 100, 111, 162, 226, 243, 245]. The distribution of Cosmic Microwave Background (CMB) anisotropies, as observed for instance by the Wilkinson Microwave Anisotropy Probe (WMAP) [113, 119, 198, 240], is compatible with the simplest class of inflationary models called *single-field inflation*.

The definition of single-field inflation is not unique: for instance, some authors consider hybrid inflation [52, 88, 164, 165] as a multi-field model, since it involves one scalar field in addition to the inflaton field (the role of the second field being to trigger the end of inflation). In this work, we call *single-field inflation* any model in which the observable primordial spectrum of scalar and tensor metric perturbations can be computed using the equation of motion of a single field. This definition does include usual models of hybrid inflation.

The goal of this paper is to derive from up-to-date cosmological data some constraints on the scalar potential $V(\phi)$ of single-field inflation. This question has already been addressed in many interesting works since the publication of WMAP 3-year results [40, 56, 64, 65, 73, 78, 129, 179, 201, 202, 220, 240] (see also [49] for earlier results). Our approach is however different, since all these references assume either that the slow-roll formalism can be applied (at first or second order), or that the scalar potential can be extrapolated from the region directly constrained by the data till the end of inflation. We want to relax these two restrictions simultaneously, and to derive constraints on the *observable part of the inflaton potential* under the only assumption that $V(\phi)$ is smooth enough for being Taylor-expanded at some low order in the region of interest. In this respect, our work is still not completely general and does not explore possible sharp features in the inflaton potential (see e.g. [56, 179] for recent proposals). Throughout the abundant literature on the inflaton potential reconstruction, the work following the closest methodology to ours is the pre-WMAP paper of Grivell and Liddle [95].

The question of whether the slow-roll formalism can be safely employed or not is intimately related to the magnitude of a possible *running of the tilt* in the primordial spectrum of curvature perturbations. In order to clarify this point, lets us first recall that the slow-roll formalism [158, 225, 249] consists in employing analytical expressions for the primordial spectrum of curvature perturbations $\mathcal{P}_{\mathcal{R}}(k)$ and gravitational waves $\mathcal{P}_h(k)$. Such expressions hold in the limit in which the first and second logarithmic derivative of the Hubble parameter H with respect to the e-fold number $N \equiv \ln a$ remain smaller than one throughout the $\Delta N \sim 10$ observable e-folds of inflation (i.e., over the period during which observable Fourier modes cross the Hubble radius). Deep inside this limit, the primordial spectra are given by

$$\mathcal{P}_{\mathcal{R}}(k) \simeq -\frac{H^2}{\pi m_P^2 (d\ln H/dN)} \ , \quad \mathcal{P}_h(k) \simeq -\frac{16H^2}{\pi m_P^2} \ , \tag{3.1}$$

where the right-hand sides are evaluated at Hubble crossing. The first-order expression of the scalar/tensor tilts $n_{S,T}$ and tilt runnings $\alpha_{S,T}$ can be easily obtained by taking the derivative of the above expressions, using the slow-roll approximation $d/d\ln k \simeq d/dN$. The derivation of higher-order expressions is more involved (see e.g. [39, 42, 44, 62, 67, 92, 101, 110, 122, 123, 145, 155, 159, 230, 250, 251]).

Current data clearly indicate that around the pivot scale at which the amplitudes, tilts and runnings are defined (usually, the median scale probed by the data), the tensor-to-scalar ratio is small and the scalar tilt is close to one. This is sufficient for proving that the two slow-roll conditions are well satisfied around the middle of the observable e-fold range. However, depending on the inflaton potential, higher derivatives $d^n \ln H/dN^n$ (with $n \geq 3$) could be large near the pivot scale, leading to a sizeable tilt running α_S and eventually to a situation in which slow-roll would hold only marginally at the beginning and/or at the end of the observable e-fold range. This explains why the two issues of large $|\alpha_S|$ and slow-roll validity are closely related (as recently emphasised in [171]).

Since models with a large running imply that the two slow-roll conditions become nearly saturated near the ends of the observable potential range, a naive

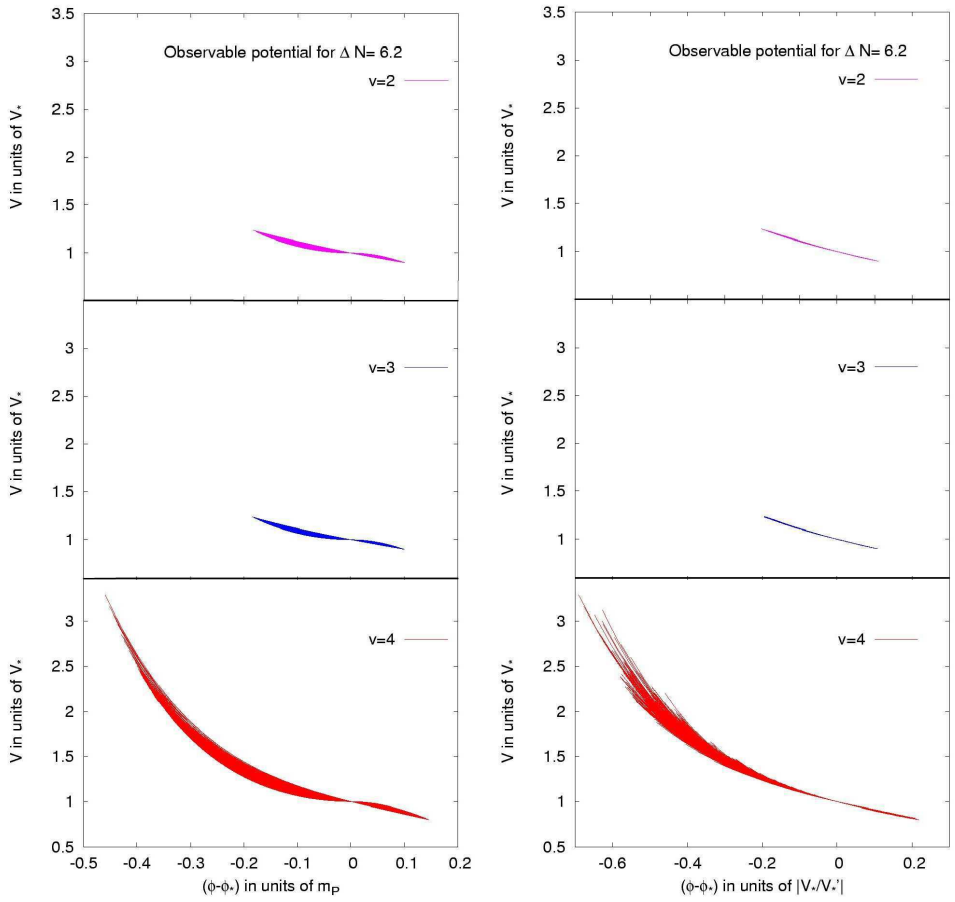

Figure 3.1: Observable region of the inflaton potential allowed at the 95% C.L. by the WMAP 3-year and Sloan Luminous Red Galaxy survey (SDSS-LRG) data, for a Taylor expansion of the potential at order $v = 2$ (top), $v = 3$ (middle) or $v = 4$ (bottom), in the vicinity of the pivot value ϕ_*. In all diagrams the potentials are normalised to their value at the pivot scale ϕ_*. For clarity, in the right diagrams, the field is expressed in units of $|V_*/V'_*|$ instead of m_P, so all curves have by definition the same slope in $\phi = \phi_*$. In practice, these plots show the superposition of 95% of the potentials from our MCMC chains with the best likelihood (after removal of the burn-in phase). Each potential is plotted in a range $[\phi_1, \phi_2]$ corresponding to Hubble exit for modes in the range $[k_1, k_2]$=$[2 \times 10^{-4}, 0.1]$ Mpc^{-1} which is most constrained by the data. This corresponds roughly to a history of 6.2 e-folds. We only show here potentials with a negative slope, but their image under the $\phi \longrightarrow -\phi$ symmetry are equivalent solutions. At first sight, on the top left diagram, $v = 2$ potentials seem to have a non-zero third derivative, but this impression comes only from the superposition of many lines with varying length and slope.

extrapolation would suggest that they cannot sustain inflation for much more than the observable $\delta N \sim 10$ e-folds. However, it is always conceptually easy to extrapolate the potential in order to get the necessary 50 or 60 inflationary e-folds after our observable universe has left the Hubble radius, or to obtain arbitrary long inflation before that time. Potentials designed in that way might not have simple analytical expressions. This should not be a major concern e.g. for physicists trying to derive inflation from string theory, in which the *landscape* designed by the multi-dimensional scalar potential can be very complicated, leading *a priori* to any possible shape for the effective potential of the degree of freedom driving inflation. However, it is clear that models inducing large running are not as simple and minimalistic as those with negligible running. But since they are not excluded, they should still be considered in conservative works such as the present one.

In section 3.2, we will follow a conventional approach and fit directly the Taylor-expanded primordial spectra to the data. Like most other authors, we will conclude that: (i) the data provides absolutely no indication for $\alpha_S \neq 0$, and (ii) given the current precision of the data, a large running is nevertheless still allowed. We will show that similar conclusions also apply to the running of the running β_S.

In section 3.3, which contains our main original results, we will fit directly the Taylor-expanded scalar potential of the inflaton to the data. Our reconstructed potentials are displayed in Fig. 3.1. Unless we impose a "no-running theoretical prior" (i.e., the prejudice that inflation is deep inside the slow-roll regime), our potentials will freely explore the region in parameter space where the running (and eventually the running of the running) are as large as found in section 3.2. So, for self-consistency, we must forget about the slow-roll formalism and compute the exact primordial spectra numerically (as Ref. [179] did for various specific expressions of the potentials). In a very nice work, Ref. [171] gave a few examples of scalar potentials leading to the largest $|\alpha_S|$ values allowed by the data, and showed that even in these cases the second-order slow-roll formalism, although inaccurate, remains a reasonable approximation. In the present systematic analysis, which explores the full parameter space of smooth inflationary potentials, we will see that this conclusion does not apply in all cases.

3.2 Fitting the primordial spectrum

Primordial spectrum parameterisation. The usual way of testing inflationary models without making too many assumptions on the inflaton potential is to fit some smooth scalar/tensor primordial spectra, parametrized as a Taylor expansion of $\ln \mathcal{P}$ with respect to $\ln k$,

$$\ln \frac{\mathcal{P}_{\mathcal{R}}(k)}{\mathcal{P}_{\mathcal{R}}(k_*)} = (n_S - 1) \ln \frac{k}{k_*} + \frac{\alpha_S}{2} \ln^2 \frac{k}{k_*} + \frac{\beta_S}{6} \ln^3 \frac{k}{k_*} ..., \tag{3.2}$$

and the same holds for $\mathcal{P}_h$ as a function of n_T, α_T and β_T. In single-field inflation, the coefficients of the scalar and tensor spectra are related through the

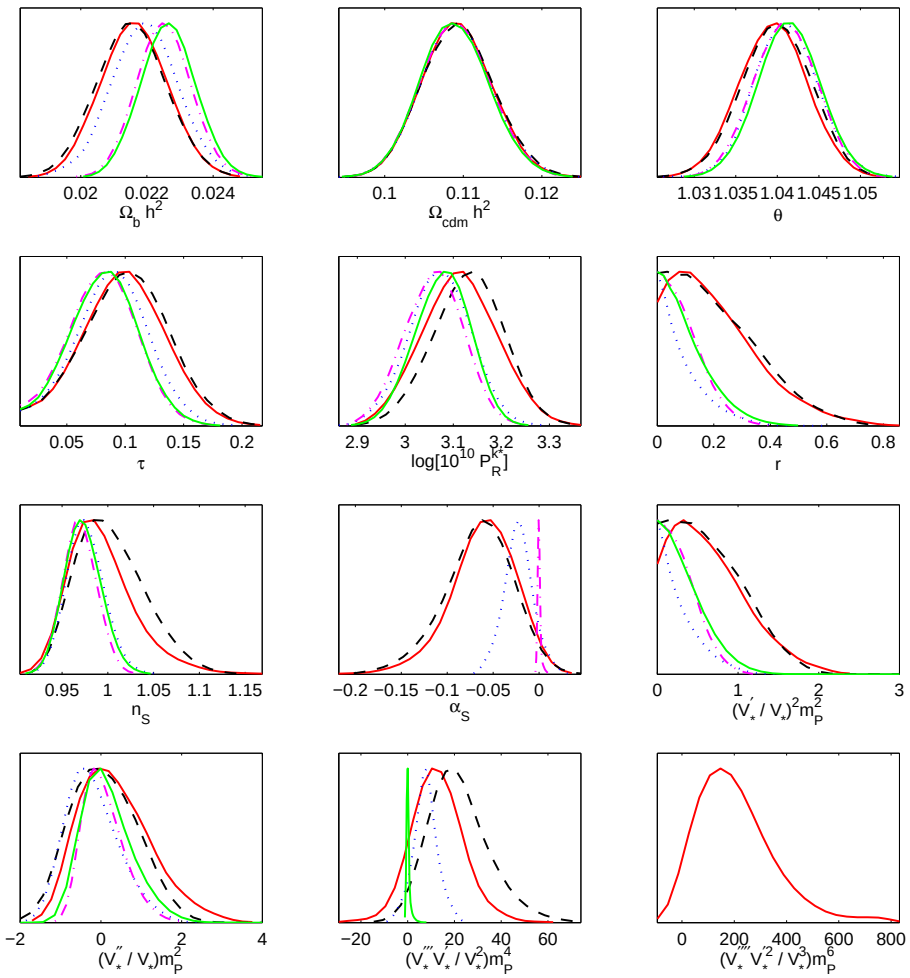

Figure 3.2: Probability distribution of cosmological and inflationary parameters for the models of section 3.2: $p = 2$ (green/light solid), $p = 3$ (black dashed), and the models of section 3.3: $v = 2$ (magenta dot-dashed), $v = 3$ (blue dotted), $v = 4$ (red/dark solid). For the runs of section 3.2, the free parameters (with flat priors) are the first eight parameters; the corresponding probability for the potential parameters are derived from second-order slow-roll formulae (involving V_* to V_*''', so the inferred value of V_*'''' remains undetermined). Instead, for the runs of section 3.3, the free parameters are the first five and the last four; the amplitude parameter in the fifth plot is then defined as $\ln\left[10^{10}\frac{128\pi V_*^3}{3V_*'^2 m_P^6}\right]$; the corresponding r, n_S and α_S are derived from the exact primordial spectra. The data consists of the WMAP 3-year results [113, 119, 198, 240] and the SDSS LRG spectrum [255].

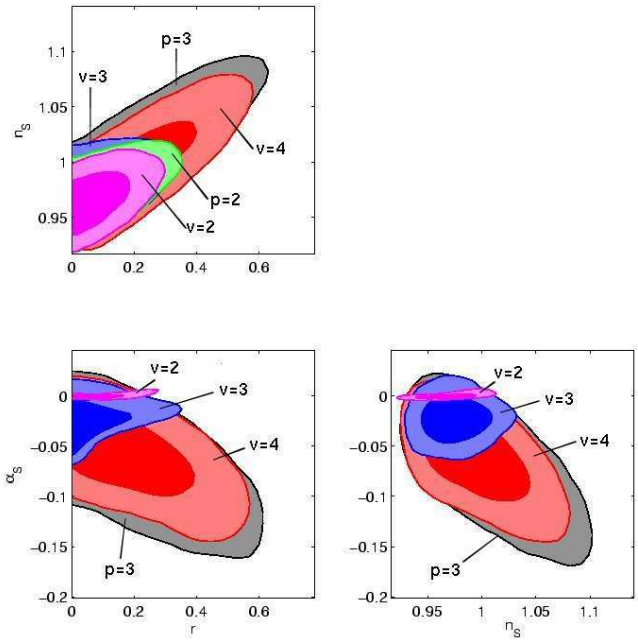

Figure 3.3: Two-dimensional 68% and 95% confidence level contours based on WMAP 3-year and the SDSS LRG spectrum for the parameters describing the primordial spectra, obtained directly from the MCMC in the case of models $p = 2$ (green) and $p = 3$ (black), or derived form the exact spectra for models $v = 2$ (magenta), $v = 3$ (blue), $v = 4$ (red).

approximate self-consistency relation

$$\frac{d\ln\mathcal{P}_h(k)}{d\ln k} \simeq \frac{1}{8}\frac{\mathcal{P}_h(k)}{\mathcal{P}_{\mathcal{R}}(k)} \tag{3.3}$$

which follows trivially from Eq. (3.1) and becomes exact deep in the slow-roll limit. The sensitivity of current data to gravitational waves is very low, with loose constraints on the *shape* of $\mathcal{P}_h$. So, even if the slow-roll formalism might become inaccurate in some cases, the data can be fitted assuming that Eq. (3.3) is exact. In other words, for practical purposes, we can safely use the hierarchy of relations derived from Eq.(3.3),

$$n_T = -r/8, \qquad \alpha_T = n_T[n_T - n_S + 1], \qquad \text{etc.}, \tag{3.4}$$

where $r \equiv \mathcal{P}_h(k_*)/\mathcal{P}_{\mathcal{R}}(k_*)$. So, if we decide to Taylor expand the scalar spectrum with p independent coefficients, the total number of free inflationary parameters in the problem is $p+1$, including the tensor-to-scalar amplitude ratio at the pivot scale.

In principle, p should be chosen according to Occam's razor: when increasing p does not improve sufficiently the goodness-of-fit, it is time to stop. In a Bayesian analysis, this question is addressed by the computation of the Bayesian evidence [15, 140, 156, 157, 199, 200, 242, 260]. However, when the evidence does

Parameter	$p=2$	$p=3$	$p=4$
$\Omega_b h^2$	0.0226 ± 0.001	0.022 ± 0.001	0.021 ± 0.001
$\Omega_{cdm} h^2$	0.109 ± 0.004	0.109 ± 0.004	0.109 ± 0.005
θ	1.041 ± 0.004	1.040 ± 0.004	1.041 ± 0.004
τ	0.08 ± 0.01	0.10 ± 0.02	0.10 ± 0.02
$\ln[10^{10}\mathcal{P}_{\mathcal{R}}^{k_*}]$	3.08 ± 0.06	3.13 ± 0.07	3.13 ± 0.07
r	< 0.13	< 0.3	< 0.3
n_S	0.97 ± 0.02	1.00 ± 0.04	1.03 ± 0.05
α_S	0	-0.07 ± 0.04	-0.07 ± 0.04
β_S	0	0	-0.04 ± 0.04
$-\ln \mathcal{L}_{\max}$	2688.3	2687.1	2686.5
E	1	1.2	1.4

Table 3.1: Bayesian 68% confidence limits for ΛCDM inflationary models with $p = 2, 3, 4$ coefficients in the logarithmic Taylor expansion of the scalar primordial spectrum. The last lines show the maximum likelihood value and the Bayesian Evidence (relative to that of $p = 2$). The data consists in the WMAP 3-year results [113, 119, 198, 240] and the SDSS-LRG spectrum [255], as implemented in COSMOMC [152].

not vary significantly as a function of p, the decision of stopping the expansion remains a personal choice to some extent, and more conservative works should consider higher p values.

The issue of varying p is important in two respects: first, one needs to know how many independent informations the data is providing, i.e., how smooth/complicated the inflaton potential needs to be (for addressing this issue, one could also perform a principal component analysis [143]); second, it is useful to know whether the bounds on a given cosmological/inflationary parameter θ_i are independent of p, or subject to variations when p increases, due to the appearance of new parameter degeneracies.

Results. In order to address these two points, we performed some global parameter fits using the public code COSMOMC [152], with p varying from two (scalar amplitude and tilt) to four (including the tilt running, as well as the running of the running). Our results are summarised in Table 3.1. The relative Bayesian evidence of each model can be easily computed, since the models are nested inside each other [260]. However, this calculation forces us to choose some explicit Bayesian priors for α_S and β_S. Pushing inflation to its limits, we notice that the second slow-roll parameter can in principle vary between plus and minus one, so the scalar tilt could take any value between zero and two. Extreme runnings could be observed in ad-hoc inflationary models such that during the observable e-folds, corresponding to four decades in k space, n_S evolves from 0 to 2 or vice-versa. So, the α_S prior can be chosen to be a top-hat centred on zero with $\Delta\alpha_S = 4/\ln(10^4) \sim 0.4$. Similarly, extreme values of β_S correspond to n_S passing through the sequence 0-2-0 or 2-0-2. This leads to a prior width

$\Delta\beta_S = 16/\ln^2(10^4) \sim 0.2$. With such priors, the Bayesian evidence E increases by a factor

$$\frac{E_{p=3}}{E_{p=2}} = [\mathcal{P}(\alpha_S = 0)\,\Delta\alpha_s]^{-1} = [2.1 \times 0.4]^{-1} = 1.2 \tag{3.5}$$

when α_S is added, and again by

$$\frac{E_{p=4}}{E_{p=3}} = [\mathcal{P}(\beta_S = 0)\,\Delta\beta_s]^{-1} = [6.2 \times 0.2]^{-1} = 1.2 \tag{3.6}$$

when β_S is introduced. These numbers are too close to one for drawing definite conclusions: the extra parameters are neither required, neither disfavoured by Occam's Razor.

Table 3.1 shows that adding α_S has a small impact on the probability distribution of $\Omega_b h^2$, τ, r, $\mathcal{P}_{\mathcal{R}}(k_*)$ and n_S, as found in previous works. However, it is reassuring to note that adding β_S leave all bounds perfectly stable, except for a small shift to higher n_s values. This suggests that including a few higher derivatives beyond α_S does not open new parameter degeneracies (this conclusion would probably break if the number of free parameters becomes much larger). Figs. 3.2, 3.3 show the likelihood distribution of each parameter as well as some two-dimensional confidence regions for models $p = 2$ (green lines) and $p = 3$ (black lines).

Impact of small CMB multipoles. The smallest multipoles in the CMB temperature and polarization maps are still controversial. In WMAP data (as well as in previous COBE data), the temperature quadrupoles and octopoles are surprisingly small, while their orientations seem to be correlated (between each other and with the ecliptic plane). Many authors have been investigating possible foregrounds or systematics which could affect these small multipoles (see e.g. [53–55, 229] and references therein). So, it is legitimate to study whether the quadrupole and octopole data have a significant impact on our bounds for the primordial spectrum parameters (a priori, these low temperature multipoles could be partially responsible for the preferred negative value of the tilt).

We repeated the $p = 3$ analysis after cutting the temperature and polarization data at $l = 2, 3$. We found that all probabilities are essentially unchanged, including that for running (the mean value only moves from -0.67 to -0.66, which is not significant given the precision of the runs). We conclude that our results are independent of the robustness of low multipole data.[1]

Impact of extra CMB data. There are also discussions about a possible small mismatch in the amplitude of the third acoustic peak probed on the one hand by WMAP, and on the other hand by Boomerang [120] or other small-scale CMB experiments. We repeated the $p = 2$ and $p = 3$ analysis including extra data

[1] This result is consistent with that of Ref. [49], which shows that evidence for running is more related to anomalies around $l \sim 40$.

from Boomerang [120], ACBAR [141] and CBI [235]. The impact on inflationary parameter is found to be very small, although in the $p = 3$ case the bound on r gets weaker by 20% and the preferred value of α_S goes down by the same amount (i.e., the case for negative running becomes slightly stronger). Other bounds are essentially unchanged. In what follows, we will not include these data sets anymore.

Expectations for the inflaton potential. In the next section, we will directly fit the inflaton potential $V(\phi)$, parametrized as a Taylor expansion near the value ϕ_* corresponding to Hubble crossing for the pivot scale k_*. We expect that a global fit with $V(\phi)$ expanded at order v will provide the same qualitative features as the previous power spectrum fit of order $p = v$:

- order $v = 2$ ($V''' = 0$) should be sufficient for explaining the data, and will not lead to significant running or deviation from slow-roll. Indeed, the smallness of r and $|n_S - 1|$ guarantees that the two slow-roll conditions are well satisfied at least near ϕ_*. In addition, with $V''' = 0$, they should remain well satisfied on the edges of the spectrum, and no significant running can be generated.
- order $v \geq 3$ ($V'''' = 0$) should not be required by the data, but remains interesting since it will explore the possibility of large running and shift the other parameter distributions as in the previous $p = 3$ case. The slow-roll parameters could then become large near the edges, so it is necessary to compute the spectra numerically rather than using any slow-roll approximation.

The results of the next section will confirm this expectation, and prove that order $v = 4$ is necessary for exploring the full range of α_s probed by the $p = 3$ run.

3.3 Fitting the scalar potential

Computing the power spectra numerically. In order to fit directly the inflaton potential, we wrote a new COSMOMC module which computes the scalar and tensor primordial spectra exactly, for any given function $V(\phi - \phi_*)$. This module can be downloaded from the website `http://wwwlapp.in2p3.fr/~lesgourgues/inflation/`, and easily implemented into COSMOMC.

In its present form, our code is not designed for models with very strong deviations from slow-roll. For such extreme models, a given function $V(\phi - \phi_*)$ would not lead to a unique set of primordial spectra $\mathcal{P}_\mathcal{R}(k)$, $\mathcal{P}_h(k)$: the result would depend on the initial conditions in phase space. We decide to limit ourselves to models such that throughout the observable range, the field remains close to the attractor solution for which $\dot{\phi}$ is a unique function ϕ. In this case, a given function $V(\phi - \phi_*)$ does lead to unique primordial spectra, and we do not need to introduce an extra parameter $\dot{\phi}_{\rm ini}$. Since the goal of this paper is to test inflationary potentials leading to smooth primordial spectra, this restriction is

sufficient. In particular, it enables to explore models for which the running α_S is large, deviations from slow-roll are significant, and analytical derivations of the spectra are inaccurate. However, our code cannot deal with the case in which inflation starts just when our observable universe crosses the horizon (for which $\dot{\phi}_{\rm ini}$ would be a crucial extra free parameter).

In COSMOMC, we fix once and for all the value of the pivot scale $k_* = 0.01$ Mpc^{-1}. Then, for each function $V(\phi - \phi_*)$ passed by COSMOMC, our code computes the spectra $\mathcal{P}_\mathcal{R}(k)$, $\mathcal{P}_h(k)$ within the range $[k_{\rm min}, k_{\rm max}] = [5 \times 10^{-6}, 5]$ Mpc^{-1} needed by CAMB, imposing that $aH = k_*$ when $\phi = \phi_*$. So, the code finds the attractor solution around $\phi = \phi_*$, computes H_* and normalises the scale factor so that $a_* = k_*/H_*$. Then, each mode is integrated numerically for k/aH varying between two adjustable ratios: here, 50 and $1/50$. So, the earliest (resp. latest) time considered in the code is that when $k_{\rm min}/aH = 50$ (resp. $k_{\rm max}/aH = 1/50$), which in the attractor solution uniquely determines extreme values of $(\phi - \phi_*)$ according to some potential. In the code this is translated to demanding that aH grows according to the aforementioned ratios: by $50k_*/k_{\rm min}$ before $\phi = \phi_*$, and by $50k_{\rm max}/k_*$ afterwards. Hence, one of the preliminary tasks of the code is to find the earliest time. If by then, a unique attractor solution for the background field cannot be found within a given accuracy (10% for $\dot{\phi}_{\rm ini}$), the model is rejected. So, we implicitly assume that inflation starts at least a few e-folds before the present Hubble scale exits the horizon. In addition, we impose a positive, monotonic potential and an accelerating scale factor during the period of interest. This prescription discards any models with a bump in the inflaton potential or a short disruption of inflation, that could produce sharp features in the power spectra.

As a result of the chosen method, the potential is slightly extrapolated beyond the observable window, in order to reach the mentioned conditions for the beginning and ending of the numerical integration. Although this seems to be in contradiction with the purpose of this paper, i.e. to probe only the observable potential, this extrapolation cannot be avoided if we want to keep the number of free parameters as small as possible. Note that the range of extrapolation is still very small in comparison with an extrapolation over the full duration of inflation after the observable modes have exited the Hubble radius.

In this approach we need not make any assumption about reheating and the duration of the radiation era. As explained in Ref. [220], the evolution during reheating determines the redshift z_* at which presently observed perturbations left the Hubble radius during inflation. Probing only the observable window of perturbations, we are allowed to let the subsequent evolution of inflation and reheating, hence the number of e-folds and thereby the redshift z_*, be unknown.

Parameterisation. The inflaton potential is Taylor expanded up to a fixed order, and we let COSMOMC probe different values for the derivatives of the inflaton potential at the pivot scale. Since Monte Carlo Markov Chains (MCMC) converge faster if the probed parameters are nearly Gaussian distributed, in fact we recombine to potential parameters in such a way as to probe nearly Gaussian

Parameter	$v=2$	$v=3$	$v=4$
$\Omega_b h^2$	0.022 ± 0.001	0.022 ± 0.001	0.022 ± 0.001
$\Omega_{cdm} h^2$	0.109 ± 0.004	0.109 ± 0.004	0.109 ± 0.004
θ	1.041 ± 0.004	1.041 ± 0.004	1.040 ± 0.004
τ	0.08 ± 0.03	0.09 ± 0.03	0.10 ± 0.03
$\ln\left[\frac{128\pi 10^{10} V_*^3}{3 V_*'^2 m_P^6}\right]$	3.06 ± 0.06	3.07 ± 0.06	3.11 ± 0.08
$\left(\frac{V_*'}{V_*}\right)^2 m_P^2$	< 0.4	< 0.4	< 0.8
$\frac{V_*''}{V_*} m_P^2$	0.1 ± 0.5	-0.2 ± 0.6	0.4 ± 0.9
$\frac{V_*'''}{V_*}\frac{V_*'}{V_*} m_P^4$	0	8 ± 5	13 ± 11
$\frac{V_*''''}{V_*}\left(\frac{V_*'}{V_*}\right)^2 m_P^6$	0	0	200 ± 150
$-\ln \mathcal{L}_{\max}$	2688.3	2687.2	2687.2

Table 3.2: Bayesian 68% confidence limits for ΛCDM inflationary models with a Taylor expansion of the inflaton potential at order $v = 2, 3, 4$ (with the primordial spectra computed numerically). The last line shows the maximum likelihood value. The data consists of the WMAP 3-year results [113, 119, 198, 240] and the SDSS LRG spectrum [255], as implemented in COSMOMC [152].

combinations. These combinations are inspired by the slow-roll expression of the spectral parameters ($\mathcal{P}_\mathcal{R}(k_*)$, n_S, α_S and r) as a function of the potential. We use an amplitude parameter $\frac{128\pi}{3}\frac{V_*^3}{V_*'^2 m_P^6}$, which is equal to $\mathcal{P}_\mathcal{R}(k_*)$ at leading order in a slow-roll expansion. The other spectral parameters consist of linear combinations of $(V_*'/V_*)^2$, V_*''/V, $(V_*'''/V_*)(V_*'/V_*)$ and $(V_*''''/V_*)(V_*'/V_*)^2$. Hence it is most likely to find nearly Gaussian shapes for these products in stead of the sole potential derivatives. For the actual expressions for the spectral parameters in terms of the inflaton potential, we refer the reader e.g. to section IV of [145].

In order to compare the results for the runs with $v = 2, 3, 4$ with those of the previous section, we calculate the spectral parameters of each model numerically. The other way around, we also invert the slow-roll expansion in order to compare the $v = 2, 3, 4$ and $p = 2, 3$ models in potential-derivative space. Defining $\epsilon_0 \equiv H(N_I)/H(N)$ and $\epsilon_{n+1} \equiv \frac{d\ln|\epsilon_n|}{dN}$, where $N = \ln\frac{a}{a_i}$ and H_i is some initial value

of the Hubble factor, the inversion is given by

$$\begin{aligned}\epsilon_1 &= \frac{r}{16}+\frac{C_1}{16}\left(\frac{r^2}{8}+(n_S-1)r\right)\\ &\quad +\mathcal{O}\left(r^3,(n_S-1)^3,\alpha_S^3\right), \qquad (3.7)\\ \epsilon_2 &= -(ns-1)+C_1\alpha_S-\frac{r}{8}-\frac{r}{8}(ns-1)\left(C_1-\frac{3}{2}\right)\\ &\quad -\left(\frac{r}{8}\right)^2(C_1-1)+\mathcal{O}\left(r^3,(n_S-1)^3,\alpha_S^3\right), \qquad (3.8)\\ \epsilon_2\epsilon_3 &= \frac{1}{8}\left(\frac{r^2}{8}+(n_S-1)r-8\alpha_S\right)\\ &\quad +\mathcal{O}\left(r^3,(n_S-1)^3,\alpha_S^3\right), \qquad (3.9)\end{aligned}$$

where $C_1=\gamma_E+\ln 2-2\simeq -0.7296$. The value of the potential and its derivatives can be expressed exactly in terms of the slow-roll parameters, which are listed up to the second derivative in [145]. The third derivative reads

$$V'''=\frac{12m_p^2H^2\sqrt{\pi}}{\sqrt{\epsilon_1}}\left(2\epsilon_1^2-\frac{3\epsilon_2\epsilon_1}{2}+\frac{\epsilon_2\epsilon_3}{4}\right). \qquad (3.10)$$

The fourth derivative of the inflaton potential would be of a higher order in the slow-roll expansion.

Results. The allowed ranges, parameter likelihoods and two-dimensional contours from all our runs are summarised respectively in Table 3.2, Fig. 3.2 and Figs. 3.3, 3.4. The allowed shape of primordial scalar and tensor spectra is shown in Figs. 3.5.

First we ran a chain for the model at order $v=2$. As expected, the results confirm those obtained fitting the spectral parameters up to order $p=2$, which can be seen in Figs. 3.2 and 3.4 and the upper left chart in Fig. 3.3, by comparing the magenta and green lines. This can be translated into the statement that fixing the running of the tilt to zero is almost equivalent to fixing third and higher derivatives of the potential to zero. The resulting bounds can be read from Table 3.2, and the correlation between V'_*/V_* and V''_*/V_* is well accounted by the relation

$$m_P^2\left[2.2\left(\frac{V'_*}{V_*}\right)^2-\frac{V''_*}{V_*}\right]=0.6\pm 0.2\ . \qquad (68\%\text{C.L.}) \qquad (3.11)$$

Note that the numerically calculated running in the models with $v=2$ is not strictly zero but allows a very small region of nonzero running. Similarly, the derived bounds from the models with $p=2$ on the potential parameters allow for very small regions of nonzero second and third derivative. This merely reflects

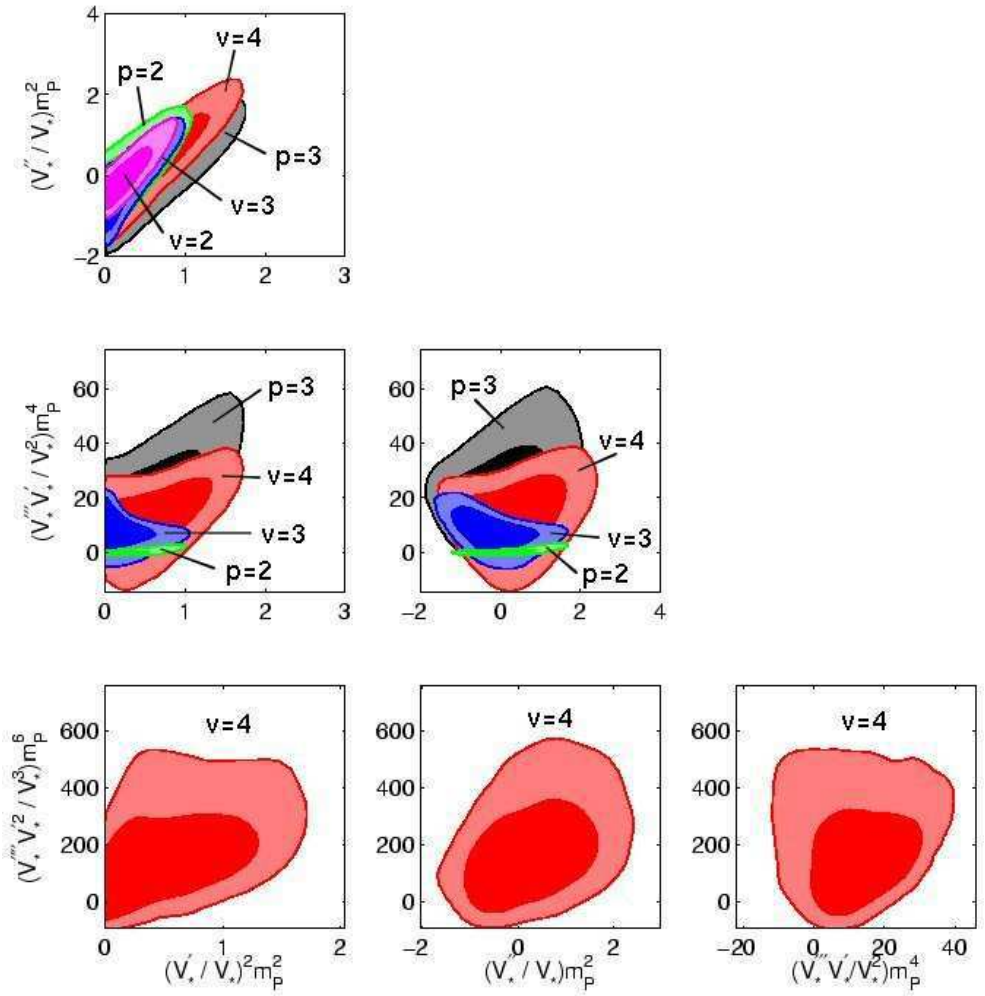

Figure 3.4: Two-dimensional 68% and 95% confidence level contours based on WMAP 3-year and the SDSS LRG spectrum, for the parameters describing the inflaton potential, obtained directly from the MCMC in the case of models $v = 2$ (magenta), $v = 3$ (blue), $v = 4$ (red), or derived from second-order formulas for models $p = 2$ (green), $p = 3$ (black).

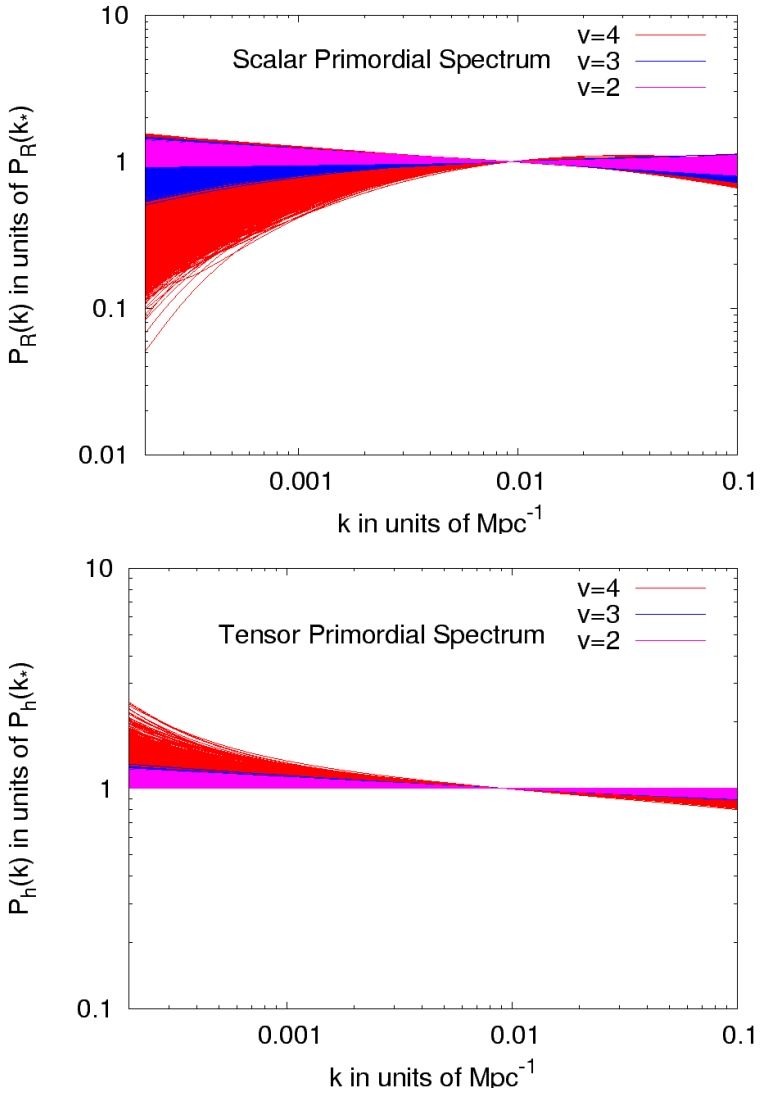

Figure 3.5: The primordial spectrum for scalar perturbations (left) and tensor perturbations (right) allowed at the 95% C.L. by WMAP 3-year and the SDSS LRG data, for a Taylor expansion of the inflaton potential at order $v = 2$ (magenta/light), $v = 3$ (blue/dark) or $v = 4$ (red/medium). In practice, this plot shows the superposition of 95% of the spectra from our MCMC chains with the best likelihood (after removal of the burn-in phase). All these spectra are computed numerically, rescaled to one at the pivot value k_*, and displayed in the range which is most constrained by our data set. Note that the shapes of the two spectra are related to each other: so, the tensor spectrum is constrained through that of the scalar spectrum, and not directly by the data, which does not have the required sensitivity.

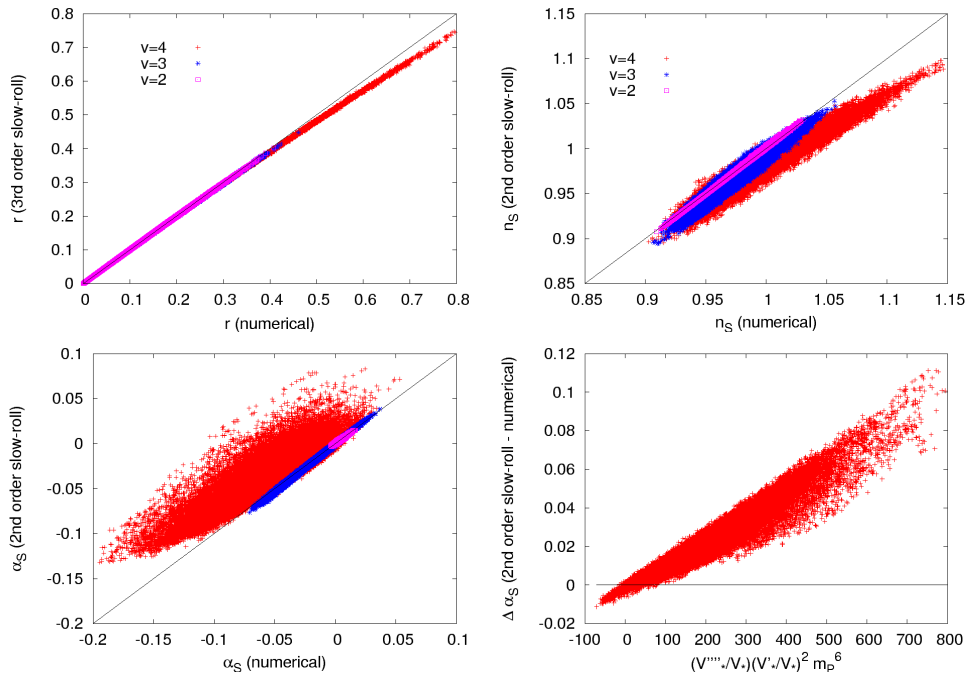

Figure 3.6: Precision test of the second-order slow-roll expansion for models allowed at the 95% C.L. by WMAP 3-year and the SDSS LRG data, based on a Taylor expansion of the inflaton potential at order $v = 2$ (magenta/light), $v = 3$ (blue/dark) or $v = 4$ (red/medium). For each model, we plot the spectral parameter r (top left), n_S (top right) and α_S (bottom left) computed at the pivot scale with two methods: by deriving the primordial spectrum computed numerically (horizontal axis), or with the second-order slow-roll formalism. We checked that the scattering of the point away from the y=x axis reflects inaccuracies in the second-order slow-roll formalism rather than in our code. The bottom right plot shows the inaccuracy in the running as a function of $V''''_* V'^2_* / V^3_*$ for the $v = 4$ model.

the expansions in different parameterisations than an indication for running (or nonzero higher derivatives of the potential).

Including a third derivative does allow for models to have a more significant running, which is clearly visible Fig. 3.5. Yet, as seen in Figs. 3.2, 3.3 and 3.4, the models with $v = 3$ (blue line) do not explore the full range of parameters which is indicated by the models with $p = 3$ (black line), in particular for α_S, and do not show as much a sign of degeneracy between $V_*'''V_*'/V_*^2$ and $V_*'^2$ as the derived potential derivatives from the models with $p = 3$, in Fig. 3.4. The relation between V'' and V'^2 remains almost unchanged. Inversely, in Fig. 3.3 we see the same effect in spectral parameter space.

The remaining discrepancy between models $v = 3$ and $p = 3$ led us to including the fourth derivative of the inflaton potential as a free parameter, i.e. $v = 4$. The resulting power spectra, shown in Fig. 3.5, show a larger negative running than in the $v = 3$ case, even with significant running of the running on the largest scales. In Fig. 3.2 we see that the model $v = 4$ (red line) does probe the same range of runnings of the tilt as allowed in the model $p = 3$. Looking at two-dimensional projections, we see that the $p = 3$ and $v = 4$ contours are closer to each other in spectral parameter space (Fig. 3.3) than in potential parameter space (Fig. 3.4): this reflects the inaccuracy of second-order slow-roll expressions, as explained in the next paragraph. In the model $v = 4$ the range for the lower derivatives of the potential is slightly larger than in the models with $v < 4$, which has its repercussions embodied in slight degeneracies between the fourth derivative and the lower derivatives.

Note that all figures containing information on the fourth derivative of the potential contain only the model $v = 4$ (red line) and not those with $p = 2$ or $p = 3$, since in the slow-roll approximation one would need to go to third order in order to infer V_*'''' from the primordial spectrum.

Finally, it is worth pointing out that the results at all orders in both parameterisations still allow for a flat (Harrison-Zel'dovich) spectrum at the 95% C.L., or for a linear potential at the 68% C.L.

Precision of the slow-roll approximation. In Fig. 3.6 we show the discrepancy between the numerical results for the spectral parameters (top left: r, top right: n_S, bottom left: α_S) and those obtained using the slow-roll approximation up to third order in the derivatives of the inflaton potential (second order in slow-roll parameters for n_S and α_S, third order for r). The numerically calculated parameters can in this context be treated as exact, since they do not involve any approximation (within first-order cosmological perturbation theory), and remain perfectly stable when we increase the precision parameters of our code. As r naturally comes out at one order higher in the slow-roll expansion than n_S and α_S, the top left plot (r) shows less discrepancy than do the plots for n_S and α_S. However, for large r there is a clear deviation from slow-roll in the results with $v = 4$ (red), up to $\sim$7%. In the plot for n_S it is clearly seen that second order slow roll is only accurate up to $\sim 3\%$ for the run with $v = 3$ (blue region). This discrepancy is important, since the data constrains n_S with a standard deviation

$\sigma \sim 2\%$. When a fourth derivative of the inflaton potential is included, second-order slow roll becomes really inaccurate, with a typical error of 10% on n_S, while the running can be wrongfully estimated by as much as $\Delta\alpha_S = 0.1$, i.e. three standard deviations given the current data. In a future work, it would therefore be useful to compute the next-order contributions to the running analytically (the bottom right diagram shows the quasi-linear dependence of α_S on the combination $V_*''''V_*'^2/V_*^3$).

3.4 Conclusions

In this work, we derived some constraints on the inflaton potential from up-to-date CMB and LSS data. Our CMB data consists in the WMAP 3-year measurement of the temperature and polarization power spectrum. We did include the first (controversial) multipoles, after checking in section 3.2 that they do not have a significant impact on the determination of the primordial spectrum tilt and running. Our analysis differs from previous works for several reasons. First, we directly fit the parameters describing the inflaton potential, instead of constraining first the primordial spectra, and reconstructing the inflaton potential afterwards. Second, we Taylor-expand the inflaton potential in the vicinity of the pivot scale at a rather high order (up to $v = 4$), and see that such a high order is important e.g. for exploring all the parameter space allowed by the data in terms of running of the scalar spectrum tilt. Third, we compute the scalar and tensor spectra for each model numerically, and find that for the models considered here this is important, since the spectra derived from the second-order slow-roll formalism are inaccurate by the same order as the observational constraints themselves.

However, the most important peculiarity of this work is our choice to focus only on the observable region of the inflaton potential, not making any assumption on the shape of the potential between the observable region and the minimum close to which inflaton stops after approximately 50 e-folds (depending on the scale of inflation). This choice has a crucial impact on the results. If we did extrapolate the inflaton potential over 50 e-folds, keeping the same order in the Taylor expansion, our models would be more severely constrained, since the requirement of 50 extra e-folds would kill many of the allowed potentials presented here[2]. We are perfectly aware of this, and wish to point out that this is one of two points of view, which are both equally sensible.

From one point of view, if one works under the prejudice that the inflaton potential should not be too complicated, then it is extremely relevant to consider the global shape of the potential and to throw away all models which cannot sustain 60 inflationary e-folds. Many papers use this approach, using sometimes Monte Carlo methods in which the potential (or the Hubble flow $H(N)$) is Taylor expanded over the 60 e-folds at high order.

[2]For instance, some limits on the potential derivatives were presented up to V''' in [110] and up to V'''' in [39]. In these works, most of the constraints on high derivatives come from the requirement of at least 50 inflationary e-folds with the extrapolated potential. Not surprisingly, the resulting bounds are much stronger that ours.

From another point of view, if one wants to address the question of what is strictly allowed by the data, then even a high-order Taylor expansion of the *full* potential sounds unsatisfactory for modelling all its possible variations during such a long history as 60 e-folds (especially if one keeps in mind that some other fields could then play a role: triggering a phase transition, inducing complicated shapes as in the string-inspired landscape scenarios, etc.). On the contrary, in this philosophy, one should only try to parametrize the inflaton potential in the range probed by cosmological data, i.e. around six or seven e-folds. This is what we did here, with a Taylor expansion up to fourth order.

The two approaches lead, of course, to radically different conclusions. For instance, in the first method, one would conclude that during the observational e-folds the inflaton must be deep in the slow-roll regime, since it is necessary to sustain a number of e-folds which is an order of magnitude higher. The running would then be very constrained [73]. In the second method, it is not a problem to satisfy slow-roll only marginally on the edges of the observable range. Even if ϵ_1 grows dangerously close to one when cluster scales exit the Hubble radius, the potential could become much flatter afterwards, and sustain any desired amount of inflation.

Our main results for the inflaton potential reconstruction are summarised in Figs. 3.1, 3.2, 3.4 and Table 3.2. We also showed up to what extent the slow-roll formalism reveals to be inaccurate in the current context in Fig. 3.6. This motivates possible future works concerning the next-order slow-roll expressions.

Following the same approach, this work could be improved by adding more large-scale structure data e.g. from Lyman-α forests or weak lensing, which have a good power for further constraining the primordial spectrum on smaller scales than the SDSS LRG data. Here we choose to use a very restricted data set, in order to derive rather conservative and robust results.

More generally, we point out that our COSMOMC module for computing the primordial spectra numerically can be used in different contexts, within COSMOMC or separately, and even (after minor modifications) for studying more complicated models producing characteristic features in the primordial spectra. The module was written in a user-friendly way and made publicly available on the website `http://wwwlapp.in2p3.fr/~lesgourgues/inflation/`.

Chapter 4

The inflaton potential: probing $H(\phi)$

In the previous chapter we gave constraints on the lowest derivates of the inflaton potential for the case where the scalar field ϕ already reached its attractor solution before the largest modes exit the horizon. The set of parameters $\{V^{(n)}\}$, where $V^{(n)} \equiv \partial_\phi^n V(\phi)\Big|_{\phi=\phi_*}$, then uniquely specified the evolution of the universe during inflation. To be more general, one should allow $\dot{\phi}$ to be a free parameter too. This would however introduce some degeneracies between parameters, taking away constraining power on $\{V^{(n)}\}$.

In this chapter, we will see that specifying $\{\dot{\phi}, V^{(n)}\}$, is equivalent to specifying some $H(\phi)$. Hence, if instead of Taylor expanding $V(\phi)$ and specifying $\dot{\phi}$, we Taylor expand $H(\phi)$, we automatically specify a unique set $\{\dot{\phi}, V(\phi)\}$ by choosing a combination of $\{H^{(n)}\}$.

Again, we numerically calculate today's observables directly from a given set of $\{H^{(n)}\}$, focusing only on the inflaton potential in the epoch during which the modes that are observable today froze in. The advantage of this new choice of parameters is that we obtain more general constraints on the inflaton potential.

4.1 Introduction

We derive new constraints on the Hubble function $H(\phi)$ and subsequently on the inflationary potential $V(\phi)$ from WMAP 3-year data combined with the Sloan Luminous Red Galaxy survey (SDSS-LRG), using a new methodology which appears to be more generic, conservative and model-independent than in most of the recent literature, since it depends neither on the slow-roll approximation for computing the primordial spectra, nor on any extrapolation scheme for the potential beyond the observable e-fold range, nor on additional assumptions about initial conditions for the inflaton velocity. This last feature represents the main improvement of this work, and is made possible by the reconstruction of $H(\phi)$ prior to $V(\phi)$. Our results only rely on the assumption that within the observable range, corresponding to ~ 10 e-folds, inflation is not interrupted and the function $H(\phi)$ is smooth enough for being Taylor-expanded at order one, two or three. We conclude that the variety of potentials allowed by the data is still large. However, it is clear that the first two slow-roll parameters are really small while the validity of the slow-roll expansion beyond them is not established.

Cosmic inflation was introduced as a simple and aesthetically elegant scenario of the early Universe evolution which is capable of explaining its main properties observed at the present time [4, 99, 161, 163, 228, 244]. As a very important byproduct it provides a successful mechanism for the quantum-gravitational generation of primordial scalar (density) perturbations and gravitational waves [1, 12, 100, 111, 191, 243, 245]. The Fourier power spectrum $\mathcal{P}_\mathcal{R}(k)$ of the former ones is observed today in the cosmic microwave background (CMB) and the large scale structure (LSS). Vice versa, at present the CMB and the LSS provide the only quantifiable observables which can confirm or falsify inflationary predictions. That is why matching concrete inflationary models to observations has become one of the leading quests in cosmology.

In the simplest class of inflationary models, inflation is driven by a single scalar field ϕ (an inflaton) with some potential $V(\phi)$ which is minimally coupled to the Einstein gravity. For these models, some new conservative bounds on $V(\phi)$ were presented recently in [150]. Until then, most post-WMAP3 studies concerning $V(\phi)$ relied on the slow-roll approximation in the calculation of perturbation power spectra and their relation to values of ϕ during inflation [40, 64, 65, 73, 78, 129, 201, 202, 240], or made an extrapolation of $V(\phi)$ from the observable window till the end of inflation [179, 211, 220] (a numerical integration of exact wave equations for perturbations to obtain primordial power spectra was also permormed in Refs. [56, 166, 171] for specific inflationary models). The extrapolation over the full duration of inflation is more constraining than the data alone. Instead, Ref. [150] focused only on the observable part of the potential to see up to what extent current data really constrains inflation.

For this class of models, the evolution of a spatially flat Friedmann-Lemaitre-Robertson-Walker (FLRW) universe can be described by [194, 225]

$$\dot{\phi} = -\frac{m_P^2}{4\pi} H'(\phi) \tag{4.1}$$

$$-\frac{32\pi^2}{m_P^4} V(\phi) = \left[H'(\phi)\right]^2 - \frac{12\pi}{m_P^2} H^2(\phi). \tag{4.2}$$

whenever $\dot{\phi} \neq 0$ and not specifically during inflation (so $H'(\phi) \neq 0$, too). Here $H(\phi(t)) \equiv \dot{a}/a$, $a(t)$ is the FLRW scale factor, a dot denotes the derivative with respect to the cosmic time t, a prime with respect to an argument, and we have set $Gm_P^2 = \hbar = c = 1$. If $V(\phi)$ is considered as the defining quantity, the initial conditions for generating the observable window are determined by the set $\{\dot{\phi}_{\rm ini}, V(\phi)\}$. In Ref. [150], the inflaton potential was parametrized as a Taylor expansion up to some order, to see up to what extent the potential can be constrained by pure observations. However, in order to reduce the number of free parameters, $\dot{\phi}_{\rm ini}$ was fixed for each model by demanding that the inflaton follows its attractor solution just when the observable modes exit the horizon. In practice this means that the results of Ref. [150] assumed that inflation started *at least* a few e-folds before the observable modes left the horizon. These preceding e-folds led to a slightly stronger bound on the potentials than the data itself could actually give, although this extra constraining power stands in no proportion to an extrapolation over the full duration of inflation.

Eqs. (4.1, 4.2) however show that when one considers $H(\phi)$ as the defining quantity, all initial conditions are already uniquely set by $H(\phi)$. Moreover, the slow-roll conditions which require, in particular, that the first term in the rhs of Eq. (4.2) is much less than the last one need not be imposed *ab initio*. In this Chapter we derive the bounds on $H(\phi)$ during observable inflation using its Taylor expansion at various orders. We infer from this some constraints on $V(\phi)$ under an even more conservative approach than in Ref. [150], since the present method requires absolutely no extrapolation outside of the observable region (either forward or backward in time). Our only restriction is to assume that

observable cosmological perturbations originate from the quantum fluctuations of a single inflaton field, which dynamics during observable inflation is compatible with a smooth, featureless $H(\phi)$.

Method. We used the publicly available code COSMOMC [152] to do a Monte Carlo Markov Chain (MCMC) simulation. We added a new module (released at `http://wwwlapp.in2p3.fr/~valkenbu/inflationH/`) which computes numerically the primordial spectrum of scalar and tensor perturbations for each given function $H(\phi-\phi_*)$, where ϕ_* is an arbitrary pivot scale in field space. This module is simpler than the one in Ref. [150], since the code never needs to find an attractor solution of the form $\dot{\phi}(\phi)$. The comoving pivot wavenumber is fixed once and for all to be $k_* = 0.01$ Mpc^{-1}, roughly in the middle of the observable range. Primordial power spectra are computed in the range $[k_{\rm min}, k_{\rm max}] = [5\times10^{-6}, 5]$ Mpc^{-1} needed by CAMB, imposing that k_* leaves the Hubble radius when $\phi = \phi_*$. In practice, this just means that for each model the code normalises the scale factor to the value $a_* = k_*/H_*$ when $\phi = \phi_*$. Note that by mapping a window of inflation to a window of observations today, our approach is independent of the mechanism of reheating. The evolution of each scalar/tensor mode is given by

$$\frac{d^2\xi_{\rm S,T}}{d\eta^2} + \left[k^2 - \frac{1}{z_{\rm S,T}}\frac{d^2 z_{\rm S,T}}{d\eta^2}\right]\xi_{\rm S,T} = 0 \tag{4.3}$$

with $\eta = \int dt/a(t)$ and $z_S = a\dot{\phi}/H$ for scalars, $z_T = a$ for tensors. The code integrates this equation starting from the initial condition $\xi_{\rm S,T} = e^{-ik\eta}/\sqrt{2k}$ when $k/aH = 50$, and stops when the expression for the observed scalar/tensor power spectrum freezes out in the long-wavelength regime. More precisely, the spectra are given by

$$\frac{k^3}{2\pi^2}\frac{|\xi_S|^2}{z_S^2} \to \mathcal{P}_{\mathcal{R}}\ , \qquad \frac{32k^3}{\pi m_P^2}\frac{|\xi_T|^2}{z_T^2} \to \mathcal{P}_h\ , \tag{4.4}$$

and integration stops when $[d\ln\mathcal{P}_{\mathcal{R},h}/d\ln a] < 10^{-3}$. If for a given function $H(\phi-\phi_*)$ the product aH cannot grow enough for fulfilling the above conditions, the model is rejected. In addition, we impose that aH grows monotonically, which is equivalent to saying that inflation is not interrupted during the observable range. If these conditions are satisfied, the power spectra are compared to observations.

We choose to parametrize H as a Taylor expansion with respect to $\phi - \phi_*$ up to a given order n varying between one and three (this choice of background parameterisation is equivalent to that in Ref. [73], as long as no extrapolation is made). Note that for $n > 1$ such an assumption excludes $\dot{\phi}$ and H' becoming zero at some value $\phi = \phi_1$ in the range involved since then $H(\phi)$ would acquire a non-analytic part beginning from the term $\propto |\phi-\phi_1|^{3/2}$ (with $V(\phi)$ being totally analytic at this point) [1]. As a cosmological background we used the standard ΛCDM-model with the free parameters shown in Table 4.1.

Results for $H(\phi-\phi_*)$. In Fig. 4.1 we show the probability distribution of each parameter marginalized over the other parameters. The corresponding 68%

[1] The case of $\dot{\phi}$ becoming zero at the beginning or during inflation requires special consideration, see [234, 246] in this respect.

Parameter	$n=1$	$n=2$	$n=3$
$\Omega_b h^2$	0.023 ± 0.001	0.023 ± 0.001	0.022 ± 0.001
$\Omega_{cdm} h^2$	0.109 ± 0.004	0.109 ± 0.004	0.110 ± 0.004
θ	1.042 ± 0.003	1.041 ± 0.004	1.040 ± 0.004
τ	0.08 ± 0.03	0.08 ± 0.03	0.09 ± 0.03
$\ln\left[\frac{4H_*^4}{H_*'^2 m_P^6} 10^{10}\right]$	3.07 ± 0.06	3.07 ± 0.06	3.09 ± 0.06
$\left(\frac{H_*'}{H_*}\right)^2 m_P^2$	0.079 ± 0.031	0.072 ± 0.056	0.081 ± 0.067
$\frac{H_*''}{H_*} m_P^2$	0	-0.035 ± 0.199	-0.079 ± 0.247
$\frac{H_*'''}{H_*} \frac{H_*'}{H_*} m_P^4$	0	0	1.53 ± 1.23
$-\ln \mathcal{L}_{\max}$	1781.7	1781.4	1780.1

Table 4.1: Bayesian 68% confidence limits for ΛCDM inflationary models with a Taylor expansion of $H(\phi - \phi_*)$ at order $n = 1, 2, 3$ (with the primordial spectra computed numerically). The last line shows the maximum likelihood. The first four parameters have standard definitions (see e.g. [150]).

confidence limits are displayed in Table 4.1, as well as the minimum of the effective χ^2 for each model. This minimum does not decrease significantly when n increases, which reflects the fact that current data are compatible with the simplest spectra and potentials, but derivatives up to H''' can be constrained with good accuracy. Note that it would be very difficult to give bounds directly on the set $\{H, H', H'', H''', ...\}$: indeed, these parameters are strongly correlated by the data, because physical effects in the power spectra depend on combinations of them. For example, at the pivot scale, the scalar amplitude is mainly determined by $(H_*^2/H_*')^2$ and the tensor-to-scalar ratio $r \equiv \mathcal{P}_h/\mathcal{P}_\mathcal{R}$ by $(H_*'/H_*)^2$. The scalar tilt n_S further depends on H_*''/H_*, and the scalar running on $H_*'''H_*'/H_*^2$. The Markov Chains can converge in a reasonable amount of time only if the basis of parameters (receiving flat priors) consists in functions of each of the above quantities, or linear combinations of them. However, we also show in the last plot of Fig. 4.1 the distribution of H_*: this information is useful since the energy scale of inflation is given by $\lambda = (3H_*^2 m_P^2/8\pi)^{1/4}$, but the displayed probability should be interpreted with care since this parameter has a non-flat prior.

The run $n = 1$ is not very interesting. Indeed, imposing H'' and higher derivatives to vanish leads to a one-to-one correspondence (at least in the slow-roll limit) between the amplitude and the tilt of the scalar spectrum. This feature is rather artificial and unmotivated. It explains anyway why the parameter H_* has exceptionally a lower bound in the $n = 1$ case [2]. Much more interesting is the $n = 2$ case for which the tensor ratio, scalar amplitude and scalar tilt are completely independent of each other, and the $n = 3$ case for which even the tilt running has complete freedom. The runs for $n = 2$ and $n = 3$ nicely converged

[2] Both $\ln A$ (the scalar amplitude) and $n_S - 1$ (the scalar tilt deviation from one) are bounded by the data. In the $n = 1$ case, these two quantities derive from H_* and H_*', which are hence both constrained independently of each other.

and constitute the main result of this work. Note also that the middle-right and lower-right graphs in Fig. 1 are compatible with each other in the following sense: though $H'*$ may not reach zero under our assumption, the quantity $H'*/H*$ may be arbitrarily small if $H*$ is allowed to be arbitrarily small, too. Thus, for cases $n = 2, 3$ when $H*$ is not suppressed at zero argument, $H'*/H*$ is not suppressed there, too.

The probability distribution for combinations of H_*, H'_* and H''_* are robust in the sense that they do not change significantly when one extra free parameter H'''_* is included: this indicates that they are directly constrained by the data. We tried to include an additional parameter $(H''''_*/H_*)(H'_*/H_*)^2 m_P^6$, but then our Markov Chains did not converge even after accumulating of the order of 10^5 samples. We conclude that current data do not have the sensitivity required to constrain $H(\phi)$ beyond its third derivative and to establish the validity of the slow-roll approximation beginning from this order. On the other hand, the first two slow-roll parameters $\epsilon(\phi) = H'^2 m_P^2/4\pi H^2$ and $\tilde{\eta}(\phi) = H'' m_P^2/4\pi H$ are really small over the observed range (tilde is used here to avoid mixing with the conformal time η). The next parameter $\xi \equiv {}^2\lambda_H = H''' H' m_P^4/(4\pi)^2 H^2$ is also small, ~ 0.01, though being of the order of ϵ and $|\tilde{\eta}|$, not ϵ^2 or $\tilde{\eta}^2$ as would follow from the standard slow-roll expansion. This smallness explains why our results for these parameters are similar to those obtained for the same background $H(\phi)$ but using the slow-roll approximation to calculate the power spectra [202] (and to those in [179], too) although some important differences exist.

Results for $V(\phi - \phi_*)$. We further processed our $n = 1, 2, 3$ runs in order to reconstruct the inflaton potential. For each run, we kept only 68% or 95% of the models with the best likelihood, and computed the corresponding inflaton potentials using Eq. (4.2). Note that the problem is fully symmetric under the reflection $(\phi - \phi_*) \leftrightarrow -(\phi - \phi_*)$. We choose to focus on one half of the solutions, corresponding to $\dot{\phi} > 0$ and hence $V'_* > 0$. Our results are shown in Fig. 4.2. They appear to be compatible with those of Ref. [150], although a detailed comparison is difficult: first, the current method is more conservative, and second, a given order in the Taylor-expansion of $H(\phi - \phi_*)$ is not equivalent to another order in that of $V(\phi - \phi_*)$. Our results are also difficult to compare with those of Ref. [211], since these authors choose to present their full allowed potentials extrapolated till the end of inflation: in principle, our Fig. 4.2 can be seen as a zoom on the directly constrained, small ϕ region in their Fig. 2.

Our results could give the wrong impression that all preferred potentials are concave. This comes from the fact that in the representation of Fig. 4.2, many interesting potentials are hidden, since they almost reduce to the point $(V_*, \Delta\phi) \to (0, 0)$. Indeed, as long as the tensor-to-scalar ratio is not bounded from below, many low-energy inflationary models with very small H_* and H'_* (and hence tiny variation of the inflaton field during the observable e-folds) are perfectly compatible with observations. It is straightforward to show that models leading to $n_S < 1$ and small r correspond to convex potentials (like e.g. new inflation with $V = V_0 - \lambda\phi^n$, or one-loop hybrid inflation with $V = V_0 + \lambda \ln \phi$), while models with same n_S and larger r derive from concave potentials (like e.g. monomial

inflation $V = \lambda\phi^\alpha$). Current data favor $n_S < 1$, and the upper bound on r is too loose for differentiating between these two situations. So, our allowed potentials can be split in two subsets: low-energy convex potentials and high-energy concave potentials, as illustrated in Fig. 4.3, in which we rescaled all allowed potentials to the same variation in V and ϕ. More generally, this large degeneracy in potential reconstruction reflects the fact that an infinitely precise measurement of the scalar spectrum $\mathcal{P}_\mathcal{R}$ would only constrain the function

$$\mathcal{P}_\mathcal{R}(k) = \left.\frac{4H^4}{m_P^4 H'^2}\right|_{k=aH} \tag{4.5}$$

(in the slow-roll approximation). This is not sufficient for inferring the correspondence between k and ϕ, and hence for a unique determination of $H(\phi)$ and $V(\phi)$. It is necessary to measure also the tensor spectrum, equal to

$$\mathcal{P}_h(k) = \left.\frac{16H^2}{\pi m_P^2}\right|_{k=aH} \tag{4.6}$$

in the same approximation, in order to diminish this degeneracy (see the related discussion in Ref. [49]). In the slow-roll approximation, the knowledge of $\mathcal{P}_h(k)$ leads to the unambiguous determination of $H(\phi)$. However, the question how unique the determination of $H(\phi)$ is, even from *both* $\mathcal{P}_\mathcal{R}(k)$ and $\mathcal{P}_h(k)$ in the generic case beyond slow-roll, is still open because of the existence of many $H(\phi)$ leading to the same perturbation spectra which may not be obtained from the slow-roll expansion at all [247]. Still, since the difference of these additional solutions from slow-roll ones is, in some sense, exponentially small for small slow-roll parameters, their existence might appear not significant from the observational point of view.

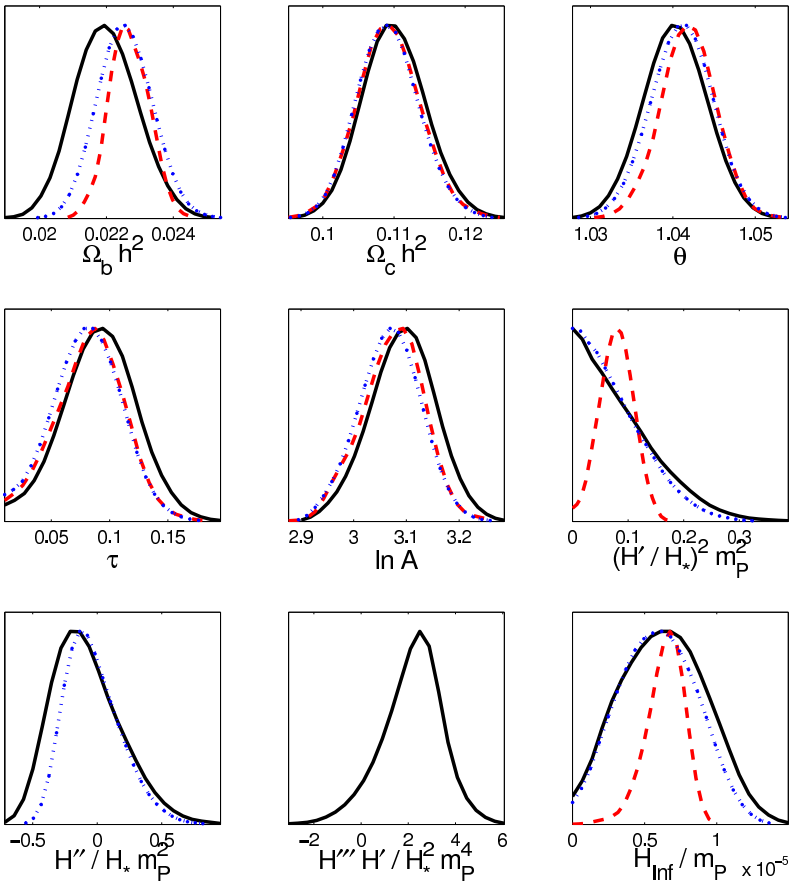

Figure 4.1: Probability distribution for the eight independent parameters of the models considered here, normalised to a common arbitrary value of $\mathcal{P}_{\max}$. The ninth plot shows a related parameter (with non-flat prior): namely, the value of the expansion rate when the pivot scale leaves the horizon during inflation. Our three runs $n = 1, 2, 3$ correspond respectively to the dashed red, dotted blue and solid black lines. The data consists of the WMAP 3-year results [113, 119, 198, 240] and the SDSS LRG spectrum [255]. The first four parameters have standard definitions (see e.g. [150]), and $\ln A$ is a shortcut notation for the parameter defined in the fifth line of Table I.

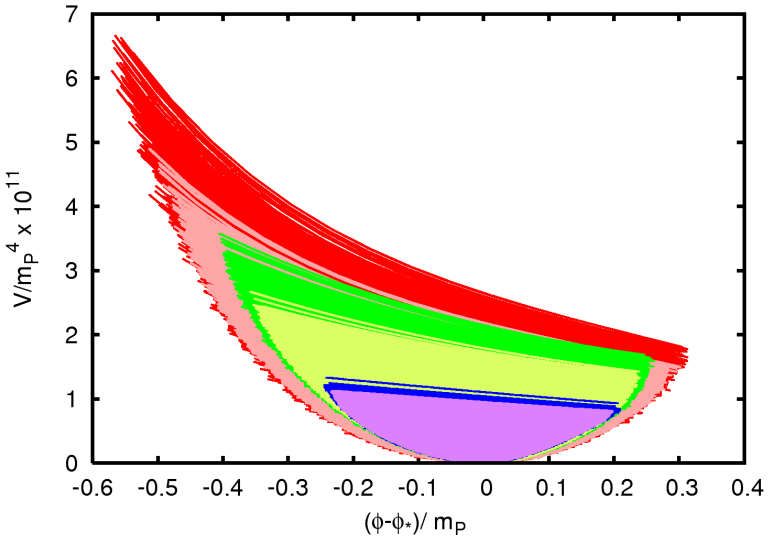

Figure 4.2: Allowed inflationary potentials $V(\phi-\phi_*)$ inferred from each of our $n=1,2,3$ runs. For each case, the light colour corresponds to models allowed at the 68% confidence levels, and the dark colour to the 95% level. The inner (bluish) region is obtained for $n=1$, the intermediate (greenish) one for $n=2$ and the outer (reddish) one for $n=3$. Each potential is plotted between the two values ϕ_1 and ϕ_2 corresponding to Hubble exit for the limits of the observable range $[k_1,k_2]$=$[2\times10^{-4},0.1]$ Mpc^{-1}: so we only see here the actual observable part of each potential. Note that this figure shows only one half of the possible solutions: the other half is obtained by reflection around $\phi=\phi_*$.

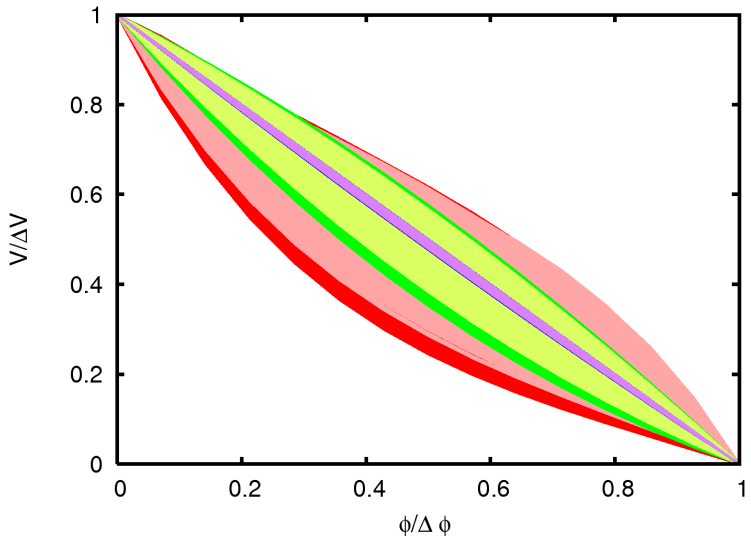

Figure 4.3: Allowed inflationary potentials $V(\phi - \phi_*)$ with the same colour/shade code as in Fig. 4.2, but a different choice of axes: each potential is now rescaled to the same variation in V an ϕ space. This shows that many allowed potentials are actually convex. The outer region still corresponds $n = 3$, the intermediate one to $n = 2$ and the inner (quasi-linear) one to $n = 1$.

Chapter 5

The inflaton potential: Slow Roll vs. Numerics

In Chapters 3 and 4 we saw that numerical computations of the spectra led to more accurate constraints on the functions $V(\phi)$ and $H(\phi)$. The focus was mainly on qualitative constraints on the inflationary history. In this chapter, we will take a closer look at the improvement of accuracy by choosing the numerical approach. We will compare two different Slow-Roll methods to our numerical results, and find that, as long as we do not extrapolate the inflationary history till the end of inflation, the numerical approach is theoretically more consistent and hence gives slightly tighter constraints on the parameters, than the analytical approximations do. The difference lies therein that the analytical approaches have no simple way of incorporating the condition that the modes that we observe actually freeze in. In other words, the analytical approaches give a spectrum for almost any choice of parameters, where some choices of parameters actually correspond to inflationary histories that last too short to produce only even the observable modes (in CMB and LSS). In our numerical code, which actually integrates the inflationary history for each mode, from the time at which the mode was in the far ultra-violet, up till the time at which the mode has frozen in for sure, we automatically reject a choice of parameters if any mode fails to freeze in. Hence, what happens is that we do not extrapolate the inflaton potential all the way till the end of inflation, but we do have to demand that all observed modes really freeze in, thereby putting slightly more stringent theoretical constraints on the shape of the potential.

5.1 Introduction

Cosmic inflation is the simplest and most robust paradigm capable of providing self-consistent initial conditions to the Hot Big Bang scenario [4, 99, 161, 163, 228, 244], as well as a mechanism for the quantum-gravitational generation of primordial scalar (density) perturbations and gravitational waves [1, 12, 100, 111, 191, 243, 245]. The Fourier power spectrum $\mathcal{P}_{\mathcal{R}}(k)$ of the former is observed today in the cosmic microwave background (CMB) and the large scale structure (LSS). Vice versa, at present the CMB and the LSS provide the only quantifiable observables which can confirm or falsify inflationary predictions. That is why matching concrete inflationary models to observations has become one of the leading quests in cosmology.

In the standard inflationary picture, the amplitude of perturbations for a given comoving Fourier mode k depends crucially on the dynamics of inflation around the time of Hubble exit for this mode. Each Hubble exit time is conveniently parameterised in terms of the number of e-folds N before inflation ends. The relation between k and N depends very much on the overall energy scale of inflation. The ensemble of modes observable in the CMB and in the quasi-linear part of the LSS power spectra corresponds to a range $\Delta N \sim 10$ called "observable inflation". The total duration of inflation is a priori unlimited, but the number of e-folds between the time at which the presently observable Universe became as large as the Hubble radius and the end of inflation can only vary in the approximate range $30 < N < 60$, that will be called "relevant inflation" throughout this paper.

The literature on inflation constraints is plethoric. For simplicity, a majority of

papers are restricted to the case in which inflation is driven by a single scalar field ϕ (an inflaton) with a canonical kinetic term, some potential $V(\phi)$ and minimal coupling to Einstein gravity (however, each of these assumptions can be relaxed and has already been studied separately). Traditional works are based on the definition of spectral parameters (amplitude, index, possibly running) for density perturbations and gravitational waves. In a first step, these parameters are fitted to the data; in a second step, one tries to infer the class of inflationary models compatible with derived bounds on spectral parameters.

In the last years, many works have gone beyond this approach, recognising that the introduction of spectral parameters puts already a strong theoretical prior on the models, and is by no means a necessary step. It is more realistic and equally efficient to fit directly to the data the (more fundamental) parameters governing the dynamics of inflation and/or the inflaton potential. Within the main stream (standard single field inflation), recently published analyses fall in two categories which are both interesting and complementary: either one assumes a particular model based on a definite form for the inflaton potential throughout relevant inflation, and derives constraints on the free parameters of this potential (top-down approach); or one employs a generic parameterisation of the potential $V(\phi)$ or another function governing inflationary dynamics, e.g. $H(\phi)$, and tries to reconstruct this function from the data (bottom-up approach). The second approach aims at avoiding theoretical priors as much as possible, and concentrating on what the data exactly tells us, although no parameterisation can be completely general: sharp features are usually excluded *ab initio* (obviously, all possible features cannot be accounted for with a reasonable number of free parameters). Even within the bottom-up approach, a distinction can be established between conservative analyses reconstructing only the part of $V(\phi)$ corresponding to observable inflation; and more aggressive analyses in which the potential (or the function $H(\phi)$) is extrapolated till the end of inflation, and subject to a prior on the minimum duration of relevant inflation (e.g. $N \geq 30$). This more aggressive method should imply varying many more parameters, since in this case the parameterisation should be accurate over 30 to 60 e-folds instead of just ~ 10. The fact of extrapolating is by itself an extra theoretical prior, since cosmological data tell us essentially nothing about the era between observable inflation and Nucleosynthesis: the end of inflation could be subject to multi-field dynamics, experience phase transitions, be split into several non-contiguous short inflationary stages, etc.

Here we address only the most conservative approach, i.e., the reconstruction of the inflationary dynamics during observable inflation, with a minimal number of assumptions. After the publication of WMAP results, this approach was followed in Refs. [73, 149, 150, 201, 202]. It was stressed in [73, 201, 202] and [149] that the quantity primarily constrained by the data is $H(\phi)$: hence, this function is the one which should be parameterised in some way and fitted to the data. The knowledge of $H(\phi)$ uniquely defines the potential $V(\phi)$, and Ref. [149] presented the collection of potentials $V(\phi)$ corresponding to the ensemble of functions $H(\phi)$ allowed by current WMAP and SDSS LRG data. The results are still plagued by degeneracies: since the energy scale of inflation is unknown, the data favours a

parametric family of inflaton potentials rather than a precise shape within the observable window. However, a lot of improvement is expected from the next generation of CMB experiments, especially the PLANCK satellite. The reconstruction of observable inflation will improve spectacularly if primordial gravitational waves are observed by PLANCK or another experiment, in the form of polarised B-modes. This would fix the tensor-over-scalar ratio r, and hence the energy scale of inflation. Even without B-modes, the Planck data would provide r-dependent constraints on the inflation potential of unprecedented precision. In this perspective, it is worth comparing the details and merits of each reconstruction method.

Choosing to concentrate on the reconstruction of $H(\phi)$ during observable inflation does not fix the method entirely, in particular as far as the computation of the primordial spectra is concerned. The authors of [73, 201, 202] employed analytic approximations of two different forms, while those of [149][1] wrote a module appended to `CAMB` [153] and `CosmoMC` [152], which derives the numerical spectra for each new set of inflationary parameters by numerically solving the exact equations. It is interesting to study whether the difference between these methods is relevant given the precision of current and future data. Beyond the issue of perturbations, different methods could also differ through different assumptions concerning the parameterisation of the background evolution, and the exact number of e-folds during which this parameterisation is (explicitly or implicitly) assumed to hold and be compatible with accelerated expansion. The goal of this paper is to compare in details these different techniques, and to see how each difference impacts the constraints obtained from current data. Although current inflaton potential reconstructions are still dominated by degeneracies, a careful understanding will be necessary before applying these methods to the highly precise data expected in the next years.

In the next section we will briefly review the theory of inflationary perturbations and discuss the exact approach, as well as two commonly used approximative methods for the calculation of the primordial perturbation spectra. In section 5.3, we will present the results of an analysis of current data and demonstrate that the bounds using the approximative methods with a naïve prior differ significantly from the constraints inferred with the exact method. We will track down the cause of these differences and compare the accuracy of the approximations in section 5.4 before we conclude in section 5.5.

5.2 Background and perturbations in single field inflation

The observable spectra of density perturbations and gravitational waves are directly related to the evolution of the Hubble parameter $H \equiv \dot{a}/a$ as a function of ϕ in the neighbourhood of an arbitrary pivot value ϕ_*. The function $H(\phi - \phi_*)$

[1] Numerical spectrum computations were also employed in various complementary approaches to the problem of constraining inflation, based on definite potentials [56, 166, 179, 220] or on a frequentist analysis with extrapolation of the potential throughout relevant inflation [211].

can in principle be reconstructed from the data without any need to assume an explicit value of ϕ_*. Each $H(\phi-\phi_*)$ defines a unique set $\left\{V(\phi-\phi_*),\dot{\phi}_{\rm ini}\right\}$ through

$$-\frac{32\pi^2}{M_{\rm Pl}^4}V(\phi-\phi_*) = [H'(\phi-\phi_*)]^2-\tfrac{12\pi}{M_{\rm Pl}^2}H^2(\phi-\phi_*), \tag{5.1}$$

$$\dot{\phi} = -\tfrac{M_{\rm Pl}^2}{4\pi}\,H'(\phi-\phi_*), \tag{5.2}$$

whenever $\dot{\phi}\neq 0$ [2] (the prime denotes a derivative with respect to ϕ, and we have set $GM_{\rm Pl}^2=\hbar=c=1$). In Ref. [149], the defining quantity $H(\phi-\phi_*)$ was Taylor-expanded up to the cubic term:

$$H(\phi-\phi_*)=H_*+H'_*(\phi-\phi_*)+\frac{1}{2}H''_*(\phi-\phi_*)^2+\frac{1}{6}H'''_*(\phi-\phi_*)^3\ , \tag{5.3}$$

which is equivalent to keeping the first three slow-roll parameters

$$\epsilon = \tfrac{M_{\rm Pl}^2}{4\pi}\left[\frac{H'}{H}\right]^2, \tag{5.4}$$

$$\eta = \tfrac{M_{\rm Pl}^2}{4\pi}\frac{H''}{H}, \tag{5.5}$$

$$\xi = \tfrac{M_{\rm Pl}^4}{16\pi^2}\,\frac{H'H'''}{H^2}, \tag{5.6}$$

in the Hubble flow hierarchy [128, 158], as in the slow-roll reconstruction approach of Refs. [72, 73, 201, 202]. Note that the universe expansion remains accelerated as long as $\epsilon<1$. For practical purposes, any parameterisation of $H(\phi)$ could be used when fitting the data with a Bayesian MCMC analysis. Besides the issue of priors on inflationary parameters, each parameterisation corresponds to a different ensemble of possible inflationary models. One can wonder how much the final results (i.e., the range of allowed potentials) depends on the parameterisation. In the following analysis we will compare the results obtained by Taylor-expanding either $H(\phi)$ or $H^2(\phi)$ at the same order, using in both cases the same flat priors on the first slow-roll parameters expressed at the pivot scale ϕ_*.

Once the ensemble of possible inflationary models has been specified, the analysis still depends on the way to calculate the perturbation spectra in single-field inflation, and on a theoretical prior on the duration of inflation. In this section we will give a very brief summary of three different approaches used in Refs. [73, 149, 201, 202]. Keep in mind that throughout this paper, we are working under the assumption of a minimal prior. In other words, we do not impose any lower

[2] Such a singularity is never reached as long as $H(\phi)$ is used as the defining quantity and has an analytic expression over the range considered. As mentioned in Ref. [149], $\dot{\phi}=0$ can be reached for a field value ϕ_1 only if H has a non-analytical expression like $(H-H_1)\propto(\phi-\phi_1)^{3/2}$ in the vicinity of ϕ_1. This cannot happen with the parameterisations used in this work (polynomial expressions for either $H(\phi)$ or $H^2(\phi)$). In addition, reaching $\dot{\phi}=0$ would imply that the field changes direction with an opposite sign for H', which is not compatible with the assumption of a single-valued function $H(\phi)$.

bounds on the number of e-folds of inflation, we only demand that the spectra of a model can be calculated with the respective methods. So, besides possible differences in the accuracy of the resulting spectra, the default implementation of the three methods will also differ in the range of parameter values that would be excluded straight away.

5.2.1 Exact spectra via mode equation

Given H as a function of ϕ during inflation, the spectrum of curvature perturbations $\mathcal{P}_\mathcal{R}$ and gravitational waves $\mathcal{P}_T$ can be calculated exactly by integrating the scalar/tensor *mode equation* (see, e.g,. [192]):

$$\frac{d^2\xi_{\rm S,T}}{d\eta^2} + \left[k^2 - \frac{1}{z_{\rm S,T}}\frac{d^2 z_{\rm S,T}}{d\eta^2}\right]\xi_{\rm S,T} = 0 \tag{5.7}$$

with $\eta = \int dt/a(t)$ and $z_S = a\dot{\phi}/H$ for scalars, $z_T = a$ for tensors. The evolution of the background is determined by

$$\dot{\phi} = -\frac{M_{\rm Pl}^2}{4\pi}\frac{{\rm d}H}{{\rm d}\phi}. \tag{5.8}$$

The $\xi_{\rm S,T}$ are usually taken to be in the Bunch-Davies vacuum when they are well within the horizon, and their evolution needs to be tracked until $|\xi_{\rm S,T}|/z_{\rm S,T}$ converges to a constant value, in order to define the observable spectra:

$$\frac{k^3}{2\pi^2}\frac{|\xi_S|^2}{z_S^2} \to \mathcal{P}_\mathcal{R}\ , \qquad \frac{32k^3}{\pi M_{\rm Pl}^2}\frac{|\xi_T|^2}{z_T^2} \to \mathcal{P}_T\ . \tag{5.9}$$

In principle, observable inflation could be interrupted for a very short amount of time, resulting in characteristic features in the spectra. In the mainstream approach, this situation is not considered for simplicity. Actually, the numerical module used in Ref. [149] eliminates models violating $\epsilon \leq 1$ at any point during the period of time the mode equation is integrated. More precisely, for any wavenumber in the range $[k_{\rm min}, k_{\rm max}] = [3\times10^{-6}, 1.2]$ Mpc^{-1} needed by `CAMB` (the pivot scale being fixed at $k_* = 0.01$ Mpc^{-1}), the module integrates Eq. (5.7) from the time at which $k/aH = 50$ and until $[{\rm d}\ln\mathcal{P}_{\mathcal{R},T}/{\rm d}\ln a] < 10^{-3}$. If for a given function $H(\phi-\phi_*)$ the product aH does not grow monotonically by a sufficient amount for fulfilling the above conditions, the model is rejected (we recall that it is equivalent to impose that aH grows or that ϵ is greater than one).

The condition $[{\rm d}\ln\mathcal{P}_{\mathcal{R},T}/{\rm d}\ln a] < 10^{-3}$ is motivated by our desire to obtain a 0.1% accuracy in the power spectra. The error made on $\mathcal{P}_{\mathcal{R},T}$ by stopping the integration of perturbations at a finite time can be estimated analytically, comparing the amplitude of the decaying mode to that of the non-decaying mode for $\mathcal{R}$ or gravitational waves during inflation. The decaying over non-decaying mode ratio evolves in a first approximation like a^{-1}, i.e., like e^{-N}. Hence, a few lines of algebra show that the derivative $[{\rm d}\ln\mathcal{P}/{\rm d}\ln a]$ is a good approximation for the relative error $[\Delta\mathcal{P}/\mathcal{P}]$ produced by stopping integration at a finite time.

Other parameters governing the precision of the power spectra calculation (like the step of integration, the choice of the initial integration time for each mode, etc.) where chosen in such way that the above source of error is the dominant one.

The numerical evaluation of the spectrum involves solving equations (5.7) for each value of k, but this does not increase the total running time of a Boltzmann code like `CAMB` by a noticeable amount. Nevertheless, there exist a number of approximations in the literature, which simplify the calculation considerably.

5.2.2 Approximation /

This method was employed in [201, 202], and relies on the validity of the analytical slow-roll approximations,

$$\mathcal{P}_{\mathcal{R}}(k) \simeq \tfrac{[1-2(C_1+1)\epsilon+C_1\eta]^2}{\pi\epsilon} \left(\tfrac{H}{M_{\rm Pl}}\right)^2\Big|_{k=aH}, \tag{5.10}$$

$$\mathcal{P}_{\rm T}(k) \simeq [1-(C_1+1)\epsilon]^2 \ \tfrac{16}{\pi} \left(\tfrac{H}{M_{\rm Pl}}\right)^2\Big|_{k=aH}, \tag{5.11}$$

with $C_1 = -2 + \ln 2 + \gamma$, where γ is the Euler-Mascheroni constant. These equations were first derived in [251] and are accurate only to first order in the slow-roll parameters, assuming additionally that ϵ and η are constant. Here, one only needs to solve one differential equation to determine $\phi(k)$,

$$\frac{\mathrm{d}\phi}{\mathrm{d}\ln k} = -\frac{M_{\rm Pl}}{2\sqrt{\pi}}\frac{\sqrt{\epsilon}}{1-\epsilon}, \tag{5.12}$$

assuming $\phi(k_*) = \phi_*$. Once $\phi(k)$ is known, the slow-roll parameters and hence the spectrum can be evaluated for each value k. In this approach, the evolution of Eq. (5.12) has to be followed throughout the observable range of wavelengths. If $\epsilon \geq 1$, equation (**??**) will diverge, so models with $\epsilon > 1$ within this range will have to be excluded when using this method. If however, the inflationary condition were violated just before or after this range, the model would not be ruled out, and the resulting spectra would likely be inaccurate.

5.2.3 Approximation //

This method is based on the usual Taylor-expansion of the spectra in log-space around a pivot scale k_* (see e.g., [144, 145]),

$$\ln \mathcal{P}_{\mathcal{R}} \simeq \ln A_{\rm S} + (n_{\rm S}-1)\ln(k/k_*) + \tfrac{1}{2}\alpha_{\rm S}\left(\ln(k/k_*)\right)^2, \tag{5.13}$$

$$\ln \mathcal{P}_{\rm T} \simeq \ln A_{\rm T} + n_{\rm T}\ln(k/k_*), \tag{5.14}$$

with the spectral indexes $n_{\mathrm{S/T}}$, and the running of the scalar tilt α_{S} given by their second-order slow-roll expressions

$$n_{\mathrm{S}} \simeq 1 + 2\eta - 4\epsilon - 2(1+C_2)\epsilon^2 - \tfrac{1}{2}(3-5C_2)\epsilon\eta + \tfrac{1}{2}(3-C_2)\xi, \quad (5.15)$$

$$\alpha_{\mathrm{S}} \simeq -\tfrac{1}{1-\epsilon}\left(2\xi + 8\epsilon^2 - 10\epsilon\eta + \tfrac{7C_2-9}{2}\,\epsilon\xi + \tfrac{3-C_2}{2}\,\eta\xi\right), \quad (5.16)$$

$$n_{\mathrm{T}} \simeq -2\epsilon - (3+C_2)\epsilon^2 + (1+C_2)\epsilon\eta, \quad (5.17)$$

where $C_2 = 4(\ln 2 + \gamma) - 5$. The slow-roll parameters only need to be evaluated at a field value ϕ_*, corresponding to the time when k_* leaves the horizon. A_{S} and A_{T} are calculated from equations (5.10) and (5.11), and the spectra follow directly. One does not need to solve any differential equations here, so the numerical implementation of this method is by far the simplest of the three. However, due to the additional assumption on the shape of the spectrum, it becomes increasingly inaccurate the further one goes away from the pivot scale.

Apart from that, in the spirit of choosing a minimal prior one would typically rule out only those models that break the $\epsilon < 1$ condition at the pivot scale, thus allowing regions in parameter space in which inflation would break down even within the observable range and making the prediction of the spectra for these models extremely unreliable.

5.3 Constraints from current data

In this section we present the constraints on inflationary parameter space from a selection of current observations, comprising CMB data from the WMAP [113, 198], Boomerang [120, 189, 206] and ACBAR [218] experiments, complemented by the galaxy power spectrum constructed from the luminous red galaxy sample of the Sloan Digital Sky Survey [255]. We analytically marginalise over the luminous to dark matter bias b^2 and the nonlinear correction parameter Q_{nl}.

We consider a ΛCDM-model with eight free parameters, on which we impose flat priors. Four of these parameters determine the initial perturbation spectra: the scalar normalisation $\ln\left[10^{10}A_{\mathrm{S}}\right]$, and the first three slow-roll parameters: ϵ, η and ξ, evaluated at the pivot scale $k_* = 0.01$ Mpc^{-1}. We emphasise once more that the numerical computation of perturbations does not refer to any slow-roll expansion, and remains self-consistent even when the field is not rolling very slowly. The fact of varying parameters which coincide with the usual slow-roll parameters is just a choice of prior in parameter space, which is particularly convenient for two reasons: first, the posterior is well-behaved with respect to these parameters and the convergence of the chains is achieved in a reasonable amount of time; second, it facilitates comparison with other works. The remaining four parameters are the baryon density ω_b, the cold dark matter density ω_{dm}, the ratio of sound horizon to angular diameter distance at decoupling θ_s, and the optical depth to reionisation τ. We use a modified version of the Markov-Chain-Monte-Carlo code `CosmoMC` [152, 153] to infer constraints on the free parameters of the model. The inflation module was made publicly available by the authors of Ref. [149] at `http://wwwlapp.in2p3.fr/~valkenbu/inflationH/`.

Table 5.1: Minimal 95%-credible intervals for the slow-roll parameters in the H- and H^2-expansion schemes, using the exact method for calculating the spectra.

	H	H^2
ϵ	0 → 0.028	0 → 0.023
η	-0.035 → 0.046	-0.035 → 0.039
ξ	-0.0026 → 0.028	-0.0053 → 0.027

5.3.1 Expansion in H vs. expansion in H^2

We first check the impact of changing the parameterisation of $H(\phi)$ (i.e., the precise ensemble of inflationary models considered) from a Taylor-expansion of order 3 in $H(\phi)$ to the same expansion in $H^2(\phi)$. In both cases, we used the same priors on inflationary parameters: hence the difference only resides in the fact that slightly different background evolutions can be achieved in both cases. The differences are summarised in table 5.1 and turn out to be very minor. This preliminary analysis shows that the parametric form assumed for $H(\phi)$ within the observable window has a minor impact. Significant differences could only be expected if the choice of parameterisation of $H(\phi)$ would allow much more freedom in one case than in the other.

In the remaining part of the paper, we shall therefore stick to the Taylor-expansion in $H(\phi)$ and perform three independent analyses, calculating the primordial spectrum either by exactly solving the mode equations, or using one of the two approximations discussed in sections 5.2.2 and 5.2.3.

5.3.2 Approximations vs. exact spectra

Our results are presented in figures 5.1 and 5.2. We do not find any significant differences in the posterior probabilities of τ, θ_s, $\omega_{\rm b}$ and $\omega_{\rm dm}$. The four parameters that determine the primordial spectra, however, are more sensitive to the method used. Note that the exact method produces tighter bounds on the slow-roll parameters, particularly on ξ.

This also has important consequences on the inferred values of derived phenomenological parameters, such as the spectral index and its running. As can be seen from table 5.2, the exact method yields significantly stronger constraints on these two parameters.

5.4 Why the difference?

There are potentially two reasons for these observed discrepancies. The first one is that the accuracy of the approximations could be insufficient within their respective "allowed" parameter space and lead to a serious bias in the parameter estimates. Note that the discrepancy occurs mostly in regions of parameter space

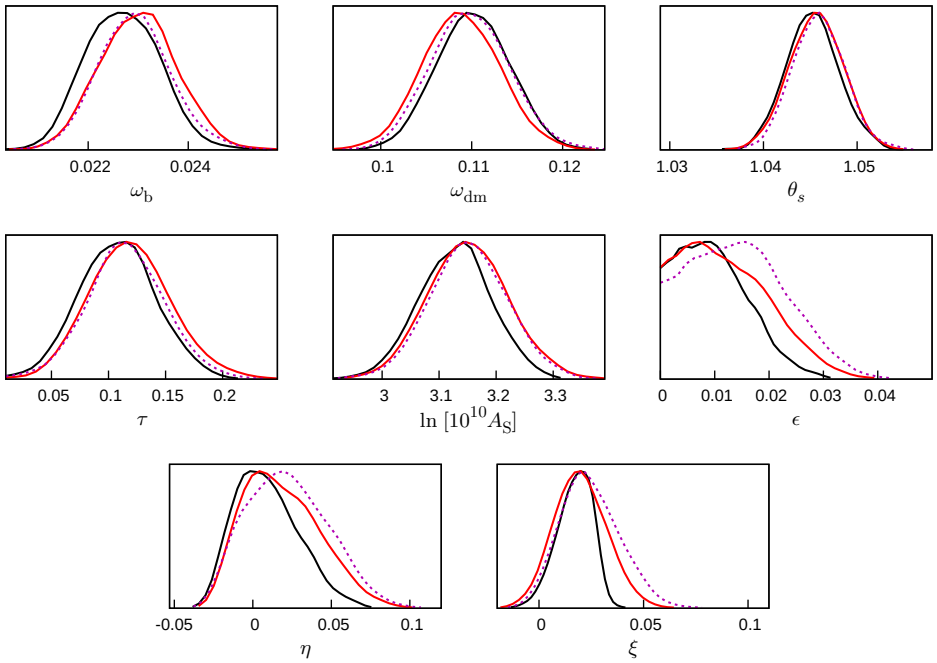

Figure 5.1: This plot shows the one-dimensional marginalised posterior distributions for the free parameters of the model. The black lines represent the results of the exact solution of the mode equation, red lines are approximation *I* and purple (dashed) lines correspond to approximation *II*.

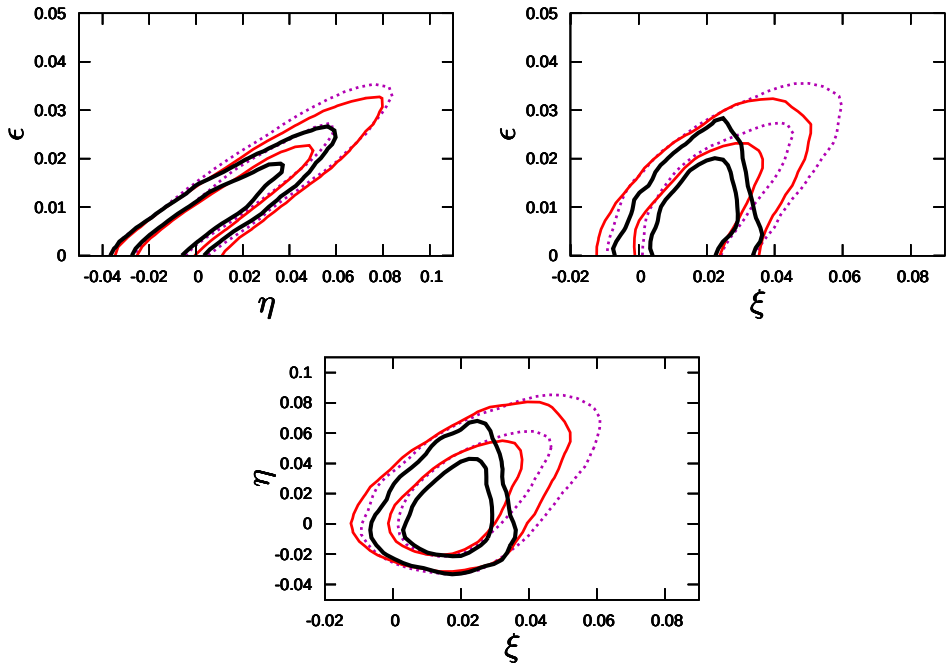

Figure 5.2: This plot shows the 68%- and 95% credible regions of the two-dimensional marginalised posterior in the (ϵ, η)- (top left), (ϵ, ξ)- (top right), and (η, ξ)-planes (bottom). The black lines denote the results of the exact solution of the mode equation, red lines are approximation *I* and thin lines correspond to approximation II.

Table 5.2: Minimal 95%-credible intervals for the spectral index and the running at a scale of $k_* = 0.01\ \mathrm{Mpc}^{-1}$. Note that these are derived parameters and the results are not independent of the choice of pivot scale.

	exact	approximation *I*	approximation *II*
n_{S}	$0.959 \to 1.049$	$0.960 \to 1.078$	$0.960 \to 1.087$
α_{S}	$-0.063 \to 0.001$	$-0.084 \to 0.009$	$-0.098 \to 0.003$

where ξ is large. The larger ξ, the more one would expect the accuracy of the approximations to degrade. However, given that the approximations are expected to be accurate to order ξ, i.e., not worse than $\sim 10\%$, an effect as large as the one we observe seems rather unlikely.

The second reason is slightly more subtle: as we discussed in section 5.2, the three methods differ in their *implicit* prior on the space of models. While approximation *II* requires $\epsilon < 1$ only at the pivot scale, approximation *I* needs us to demand that this condition be fulfilled in the entire observable window of ~ 10 e-folds, corresponding to Hubble exit for modes in the $[k_{\mathrm{min}}, k_{\mathrm{max}}]$ range. In the exact numerical approach, we require $\epsilon < 1$ for the whole integration time, which starts when $aH/k_{\mathrm{min}} = 1/50$ instead of one, and ends when $|\xi_{\mathrm{S,T}}|/z_{\mathrm{S,T}}$ freezes out, i.e., a few e-foldings after $aH/k = 1$, corresponding to an even more restrictive prior.

It was pointed out in Refs. [73, 172] that for models with large positive values of ξ (> 0.05) and no higher derivatives, inflation tends to end within a few e-foldings of the pivot scale leaving the horizon[3]. This is consistent with our results, since the more restrictive priors lead to tighter bounds on ξ.

5.4.1 The prior issue

To verify that the differences actually stem from the choice of priors and not from a lack of accuracy, we post-processed our Markov chains of the approximate methods, discarding all models for which inflation is interrupted in the range of wavelengths required for the exact calculation.

In a first step, we remove only those models for which the inflationary condition is violated *before* the pivot scale leaves the horizon, when aH is in the range $[k_{\mathrm{min}}/50, k_*]$. These are models for which the assumption of the Bunch-Davies vacuum initial condition is violated at least for the largest observable wavelengths. Only a mere 0.02% of the models in the chains using approximation *I*, and 0.01% for approximation *II*, fall victim to the cut[4]. This is probably connected to the

[3] If higher derivatives are present this conclusion can be weakened, see, e.g., [10, 171].

[4] Here, and in the following, we quote a weighted fraction of models, i.e., $(\sum_j w_j^{\mathrm{bad}})/\sum_i w_i)$, where w_i are the statistical weights of the points in the Markov chains, and w_j^{bad} are the weights of the models killed by the prior.

Table 5.3: Value of the slow-roll parameters at the pivot scale for the models referred to as A and B in the text. The corresponding curvature spectra computed with each method are shown in Figure 5.3.

model	ϵ	η	ξ
A	1.1446×10^{-3}	-4.1728×10^{-3}	3.4911×10^{-2}
B	2.6159×10^{-2}	7.5254×10^{-2}	3.3839×10^{-2}

dislike of the data for models with large negative ξ, which is required if we want inflation to start only just before the observable range.

Imposing the same additional prior as in the exact method (that inflation holds till the time of freeze out for each mode), $\sim 20\%$ of the approximation *I* points and $\sim 34\%$ of the approximation *II* points are removed. After weeding out the bad models, the bounds of the approximations perfectly agree with the ones derived using the exact method, their marginalised posteriors are virtually indistinguishable. This confirms our suspicion that the different priors are responsible for the discrepancy between the methods.

5.4.2 Comparison of accuracy

Having seen that the prior plays a very important role, it is nonetheless interesting to take a closer look at how the approximations compare to the exact method in terms of accuracy.

In order to compare the accuracy of the three methods described previously, we took the 95% best-fitting spectra obtained using approximations *I* and *II* and for each model in the chains we again computed the curvature spectrum in either of the approximations and numerically in order to compare. We searched for the maximum discrepancy between the approximated spectrum (with method *I* or *II*) and the numerical one, in each of the two ranges $[k_{\rm min}, k_*]$ and $[k_*, k_{\rm max}]$, with $k_{\rm min} = 3 \times 10^{-6}$, $k_* = 0.01$, $k_{\rm max} = 1.2$, in units of $1/$Mpc, corresponding to the range of wavelengths the data are most sensitive to. Note that the spectrum for a model can only be computed numerically if the model meets the prior condition on the duration of inflation. Hence the comparison done here is for models that are already preselected by that particular prior, whereas in the actual chains many points exist that give a much larger discrepancy due to the different prior.

In Figure 5.3 we plot the most discrepant models in the $[k_*, k_{\rm max}]$ range, that we call A (for approximation *I*) and B (for approximation *II*). The corresponding slow-roll parameters evaluated at the pivot scale are given in Table 5.3. For approximation *II* we find a maximum discrepancy in $\mathcal{P}_\mathcal{R}$ of 83% below k_*, and 19% above (model B). For *I*, the difference reduces to 33% below k_* and 8% above (model A). So, approximation *I* is doing better on both sides of the pivot scale.

Indeed, it appears that approximation *I* captures the spectrum shape very

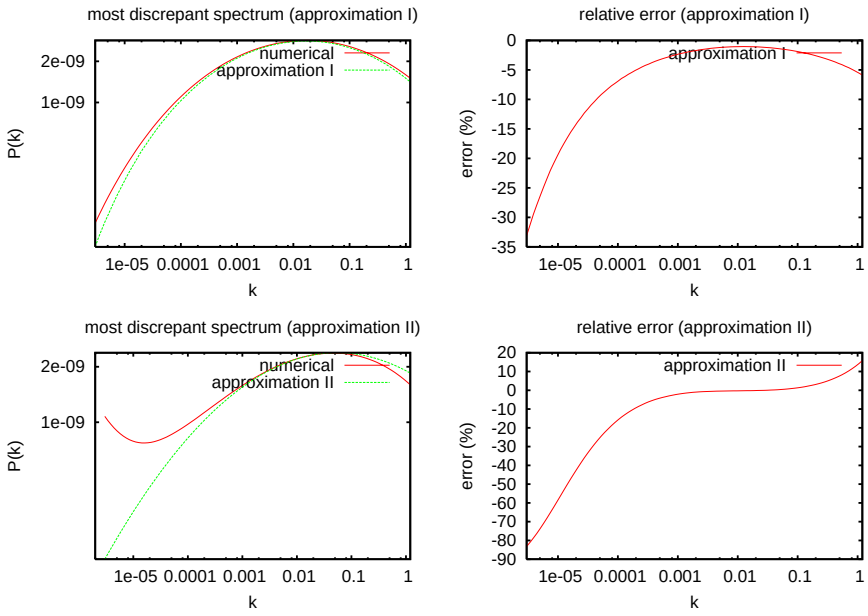

Figure 5.3: *Left:* Curvature spectrum obtained from the exact numerical method or from approximation *I* or *II*, for the most discrepant models in the range $k \in [3 \times 10^{-6}, 1.2]$ Mpc^{-1} selected among the 95% best-fitting spectra. *Right:* The corresponding relative differences. The discrepancy is large only for scales close to $k_{\rm min}$, which have a relatively small statistical weight.

well, but not its amplitude. This is not surprising since in *I*, the expression for the amplitude is first-order in the slow-roll expansion. The next-order contribution to this approximation should include the parameter ξ, with a positive coefficient. Since the data allows large values of $|\xi|$ only when ξ is positive, approximation *I* yields a systematic underestimation of the amplitude. This approach could be straightforwardly improved by computing the curvature amplitude at the next order. In contrast, approximation *II* tends to give the wrong shape, but since it includes one more order in the slow-roll expansion it can give a better estimate of the amplitude for k not too far from k_*.

However, the main result of this section is that the difference between the various spectra is very small, since a large discrepancy is only encountered on scales close to $k_{\rm min}$, which have a relatively small statistical weight in the process of accepting or rejecting a model. For both approximations the error in the larger part of the spectrum is of the order of 5%. Current data does not reach such good sensitivity, especially if we keep in mind that for the largest k values the curvature spectrum is mainly constrained by the SDSS data, which is always marginalised over an unknown bias parameter. For the particular models shown here, the difference in the effective χ^2 obtained when fitting either the approximated or the numerical spectrum to the data is $|\Delta\chi^2_{\rm eff}| = 6.7$ for approximation *I* (model A) and $|\Delta\chi^2_{\rm eff}| = 5.9$ for approximation *II* (model B). One should keep in mind though, that these are just the most extreme deviations, at the edge of allowed parameter space. On average, the inaccuracies are too small to have a significant effect on the inferred bounds. However, with future datasets one can expect the $|\Delta\chi^2_{\rm eff}|$ to become even larger, possibly resulting in biased estimates. Hence, we recommend using the exact numerical approach, since it does not make the analysis longer or more difficult.

The conclusions reached in this section apply to a particular class of inflationary models, namely those described by Eq. (5.3) with parameter ranges limited by current WMAP and SDSS results. Allowing for more freedom in $H(\phi)$, one would expect stronger deviations between the analytical and numerical approaches. Conversely, imposing a constraint on the total number of e-folds for relevant inflation, one would select models which are deeper within slow-roll and obtain even smaller discrepancies. We have limited our discussion to the scalar spectrum, since there is, at present, no evidence for anything but a subdominant tensor contribution in the available data. This may of course change if a primordial B-mode polarisation of the CMB is detected in the future.

5.5 Discussion

We have compared various alternative methods for putting constraints on the observable window of inflationary dynamics, assuming single-field inflation with a smooth behaviour. One could fear that the results would depend very much on the way to compute the spectrum, or on the parameterisation of $H(\phi)$ (i.e., the ensemble of models considered). We point out that with current data these differences are subdominant. The results are mainly affected by the exact prior on

the background. By focusing on the allowed window, one hopes to be conservative and to get results dictated by the data only; however these results are very sensitive to the edges of the interval in field space over which accelerated expansion is required. In other words, the upper bound on ξ is given by this constraint rather than the shape of the perturbation spectrum. Current analyses agree with each other, but only within a factor two, due to this difference. This dependence of the final results on the choice of prior may sound worrisome, particularly if it is one's aim to keep the analysis as general as possible.

It seems as though the priors we initially chose to use with approximations *I* and *II* are less restrictive, and would therefore lead to a more conservative result. Unfortunately however, combining these methods with their respective priors on the space of allowed models is fraught with a severe consistency problem. Both priors allow models in regions of parameter space where the approximations are known to break down, and yield results for the spectrum that cannot be trusted. Approximation *II*, for instance, allows models in which inflation is interrupted within the observable range. Such an event would lead to very distinct signatures, like a cutoff, yet the approximation would still predict a smooth spectrum. It is therefore sensible to expect that inflation lasted at least over the whole observable range. But even that will not be sufficient: if inflation started only just before the observable range, the assumption that the modes start out in the Bunch-Davies vacuum can no longer be justified, and the approximations fail. If, on the other hand, inflation ends just after the smallest observable scale leaves the horizon, the corresponding mode will not have time to freeze out. In fact it would re-enter the horizon right away, and there is no telling (without making further assumptions) in what shape the spectrum would arrive at later times when it is relevant for the determination of the CMB anisotropy spectra.

Hence, it is reasonable to demand a proper vacuum initial condition and a freeze-out of the modes. One could in principle further limit the space of allowed models by constraining the minimum number of e-folds before the end of inflation to a certain number, usually taken to be ≥ 30. However, this would require a daring extrapolation of our simple Taylor-expansion over a huge range of e-folds, where even a tiny higher derivative of the Hubble parameter would eventually take over. In this paper, therefore, we did not want to make any additional assumptions about what happens after the freeze-out.

There are, however, two points at which the prior of the self-consistent numerical approach is slightly arbitrary, corresponding to the two end points of the interval over which we track the background dynamics. The first one is the large scale end, determined by the time at which we choose the initial conditions for the k_{min}. We picked $k_{\mathrm{min}}/50$ as a starting point, but other choices may have been equally good. Fortunately, the data conspire to make this choice have little impact on the final results: only about 0.1% of the models in our chains generated with the laxer prior can be rejected due to inflation starting "too late".

The more critical issue is the small scale end of the interval. Its choice is connected with the question when a mode can be considered to have frozen out, which is set by the limiting value of $[\mathrm{d}\ln\mathcal{P}_{\mathcal{R},T}/\mathrm{d}\ln a]$ at which we stop integrating.

The final results for the posterior are mildly dependent on the choice of this limit, which should eventually be chosen such that the resultant uncertainty in the spectra is smaller than the sensitivity of the data. For this reason, we choose here $[\mathrm{d}\ln\mathcal{P}_{\mathcal{R},T}/\mathrm{d}\ln a] < 10^{-3}$, corresponding to a 0.1% accuracy in the power spectra.

We would like to emphasise once again that the differences in the results are not inherent to the approximations used, but rather due to the attempt to implement them with a minimal prior. Our results also show that if one were to impose a non-minimal prior on the number of e-foldings beyond the observable range, the approximations would lead to the same results as the exact method.

In the future, we expect more robust constraints from high-precision experiments, such as, e.g., the Planck satellite. In turn the difference between the various methods for computing the spectra will become even more relevant. In the light of our results, we recommend using the exact numerical approach for a self-consistent analysis of inflationary dynamics.

Chapter 6

The inflaton potential: Prior dependence of parameters

In this Chapter, we focus on one aspect of the more general analyses in the previous Chapters: the absolute scale of inflation. As explained in Chapter 1, we need a non-zero detection of tensor modes in order to be able to give a strict lower bound on the scale of inflation. At present, this detection has not yet been made. But, up to what extend can we already estimate the scale of inflation? In the previous chapter it seemed that some nonzero value of $H_{\rm inf}$ is favoured, in Fig. **??**. In the following, we will show how with a lack of constraining observations, the choices one inevitably has to make in statistics will influence the outcome of an analysis. We show that, in the case of the scale of inflation, by choosing a different parameterisation of the same physics, one can provoke a seeming lower bound on the scale of inflation. The goal of this chapter is to explore a solution to this uncertainty, the notion of Bayesian complexity, and show that this quantity should be used in order to test up to what extent the outcome of an analysis is dependent on the priors (parameterisation and parameter ranges) chosen.

6.1 Introduction

Shortly after its introduction [4, 99, 161, 163, 228, 244], inflation was found to produce a nearly flat Gaussian spectrum of adiabatic density perturbations that could have been the seeds of observed structure in the Universe [1, 12, 100, 111, 191, 243, 245]. The simplest model of inflation is that of a slowly rolling scalar field [158, 225, 249], which naturally produces a close to flat primordial spectrum. While the available observations are remarkably consistent with such a spectrum, unfortunately one can obtain virtually any scalar spectrum by simply adjusting the shape of the inflaton potential at early times, and therefore present results are strongly suggestive, but not yet unimpeachable evidence that inflation actually occurred.

There are other more generic predictions of inflation that could be subject to testing, however. For example, a single rolling scalar field during inflation produces perturbations that are very close to Gaussian. A detection of significant primordial non-Gaussianity in the cosmic microwave background (CMB) could rule out simple slow-roll inflation [271]. A second possibility is the fact that inflation generally produces a spectrum of tensor perturbations, which could, among other effects, produce an observable B-mode polarization in the CMB [124, 233], albeit plagued by uncertainties [180, 190]. Note that tensor perturbations are not the only source of B-mode polarization [8, 18, 63, 276], and noninflationary transitions can also produce a similar background [121, 137]. Nevertheless, observation of both the scalar spectrum and the tensor spectrum could at least test the predictions of slow-roll (SR) inflation, through the consistency relation

$$n_{\rm T} = -r/8, \qquad \alpha_{\rm T} = n_{\rm T}[n_{\rm T} - n_{\rm S} + 1], \qquad \text{etc.}, \tag{6.1}$$

where $n_{\rm T}$ is the tilt of the tensor spectrum, r is the ratio of the amplitudes of the tensor and scalar spectra, $\alpha_{\rm T}$ is the running of the tensor spectrum and $n_{\rm S}$ is the tilt of the scalar spectrum. A tensor spectrum has not been detected so far, and

many future experiments have been proposed to search for a gravitational waves signal from inflation [22, 130, 142, 169, 170, 196, 210, 222, 254, 275].

With only observations that constrain the scalar spectrum, one might hope to gain some information on the inflaton potential [50, 51, 263]. However the plethora of different models of inflation make such a task difficult. Nevertheless, obtaining any information one can on the potential using the observed scalar perturbations could give information about the possibility of observing tensor perturbations. In Ref. [168] the following relation between the change in value of the scalar field ϕ and the tensor-to-scalar ratio r, holding deep inside the slow-roll approximation, was pointed out,

$$\frac{1}{m_{\rm P}}\frac{\Delta\phi}{\Delta N} \simeq \sqrt{\frac{r}{64\pi}}, \tag{6.2}$$

where N is the number of e-folds the Universe grows *during* the change $\Delta\phi$ of the scalar field. That is, when focusing on only a small part of the potential, and not necessarily on the whole duration of inflation, ΔN can correspond to a number much smaller than the total number of e-folds of inflation, $N \sim 60 - 70$. Hence, relation (6.2) relates the flatness of the potential to the relative amplitude of tensor perturbations. Throughout this work we use $Gm_{\rm P}^2 = \hbar = c = 1$.

As the only current probe of the mechanism of inflation is the observed spectrum of density perturbations in the Universe, Refs. [73, 103, 149, 150, 201, 202] concentrated on reconstructing the inflaton potential only in the observational range. It was found in Ref. [149] that in the observational range naturally $\Delta\phi < m_{\rm P}$ and $\Delta N \sim 22$. This bound on ΔN comes from the condition that the smallest observable modes actually freeze in [103]. The bound on $\Delta\phi$ can then be understood from Eq. (6.2) as the data prefer models with r smaller than at most 0.4 (depending on the data used).

The reconstruction of the inflation potential gave a weak upper limit on r, fully consistent with $r = 0$. More recently, however, at least one group has claimed that recent data imply a nonzero lower limit on r [65].

Obviously it is important to clarify this situation, especially when the results would have such great significance, and when a dedicated satellite mission to probe for primordial B modes associated with a nonzero tensor signal, is being considered.

In cases such as this, it is useful to take a Bayesian approach and to consider how effective the data really are at constraining parameters. Thus, one must consider not merely *a posteriori* probability estimations, but also the effect of prior assumptions (see [200] for some discussion of this issue). If the results depend crucially on the latter, then the parameter estimates one derives from the data must be taken with a grain of salt.

The purpose of this paper is to explicitly explore precisely this question at the current time, in order to help solidify expectations for future measurements of this important and fundamental quantity arising from inflation. Specifically we first explore to what extent the priors one assumes in the analysis affect the expected value of r.

One might argue that with little knowledge of the relevant physics, it is perhaps pointless to argue strongly on behalf of one set of priors or another at this point. It does make sense, however, to examine how robust the conclusions one draws are, under different prior assumptions. (See also work to appear by Vaudrevange and colleagues [26, 270].) This work focuses on the effect of taking a flat prior on the Hubble factor during inflation, and its derivatives with respect to the scalar field value ϕ. We will show that a change of parameterisation, but not of physical model, in this case can lead to significantly different bounds on parameters, some of which may mildly hint at a larger value of r as well.

In this regard we note that in Ref. [65], a lower bound on the tensor-to-scalar ratio has been found which one might be tempted to ascribe to a choice of prior. An important difference between their result and ours however is that their lower bound on the tensor-to-scalar ratio is caused by a theoretical prior: the models they allow can only be consistent with today's observed scalar amplitude and tilt if the tensor-to-scalar ratio is significant. In the present work however, the prior on allowed models is as broad as possible, *a priori* not ruling out any combination of inflationary parameters.

Next, in order to explore the general significance of any derived lower bound on r based on a choice of priors, we examine the Bayesian complexity parameter associated with the current data. This gives a very useful tool to explore how many free parameters the data can usefully constrain. As we demonstrate, for many inflationary parameterisations, the data are currently simply not powerful enough to add information beyond the prior, for all the parameters, explaining the prior-dependence of estimates of r that we have found. Thus, we argue that existing data at best provide a rough upper bound on r, rather than providing a robust estimate of its posterior probability distribution.

In Sec. 6.2 we discuss the relation between different flat priors, and explain how to translate posterior probability densities from one prior to another. In Sec. 6.3 we apply a flat prior on the value of the Hubble parameter and its derivatives during inflation, fit it to the data, and discuss the results for both prior dependence and Bayesian complexity. We conclude in Sec. 6.4.

6.2 Priors and posteriors

When faced with the problem of estimating parameters from data, Bayesian inference enjoys a great popularity among cosmologists (see [261] for a recent review). An essential ingredient of any Bayesian inference is the prior distribution, which encodes our knowledge about these parameters before any data are taken. With a suitable basis of parameter space $\{x_i\}$ chosen, it is often tacitly assumed that the prior is *flat* – signifying our lack of information about this parameter in the absence of data. In other words, the prior probability of an interval Δx_i to contain the true value of the x_i is taken to be constant over the entire domain of definition of parameter space.

However, while in some problems there is a naturally preferred basis of parameter space, this need not always be the case, and an alternative, equally well

motivated parameterisation $\{y_i\}$ may exist. It is straightforward to show that generally, a prior in basis $\{x_i\}$ does not correspond to the same prior in basis $\{y_i\}$. Labelling a prior A on $\{x_i\}$ by $\pi_x^{(A)}$, the corresponding prior on $\{y_i\}$ is given by

$$\begin{aligned}\int \pi_x^{(A)} d^n x &= 1 \\ &= \int \pi_x^{(A)} \left|\frac{dx_i}{dy_j}\right| d^n y \\ &\equiv \frac{1}{V_y} \int \pi_y^{(A)} d^n y, \end{aligned} \tag{6.3}$$

$$\pi_y^{(A)}(\vec{y}) \propto \pi_x^{(A)}\left(\vec{x}(\vec{y})\right) \left|\frac{dx_i}{dy_j}\right|, \tag{6.4}$$

where $V_y = \int d^n y$. Hence a flat, non-informative prior in one basis does not necessarily equal a non-informative prior in another, making the choice of basis equivalent to the choice of prior, and by consequence, extending its influence to the posterior and the inferred parameter constraints, unless the data become informative enough. This problem was identified in [15, 17, 32] in the context of isocurvature models; here we will argue that inflationary parameters, including estimates of the tensor-to-scalar ratio, can also be affected.

6.2.1 Importance sampling

If from earlier analyses one knows that the bounds on parameters in set $\{x_i\}$ have Gaussian-like shapes, and the sets $\{x_i\}$ and $\{y_i\}$ are nonlinearly related, one can expect that correlations between parameters in set $\{y_i\}$ are of nontrivial shape. In that case a Metropolis-Hastings algorithm, which is what we will use later on, will have difficulty exploring parameter space properly within an acceptable amount of time. A solution to this problem is importance sampling, which is the act of picking points according to one posterior distribution, but transforming the chance of accepting the point to another posterior distribution. In this way the algorithm walks through parameter space according to directions in the 'easier-to-explore' $\{x_i\}$-space, but performing the statistics as if working in $\{y_i\}$-space. The resulting chains will be distributed according to the prior chosen in $\{y_i\}$-space. Let A denote statistics with a flat prior on $\{x_i\}$, and let B denote statistics with a flat prior on $\{y_i\}$. In the Metropolis-Hastings algorithm, the chance of accepting a proposed step is directly related to the ratio of its posterior and the posterior of the previous point. Hence a constant multiplicative factor in the posterior is irrelevant, and we can neglect the volume term in Eq. (6.4). By consequence, any constant prior corresponds to a flat prior, such that the conversion to be done is

$$\pi_y^{(B)}(\vec{y}) = \left|\frac{dy_i}{dx_j}\right| \pi_y^{(A)}(\vec{y}) = \text{constant}, \tag{6.5}$$

$$\mathcal{P}^{(B)}(\vec{y}(\vec{x})) = \left|\frac{dy_i}{dx_j}\right| \mathcal{P}^{(A)}(\vec{x}). \tag{6.6}$$

There are two distinct places in the analysis in which the correction for the prior can be applied. One option, which we shall refer to as *post-sampling*, is to take the converged chains of an analysis performed under prior (A), and multiply the weight of each point in the chain by the Jacobian as in Eq. (6.6).

The advantage is that one can post-process readily available chains to present a new prior, which takes practically no time. A possible drawback is that the chains, that converged for an analysis under prior A, may have too few (or no) points in the regions of parameter space important under prior B.

The second option is explicit importance sampling of the second distribution, in which one, during the Monte-Carlo process, transforms the posterior of a point to reflect the correct prior, by applying Eq. (6.6) before the decision about acceptance of the point is taken. The advantage is that the convergence statistics will now be performed for the correct probability density, hence important regions will have enough points in the chains. A drawback is that the analysis has to be performed from scratch, which can be time consuming.

6.2.2 Cosmological parameters

When constraining the parameters of ΛCDM cosmologies, it is a popular choice to take flat priors on $\{\Omega_{\rm c}h^2, \Omega_{\rm b}h^2, \tau, \theta\}$ (the dark matter density, the baryon density, the optical depth to reionisation, and the ratio of sound horizon to angular diameter distance at decoupling, respectively) and for the primordial power spectrum a flat prior on either $\{\ln A_{\rm S}, n_{\rm S}, \alpha_{\rm S}\}$ (the amplitude, tilt, and running of the spectrum) or $\{\ln A_{\rm S}, \epsilon_i\}$, with $\{\epsilon_i\}$ some basis of slow-roll (SR) parameters. In the SR-basis of Hubble-flow parameters, the dynamics of inflation are hidden in these parameters by

$$A_{\rm S} = \frac{4H_*^4}{H_*'^2 m_{\rm P}^4}, \tag{6.7}$$

$$\epsilon = \frac{m_{\rm P}^2}{4\pi}\left(\frac{H_*'}{H_*}\right)^2, \tag{6.8}$$

$$H_* = \frac{m_{\rm P}^2}{2}\sqrt{\pi A_{\rm S}\epsilon}. \tag{6.9}$$

where $H_{\rm Inf} = H_*$, '$_*$' denotes evaluation at the pivot scale, and $'$ denotes derivation with respect to the field value of the inflaton. This means that in all these analyses the posterior distribution of the derived parameter $H_{\rm Inf}$ is obtained with a non-flat prior.

In Fig. 6.1 we show the Jacobian $\left|\frac{dx_i}{dy_j}\right| = \frac{4H_*'^2 m_{\rm P}^6}{H_*^6}$ relating the coordinate

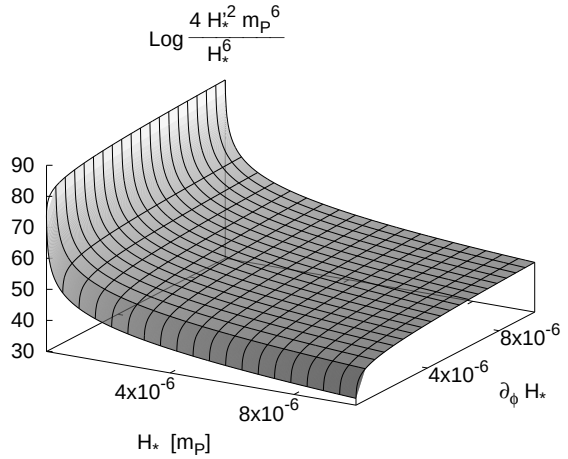

Figure 6.1: The Jacobian $\left|\frac{dx_i}{dy_j}\right|$for the coordinate transformation from set $\{x_i\}$ to set $\{y_i\}$. It is clear that a flat prior on set $\{x_i\}$ strongly favors small values for H_* compared to a flat prior on set $\{y_i\}$, as $\pi_y^{(A)} \sim \pi_x^{(A)} \left|\frac{dx_i}{dy_j}\right|$.

transformation between sets

$$\{x_i\} \equiv \left\{ \ln \frac{4H_*^4}{H_*'^2 m_{\rm P}^4}, \left(\frac{H_*'}{H_*}\right)^2 m_{\rm P}^2, \frac{H_*''}{H_*} m_{\rm P}^2, \frac{H_*''' H_*'}{H_*^2} m_{\rm P}^4 \right\} \tag{6.10}$$

$$\{y_i\} \equiv \left\{ \frac{H_*}{m_{\rm P}}, H_*', H_*'' m_{\rm P}, H_*''' m_{\rm P}^2 \right\}, \tag{6.11}$$

corresponding up to a constant to the ratio $\pi_y^{(A)}/\pi_x^{(A)}$. A flat prior on set $\{y_i\}$ (prior B) favors high values of H_* when compared to a flat prior on set $\{x_i\}$ (prior A).

Once the data come into play, the amplitude $A_{\rm S}$ will essentially be fixed. Since $A_{\rm S} \propto H_*^2/\epsilon$, higher values of H_* will need to be offset by higher values of ϵ. In the slow-roll regime, ϵ is related to the tensor-to-scalar ratio r by

$$r \simeq 16\epsilon = \frac{4m_{\rm P}^2}{\pi}\left(\frac{H'}{H}\right)^2, \tag{6.12}$$

and hence we can expect prior B to prefer a larger tensor contribution, compared to prior A. Equation (6.12) also shows that a flat prior on ϵ roughly corresponds to a flat prior on r.

6.3 Flat prior on $H_{\rm Inf}$

In order to probe the scale of inflation, we numerically integrate the perturbation equations of the inflaton in a background described by a Taylor-expansion of $H(\phi)$, as discussed in [149, 150], and constrain the free parameters using temperature and polarization data from the five year data release of the Wilkinson Microwave Anisotropy Probe (WMAP) satellite (WMAP5) [70], as well as the power spectrum of luminous red galaxies from the Sloan Digital Sky Survey (SDSS-LRG) [255]. The parameter estimation is done using the Metropolis-Hastings algorithm, employing a modified version of the publicly available code `CosmoMC` [152] together with our own module for inflationary perturbations (which is available for download at `http://wwwlapp.in2p3.fr/~valkenbu/inflationH/`). The parameters describing the model are either $\{\Omega_{\rm c}h^2, \Omega_{\rm b}h^2, \tau, \theta\} + \{x_i\}$ or $\{\Omega_{\rm c}h^2, \Omega_{\rm b}h^2, \tau, \theta\} + \{y_i\}$. We include the calculation of tensor perturbations.

As a consequence of this exact numerical treatment of perturbations, we automatically impose a consistent inflationary prior (in the following this is referred to as "inflationary consistency"). By numerically integrating the perturbation equations until the actual freeze-in of all modes, this method requires inflation to occur over the observable range, which constrains parameters more strongly than a naive application of the SR-approximation. As pointed out in Ref. [103], a naive implementation of the SR-approximation allows for inconsistent models, for which small scale modes actually do not freeze in, even though the approximation provides a spectrum. We make no prior assumption on the total length of inflation other than the length needed to produce the observed power spectrum of perturbations. That is, we remain conservative about the mechanism of inflation during the unobserved epoch, between horizon exit of the smallest observable modes and the end of inflation.

As a consistency check we performed both described methods, post-sampling and importance sampling. In Fig. 6.2 we show the one dimensional marginalised posterior distributions of the four cosmological parameters describing the physics after inflation, comparing the analyses with prior A, the post-sampled chains from prior A to prior B, and the chains with prior B (importance sampled). The post-sampled and importance sampled analyses completely agree, which shows that the chains that converged under prior A have enough samples in the typical set of the posterior distribution under prior B. As should be expected, the four parameters shown in Fig. 6.2 are not affected by the change in prior. In Fig. 6.3 we show the posterior distributions of parameters describing the inflationary evolution. The main change is in the posterior of the parameter $\left(\frac{H'}{H}\right)^2 m_{\rm P}^2$, which has a higher preferred value under prior B than under prior A. This result is in agreement with the expected effect, illustrated in Fig. 6.1.

The scale of inflation and the tensor-to-scalar ratio are shown in Fig. 6.4. Both parameters, which are related, have a higher preferred value under prior B.

For illustration, in Fig. 6.4, we also show a post-sampled distribution with a flat prior on $\{\ln H_*, H'_*, H''_*, H'''_*\}$. Also this prior gives a higher value for H_* and r than prior A does. Note that under both prior A and prior B, we find a

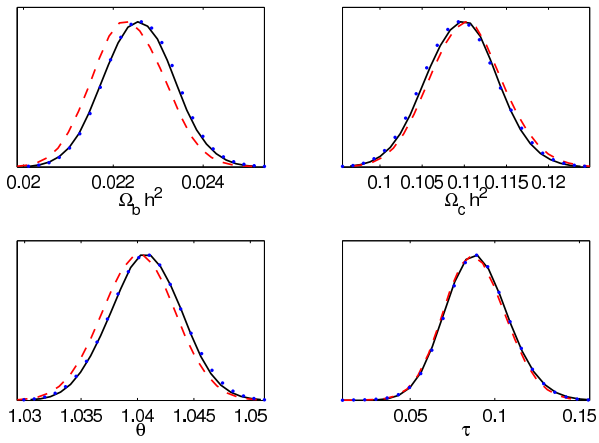

Figure 6.2: The marginalized posterior distributions of cold dark matter density ($\Omega_{\rm c}h^2$), the baryon density ($\Omega_{\rm b}h^2$), the ratio of sound horizon to angular diameter distance at decoupling (θ) and the optical depth to reionisation (τ), under prior A (red dashed line), post-sampled from prior A to prior B (blue dotted line) and under prior B (black solid line). The post-sampled distributions are hardly visible as they practically completely agree with the importance sampled distributions.

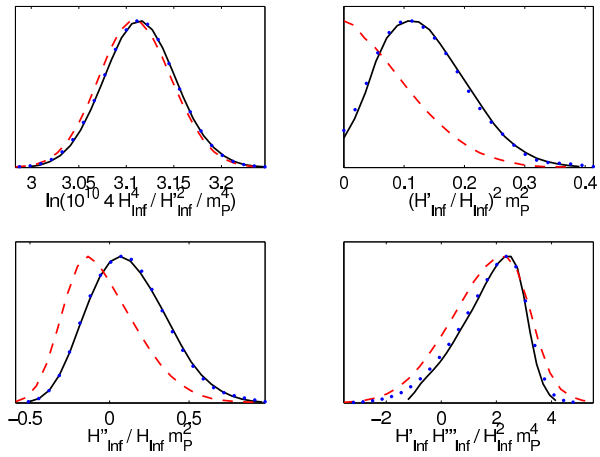

Figure 6.3: The marginalized posterior distributions of the parameters describing the evolution of the Universe during inflation, for the same analyses as in Fig. 6.2. Again the post-sampled distribution (blue dotted line) is hardly visible due to its good agreement with the importance sampled distribution (black solid line). The main change under the transformation of priors is seen in the posterior of $\left(\frac{H'}{H}\right)^2 m_{\rm P}^2$, in agreement with the prediction in Fig. 6.1.

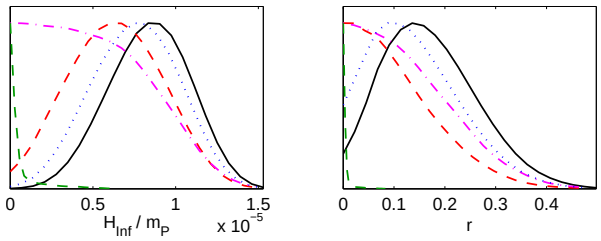

Figure 6.4: The marginalized posterior distributions for the scale of inflation, $H_{\rm Inf}$, and the scalar-to-tensor ratio, r, under prior A (red dashed line), under prior B (black solid lide), post-sampled to a Jeffreys prior on H_* (thin blue dotted line) and under a flat prior on $\{A_s, \ln\epsilon, \frac{H''_*}{H_*}m_{\rm P}^2, \frac{H'''_*H'_*}{H_*^2}m_{\rm P}^4\}$ (green dashed, close to zero for both figures). Prior B corresponds to a flat prior on $H_{\rm Inf}$, whereas prior A roughly corresponds to a flat prior on r, as explained in the text. Prior B pushes both $H_{\rm Inf}$ and r up in value. Also shown is the mean likelihood over each $(8-1)$–dimensional parameter space for all values of H and r (dashed-dotted, magenta).

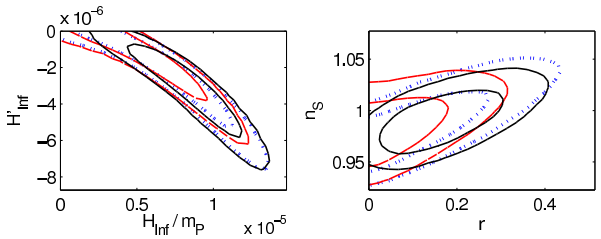

Figure 6.5: Two dimensional marginalised posterior distributions for two illustrative cases, comparing prior A (red dashed line), prior B (black solid) and a noninflationary analysis, probing the four cosmological parameters plus the set $\{\ln A_{\rm S}, n_{\rm S}, \alpha_{\rm S}, r\}$ describing the primordial spectrum (blue dotted line). All inner contours correspond to 68% CL bounds, all outer contours correspond to 95% CL bounds. *Left:* the curved correlation shape between $\partial_\phi H_{\rm Inf}$ and $H_{\rm Inf}$ illustrates the need for importance sampling when taking a flat prior on these parameters. *Right:* both r and $n_{\rm S}$ are pushed up by prior B.

lower r than the combined analysis of the WMAP three year data and SDSS-LRG in Ref. [255], which is due to our inflationary prior: integrating the modes until actual freeze-in, means demanding inflation for about 22 e-folds, which forces the inflaton potential to be relatively smooth. The smoothness of the potential pushes ϵ down and thereby also r. Likewise the scalar tilt $n_{\rm S}$ is pushed toward unity, as is shown in Fig. 6.5 where the two dimensional parameter correlations are shown for two illustrative cases, $H_{\rm Inf}$ versus $\partial_\phi H$, and r versus $n_{\rm S}$. The former illustrates the nonlinear correlation between the parameters $H_{\rm Inf}$ and $\partial_\phi H$ in the data. The curved shape of the posterior probability contour indicates that it would take a Metropolis-Hastings sampler a long time to random-walk from one lobe to another if steps are only to be taken in either horizontal or vertical direction, or a linear combination of both, in the plane of this plot. By using importance sampling, steps are taken in correlated directions, significantly speeding up the process. The latter shows both the effect of the inflationary prior, present in both analyses, and the effect of going from prior A to prior B. In both analyses the value of ϵ is relatively close to zero, however it is larger under prior B.

It is interesting to note that we also find an apparent lower bound on the scale of inflation, even for a flat prior on H_*. In fact, this phenomenon is related to our choice of prior on ϵ (or H'_*, under prior B). Let us illustrate the effect in the example of prior A. The dislike of the data for a large tensor contribution leads to an upper bound on ϵ due to Eq. (6.12). In order to reproduce the observed amplitude of fluctuations, $A_{\rm S} \sim H_*^2/\epsilon$ implies also an upper bound on H_*. However, as a consequence of the flat prior on ϵ, extremely small values of ϵ, while certainly allowed by the data, are assigned an exponentially suppressed probability, with a preference for ϵ of the order of magnitude of its upper bound. Since $A_{\rm S} \sim H_*^2/\epsilon$, we also have a suppression of small values of H_*, with a peak slightly below the upper bound. If we instead take the prior to be flat on the logarithm of ϵ (i.e., a Jeffreys prior on ϵ), we do not see such a suppression. However, the results for the Jeffreys prior on ϵ must be interpreted with care as they are highly dependent on the lower bound. For numerical reasons we took a lower bound of $\ln\epsilon > -57$. Had we taken an even smaller lower bound, the lines would be even closer to zero. A similar result can be anticipated for a flat prior on $\ln H'_*$ in the $\{y_i\}$ parameterisation. That this dependence on the lower bound does not occur under the Jeffreys prior on H but a flat prior on H' is explained by the same reasoning as the apparent lower bound on H.

In addition to the posteriors, Fig. 6.4 shows the mean likelihood over each $(8-1)$–dimensional parameter space for all values of H and r. This is a prior-independent quantity with no probabilistic information (i.e., it is not a probability density). It serves as an approximation for the profile likelihood. The profile likelihood is the best fit that can be achieved given a certain parameter value. The discrepancy between the mean likelihood and the various posteriors indicates that the various lower bounds in the posteriors are results of either volume effects in the process of marginalization, the choice of prior, or a combination of both. The mean likelihood shows that a good fit can even be achieved for very small values of r and $H_{\rm Inf}$. In fact the best fit we found lies at $r = 4 \times 10^{-2}$ and

$H_{\rm Inf} = 4 \times 10^{-6} m_{\rm P}$. This certainly does not coincide with the peaks of the posteriors found for priors A and B.

In Fig. 6.5 we also compare derived parameters from the different analyses with the bounds obtained on these parameters when using no inflationary prior and simply fitting a primordial power spectrum,

$$P(k) = A_{\rm S} \left(\frac{k}{k_*} \right)^{n_{\rm S} - 1 + \frac{1}{2}\alpha_{\rm S} \ln \frac{k}{k_*} + \ldots}, \tag{6.13}$$

and a consistent tensor spectrum, described by r and consistency relations between the tensor spectral tilt ($n_{\rm T}$) and the scalar parameters, to the same data. Calculating $\{H_{\rm Inf}, H'_{\rm Inf}\}$ from $\{A_{\rm S}, n_{\rm S}, \alpha_{\rm S}, r\}$ is done using the relations given in Ref. [150]. The curved shape of the correlation between $H'_{\rm Inf}$ and $H_{\rm Inf}$ reflects the need for importance sampling. The 95% confidence level (CL) contours under prior A correspond to the 95% CL contours from the spectral fit for small values of $H'_{\rm Inf}$, whereas the 95% CL contours under prior B correspond to the spectral fit for large values of $H'_{\rm Inf}$. An important conclusion to draw here is that both priors A and B allow most of parameter space that is allowed by the spectral fit, which has no inflationary prior.

In the $n_{\rm S}$-r–plane, prior A clearly pushes r down with respect to merely performing a spectral fit because of the demand that inflation lasts long enough to produce the full observed spectrum under a flat prior on virtually the same parameters, whereas prior B pushes r up, in spite of the same condition on the duration of inflation.

In the absence of clearly favoured theoretical models, the beauty of various priors is, alas, largely in the eye of the beholder. Nevertheless we emphasise that both priors A and B do not exceed the spectral limits but do probe practically the whole range allowed without the requirement of persistent inflation. More interestingly, the 68% CL contour for prior B actually yields a nonzero lower bound for r. Marginalised over all parameters, the posterior of r gives, at 68% CL, $0.061 < r < 0.243$, however at 95% CL r is still consistent with zero. While this may hint at a nonzero amplitude of tensor modes, our analysis underscores the prior model dependence of this result and thus we do not put much stake in it here. Nevertheless, it does suggest that future polarization searches for tensor modes may have a better chance of detection than otherwise suggested.

Bayesian Complexity

When selecting models and priors, a quantity that can distinguish between models is the Bayesian evidence, which rewards both the predictivity and the conciseness of a model, and gives preference to the model with the best balance between the two characteristics. When the Bayesian evidence cannot distinguish between two models, a secondary quantity to make the comparison is the Bayesian complexity [140, 241],

$$\mathcal{C}_{\rm b} \equiv \overline{\chi^2} - \chi^2(\hat{\theta}), \tag{6.14}$$

	Prior A	Prior B	$\{A_{\rm S}, n_{\rm S}, \alpha_{\rm S}, r\}$	$\{A_s, \ln\epsilon, \frac{H_*''}{H_*}m_{\rm P}^2, \frac{H_*'''H_*'}{H_*^2}m_{\rm P}^4\}$
C_b	6.98 ± 0.03	7.80 ± 0.03	7.76 ± 0.06	6.25 ± 0.8

Table 6.1: Bayesian complexity for different choices of prior. This number should be compared to the number of free parameters, which is eight for all models considered here.

where the effective χ^2 is defined as $-2\ln\mathcal{L}$, with the likelihood $\mathcal{L}$, and $\hat{\theta}$ denotes the best fit point, and the overline denotes the mean over the posterior. The Bayesian complexity measures the information gain when going from the prior to the posterior, and can be interpreted as a measure of the number of parameters the data can constrain in a model, or conversely the number of parameters a model effectively needs to fit the data. Along the same lines, if the Bayesian complexity is smaller than the actual number of free parameters of a model, this could be taken as a sign that the model contains "unnecessary" degrees of freedom, i.e., parameters on which we do not gain information from the data.

Note that the Bayesian complexity itself contains no information about the goodness of fit of a model, or the evidence of one model over another, but gives an additional measure on the number of parameters in a model that is justified by the data. Without an evidence calculation, the complexity can still be useful for telling whether parameters are mostly bounded by either the data or the prior. In this work we are interested in the question which priors (with the same underlying model) constrain parameters beyond the constraining power of the data, and which priors allow the data to give information on parameters.

The Bayesian evidence cannot be reliably calculated from the Markov-chain Monte Carlo (MCMC) chains obtained doing the parameter estimation, as these chains have a lack of information on the tails of the parameter distributions. An elaborate analysis would be necessary, e.g. using nested sampling [193]. The Bayesian complexity, however, can be readily calculated from the chains. In Table 6.1, we show the Bayesian complexity for the same model under the different priors.

For prior A we find a complexity of 6.98 ± 0.03, for eight free parameters. This indicates that the data do not give any information on one of the free parameters. Most likely this is due to $\frac{H_*'''H_*'}{H_*^2}m_{\rm P}^4$ which is more tightly constrained by imposing inflationary consistency than by the data, as explained in Ref. [103]. Compared to prior A, prior B has more volume in regions constrained by the data, increasing the amount of information gained and pushing up the complexity to 7.80 ± 0.03. Compared to that, in the $\{A_s, \ln\epsilon, \frac{H_*''}{H_*}m_{\rm P}^2, \frac{H_*'''H_*'}{H_*^2}m_{\rm P}^4\}$ basis the opposite happens, as ϵ is pushed much closer to zero, such that the data give no new information on this parameter, decreasing the complexity. For the "phenomenological" parameter set $\{A_{\rm S}, n_{\rm S}, \alpha_{\rm S}, r\}$ with flat priors, no inflationary consistency is imposed. Therefore, in this basis, $\alpha_{\rm S}$ has no theoretical prior constraints and can be constrained by the data.

An increase in the complexities under prior B and the phenomenological prior compared to prior A should not be taken to mean that these prior choices are superior. Indeed, in all cases the complexity value is less than 8, which is the number of inflationary parameters under consideration. Rather, we take this as an indication that the data is highly sensitive to the choice of parameterisation of inflationary models, in particular the choice of prior distribution for r, and hence the posterior probability densities reflect far more the choice of volume of prior parameter space than the impact of the data.

6.4 Conclusion

Our paper makes explicit an important and well-known fact regarding the effort to constrain cosmological parameters: the importance of prior assumptions in the analysis must not be neglected. We have demonstrated in a variety of ways that this situation is relevant to the current issue of a possible nonzero value of r and expectations for future CMB missions. In the absence of clear theoretical direction, it is important therefore to consider the divergence of results obtained by presumably equally well motivated priors. We have demonstrated here how to relate flat priors on different parameterisations of the same physics, and applied a change of parameterisation to the reconstruction of the inflaton potential, choosing a flat prior on the parameters that may be better motivated by the physics of inflation, as opposed to parameters describing the observable quantities. The main change, seen in Figs. 6.4 and 6.5, is an increase of the preferred value for the tensor-to-scalar ratio r, moving from $0 < r < 0.18$ to $0.061 < r < 0.243$ at 68% CL We stress once again that this new preferred range does not imply that the data now prefer a nonzero value of r, since at 95% CL r is consistent with zero under all used priors. The fact that for certain choices of parameterisation the complexity is less than the number of free parameters, eight, indicates that the data is currently insufficient to fully constrain the models. Rather, our calculation of the complexity shows that for prior B, which gives the increased range in r, the data are simply sensitive to more of the parameter volume. Thus we consider the mean likelihood to be a more meaningful quantity here. In particular information on the parameters r and $H_{\rm Inf}$ under prior B is primarily gained on the upper bound.

As a result we emphasise that the mean likelihood for the parameters we considered gives an indication of neither a nonzero scale of inflation nor a nonzero tensor-to-scalar ratio. Nevertheless, the fact that one plausible parameterisation of the data increases the posterior probability of these quantities to be nonzero, suggests that from a Bayesian point of view the motivation for probing for tensor modes may be slightly enhanced as a result of our analysis.

Part III

Constraints from secondary anisotropies

Chapter 7

The integrated Sachs-Wolfe effect: constraining the neutrino mass

In Part II, we used observations to constrain inflation and the spectrum of primordial perturbations, already present at the beginning of the radiation era. The CMB photons do not only carry information about the cosmic perturbations up till the moment of decoupling (primary anisotropies), they also gain information on their way to us (secondary anisotropies). The photons have interactions with their surroundings, still after decoupling, albeit at a much lower level than before decoupling (otherwise they would probably loose the information about the primordial spectrum). One of the ways of interacting is purely gravitational of origin. The CMB photons pass through gravitational potential wells and hills. If such a well is constant in time, a photon exits the well at the same energy as at which it entered. If the well however changes with time while the photon crosses it, the photon will gain or loose energy, depending on whether the well shallowed or steepened. When this process occurs at the same redshifts and scales as at which we observe large scale structure, a correlation will appear between the large-scale-structure power spectrum and the CMB power spectrum. This effect has in fact been observed, and is used to constrain Dark Energy, since Dark Energy will cause the gravitational potential on large scales too dilute. Dark Energy is however not the only quantity that can change the growth of linear gravitational potentials with respect to a pure CDM-universe.

Neutrinos play a particular role in the matter power spectrum as well. Depending on their mass, neutrinos will not participate in the gravitational infall of matter on scales smaller than a typical scale. There is a simple relation between this typical scale and the total mass of the neutrinos, as we will see in the following. On the scales at which the neutrinos do not participate in the formation of structure, the formation of structure will be slightly slower than if all mass would be in dark matter and baryons. Hence, in momentum space, the matter power spectrum will show a slight change in slope, which will start at the scale set by the neutrino mass. Besides, as opposed to a pure CDM universe, the gravitational potentials will not be exactly constant during matter domination. Hence, neutrinos of a certain mass, will induce a non-zero cross correlation between the CMB and the LSS, in a scale dependent manner. It is the scale dependence that lets us make the distinction between the effect of Dark Energy and the effect of the mass of the neutrino. In the following, we will explore up to what extent the neutrino mass could be constraint using this effect.

7.1 Introduction

As photons pass through a changing gravitational potential well, they experience a redshift or a blueshift, depending on whether the well grows or decays respectively. Cosmic microwave background (CMB) photons can experience such variations between the time of last scattering and their detection now. This effect was first described by Sachs and Wolfe in 1967 [224], and hence is dubbed the integrated Sachs-Wolfe effect (ISW). During a Cold Dark Matter (CDM) and/or baryon dominated era, the gravitational potential distribution remains frozen, and the ISW effect has no net effect on the blackbody temperature of CMB photons.

This property is crucially related to the fact that non-relativistic matter (like CDM and baryons) has a vanishing sound speed, and experiences gravitational clustering on all sub-Hubble scales after photon decoupling, as described by the Poisson equation. In such a situation, the universal expansion and the gravitational contraction compensate each other in such a way as to maintain a static gravitational potential. However, when the expansion rate is affected by any type of matter with a non-vanishing sound speed, e.g. during Dark Energy (DE) domination, the gravitational perturbations decay and the cosmic photon fluid experiences a blue shift, acquiring extra temperature perturbations related to the intervening pattern of matter perturbations. It was first proposed by Crittenden and Turok in 1995 [57] to cross correlate maps of temperature perturbations in the CMB with those of matter over-densities in large scale structures (LSS), in order to measure a possible acceleration of the universe's expansion. However, the CMB and LSS data available at that time were not good enough for such an ambitious goal, and the first strong indication of a positive acceleration came in 1998 from the side of type-Ia supernovae [204, 219]. Analyses of the first (2003) and second (2006) data releases of the Wilkinson Microwave Anisotropy Probe (WMAP) [239, 240] were the first to indicate the existence of Dark Energy independent of acceleration, by means of the location of the second peak in the CMB power spectrum. Simultaneously, a number of interesting papers presented the first detections of the ISW effect by cross-correlating WMAP anisotropy maps with various LSS data sets [3, 27, 35, 37, 80, 81, 91, 185, 197], now able to give an independent measure for the acceleration of the expansion of the universe.

The domination of Dark Energy is not the only source of gravitational potential evolution and of a net ISW effect. On small cosmological scales, as soon as matter perturbations exceed the linear regime, gravitational perturbations start to grow and to redshift CMB photons. This effect, called the Rees-Sciama effect, has not been significantly detected until now [214]. CMB photons can also be scattered by gravitational lensing [232] and by the Sunyaev-Zeldovich (SZ) effect [253] (see [2, 3, 80] for detections in CMB-LSS cross-correlation analysis). An other party expected to affect the evolution of gravitational perturbations –at least by a small amount– is the background of massive neutrinos. Over thirty years ago massive neutrinos were proposed as a Hot Dark Matter (HDM) candidate, and later ruled out as the dominant dark component, since HDM tends to wash out small scale over-densities during structure formation [212]. Observed neutrino oscillations however constrain neutrinos to have a mass [79, 173]. In addition, the presence of a Cosmic Neutrino Background (CNB) is strongly suggested on the one hand by the abundance of light elements produced during primordial nucleosynthesis [60, 175, 248], and on the other hand by CMB anisotropies [13, 16, 58, 59, 61, 102, 104, 107, 116, 116, 207, 262]. Therefore, a small fraction of HDM is expected to coexist with the dominant CDM component. On small cosmological scales (for instance, cluster scale), the free-streaming of massive neutrinos should induce a slow decay of gravitational and matter perturbations [25], acting during both matter and Dark Energy domination. This effect depends on the total neutrino mass summed over all neutrino families,

$m_\nu = \sum_i m_i$, unlike laboratory experiments based on tritium decay or neutrinoless double-beta decay, which probe different combinations: hence, a cosmological determination of the total neutrino mass would bring complementary information to the scheduled particle physics experiments [105, 146]. The free streaming of massive neutrinos has not yet been detected [106], but there are good prospects to do so in the future, since the smallest total neutrino mass allowed by data on atmospheric neutrino oscillations ($m_\nu \geq \sqrt{\Delta m^2_{\rm atm}} \sim 0.05$ eV) implies at least a 5% suppression in the matter/gravitational small-scale power spectrum [105, 146]. A positive detection –even in the case of minimal mass– could follow from the analysis of future galaxy/cluster redshift surveys [109, 147, 273], weak lensing surveys [108, 238], Lyman-α forest analysis, cluster counts [273], etc. The goal of measuring the neutrino mass from cosmology is very ambitious since each of these methods suffers from its own source of systematics (bias issues, modelling of non-linear clustering, ...). Therefore, a robust detection could only be achieved by comparing the results from various types of experiments.

The goal of this work is to describe a possible cosmological determination of the absolute neutrino mass scale through the ISW effect induced by neutrino free-streaming on CMB temperature maps, using as an observable the cross-correlation function of galaxy-temperature maps. This possibility was investigated previously by Ichikawa and Takahashi [117] (and suggested again recently in [126]). As neutrinos slow down the growth of structure, we expect the blueshift caused by an accelerated expansion to be more pronounced if neutrinos have a larger mass. On the other hand, the distribution of matter inducing the late ISW effect is smoother in case of free-streaming by massive neutrinos. These two antagonist effects should in principle induce some mass-dependent variations in the galaxy-temperature cross-correlation function.

In section 7.2 of this paper we give an outline of the theory of the ISW-effect in the presence of a neutrino mass. In section 7.3, we use some mock data with properties inspired from the Planck satellite, Dark Energy Survey (DES) and Large Synoptic Survey Telescope (LSST) in order to show the potential impact of this method in the future.

7.2 The galaxy-ISW correlation in the presence of neutrino mass

7.2.1 Definitions

The observed galaxy overdensity δ_G in a given direction $\hat{n}$ is defined as

$$\delta_G(\hat{n}) = \int dz\, b(z)\phi_G(z)\delta_m(\hat{n}, z), \tag{7.1}$$

where z denotes redshift, $b(z)$ is the redshift dependent bias function relating the observed galaxy over-density to the total matter over-density, and $\phi_G(z)$ is the galaxy selection function which can be chosen such that only galaxies within a certain range of redshift are considered.

The observed CMB temperature map

$$\Delta_T(\hat{n}) \equiv \frac{T(\hat{n}) - T_0}{T_0} \tag{7.2}$$

results from various contributions, classified as primary or secondary anisotropies. By definition, secondary anisotropies are induced after photon decoupling and can be correlated to some extent with the surrounding large scale structure. The ISW component is one of these terms, and can be obtained by integrating the scalar metric perturbations (or just the Newtonian gravitational potential on sub-Hubble scales) along each line-of-sight between the last scattering surface and the observer. If the gravitational potential is written as a function of direction $\hat{n}$ and redshift z, the ISW term reads

$$\Delta_T^{ISW}(\hat{n}) = -2 \int_0^{z_{\rm dec}} dz \, \frac{d\Phi}{dz}(\hat{n}, z). \tag{7.3}$$

where $z_{\rm dec}$ is the redshift at decoupling. Immediately after decoupling and before full matter domination, the gravitational potential does vary with time: this is known as the early ISW (eISW) effect, in contrast with the late ISW (lISW) in which we are presently interested. The two maps Δ_T^{eISW}, Δ_T^{lISW} can be computed separately by cutting the above integral in two pieces at some intermediate redshift z_* chosen during full matter domination, when the gravitational potential is static. Note that in presence of massive neutrinos, the potential is never really static on small scales, so the quantity Δ_T^{lISW} might not be uniquely defined. Anyway, this question is not relevant in practice. The observable quantity is not the late ISW auto-correlation function $\langle \Delta_T^{lISW}(\hat{n}) \Delta_T^{lISW}(\hat{n}') \rangle$, but only its cross-correlation with a given survey $\langle \Delta_T^{lISW}(\hat{n}) \delta_G(\hat{n}') \rangle$. Then, the redshift distribution $\phi_G(z)$ selects the range in which the ISW effect is being probed, and the choice of z_* becomes irrelevant provided that z_* remains larger than the redshift of all objects in the survey: $\phi_G(z_*) \simeq 0$.

Assuming that the galaxy-temperature cross-correlation function arises solely from the late ISW effect (i.e., assuming that other secondary anisotropies potentially correlated with LSS can be separated or have a negligible amplitude, which is a good assumption on the scales considered hereafter), we can relate the galaxy-temperature correlation multipoles to the real-space correlation function $\langle \Delta_T^{lISW}(\hat{n}) \delta_G(\hat{n}') \rangle$. In the Limber approximation (see Appendix B), one gets

$$\begin{aligned} C_l^{TG} = & \frac{3\Omega_m H_0^2}{(l+1/2)^2} \\ & \times \int_0^{z_*} dz \, b(z) \phi_G(z) H(z) a(z) \left[\partial_z \frac{P(k,z)}{a(z)^2} \right]_{k=\frac{l+1/2}{r(z)}}, \end{aligned} \tag{7.4}$$

where $r(z)$ is the conformal distance up to redshift z, $H_0 = 100h$ km/s/Mpc is the Hubble parameter today, and the matter power spectrum is defined as $\langle \delta_m(\vec{k}, z) \delta_m(\vec{k}', z) \rangle \equiv P(k, z) \; \delta^3(\vec{k} - \vec{k}')$. Note that we used the Poisson equation

in flat space in order to relate the gravitational potential Φ to the matter over-density δ_m, and assumed $a(0) = 1$ by convention. Finally, the multipoles C_l^{TG} define the angular correlation function in a Legendre polynomial basis (p_l),

$$w^{TG}(\theta) = \sum_l \frac{2l+1}{4\pi} p_l(\cos\theta) C_l^{TG}. \tag{7.5}$$

Eq.(7.4) is often written in a form which assumes that the matter power spectrum is a separable function of wavenumber and redshift. This applies to the case of a (flat) ΛCDM universe, for which one can write

$$P(k,z) = D(\Lambda;z)^2 a(z)^2 P(k,0) \tag{7.6}$$

with $\partial_z D = 0$ during full matter domination and $\partial_z D > 0$ during Λ domination. Figure 7.1 (left) shows the evolution of D as a function of z for $\Omega_\Lambda = 1 - \Omega_m = 0.69$. In the case of time-varying Dark Energy, the situation is qualitatively similar, and D just depends on more free parameters than Λ. In the rest of this paper, we will just write this function as $D(z)$ for concision.

7.2.2 Effect of neutrino masses

In models with massive neutrinos, the spectrum is not a separable function anymore (in other words, the linear growth factor is scale-dependent), and Eq.(7.4) cannot be further simplified. However, in order to make analytical estimates of the impact of neutrino masses on C_l^{TG}, it is possible to use some approximate solutions valid only on the largest and smallest wavelength (see [146] and [126] for more details). First, for wavelengths larger than the maximum value of the neutrino free-streaming scale, reached at the time of the transition to the non-relativistic regime, the power spectrum P^{f_ν} is completely unaffected by neutrino masses, and identical to that in a massless neutrino model with the same cosmological parameters (in particular, the same Ω_m and h) noted as P^0:

$$\begin{aligned} \forall k < k_{\rm nr}, \qquad & P^{f_\nu}(k,z) = [D(z)a(z)]^2 P^{f_\nu}(k,0) \\ \text{with} \qquad & P^{f_\nu}(k,0) = P^0(k,0)\ . \end{aligned} \tag{7.7}$$

On the other hand, for wavelengths smaller than the the free-streaming scale today, both the linear growth factor and the amplitude today are affected by neutrino masses, approximately like:

$$\begin{aligned} \forall k > k_{\rm fs}, \qquad & P^{f_\nu}(k,z) \simeq [D(z)a(z)]^{2-\frac{6}{5}f_\nu} P^{f_\nu}(k,0) \\ \text{with} \qquad & P^{f_\nu}(k,0) \simeq [1 - 8f_\nu] P^0(k,0)\ , \end{aligned} \tag{7.8}$$

where $f_\nu = \Omega_\nu/\Omega_m$ stands for the neutrino density today relative to the *total* matter density (so Ω_m includes baryons, hot and cold dark matter). Here $D(z)$ is always the same function, computed either for $f_\nu \neq 0$ on large scales, or for $f_\nu = 0$ on any scale, with a common value of Ω_Λ (or of Dark Energy parameters).

The first approximation in Eqs. (7.8) is very accurate, as shown in Fig. 7.1 (left) where we compare the precise linear growth factor obtained numerically with the above solution. The second approximation is poorer, but more accurate ones can be found e.g. in Refs. [126, 146].

Assuming that the galaxy selection function is very peaked around a median redshift z_m, the multipole C_l^{GT} probes mainly fluctuations around the scale $k \sim l/r(z_m)$. If l is larger than $k_{\rm fs}\, r(z_m)$, C_l^{GT} is affected by neutrino masses through the term between brackets in Eq. (7.4). Using Eqs. (7.8), this term varies with f_ν like:

$$\partial_z \frac{P^{f_\nu}(k,z)}{a(z)^2} \simeq \left[(1+C(z)f_\nu)\,(1-8f_\nu)\right] \partial_z \frac{P^0(k,z)}{a(z)^2}\ , \tag{7.9}$$

$$\text{with} \qquad C(z) = \frac{3}{5}\left(\frac{1}{1+z}\frac{D}{D'} - 1\right)\ .$$

For a typical Dark Energy model, the density fraction $\Omega_{\rm DE}$ becomes negligible for $z > 2$ [1], and hence the ratio D'/D is tiny. So, at hight redshift, the net effect of the neutrino mass is to increase the integrand in C_l^{TG} like:

$$\partial_z \frac{P^{f_\nu}(k,z)}{a(z)^2} \simeq \left[\frac{3}{5}\frac{f_\nu(1-8f_\nu)}{1+z}\frac{D}{D'}\right]\ \partial_z \frac{P^0(k,z)}{a(z)^2}\ . \tag{7.10}$$

This just reflects the fact that at high redshift, the ISW effect would be null on all scales for $f_\nu = 0$, while for $f_\nu > 0$ it is still active on small scales. However, for $z < 2$, D'/D becomes larger, and for typical values of $\Omega_{\rm DE} \sim 0.7$ there is always a redshift below which $C(z)$ is smaller than eight. Then, the term between brackets in Eq. (7.9) is smaller than one, and the net effect of neutrino masses is to decrease $\partial_z[P/a^2]$. In Fig. 7.1 (right), we plot the function $C(z)$ in the case of a cosmological constant with $\Omega_\Lambda = 0.69$. We see that $C \sim 8$ for $z \sim 2$; so, around this redshift and for $l > k_{\rm fs}\, r(z_m)$, the net effect of neutrino masses on C_l^{GT} changes of sign.

In summary, if z_m is small, the expected effect of neutrino masses on the cross-correlation multipoles C_l^{GT} consists in a step-like suppression at large l's, qualitatively similar to that observed in the galaxy auto-correlation multipoles C_l^{GG}. However the suppression factor is smaller, since the lack of power in the matter power spectrum caused by neutrino free-streaming is balanced by the excess of ISW effect due to the behaviour of the linear growth factor in presence of massive neutrinos. When z_m increases, the boost related to the ISW effect is seen more clearly, and ultimately, when z_m is chosen before dark energy domination, the net effect of neutrino masses is to increase C_l^{GT} at large l.

In order to check and quantify these effects, we computed the cross-correlation multipoles C_l^{TG} (and also for comparison the auto-correlation multipoles C_l^{GG}) for two different cosmological models, sharing the same parameters $\Omega_b = 0.053$,

[1] in the case of "early Dark Energy" models, this statement can only be marginally true (see e.g. in [68, 69])

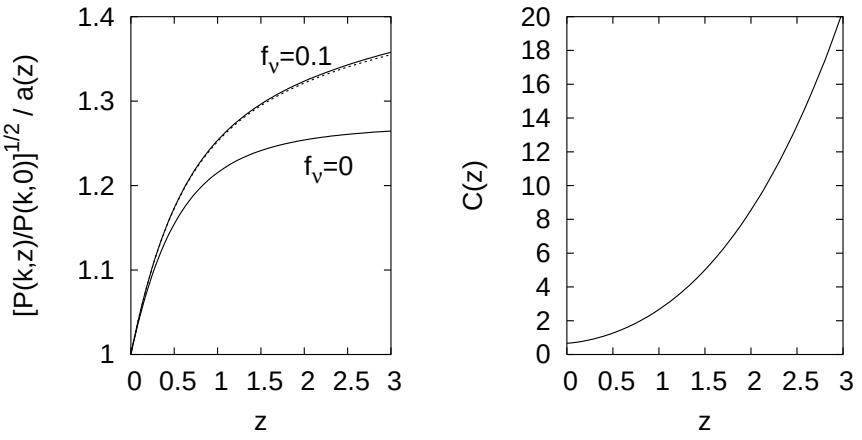

Figure 7.1: *(Left)* Redshift evolution of the small-scale linear growth factor, defined here as $[P(k,z)/P(k,0)]^{1/2}/a(z)$ for $k \sim 10\,h\mathrm{Mpc}^{-1}$, and obtained numerically with CAMB for $\Omega_\Lambda = 0.69$. The lower curve corresponds to $f_\nu = 0$ and is exactly equal to the quantity $D(z)$ defined in Eq.(7.6). The upper, solid curve corresponds to $f_\nu = 0.1$, and is well approximated by the dotted curve, which corresponds to the first of Eqs.(7.8). *(Right)* The function $C(z)$, defined in Eqs.(7.9), computed here for $\Omega_\Lambda = 0.69$. Roughly speaking, the effect of neutrino masses on C_l^{TG} changes of sign when this function crosses eighth.

$\Omega_m = 0.31$, $\Omega_\Lambda = 0.69$, $h = 0.65$, $A \equiv \ln[10^{10}k^3\mathcal{R}^2]_{k=0.01/\mathrm{Mpc}} = 3.16$, $n_s = 0.95$, but with two different values of the neutrino density fraction $f_\nu = \Omega_\nu/\Omega_m$, equal to 0 or 0.1 (corresponding to three neutrino species sharing the same mass $m_\nu = 0$ or $m_\nu \simeq 0.41$ eV). We adopted a galaxy selection function of the form

$$\phi_G(z) = \frac{3}{2}\frac{z^2}{z_0^3}\exp\left[-\left(\frac{z}{z_0}\right)^{\frac{3}{2}}\right] , \tag{7.11}$$

peaking near the median redshift $z_m \equiv 1.4z_0$. For illustrative purposes, we choose the four values $z_m = 0.1, 1, 2, 3$, although in practice it would be very challenging to map $\delta_G(\hat{n})$ for $z \geq 2$: presently, available data with a reasonable signal-to-noise ratio range only from $z \sim 0.1$ to $z \sim 1.5$.

In Fig. 7.2 we plot the ratio of the multipoles C_l^{TG} in the two models, compared with the same ratio for C_l^{GG}. The free-streaming of massive neutrinos is responsible for the step-like suppression of C_l^{GG}, like in the power spectrum $P(k)$. The value of z_m controls the angle under which the free-streaming scale is seen in the map $\delta_G(\hat{n})$, and hence the scale at which the suppression occurs in multipole space. As expected from the previous discussion, the neutrino mass effect on C_l^{TG} is similar to that on C_l^{GG} for small $z_m < 1$, although the suppression factor is slightly smaller, due to the excess of ISW effect in presence of massive neutrinos. For $z_m \geq 1$, the amplification effect due to this excess has a clear and distinct signature at $l \geq 100$, and for $z_m \sim 2$ the ratio displayed in Fig. (7.2) has a dip around $l \sim 150$. Unfortunately, we will see in Sec. 7.2.3 that for $l \geq 100$ this

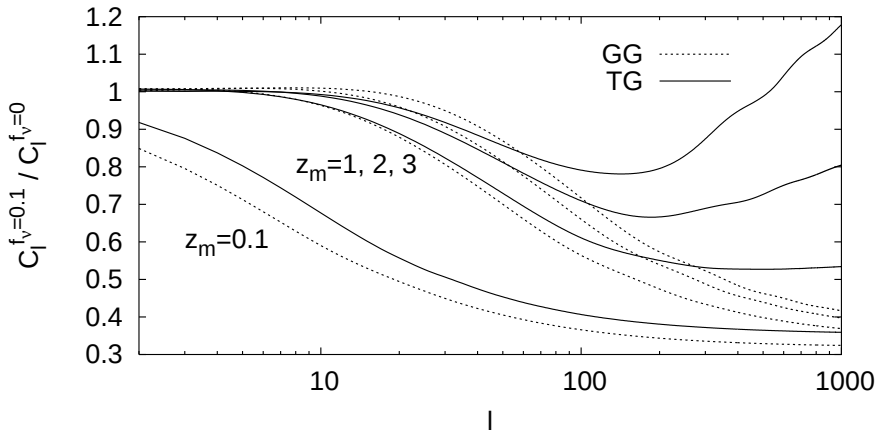

Figure 7.2: Ratio of the cross-correlation multipoles C_l^{TG} and auto-correlation multipoles C_l^{GG} obtained for two cosmological models with neutrino density fractions equal to $f_\nu = 0.1$ or 0, and the same value of other cosmological parameters (see the text for details).

effect is masked by primary CMB anisotropies, which play the role of white noise for the present purpose.

In Fig. 7.3, we plot directly the multipoles C_l^{TG} for the same two models. The effect of neutrino masses is clearly visible for all $l > 2$ at $z_m = 0.1$, while for $z_m \geq 1$ it is necessary to reach $l \geq 20$ in order to see a difference (since the maximum free-streaming scale is seen under a smaller angle at higher redshift). Remembering that the effect of neutrino masses on large l's can be split in two contributions, a matter power suppression and an excess of ISW, it is clear from the previous discussion that the latter effect contributes at all redshifts, but its most obvious manifestation is the fact that C_l^{TG} increases with f_ν for large l's. However, we will see in Sec. 7.2.3 that only the region with $l \leq 100$ can be probed by observations: then, the neutrino-induced ISW effect is significant, but smaller that the opposite suppression effect.

In Fig. 7.4, we plot the corresponding angular correlation functions $w^{TG}(\theta)$. In this representation, the fine-structure of the high-l multipole spectrum is by construction averaged out, and it is not possible to see an amplification at high z_m and small θ. The suppression caused by neutrino masses is visible for $z_m = 0.1$ at $\theta \leq 15^o$, and for $z_m \geq 1$ at $\theta \leq 2^o$.

In all these plots, we used only the linear perturbation theory. Doing so, the angular cross-correlation functions depend on the matter power spectrum inside the linear regime. To prove it, we compute again $w^{TG}(\theta)$ from the non-linear power spectrum obtained by applying HALOFIT corrections [236] to the linear one. The result, superimposed in Fig. 7.4, is indistinguishable from that of linear theory. This shows that non-linear effects on the evolution of matter perturbations has much less impact than that of adding a neutrino mass. This is also true for the multipoles C_l^{TG}, excepted for the smallest redshifts and highest l's (for $z_m = 0.1$, non-linear effects become important for $l > 100$).

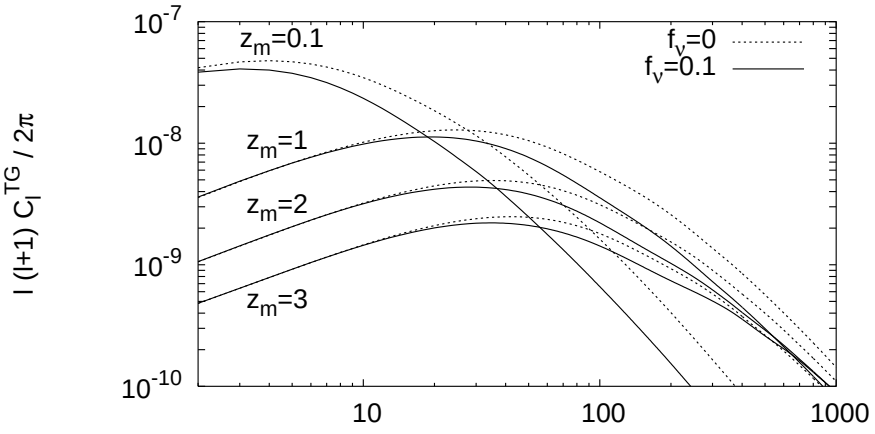

Figure 7.3: Dimensionless cross-correlation spectrum in multipole space, $l(l+1)C_l^{TG}/2\pi$, for the same cosmological models as in Fig. 7.2 (i.e., with three neutrino species sharing the same mass $m_\nu = 0$ or $m_\nu \simeq 0.41$ eV).

7.2.3 Detectability

For a set of full-sky CMB and LSS experiments measuring the temperature multipoles a_{lm}^T (resp. galaxy-density multipoles a_{lm}^G) with a noise spectrum N_l^T (resp. N_l^G), the cross-correlation spectrum C_l^{TG} can be reconstructed from the estimator

$$\tilde{C}_l^{TG} = \frac{\sum_{m=-l}^{l} a_{lm}^{T*} a_{lm}^G}{2l+1} \tag{7.12}$$

with a variance σ_l^{TG} given by

$$(\sigma_l^{TG})^2 = \frac{(C_l^{TG})^2 + (C_l^{TT} + N_l^{TT})(C_l^{GG} + N_l^{GG})}{2l+1} \ . \tag{7.13}$$

Note that the estimator is not Gaussian, especially for small l's: so, σ_l^{TG} is only an estimate of the true (asymmetric) error bar on the reconstructed power spectrum. If the cross-correlation map can be reconstructed only inside a fraction $f_{\rm sky}$ of the full sky, in first approximation σ_l^{TG} should be multiplied by $f_{\rm sky}^{-1/2}$. The variance is further reduced by $\sqrt{\Delta l}$ in case of data binning with bin width (Δl). Note that in this case the covariance matrix is no longer diagonal, but nevertheless using a diagonal matrix under these approximations has been shown to work well, compared to the exact treatment, if we choose an adequately large binning [36]. In practice, for the multipole range in which we are interested, the CMB noise spectrum N_l^{TT} is much smaller than C_l^{TT} for experiments like WMAP and beyond, and can be safely neglected in the above expression. For a LSS survey consisting in a catalogue of discrete objects (galaxies, clusters, etc.), the noise spectrum is usually dominated by the shot noise contribution $N_l^{GG} \simeq 1/\bar{N}$, where $\bar{N}$ represents the mean number of objects per steradian. The largest

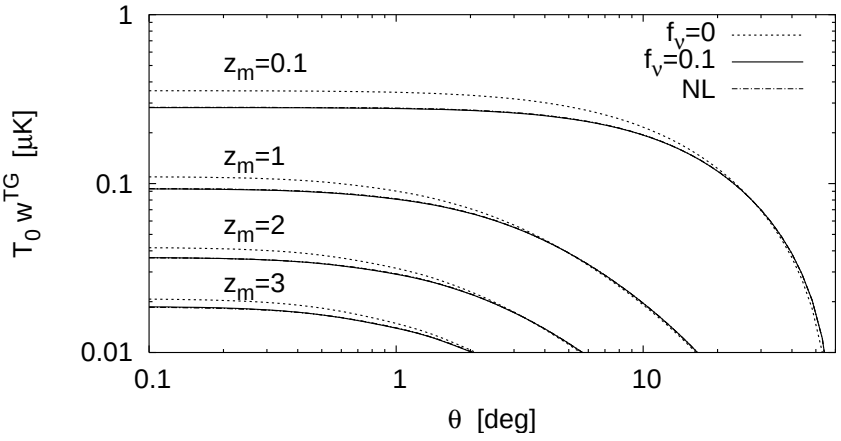

Figure 7.4: Angular cross-correlation function, multiplied by the average CMB temperature and displayed in units of micro-Kelvins, for the same cosmological models as in Figs. 7.2,7.3. We also plot the same functions including non-linear (NL) corrections to the matter power spectrum: they are indistinguishable from the linear ones.

ongoing/future surveys (e.g. SDSS) should reach typically the order of 10^8 or even 10^9.

In Fig. 7.5, we show the typical error bar that could be expected from a cross-correlation map with coverage $f_{\rm sky} = 0.65$ (corresponding to the usual galactic cut in CMB maps), using an ambitious LSS survey with surface density $\bar{N} = 10^9 {\rm st}^{-1}$ in each redshift bin. We assumed $b(z) \sim 1$ for simplicity. These assumptions correspond essentially to the best measurement that could ever be done, since for such a high surface density the variance of the estimator of a single multipole product $a_{lm}^{T*} a_{lm}^{G}$ is not affected by instrumental noise, and reduces to

$$\sigma_{lm}^{TG} = C_l^{TG} \sqrt{1 + \frac{C_l^{TT} C_l^{GG}}{(C_l^{TG})^2}} \ . \tag{7.14}$$

This expression can be interpreted as the product of the cosmic variance term C_l^{TG} times an enhancement factor depending on the correlation coefficient $(C_l^{TG})^2/(C_l^{TT} C_l^{GG})$. At large l's, the late ISW contribution to the total temperature anisotropy becomes vanishingly small, and the primary anisotropy plays the role of a large noise term, which cannot be removed. In this limit, the correlation coefficient is much smaller than one, and the variance σ_{lm}^{TG} gets correspondingly enhanced. Fig. 7.5 shows that the spectrum C_l^{TG} can be reconstructed to some extent only in the range $l \leq 100$; beyond, one could only derive upper bounds. Note that the error bar for each bin is roughly of the same order of magnitude as the effect of neutrino masses when f_ν varies from 0 to 0.1. In Fig. 7.5, we also show the error degradation when $f_{\rm sky}$ is reduced to 0.25 and $\bar{N}$ to $7 \times 10^8 {\rm st}^{-1}$ in each redshift bin. Finally, in Fig. 7.6, we plot the corresponding error bars for $w^{TG}(\theta)$. Note that the synthetic error bars for $w^{TG}(\theta)$ are correlated with each

other, unlike those for C_l^{TG}. On small angular scales $\theta \leq 1$ (where the effect of neutrino masses is maximal) the 1σ error on $w^{TG}(\theta)$ is of the order of 25%.

We conclude from these estimates that the temperature-galaxy correlation power spectrum C_l^{TG} is potentially sensitive to the neutrino mass in the observable range $10 < l < 100$, as well as the angular correlation function $w^{TG}(\theta)$ for $\theta < 5^o$ at $z = 0.5$ or $\theta < 3^o$ at $z = 1$. Unfortunately, the enhancement of the ISW effect due to the impact of massive neutrinos on the linear growth factor is not directly visible: it would require precise data at high l and high redshift, for which the late ISW effect is masked by primordial anisotropies. The net effect of massive neutrinos on the observable part of C_l^{TG} and on $w^{TG}(\theta)$ is a suppression, caused by the usual free-streaming effect. However this effect is non-trivial in the sense that C_l^{GG} and C_l^{TG} depend on f_ν through different relations, due to the fact that the ISW term involves a time-derivative of the gravitational potential while the galaxy over-density does not. Hence, the galaxy-temperature correlation spectrum can bring some information on neutrino masses which is not already contained in the sole galaxy auto-correlation spectrum. In the next section, we will quantify this statement by performing a parameter extraction from mock data accounting for future experiments.

7.3 An MCMC analysis of mock data

For a given data set consisting in various maps (i.e. multipoles a_{lm}^X) covering a fraction $f_{\rm sky}$ of the full sky and assumed to obey Gaussian statistics, the likelihood function $\mathcal{L}$ is often approximated as

$$\mathcal{L} \propto \Pi_l \left\{ (\det C_l^{\rm th})^{-1/2} \exp\left[-\frac{1}{2} {\rm Trace}\, C_l^{\rm obs} C_l^{\rm th\,-1} \right] \right\}^{(2l+1) f_{\rm sky}} . \qquad (7.15)$$

where $C_l^{\rm obs}$ is the data covariance matrix defined by $[C_l^{\rm obs}]_{XY} = \langle a_{lm}^X a_{lm}^Y \rangle$, and $C_l^{\rm th}$ the assumed theoretical covariance matrix for a given fit, which contains the sum of each theoretical power spectrum $C_l^{XY\,\rm th}$ and of the instrumental noise power spectra N_l^{XY}, estimated by modelling the experiment. Of course, the data covariance matrix reconstructed from the observed maps is also composed of signal and noise contributions. Simulating a future experimental data set amounts in computing the noise spectra N_l^{XY}, given some instrumental specifications, and generating randomly some observed spectra $C_l^{XY\,\rm obs}$, given the theoretical spectra $C_l^{XY\,\rm fid}$ of the assumed fiducial model and the noise spectra N_l^{XY}. However, for the purpose of error forecast, it is sufficient to replace simply $C_l^{XY\,\rm obs}$ by the sum $C_l^{XY\,\rm fid} + N_l^{XY}$: this just amounts in averaging over many possible mock data sets for the same model, and does not change the reconstructed error on model parameters [205].

For instance, if one wants to estimate future errors for a CMB experiment, the maps to consider are temperature and E-polarization: $X \in \{T, E\}$ (here, for simplicity, we consider models with no gravitational waves and discard B-

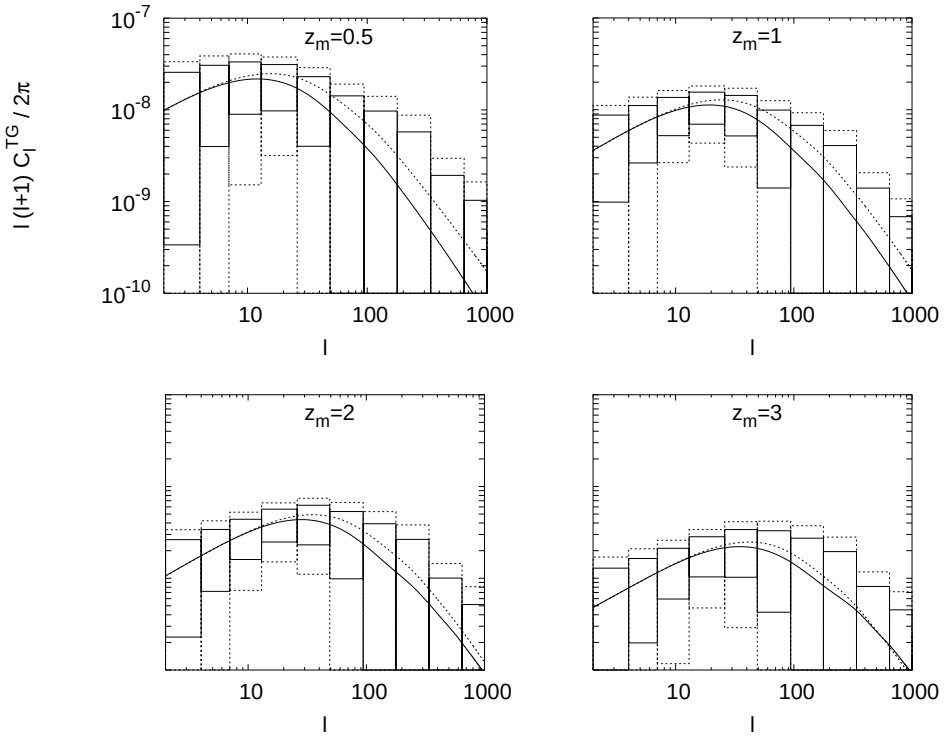

Figure 7.5: 68% error forecast on the power spectrum C_l^{TG}, which is displayed for the same two cosmological models as in Figures 7.2, 7.3 (with $f_\nu = 0$ or 0.1). The smallest error boxes assumes a LSS survey with sky coverage $f_{\rm sky} = 0.65$ and surface density $\bar{N} = 10^9 {\rm st}^{-1}$ in each redshift bin. The binning in multipole space can be read from the width of each box. The largest error boxes correspond to $f_{\rm sky} 0.25$ and $\bar{N} = 7 \times 10^8 {\rm st}^{-1}$.

polarization). The covariance matrices then read

$$C_l^{\rm obs} = \begin{pmatrix} C_l^{TT\,{\rm fid}} + N_l^{TT} & C_l^{TE\,{\rm fid}} \\ C_l^{TE\,{\rm fid}} & C_l^{EE\,{\rm fid}} + N_l^{EE} \end{pmatrix} , \qquad (7.16)$$

$$C_l^{\rm th} = \begin{pmatrix} C_l^{TT\,{\rm th}} + N_l^{TT} & C_l^{TE\,{\rm th}} \\ C_l^{TE\,{\rm th}} & C_l^{EE\,{\rm th}} + N_l^{EE} \end{pmatrix} . \qquad (7.17)$$

Should one consider the combination of CMB data with a future galaxy redshift survey decomposed in N maps associated to N redshift bins, the matrices would become $2 + N$ dimensional, with an extra block

$$[C_l]_{2+i,2+j} = C_l^{G_i G_j} + \delta_{ij} N_l^{G_i G_i} \ , \quad i = 1, ..., N, \qquad (7.18)$$

as well as non-diagonal coefficients $[C_l]_{1,2+i} = C_l^{TG_i}$ accounting for the late ISW effect. Note that all non-diagonal coefficients have no noise term, since the noise contributions in two different maps are expected to be statistically uncorrelated at least at first order.

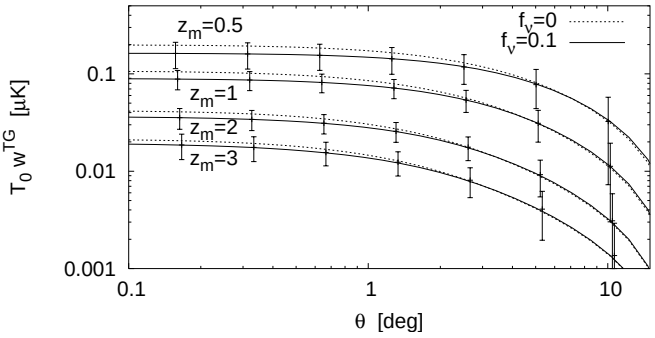

Figure 7.6: 68% error forecast on the angular correlation function w^{TG}, which is displayed for the same two cosmological models as in Figures 7.2, 7.3 (with $f_\nu = 0$ or 0.1). The error bars assume a LSS survey with sky coverage $f_{\rm sky} = 0.65$ and surface density $\bar{N} = 10^9 {\rm st}^{-1}$ in each redshift bin. The spacing between each error bar reflects the binning width chosen in angular space.

Finally, the option which is most interesting in our context, is to assume that the galaxy density auto-correlation maps are not known (or just not considered, because they could be plagued by some systematic effects), and that CMB data are only combined with the cross-correlation data, i.e. with N observed power spectra spectra $C_l^{TG_i{\rm obs}}$. This is exactly what is being done in the current literature, in which authors try to get some new independent bounds on Ω_Λ from CMB plus CMB-LSS cross-correlation data, without employing LSS auto-correlation maps. In the approximation of Gaussian-distributed $C_l^{TG_i}$ with central value $C_l^{TG_i{\rm th}}$ and covariance given by

$$[{\rm Cov}_l]_{ij} \equiv \left\langle \left(C_l^{TG_i} - \langle C_l^{TG_i} \rangle \right) \left(C_l^{TG_j} - \langle C_l^{TG_j} \rangle \right) \right\rangle$$
$$= \frac{C_l^{TG_i{\rm th}} C_l^{TG_j{\rm th}} + (C_l^{TT{\rm th}} + N_l^{TT})(C_l^{G_iG_j{\rm th}} + \delta_{ij} N_l^{G_iG_i})}{(2l+1) f_{\rm sky}} \,, \qquad (7.19)$$

the likelihood of the cross-correlation data reads

$$\mathcal{L} \propto \Pi_l \left(\det {\rm Cov}_l \right)^{-1/2} \exp \left[-\frac{1}{2} \sum_{ij} \Delta_l^i \left[{\rm Cov}_l \right]_{ij}^{-1} \Delta_l^j \right] \qquad (7.20)$$

with $\Delta_l^i \equiv C_l^{TG_i{\rm obs}} - C_l^{TG_i{\rm th}}$. The total likelihood is then the product of the CMB and cross-correlation likelihoods.

In this section, we will focus on three ambitious future experiments: the Planck satellite, to be launched in 2008, which is expected to make the ultimate measurement of CMB temperature anisotropies, dominated by cosmic variance rather than noise up to very high l; the Dark Energy Survey (DES); and the Large Synoptic Survey Telescope (LSST), designed primarily for a tomographic study of cosmic shear, which would provide as a byproduct a very deep and wide galaxy

redshift survey (close to ideal for the purpose of measuring the CMB-LSS cross-correlation since $N_l^{G_iG_i} < C_l^{G_iG_i}$ at least for multipoles $l < 100$). For Planck, we computed the noise-noise spectra, N_l^{TT} and N_l^{EE}, like in Ref. [148], with nine frequency channels. For the DES-like survey, we followed Ref. [208] and assumed a total number of galaxies of 250 million in a 5000 square degree area on the sky (or $f_{\rm sky} = 0.13$), with an approximate 1-σ error of 0.1 in photometric redshifts, divided in four redhsift bins with mean redshifts $z_i \in \{0.3, 0.6, 1, 1.3\}$, with the same selection functions as in Ref. [208]. For LSST, we used the same modelling as in [167], with a net galaxy angular number density of 80 per square arc-minute and a coverage of $f_{\rm sky} = 0.65$. The galaxies are divided into six redshift bins with mean redshifts $z_i \in \{0.49, 1.14, 1.93, 2.74, 3.54, 4.35\}$. For each bin the selection function, estimated bias b_i and galaxy density n_i are provided in [167] (Fig. 2, Eq. (16) and Table I). The noise spectra $N_l^{G_iG_i}$ are then simply given by $1/n_i$.

We used the public code COSMOMC [152] to do a Monte-Carlo Markov Chain (MCMC) analysis, fitting the theoretical galaxy-temperature correlation to the mock data. For this purpose, we have written a module which computes the correlation multipoles following Eq. (7.4) and the likelihood of the mock data given each model as described above.

We then ran our modified version of CosmoMC for a model with eight parameters: the usual six of minimal ΛCDM (baryon density $\Omega_b h^2$, dark matter density $\Omega_{dm} h^2$, angular diameter of the sound horizon at last scattering θ, optical depth to reionisation τ, primordial spectral index n_s, primordial amplitude $\log[10^{10} A_s]$) plus the total neutrino mass m_ν and the equation-of-state parameter w. Our fiducial model was close to the WMAP best-fitting model with $m_\nu = 0$ and $w = -1$. We considered three possible combinations of data: Planck alone, Planck plus its cross-correlation with DES or LSST (but no information on galaxy auto-correlations), and finally Planck plus LSST, using all information and including the correlation. The probability of each parameter is displayed in Fig. 7.7 for each of these four cases called respectively CMB (Planck), CMB+GT (Planck+DES or Planck+LSST) and CMB+GT+GG (Planck+LSST).

Obviously the combination CMB+GT+GG does a much better job than CMB+GT for constraining all parameters (and most spectacularly w and m_ν). This is mainly due to the fact that the GT cross-correlation is partly screened by primary temperature anisotropies, while the GG signal does not have such an intrinsic noise contribution. We even try to repeat the CMB+GT+GG analysis with all $C_l^{GT_i}$ correlations set to zero, and found no noticeable difference, showing that most sensitivity comes from GG rather than GT terms. However, the comparison between CMB alone and CMB+GT is still interesting *per se*. In fact, we are dealing here with an idealised situation, but in the future the GG auto-correlation signal could appear to be plagued by various systematic effects. In this case, independent information coming from the cross-correlation signal alone might be a useful piece of evidence in favour of the preferred model. Also, if the galaxy bias turns out to be very difficult to estimate with high enough accuracy, one may adopt the point of view of using the GG signal to measure bias, and the CMB+GT signal to estimate the best-fit parameters in some iterative scheme.

In this prospective, it is interesting to note that the CMB+GT combination from Planck and LSST increases significantly the sensitivity of Planck alone mainly for $\Omega_{dm}h^2$ (by 30%), w (by 83%) and m_ν (by 38%). As a consequence, the sensitivity to the related parameter Ω_Λ increases by 76%. For our fiducial model with $m_\nu = 0$, the 95% confidence level upper bound on the total neutrino mass shrinks from 0.77 eV to 0.54 eV (for another fiducial model with $m_\nu > 0$ the sensitivity can only be larger than that, see e.g. [147]). At this level of sensitivity, the parameter m_ν is not correlated with Ω_Λ or w, as can be checked by looking at two-dimensional marginalised likelihood contours in Figure 7.8. We conclude that the cross-correlation signal derived from Planck and LSST would have some useful sensitivity to both neutrino masses and dark energy parameters. Instead, the correlation between Planck and DES does not bring significant new information with respect to Planck alone.

Ichikawa and Takahashi [117] performed a similar forecast for Planck and LSST (with slightly different specifications), using a Fisher matrix analysis rather than MCMC approach. They find a smaller sensitivity of the cross-correlation data to neutrino mass than we do, possibly because of the various approximations entering into the Fisher matrix approach.

7.4 Conclusions

We have studied here the possibility to use the cross-correlation between CMB and galaxy density maps as a tool for constraining the neutrino mass. On one hand massive neutrinos reduce the cross-correlation spectrum because their free-streaming slows down structure formation; on the other hand, they enhance it because of the behaviour of the linear growth in presence of massive neutrinos. Using both analytic approximations and numerical computations, we showed that in the observable range of scales and redshifts, the first effect dominates, but the second one is not negligible. Hence the cross-correlation between CMB and LSS maps could bring some independent information on neutrino masses. We performed an error forecast analysis by fitting some mock data inspired from the Planck satellite, Dark Energy Survey (DES) and Large Synoptic Survey Telescope (LSST). For Planck and LSST, the inclusion of the cross-correlation data increases the sensitivity to m_ν by 38%, w by 83% and $\Omega_{dm}h^2$ by 30% with respect to the CMB data alone. With the fiducial model employed in this analysis (based on eight free parameters) the standard deviation for the neutrino mass is equal to 0.38 eV for Planck alone and 0.27 eV for Planck plus cross-correlation data. This is far from being as spectacular as the sensitivity expected from the measurement of the auto-correlation power spectrum of future galaxy/cluster redshift surveys or cosmic shear experiments, for which the predicted standard deviation is closer to the level of 0.02 eV, leading to a 2σ detection even in the case of the minimal mass scenario allowed by current data on neutrino oscillations (see [146] for a review). However, the method proposed here is independent and affected by different systematics. So, it remains potentially interesting, but only if the neutrino mass is not much smaller than $m_\nu \sim 0.2$ eV.

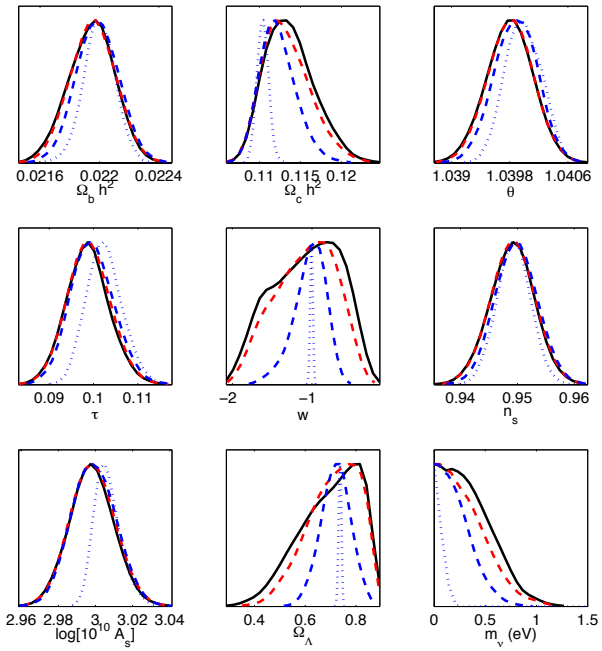

Figure 7.7: Marginalised probability of cosmological parameters obtained by fitting some mock data mimicking the properties of Planck, DES and LSST. The solid black curves accounts for CMB only, the red dashed for CMB+GT with Planck+DES, the blue dashed for CMB+GT with Planck+LSST, and the dotted blue for CMB+GT+GG with Planck+LSST (these combinations are precisely defined in the text). In each of these cases the cosmological model consists in ΛCDM (six parameter) plus an arbitrary total neutrino mass m_ν and equation-of-state parameter w. So, only eight of the above nine parameters are independent (as a consequence the prior for Ω_Λ is non-flat). The mock data is based on a fiducial model with $m_\nu = 0$ and $w = -1$.

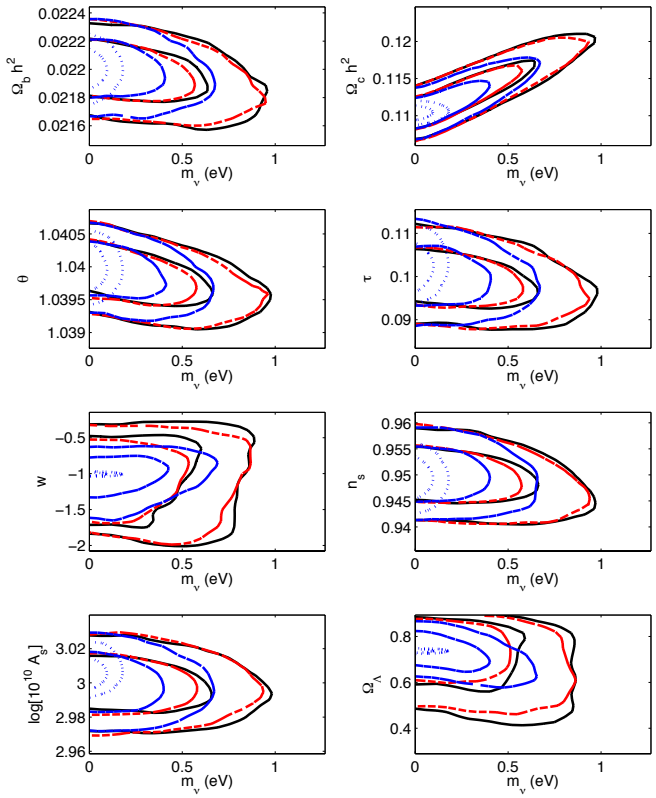

Figure 7.8: Two-dimensional marginalized likelihood contours involving m_ν obtained by fitting some mock data mimicking the properties of Planck, DES and LSST. The solid black curves accounts for CMB only, the red dashed for CMB+GT with Planck+DES, the blue dashed for CMB+GT with Planck+LSST, and the dotted blue for CMB+GT+GG with Planck+LSST (these combinations are precisely defined in the text). For each case, the two lines represent the 68% and 95% confidence levels.

Chapter 8

The Rees-Sciama effect: apparent acceleration from structure formation in trouble.

We saw that secondary anisotropies can be used to constrain cosmological parameters, such as Dark Energy and the neutrino mass. In this Chapter, we will use the observed CMB power spectrum in order to put limits on a particular class of cosmological models, simply by means of an absence of large secondary anisotropies in the observed CMB.

Swiss-Cheese models try to explain the dimness of observed distant supernovae as a consequence of large gravitational inhomogeneity of the universe, in stead of invoking a cosmological constant of Dark Energy. The gravitational inhomogeneities can have a certain lensing effect, that causes the distant supernovae to appear as if they were in a universe with an accelerated expansion, while the actual expansion is not accelerating.

These strong gravitational inhomogeneities have a non-linear evolution, and are not constant in time. As explained in the previous chapter, such time evolution of the gravitational potential leaves an imprint on the CMB. We show that for a large range of parameters describing these models, the Swiss-Cheese universe exhibits such large secondary anisotropies that they can safely be ruled out.

8.1 Introduction

Ever since it was observed that distant supernovae (SN), of type Ia, appear dimmer than expected in a matter dominated spacetime [9, 219], when combined with measurements of the local Hubble factor [82], cosmologists are led to the conclusion that the recent expansion of the universe definitely accelerates. Observations of the Cosmic Microwave Background (CMB) prefer a large angular diameter distance to $z = z_{\rm dec} \sim 1100$, which in ΛCDM indicates a close to spatially flat universe [134, 141, 182, 216, 237]. Given constraints on the matter content of the universe, from CMB and Large Scale Structure, this is achieved when a Cosmological Constant is present, given the assumption that the locally observed Hubble factor is equal to the global Hubble factor. The amount of clustering of galaxies is slowed down by accelerated expansion with respect to a pure cold dark matter universe [74]. The latest addition to this impressive evidence are the observed Baryon Acoustic Oscillations (BAO), which provide an observation of one length scale at different redshifts, and thereby measure the expansion over different times [76, 203].

Presented as such, the evidence for acceleration is convincing, see Ref. [231] though for critique. However, a number of assumptions needs to be made in order to come to the conclusion that a Cosmological Constant or a form of Dark Energy (DE) is there. If the locally observed Hubble factor cannot be extrapolated to the global expansion rate, as is the case if, *e.g.*, the observer lives in a large void, the observed angular diameter distance of SN may be explained without DE [5–7, 20, 38, 43, 45, 46, 85–87, 89, 115, 118, 176, 186–188, 256–259, 268]. Spatial flatness would in that case be achieved with a matter density equal to the critical density, $\Omega_{\rm M} = 1$, fitting the CMB [115]. A globally small Hubble constant is needed in that case to explain the age of the universe [138]. The clustering of galaxies can also be caused by a hot dark matter component, such as neutrino's

with a mass of $m_\nu \sim 0.5$ eV [115]. The BAO data are obtained as interpreted data, in the sense that one has to apply a fiducial cosmology to the data in order to abstract the BAO. To our knowledge this has only been done assuming an FLRW-universe, and it is unclear how the BAO would be affected by applying different fiducial models.

There is an ongoing debate as to whether today's universe is properly described by a perturbed FLRW-metric, assuming large scale homogeneity and isotropy, or not. See Refs. [21, 131] for explications why the usual argument, that the universe today is everywhere described by a small Newtonian potential, may not be sufficient to rule out the role of inhomogeneities. If the universe is properly described by the FLRW-metric, then the evidence for DE is compelling. If it is not, then we need to understand why we observe an apparent acceleration, which is phenomenologically well described by ΛCDM. Many works have been devoted to possibilities linking the apparent acceleration to structure formation and to a departure from homogeneity of the Universe, none of them however convincing the community that structure formation explains the observations without the need for DE. See Refs. [33, 77, 132, 139, 215] for reviews.

Here we will focus on one such proposition: the Swiss-Cheese Cosmology [21, 24, 29–31, 48, 90, 97, 98, 125, 136, 177, 178, 252, 269, 274]. The Swiss-Cheese Cosmology is described globally by an FLRW-metric, but locally contains holes (voids surrounded by a mass shell) described by a Lemaître-Tolman-Bondi metric (LTB). The holes match flawlessly to the FLRW-metric at the borders, and are mass compensated in such a way that, from outside such a hole, the global effect of a patch containing such a hole is as if it were FLRW (cheese), due to Birkhoff's theorem [75]. The Swiss-Cheese[1] toy model is an exact solution to the Einstein equations, hence does not suffer from averaging problems. Its goal is to approximate today's inhomogeneous universe in an exactly solvable manner, with most of the matter in structures, separated by voids. Recently it was shown that if curvature is a function of space, large local curvature at low redshift, as in this model, is hardly constrained by observations [47].

The general idea of the Swiss-Cheese Cosmology is that photons travel through holes and structures, where holes have a lensing effect such that distant supernovae, observed through a number of holes, appear dimmer than in a homogeneous EdS Universe. This effect has been explored in the literature and it was found:

- that if holes are perfectly aligned, a lensing effect can mimic a DE of about $\Omega_{\rm DE} = 0.4$,
- however, that averaged over many random distributions of holes, the effect vanishes, given that the holes are spherical.

In this work, we will show that, besides the on average disappearing of the lensing effect, the Swiss-Cheese Cosmology leaves a significant imprint on the CMB. It has been claimed that the effect that the holes have on the redshift

[1] The author must express his doubts about the name 'Swiss Cheese'. The name implies that only *swiss* cheese contains holes, and at the same time that *all* swiss cheese contains holes.

of photons is marginal in comparison with the redshift at which the distant supernovae are observed. This reasoning does hold, but the effect is significant when compared to the observed anisotropies in the CMB-temperature, which are of the order $\mathcal{O}(10^{-5})$. For the first time we will show full sky CMB-maps in a Swiss-Cheese Cosmology, for different realisations, each realization with a different constant size of holes, $r_{\rm hl}$. When showing these maps, we neglect the primordial power spectrum of the CMB-anisotropies, as the secondary anisotropies in most of the cases are overwhelmingly larger. These anisotropies are due to the Rees-Sciama [94, 181, 217] effect, a non-linear late integrated Sachs-Wolfe effect due to structure formation.

At the same time, we will show full sky maps of the angular diameter distance, $d_{\rm A}$, at a fixed redshift in each direction. We confirm the results of Ref. [269], that averaged over all directions, the angular diameter distance will appear as if the universe were exactly EdS, at least when the holes are spherical. This leads to the conclusion that a Swiss-Cheese model that has predominantly holes with a radius larger than 35 Mpc is ruled out, since it either cannot explain the supernovae in *every* direction, or it will leave a significant Rees-Sciama imprint on the CMB that is already ruled out by observations.

Our conclusion only applies to cosmologies in which the universe contains a very large number of large voids. In principle a smaller number of large voids is not ruled out by our analysis. In such a case, however, the voids would play no role at all in explaining the distant supernovae, which is not part of the scope of this paper.

We find that, in the density profile we consider, the maximal effect that the structure can have of the luminosity-distance-redshift relation is only marginally dependent on the size of the holes. This is a different conclusion than the one drawn in Refs. [21, 29]. We will briefly address this difference.

The different dependence on the size of holes, for different choices of density profile, leaves the door open to an 'Apollonian Gasket-like configuration'[2], in which the universe on average is FLRW, but locally is FLRW nowhere. In that case, an observer would see through holes in all directions. The CMB, if the configuration is such that all holes are sufficiently small, would be left in agreement with established perturbation theory. The holes can not be spherical, though, as the cancellation on average of the lensing effect [269] still applies to tiny holes as well. Probing such a configuration goes beyond the scope of this work, as the model would need significant changes: the holes must be typically smaller than $r_{\rm hl} \sim 35$ Mpc, they must not be spherical, and they must be such that in all directions the chance of looking through holes is higher than looking through cheese. Altogether this poses serious difficulties for the Swiss-Cheese model. Besides, one might question if such a configuration approaches nature in any way, and if the effect remains significant with more natural density profiles.

In section 8.2 we will briefly overview the metric and related equations de-

[2]The Apollonian Gasket is a fractal, constructed by starting out with three tangent circles, and subsequently filling areas between those circles with circles tangent to the previously drawn circles. See Ref. [174], and figure 1 in [178].

scribing the Swiss-Cheese cosmology and we will present the techniques used to calculate the full-sky maps of temperature and angular diameter distance. In section 8.3 we present the full-sky CMB in a Swiss-Cheese universe, for different typical hole sizes. In section 8.4 we will discuss the overall effect of the Swiss Cheese on distance measures. We conclude in section 8.5.

8.2 The Model

8.2.1 The metric and geodesics

The metric We define the Swiss-Cheese model identical to the model in Ref. [178]. In the Swiss-Cheese model, the metric is anywhere of the LTB form

$$ds^2 = -dt^2 + \frac{Y'^2(r,t)}{W^2(r)}dr^2 + Y^2(r,t)d\Omega^2, \tag{8.1}$$

where $Y'(r,t) \equiv \partial_r Y(r,t)$. We can choose the coordinate system such that the universe is divided in equally sized cubic boxes, with sides of length $2r_{\rm ch}$, each with the origin of its own coordinate system in the centre of that box. The time coordinate t is scaled such that $t_0 = 0$ corresponds to today, and $t = -1$ corresponds to the time of the Big Bang.

In the cheese, we recover the FLRW-metric by setting $Y_{\rm ch}(r,t) = ra_{\rm ch}(t)$ and $W^2_{\rm ch}(r) = 1 - kr^2$. In the holes, the metric is determined by

$$\dot{Y}_{\rm hl}(r,t) = \sqrt{\frac{M(r)}{3\pi Y_{\rm hl}(r,t)} + 2E(r)}, \tag{8.2}$$

with initial conditions at time $\bar{t} = -0.8$,

$$W^2_{\rm hl}(r) - 1 \equiv E(r) = \frac{1}{2}H^2_{\rm FLRW}(\bar{t})r^2 - \frac{1}{6\pi}\frac{M(r)}{r}, \tag{8.3}$$

$$M(r) \equiv 4\pi \int_0^r \rho(u) Y^2_{\rm hl}(u,\bar{t}) Y'_{\rm hl}(u,\bar{t}) du, \tag{8.4}$$

$$\rho(r) = \begin{cases} Ae^{-\frac{(r-r_{\rm M})^2}{2\sigma^2}} + \epsilon & \text{for } r < r_{\rm hl}, \\ \rho_{\rm ch} & \text{for } r > r_{\rm hl}, \end{cases} \tag{8.5}$$

$$Y(r,\bar{t}) = r. \tag{8.6}$$

In this setup, the free parameters are those describing the matter distribution in the holes: the size of the spherical LTB-metric $r_{\rm hl}$, the minimum density ϵ, the energy density scale A, the comoving radius at which the peak of the mass distribution resides $r_{\rm M}$, the comoving width of the mass shell σ, and the FLRW-energy density $\rho_{\rm ch}$. The mass distribution is constant in time, and a function of comoving radius r only. In physical coordinates, however, mass will be moving outwards to form a shell close to the border of the LTB-patch.

The LTB-evolution is 'switched on' manually at time $\bar{t} = -0.8$, such that at $-1 < t < -0.8$ spacetime is described by the homogeneous and isotropic FLRW-metric everywhere. In this way, the energy density and the scale factor are described by continuous functions of time everywhere. The spatial curvature $W(r)$, Eq. (8.3), however, appears instantaneously at time $t = \bar{t}$. This discontinuity plays no role in the quantities investigated here, henceforth it is taken for granted in this toy model.

For the derivation of and motivation for the choices made above, we refer the reader to Ref. [178].

Geodesic equations As a consequence of the spherical symmetry of each coordinate patch, any geodesic will lay in a spatial plane. Hence, without loss of generality, we can write the geodesic equations as four independent equations, as in Refs. [30, 178],

$$\frac{dz}{d\lambda} = -\frac{\dot{Y}'(r,t)}{Y'(r,t)}\left((z+1)^2 - \frac{c_\phi^2}{Y^2(r,t)}\right) - c_\phi^2\frac{\dot{Y}(r,t)}{Y^3(r,t)}, \quad z(0) = 0, \tag{8.7}$$

$$\frac{dt}{d\lambda} = z + 1, \qquad t(0) = 0, \tag{8.8}$$

$$\frac{dr}{d\lambda} = \frac{W(r)}{Y'(r,t)}\sqrt{(z+1)^2 - \frac{c_\phi^2}{Y^2(r,t)}}, \qquad r(0) = r_{\rm obs}, \tag{8.9}$$

$$\frac{d\phi}{d\lambda} = \frac{c_\phi}{Y^2(r,t)}, \qquad \phi(0) = \phi_{\rm obs}, \tag{8.10}$$

where $r_{\rm obs}$ and $\phi_{\rm obs}$ define the location of the observer.

The constant c_ϕ is defined by the physical angle between the photon geodesic and a radial geodesic pointing (which itself has $c_\phi = 0$) towards the photon geodesic. At any time in any point, the constant c_ϕ satisfies the relation,

$$\cos\alpha = g^i(y)x^i(y)g_{ij}(y), \tag{8.11}$$

$$c_\phi = (1+z)Y(r,t)\sin\alpha, \tag{8.12}$$

where $\vec{g}$ denotes the spatial direction of the geodesic at point y, and $\vec{x}$ denotes the spatial part of a radial geodesic pointing to coordinate y.

8.2.2 Dimensions and configurations

We chose the parameters as in Ref. [178], being $r_{\rm ch} = r_{\rm hl} = 0.042\kappa$, $\epsilon = 0.0025$, $\sigma = r_{\rm hl}/10$, $r_{\rm M} = 0.037\kappa$, $A = 50.59$ and $\rho_{\rm FLRW} = 25$, with however a freedom to chose the rescaling factor κ. For any κ, in physical dimensions these numbers correspond to holes with a radius of 350κ Mpc, in cubes with sides of length $l = 2r_{\rm ch} = 700\kappa$ Mpc, and $5/\kappa$ holes between the observer and $t = -0.8$ in an optimal direction, as illustrated in figure 8.1. The cheese is chosen to be

Quantity	Notation	Unit	Value
mass density	$\rho(r,t)$, $\bar{\rho}(r,t)$	ρ_{C0}	9.2×10^{-30} g cm^{-3}
time	t, T, $\bar{t}$, t_{BB}, T_0	$(6\pi\rho_{C0})^{-1/2}$	9.3 Gyr
comoving radial coordinate	r	$(6\pi\rho_{C0})^{-1/2}$	2857 Mpc
metric quantity	$Y(r,t)$	$(6\pi\rho_{C0})^{-1/2}$	2857 Mpc
expansion rate	$H(r,t)$	$(6\pi\rho_{C0})^{1/2}$	$\frac{3}{2}H_{0,\,Obs}$
spatial curvature term	$W(r)$	1	—

Table 8.1: The units used throughout this work, where $c = 16\pi G_{\rm N} = 1$. The present critical density is $\rho_{C0} = 3H^2_{0,\,Obs}/8\pi$, with $H_{0,\,Obs} = 70$ km s^{-1} Mpc^{-1}. Table taken from Ref. [178]

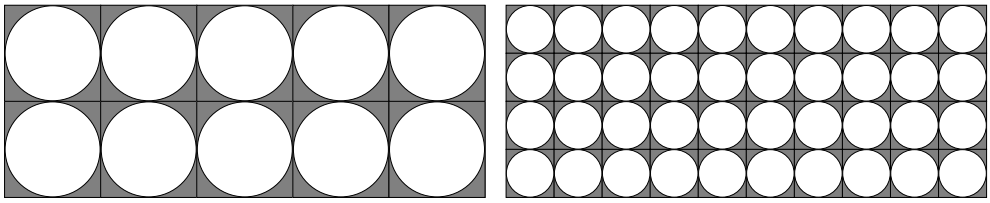

Figure 8.1: A two-dimensional illustration of the configuration of holes throughout the cheese. Gray corresponds to the FLRW-metric, white corresponds to the LTB-metric. The difference between the left and the right illustration is $\kappa_{\rm left} = 2\kappa_{\rm right}$. Throughout this work we will always have one size for all holes within each realisation of a Swiss-Cheese universe.

spatially flat, with $\Omega_{\rm M}$=1, *i.e.*, EdS. We use units in which $c = 16\pi G_{\rm N} = 1$. The translation from these dimensions to physical dimensions is given in Table 8.1. Given the freedom to rescale, the choice of normalisation is arbitrary. Throughout this work we will always have one size for all holes on a regular lattice within each realisation of a Swiss-Cheese universe. Secondly, we will always place the observer in the cheese, at a spot where two adjacent holes are closest to each other. There is no particular reason to choose this location, other than for simplicity, and this choice is not important for the conclusions.

8.2.3 Different methods for the angular diameter distance

The angular diameter distance, $d_{\rm A}$, is defined as the ratio of the size of an object at some distance of an observer, and the angular diameter at which it is observed. When, in the configuration of aligned bubbles, an observer is located in the cheese at a point where two adjacent bubbles are closest to each other, and the observer sees a source for which the geodesic connecting the observer and the centre of the source is a straight line exactly through the centres of a number of bubbles, the angular diameter distance to that source amounts to

$$\tilde{d}_{\rm A}(\lambda) = \frac{Y(r(\lambda), t(\lambda)) \sin\phi(\lambda)}{\alpha}, \tag{8.13}$$

with α the small angle between the radial geodesic and a geodesic from an edge of the source to the observer, the latter geodesic described by $r(\lambda)$, $t(\lambda)$ and $\phi(\lambda)$ [178]. For small α this quantity is independent of α. In an actual (numerical) calculation, one can integrate the geodesic equations for successively smaller alpha, until the quantity $\tilde{d}_{\rm A}$ converges to the same number along the geodesic.

Eq. (8.13) obviously only holds for the special case of the aforementioned purely radial geodesic connecting source and observer. The same method could be used in any direction, shooting two photons in almost but just not the same direction. This method would be computationally expensive though, since for each direction one has to reintegrate several times the geodesic equation, at very high accuracy such that the relative error in the tiny displacement orthogonal to the direction of the photon is small. The orthogonal displacement itself will already be extremely small compared to the distance travelled along the geodesic, given the small angle at which one shoots.

In stead, equations describing the exact beam size along the geodesic are, as in [30],

$$\frac{d\theta}{d\lambda} = -\frac{2}{3}\rho(r,t)\left(\frac{dt}{d\lambda}\right)^2 - \theta^2 - \sigma^2 \tag{8.14}$$

$$\frac{d\sigma}{d\lambda} + 2\theta\sigma = \frac{2}{3}\left(\frac{d\phi}{d\lambda}\right)^2 Y(r,t)^2\left(\rho(r,t) - \frac{3M(r)}{4\pi Y(r,t)^3}\right) \tag{8.15}$$

$$\frac{1}{\sqrt{A}}\frac{d^2\sqrt{A}}{d\lambda^2} = -\frac{2}{3}\rho(r,t)\left(\frac{dt}{d\lambda}\right)^2 - \sigma^2. \tag{8.16}$$

Here A denotes the beam size, θ is the beam expansion, defined through $\theta = \frac{1}{2A}\frac{dA}{d\lambda}$, and σ denotes the beam shear. The beam stretching becomes $\theta \pm \sigma$ in two orthogonal directions. We refer the reader to Refs. [30, 223] for further explanations. The angular diameter distance $d_{\rm A}$ and the luminosity distance $d_{\rm L}$ to an observer at any point along a geodesic pointing from / to the observer then become,

$$d_{\rm A}(\lambda) = \sqrt{\frac{A(\lambda)}{\Omega_{\rm source}}} \tag{8.17}$$

$$d_{\rm L}(\lambda) = (1+z)^2 d_{\rm A}(\lambda), \tag{8.18}$$

with $\Omega_{\rm source}$ the solid angle at which the source is observed. The initial conditions for a beam are,

$$\left.\frac{d\sqrt{A}}{d\lambda}\right|_{\lambda=0} = \sqrt{\Omega_{\rm source}}, \tag{8.19}$$

$$\left.\sqrt{A}\right|_{\lambda=0} = 0. \tag{8.20}$$

With these initial conditions, θ and σ are ill-defined at the initial conditions, as $\lim_{\lambda\to 0}\theta = \infty$. If we write $\xi = A\sigma$, we find the only relevant equations,

$$\frac{d\xi}{d\lambda} = \frac{2}{3}A\left(\frac{d\phi}{d\lambda}\right)^2 Y(r,t)^2\left(\rho(r,t) - \frac{3M(r)}{4\pi Y(r,t)^3}\right) \tag{8.21}$$

$$\frac{d^2\sqrt{A}}{d\lambda^2} = -\frac{2}{3}\sqrt{A}\;\rho(r,t)\left(\frac{dt}{d\lambda}\right)^2 - \frac{\xi^2}{A^{3/2}}, \tag{8.22}$$

with the extra initial condition $\xi|_{\lambda=0} = 0$, if we demand that σ is well behaved, *i.e.* finite, at all times. With these equations, the calculation of the angular diameter distance, and thereby the luminosity distance, amounts to simply including two more equations in the (numerical) integration scheme. Since $d_{\mathrm{L}} = (1+z)^2 d_{\mathrm{A}}$, hereafter we will mainly focus on d_{A} for simplicity.

We checked that both the intuitive, Eq. (8.13), and the exact, Eqs. (8.21, 8.22), method agree in the case where both can be applied.

8.2.4 Using 2D geodesic equations in a 3D setup

The spatial plane in which the photon's geodesic lays, is defined by the spatial part of a radial geodesic and the spatial part of the photon's geodesic. In the practice of this calculation, a photon exits one coordinate patch (A) and enters another patch (B) when one of its cartesian coordinated reaches r_{ch}. Let $\vec{g}$ denote the spatial direction of the geodesic in cartesian coordinates, let $\vec{x}_0^{\mathrm{A}}$ denote the cartesian coordinates at which the geodesic *entered* patch A, and let $\hat{v} \equiv \vec{v}/|\vec{v}|$ for any spatial vector $\vec{v}$. In cartesian coordinates, the direction $\vec{g}$ is invariant under translations, hence invariant under a transformation from one coordinate patch to another. This simplification only holds because the transformation is done at a point where spacetime is described by the spatially flat FLRW-metric. During a time step of integration of the geodesic equation, corresponding to photons leaving patch A, whilst moving in a plane spanned by the orthonormal vectors $\hat{e}_1^{\mathrm{A}}$

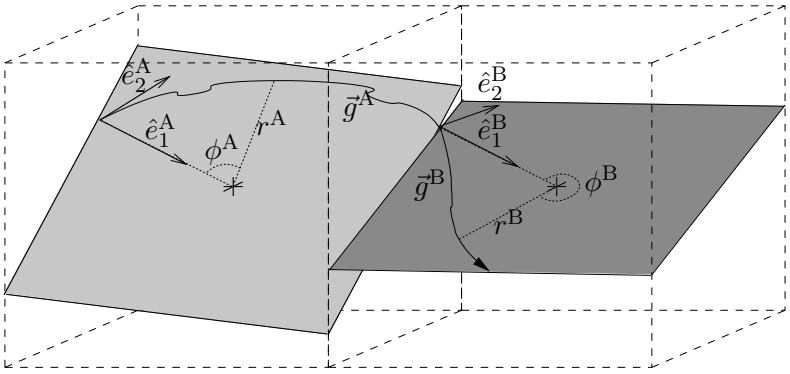

Figure 8.2: A cartoon of a geodesic in two adjacent patches. The geodesic is always in a plane in each patch, spanned by orthonormal vectors $\hat{e}_1$ and $\hat{e}_2$, both defined when entering a patch. At the exact border of the coordinate patches we have in three-dimensional cartesian coordinates $\vec{g}^{\mathrm{B}}(\lambda_{\mathrm{cross}}) = \vec{g}^{\mathrm{A}}(\lambda_{\mathrm{cross}})$.

and $\hat{e}_2^{\mathrm{A}}$, the transformation at the border at time λ_{cross} is done as follows:

$$\vec{g}^{\mathrm{B}}(\lambda_{\mathrm{cross}}) = \vec{g}^{\mathrm{A}}(\lambda_{\mathrm{cross}}), \tag{8.23}$$

$$\vec{x}_0^{\mathrm{B}} = \vec{x}_0^{\mathrm{A}} + \vec{e}_1^{\mathrm{A}} r_{\mathrm{A}} \cos\phi_{\mathrm{A}} + \vec{e}_2^{\mathrm{A}} r_{\mathrm{A}} \sin\phi_{\mathrm{A}} \pm \begin{pmatrix} 0 \\ 0 \\ 2r_{\mathrm{ch}} \end{pmatrix}, \tag{8.24}$$

$$\hat{e}_1^{\mathrm{B}} = \hat{x}_0^{\mathrm{B}}, \tag{8.25}$$

$$\hat{e}_2^{\mathrm{B}} = \frac{(\hat{e}_1^{\mathrm{B}} \cdot \hat{g}^{\mathrm{B}})\hat{e}_1^{\mathrm{B}} - \hat{g}^{\mathrm{B}}}{|(\hat{e}_1^{\mathrm{B}} \cdot \hat{g}^{\mathrm{B}})\hat{e}_1^{\mathrm{B}} - \hat{g}^{\mathrm{B}}|}, \tag{8.26}$$

$$r^{\mathrm{B}} = \left|\vec{x}_0^{\mathrm{B}}\right|, \tag{8.27}$$

$$\phi^{\mathrm{B}} = 0, \tag{8.28}$$

$$\cos\alpha^{\mathrm{B}} = g^i x_{\mathrm{B}}^i g_{ij}^{\mathrm{B}}, \tag{8.29}$$

$$c_\phi^{\mathrm{B}} = (1+z)Y(r,t)\sin\alpha^{\mathrm{B}}. \tag{8.30}$$

where all quantities are evualated at λ_{cross}. The integration then continues in box B with initial values r_{B} and ϕ_{B}, defined in the plane spanned by the orthonormal vectors $\hat{e}_1^{\mathrm{B}}$ and $\hat{e}_2^{\mathrm{B}}$. In this example we assumed that it is the third cartesian coordinate of vector $\vec{g}$ that hits the border of the patch. Figure 8.2 gives a visual explanation of the relation of different vectors.

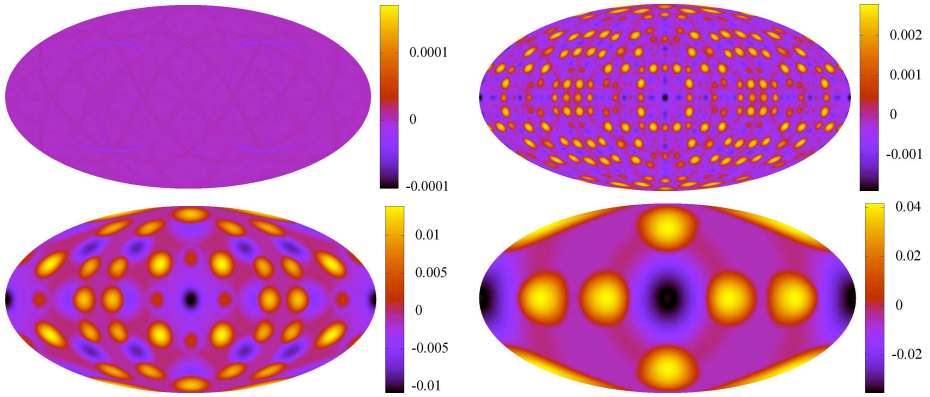

Figure 8.3: Full-sky maps of secondary CMB-anisotropies induced by the Swiss-Cheese structure, in Mollweide-projection. The quantity shown is $\frac{T-\bar{T}}{\bar{T}}$. These temperature maps would be observed in Swiss-Cheese universes with holes of size $r_{\mathrm{hl}} = 3.5$ Mpc (upper left figure), $r_{\mathrm{hl}} = 350$ Mpc (upper right figure), $r_{\mathrm{hl}} = 875$ Mpc (lower left figure) and $r_{\mathrm{hl}} = 1.75$ Gpc (lower right figure). The cold spots correspond to photons that experienced a large Rees-Sciama effect, hot spots correspond to photon's that traveled through a non-integer number of holes, and all ring-like structures are artefacts of the regular distribution of holes in this configuration.

8.3 The CMB

8.3.1 Temperature maps and their power spectra

As the universe is described by the matter-dominated FLRW-metric at $-1 < t < \bar{t} = -0.8$, photons obtain no anisotropies from the Swiss-Cheese structure in that period. It suffices to integrate photon geodesics backwards in time from today back to $t = \bar{t}$, and then to compare redshift a photon has experienced with the redshift experienced on average in all directions. This translates directly to a relative temperature difference, as $T \propto a^{-1} \propto 1 + z$. Hence, shooting photons in all directions and obtaining the redshift at time $\bar{t} = -0.8$ as a function of direction, one obtains a temperature anisotropy map of the CMB with only secondary anisotropies, caused solely by the Swiss-Cheese matter distribution.

We show full-sky CMB anisotropy maps for four different hole sizes in figure 8.3. The quantity shown is $\frac{T-\bar{T}}{\bar{T}}$, where $\bar{T}$ is an average over all directions. In each direction, the photon departed at the same time $t = \bar{t}$, towards us. The hole sizes for these maps are $r_{\mathrm{hl}} = 3.5$ Mpc (top left), $r_{\mathrm{hl}} = 350$ Mpc (top right), $r_{\mathrm{hl}} = 875$ Mpc (bottom left) and $r_{\mathrm{hl}} = 1.75$ Gpc (bottom right). The angular power spectra, C_l's, of the CMB-temperature anisotropy autocorrelation in different configurations are displayed in figure 8.4. They have been calculated using the Healpix package [93]. The power spectra displayed are defined in general for

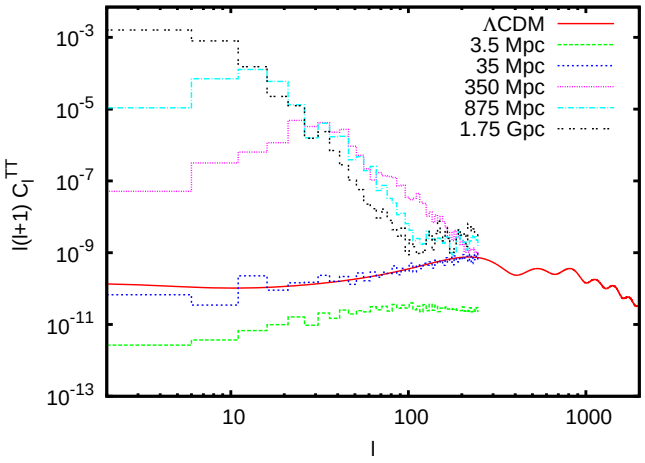

Figure 8.4: The $C_l^{\rm TT}$ of secondary anisotropies for different Swiss-Cheese cosmologies, in bins of 5 multipoles. For comparison we plot the full $C_l^{\rm TT}$-spectrum in a standard ΛCDM cosmology with $\Omega_{\rm baryon} = 0.045$, $\Omega_{\rm cdm} = 0.245$, $\Omega_{\rm k} = 0$, $\Omega_{\rm DE} = 0.71$, $h = 0.7$ (red solid line, unbinned). A Swiss-Cheese universe with holes of radius smaller than 35 Mpc, potentially leaves the CMB unaltered with respect to the standard cosmological model. Note the numerical limitations beyond the ankle at high $l \sim 100$, as discussed in the text.

any quantity X as,

$$a_{lm}^X \equiv \int_0^{2\pi} d\phi \int_0^{\pi} d\theta \; \frac{X(\theta,\phi) - \bar{X}}{\bar{X}} \; Y_{lm}(\theta,\phi) \tag{8.31}$$

$$C_l^{XX} \equiv \frac{1}{2l+1} \sum_{m=-1}^{m=l} \left| a_{lm}^X \right|^2 , \tag{8.32}$$

with Y_{lm} being the spherical harmonics.

8.3.2 Numerical limitations

Before discussing the power spectra, a note about numerical limitations needs to be made. We can only consider the power spectra up to the multipoles as displayed, because for even higher multipoles l, a much larger resolution in the maps would be needed. Even higher resolution would be computationally expensive, up to the point where numerical errors in the integration will dominate the anisotropy at such small scales.

All spectra show an ankle at about the same multipole $l \sim 100$. The spectrum beyond this ankle cannot be trusted, as the ankle is already an aliasing artefact of the resolution of choice. When the resolution is increased, the ankle goes down and moves to higher l, for all five configurations displayed. The resolution chosen, 3×10^6 pixels per map, is at the limit of the computational resources at hand,

with our code as is[3].

8.3.3 Discussion

By eye one already sees, in figure 8.3, that the maximum temperature anisotropy is much larger than the observed average CMB-temperature anisotropy, notably for larger holes. The centre of each map points in the special direction of exactly aligned holes. The cold spots are directions in which the photons travel through an optimal (read largest) number of holes. These are in fact cold, and not hot, spots because travelling through many holes, implies crossing many shells of in falling matter as well. What is observed here is actually the Rees-Sciama effect. The hot spots correspond to directions in which the photon at $t = \bar{t}$ was in a region that became a hole. *I.e.*, the photon has not travelled through an integer number of holes. When crossing an entire hole, a photon passes both regions in which the matter, falling outwards to form a shell around the hole, falls against the direction of photon and regions in which the matter falls in the same direction as the photon. Any Rees-Sciama effect mostly cancels in that case. When the photon is in the middle of a region that will become a hole when the matter starts falling, the photon automatically will only experience the metric of matter that falls in the direction of the photon path. In that hole, the cancellation will not happen, hence the photon relatively gains energy. One might wonder wether these hotspots are natural, and if it would not make more sense to constrain the number of holes that a photon crosses to be integer, for $-0.8 < t < 0$. Firstly, if the Swiss Cheese is a toy model for structure formation, then there is nothing unnatural about the period when the matter perturbations undergo the transition from linear to non-linear perturbations. In the linear regime, the potentials do not change. But still, if the photon happens to cross such a potential well at the time of transition, the photon will become part of a similar hot spot as in this toy model. Secondly, the temperature deviation of the hot spots from the average temperature is about the same as the deviation of the cold spots. It is likely that removing the hot spots would only change the angular correlation by a factor of two. This should be investigated though, keeping in mind that by eye one cannot do much statistics on a picture. In this work we choose to stick to one well-defined model.

In each map one also observes the same circular ring of average temperature, centred on the map. In the projection and orientation chosen, this ring corresponds to the plane surrounding the observer in which the photons always travelled through cheese only. This is a direct consequence of the regular distribution of holes chosen. Other observed lines, especially visible in the map of smaller holes, are similarly artefacts of special directions in the regular distribution of holes.

Let us consider the angular power spectra, C_l's, of the autocorrelation for

[3]The calculations were performed on an MPI-grid. For the largest holes, the computation of one map takes about one hour on 16 cpu's. For the tiniest holes, the computation of a map takes about 30 hours on 128 cpu's.

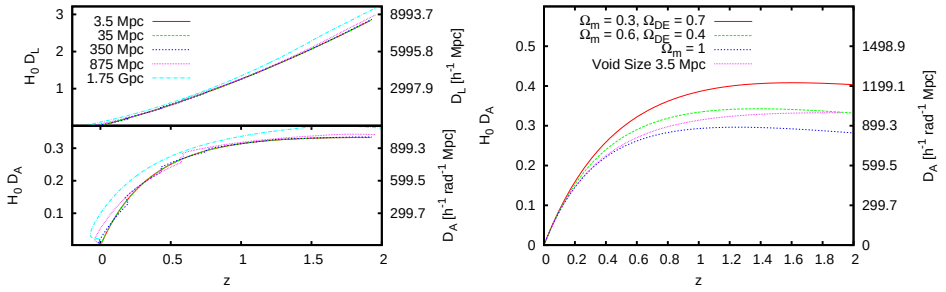

Figure 8.5: *Left:* The maximum luminosity distance (top) and the maximum angular diameter distance (bottom) achievable as a function of redshift z, for Swiss-Cheese universes with five different hole sizes. These distances would be observed when looking through a series of perfectly aligned holes. Note that the maximum lensing effect only marginally changes with hole size. This indicates that the ratio between time spent in 'cheese' and time spent in 'holes' along the history of a photon path is the quantity that defines the observed distances, as opposed to the physical size of the holes. *Right:* The angular diameter distance as a function of redshift z, comparing the Swiss-Cheese model with three different spatially flat FLRW-solutions.

these maps, in figure 8.4. The spectra are binned in bins of five multipoles. The Swiss-Cheese spectra must be considered as additional secondary anisotropies in the CMB, since the primary power spectrum has been ignored. For comparison the power spectrum of the CMB, as it would be observed today in the standard ΛCDM universe, is displayed. For holes of radius $r_{\rm hl} = 35$ Mpc, the secondary anisotropies are of the same magnitude as the CMB observed today. This means that a Swiss-Cheese universe with all holes smaller than 35 Mpc potentially leaves the CMB as observed unaltered. For example, the secondary anisotropies for holes of radius 3.5 Mpc are up to two orders of magnitude smaller than the observed anisotropies. A decrease of the Rees-Sciama effect with decreasing hole-size was also foreseen in Refs. [21, 178]. In a more realistic distribution of holes, the size of holes is not a fixed number. In that case, probably a few holes larger than $r_{\rm hl} \sim 35$ Mpc amongst smaller holes, would leave an imprint on the CMB small enough to agree with observations.

8.4 Angular diameter distance - redshift relation

8.4.1 The same maximum distance for all hole sizes up to 1.75 Gpc

In the right of figure 8.5, we repeat for illustration a comparison of $d_A(z)$ for different FLRW-cosmologies and one particular Swiss-Cheese cosmology, similar to Ref. [178]. Here we focus on the maximum deviation in d_A with respect to an FLRW-cosmology with $\Omega_{\rm matter} = 1$. At redshift $z \sim 1.92$, in this Swiss-Cheese cosmology $d_{\rm A}$ corresponds to that in a flat FLRW-universe with $\Omega_\Lambda = 0.4$. In Ref. [177] it was argued, however, that a good fit over the whole curve to a

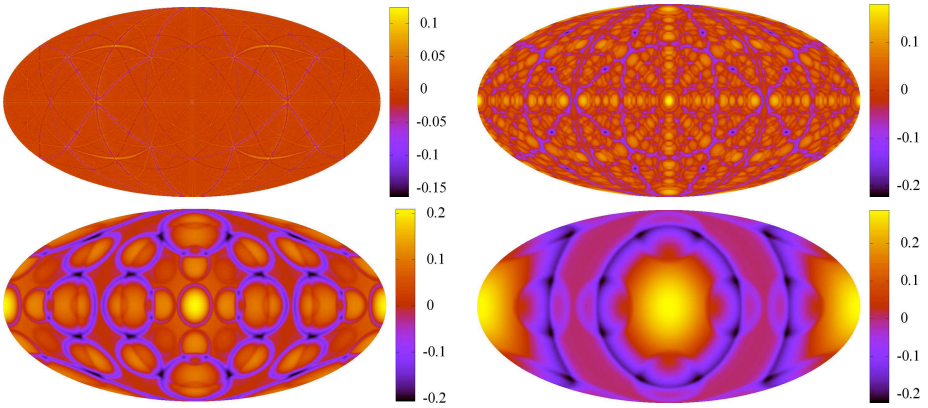

Figure 8.6: The full-sky maps of the angular diameter distance at $z = 1.92$ induced by the Swiss-Cheese structure. The quantity shown is $\frac{d_{\rm A}-\bar{d}_{\rm A}}{\bar{d}_{\rm A}}$. Again these are maps in Swiss-Cheese universes with holes of size $r_{\rm hl} = 3.5$ Mpc (upper left figure), $r_{\rm hl} = 350$ Mpc (upper right figure), $r_{\rm hl} = 875$ Mpc (lower left figure) and $r_{\rm hl} = 1.75$ Gpc (lower right figure). In contrast with the redshift maps, in the angular diameter distance, the *maximum* anisotropy does not depend on the size of the holes.

cosmology with $\Omega_\Lambda = 0.75$, is actually achieved by a Swiss-Cheese universe with five holes of radius 250 Mpc between the observer and $t = \bar{t}$. Since we are dealing with a toy model that probes the ability of structure formation to explain the observed acceleration, we prefer to probe the maximum achievable effect at high redshift, over finding the best out of a set of perhaps mediocre fits.

In the left of figure 8.5, the maximum $d_{\rm A}$ is compared for all models. The maximum $d_{\rm A}$ for all models lies in the direction of perfectly aligned holes. In nature such a direction is unlikely to exist, but a more natural distribution of holes goes beyond our scope here. The maximum effect on $d_{\rm A}$ is only marginally dependent on the size of holes. This conclusion seems in contradiction with conclusions drawn in Refs. [21, 29], which we address at the end of this section.

8.4.2 Distribution in different directions

In figure 8.6 we show a full sky map of the angular diameter distance at a fixed redshift, namely the maximum redshift found in the temperature map of each cosmology at $t = \bar{t}$, which for each cosmology is close to $z = 1.92$. This means that in most directions the redshift of a photon was slightly less at time $t = \bar{t}$, hence the integration was continued through cheese only up to the right redshift. Interestingly, the maximum anisotropy in angular diameter distance is the same for all models, which was illustrated in the left of figure 8.5.

In Ref. [269] it was already shown that, for holes of radius 350 Mpc, the average $d_{\rm A}$ corresponds to that of a cheese-only universe. In figure 8.7 we show the angular power spectrum of the autocorrelation in the angular diameter map, $C_l^{\rm d_A d_A}$. This figure illustrates that, even though the maximum effect of the Swiss

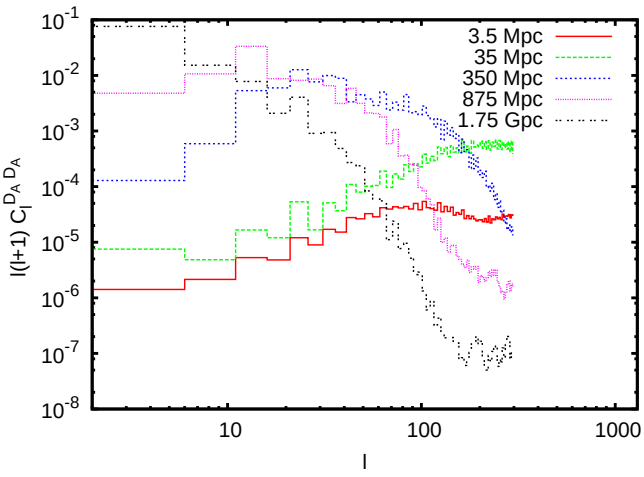

Figure 8.7: The $C_l^{d_{\rm A} d_{\rm A}}$'s for different cosmologies, in bins of 5 multipoles. Even though the maximum observed $d_{\rm A}$ is independent of the size of holes, the average anisotropy goes down with decreasing hole size. This is because the number of special directions decreases with decreasing hole size.

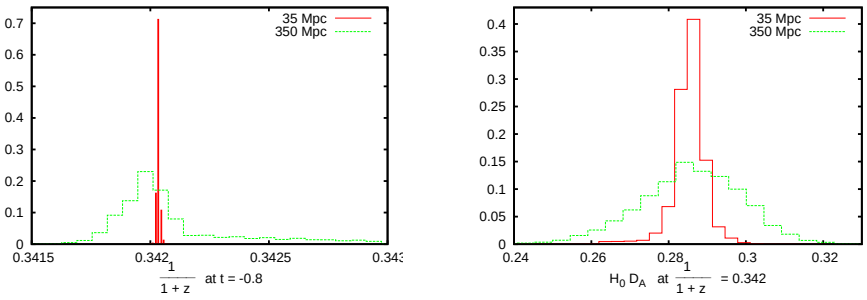

Figure 8.8: *Left:* The distribution of redshift of photons in all directions, at fixed time. Clearly, for smaller holes, the variance in redshift decreases. *Right:* The distribution of angular diameter distance of photons in all directions, at fixed redshift. Again, for smaller holes, the variance decreases.

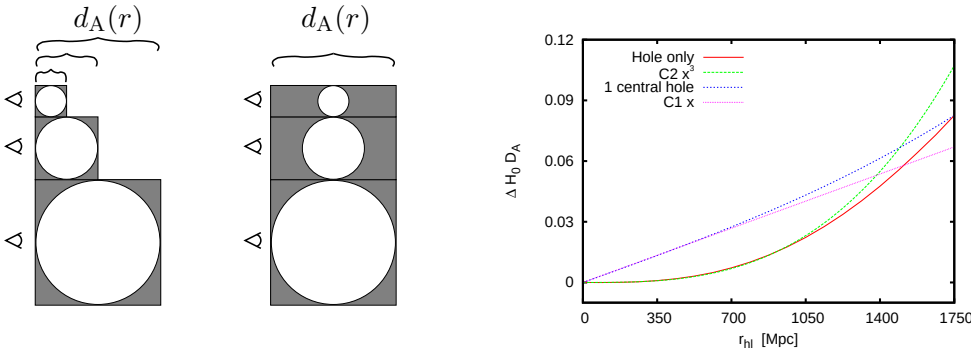

Figure 8.9: An ambiguity when speaking of the effect of the size of holes on $d_{\rm A}$. *Left:* Two sketches of methods comparing hole sizes. The first method considers only distance traveled through a hole, and compares $d_{\rm A}$ at the exit of that hole to that of an cheese-only photon. The second method considers one central void embedded in cheese, and compares $d_{\rm A}$ at the end of the same total comoving distance through a hole and cheese. *Right:* Using the first comparison method we recover the behaviour that is found in Refs. [21, 29], $\Delta d_{\rm A} \propto r_{\rm hl}^3$ (red, solid). Using the second method, we find a different behaviour which is closer to $\Delta d_{\rm A} \propto r_{\rm hl}$ (blue, dashed).

Cheese on $d_{\rm A}$ is about the same for all hole sizes, the number of special directions in which there is a high effect (or anti-effect), decreases with decreasing hole size. The smaller the size of holes is, the smaller the standard deviations in d_A will be. This is also apparent in figure 8.8, where the distributions of redshift z and the angular diameter $d_{\rm A}$ are compared for Swiss-Cheese universes with two different hole sizes. The standard deviation in redshift goes down from $\sigma_{\frac{1}{1+z}} = 2.6 \times 10^{-4}$ for $r_{\rm hl} = 350$ Mpc to $\sigma_{\frac{1}{1+z}} = 3.8 \times 10^{-5}$ for $r_{\rm hl} = 35$ Mpc. Similarly for the angular diameter distance, it goes down from $\sigma_{d_{\rm A}} = 1.3 \times 10^{-2}$ to $\sigma_{d_{\rm A}} = 4.3 \times 10^{-3}$.

8.4.3 Dependence on the size of holes

In Refs. [21, 29] it was found that the effect of one hole on $d_{\rm A}$, with respect to a cheese-only passage, goes as $\Delta d_{\rm A} \equiv d_{\rm A}^{\rm hole} - d_{\rm A}^{\rm cheese} \sim r_{\rm hl}^3/R_{\rm H}^3$, with $R_{\rm H}$ the Hubble radius. Increasing the number of holes with $N_{\rm hl} \sim R_{\rm H}/r_{\rm hl}$, this would mean that the maximum effect scales as $d_{\rm A,max} \sim r_{\rm hl}^2/R_{\rm H}^2$. As total lensing effect is crucial to the success of a Swiss-Cheese model, this contradictions deserves more attention. The difference in size-dependence may be an artefact of the modelling. However we find a difference at the analytical level, before even deciding which model to take. Let us explain why we come to a different conclusion.

The calculations in Refs. [21, 29] consider one hole at a time, and one hole only. The effect of several holes does however not grow linearly with the number of holes. It may happen to do so for a particular modelling, but in general it will not. In figure 8.9 we show the results of two different approaches. The first

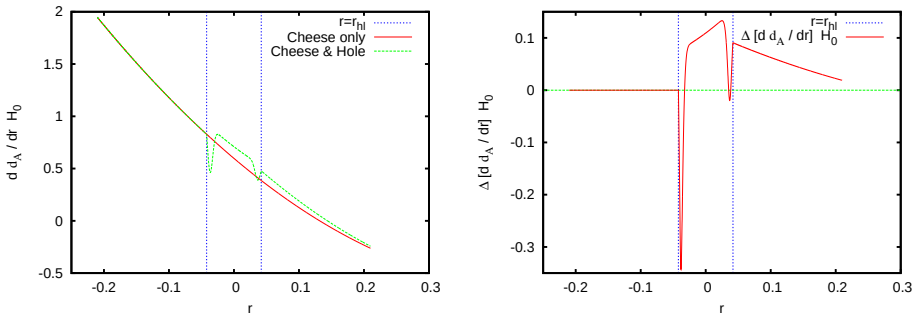

Figure 8.10: *Left:* A comparison of the $d\,\mathrm{d_A}/dr$ along the trajectories of two photons. Time increases from right to left, and the initial conditions are chosen such that an observer today (at $r = -0.21$) sees a source through cheese only (red solid line) and a source through one central hole, with $r_{\mathrm{hl}} = 350$ Mpc, centred between the observer and $t = \bar{t}$ (green dashed line). Both sources are observed at the same solid angle, which translates to $d\,\mathrm{d_A}/dr$ at the observer. They have however a different size, which translates to $d\,\mathrm{d_A}/dr$ at the source. That means that the source at $r = 0.21$ behind the hole must have a larger area in order to be observed under the same solid angle, and hence has a larger angular diameter distance. The key point in this figure is the difference in $d\,\mathrm{d_A}/dr$ at both sides of the hole. *Right:* $\Delta[d\,\mathrm{d_A}/dr]$ shows the suppressing effect the hole has on the derivative of the area of the beam, causing the source to be observed under smaller solid angle than a source of the same size seen through cheese only. Hence, once a photon passes a hole, the lensing effect of the hole continues playing a role beyond the hole, by having changed the initial conditions of the integration beyond the hole.

approach considers only one hole. If one starts an integration when entering a hole, and stops when exiting the hole in order to compare d_{A} with the value found when travelling the same distance through cheese, we recover in fact the foreseen effect of $\Delta d_{\mathrm{A}} \propto r_{\mathrm{hl}}^3$. In the second approach, we consider a photon passing one hole along a fixed distance, where all space outside the single hole is necessarily cheese. In this case we do not find the same behaviour, but the size dependence seems to be more like $\Delta d_{\mathrm{A}} \propto r_{\mathrm{hl}}$.

The reason for this discrepancy is that, after passing a void, the quantity $\frac{d\sqrt{A}}{dr}$ (see equations (8.20,8.22)) keeps a deviation from the same quantity for a cheese-only photon, as shown in figure 8.10. Hence, if one were to consider the part of the integration, starting only beyond the patch, the initial conditions for the cheese-only photon and the photon that passed through the hole are different. The quantity $\frac{d\sqrt{A}}{d\lambda}$ can be interpreted as a measure of divergence / convergence of the beam. Changing this quantity necessarily changes the final beam size, even when no more holes are on the way. There is no reason to believe that this quantity obtains no change from a hole, as 'the magnification of the beam, is proportional to the integrated column density along the beam's path' [269]. The integration is performed over the past light cone of a photon. The photon spends more time in the void of a hole than it does in the shell of a hole, therefore there is no cancellation of the defocussing effect when leaving a hole. In fact, a closer

look at Eqs. (8.7-8.10,8.21,8.22) for the special case of a radial photon, such that $c_\phi = \xi = 0$, shows us,

$$\begin{aligned}\frac{d^2\sqrt{A}}{dr^2} &= -\frac{2}{3}\sqrt{A}\,\frac{Y'(r,t)^2\rho(r,t)}{W(r)^2} \\ &\quad + \frac{d\sqrt{A}}{dr}\left[\frac{Y''(r,t)}{Y'(r,t)} - \frac{W'(r)}{W(r)} + \frac{\dot{Y}'(r,t)}{W(r)}\right], \\ &= \sqrt{A}\;F_1(r,t) + \frac{d\sqrt{A}}{dr}F_2(r,t). \end{aligned} \tag{8.33}$$

Here we used,

$$\frac{d^2}{dr^2} = \left(\frac{d\lambda}{dr}\right)^2\frac{d^2}{d\lambda^2} + \frac{d^2\lambda}{dr^2}\frac{d}{d\lambda}, \tag{8.34}$$

in order to be able to unambiguously compare photons along different geodesics, with different affine parameters λ but with the same coordinates r and t. Now let us compare two photons, that entered a patch with the same initial conditions, and let one of them see only cheese. At the exit of the hole, the difference in $\frac{d^2\sqrt{A}}{dr^2}$ is,

$$\Delta\left[\frac{d^2\sqrt{A}}{dr^2}\right] = \Delta\left[\sqrt{A}\right]\;F_1(r_{\rm hl},t) + \Delta\left[\frac{d\sqrt{A}}{dr}\right]F_2(r_{\rm hl},t) \tag{8.35}$$

where in we use the notation $\Delta[Q] = Q_{\text{hole photon}}(r_{\rm hl}) - Q_{\text{cheese photon}}(r_{\rm hl})$.

First consider $F_1(r_{\rm hl},t)$ and $F_2(r_{\rm hl},t)$. These are functions of background quantities only, evaluated at $r = r_{\rm hl}$ where all background quantities are supposed to continuously match from the hole to the cheese. Hence, these functions are the same for all photons, no matter whether they saw a hole or cheese only, no matter what initial conditions their beam had. By construction we have $\Delta\left[\sqrt{A}\right] \neq 0$, since that is the whole purpose of the Swiss-Cheese structure. Therefore, beyond the hole, one expects that at least either $\Delta\left[\frac{d\sqrt{A}}{dr}\right] \neq 0$ or $\Delta\left[\frac{d^2\sqrt{A}}{dr^2}\right] \neq 0$ if $\Delta\left[\sqrt{A}\right] \neq 0$, proving that the defocussing effect of the hole carries beyond the hole.

The reader should keep in mind that the defocussing effect is of importance when one considers the maximum effect one hole can have on $d_{\rm A}$, even beyond the passage of that particular hole. Remember that we are considering the divergence of a beam, after having passed a hole, which is the derivative of the angular diameter distance. However, as it has been shown in Refs. [269] that the average effect of one hole on the angular diameter distance disappears when averaged over angles of incidence, it is likely that the average effect of one hole on the divergence of the beam (which, as we just discussed, influences the angular diameter distance beyond the hole) will also disappear on average.

A final remark to make here, is a reminder that we are dealing with a toy model. The model is constructed manually and ideally. The defocussing by the hole may be an artefact of the modelling, and may disappear in a more realistic model. We showed that in idealised models it is most likely that the divergence of a beam *is* altered by a hole, but this gives no guarantee for more realistic models.

8.5 Discussion and conclusion

For the first time we have performed a full sky simulation of the CMB in Swiss-Cheese universes, in realisations with different hole sizes. We have shown that if all holes have a radius larger than $r_{\rm hl} = 35$ Mpc, the Swiss-Cheese model can be ruled out on basis of the observed CMB. One could try to change the density profile of the holes, but in order to leave the CMB intact, that new profile would necessarily be closer to FLRW, hence no longer reproducing the wanted angular diameter distance effect.

Another option to try to save the model is to decrease the size of holes. We find that for small holes, the maximum angular diameter effect remains the same as for larger holes. However, the probability that special directions exist, in which one sees through the centres of a series of perfectly aligned holes, decreases with decreasing hole size, at least in the case of holes on a lattice, as in this work.

In Refs. [269, 274] it was argued that (spherical) mass compensated holes in a Swiss-Cheese universe cannot make the average angular diameter distance depart from the EdS-case, when the observer is outside the hole. Not surprisingly, we confirm this result. Moreover, we have shown that even though the average $d_{\rm A}$ does not change, the anisotropy in CMB-temperature due to the same hole does in fact differ significantly from the EdS-case, which in principle should not depend on the sphericalness of a hole, but on the mere fact that the observer sees both through and past the side of the hole, inevitably leaving a Rees-Sciama imprint on the CMB.

These findings together lead to the conclusion that the Swiss-Cheese universe, as considered here, with mass compensated holes, all of them larger than $r_{\rm hl} = 35$ Mpc, spherical or not, is ruled out. Based on the findings in Ref. [269], and the findings in this work with respect to the variance in $d_{\rm A}$ in different directions that decreases with decreasing hole size, also Swiss-Cheese universes with *spherical* mass compensated holes of radius smaller than $r_{\rm hl} = 35$ Mpc are ruled out.

This conclusion applies to all Swiss-Cheese-like models in which the universe is saturated with mass compensated voids, and that try to explain the angular diameter distance at high redshift. We did not consider the case where our local Hubble volume contains just a small number of voids, without being saturated with them. Such a scenario remains interesting in order to explain anomalies in the CMB, such as the cold spot [181]. However, such a scenario is in principle unrelated to possible alternative explanations for the observed accelerated expansion.

We have shown that the maximum effect of holes on $d_{\rm A}$ has weaker, if not zero, dependence on the size of the holes than previously claimed in the literature, due to the defocussing effect a hole has, which carries influence beyond the hole. We

assessed the importance of taking into account this defocussing, when addressing the effect of different hole sizes. This effect could be due to the modelling of the density profile. The model dependence should be more carefully assessed, before definitive conclusions can be drawn. It remains to be investigated as well, what the effect would be of non-spherical holes, with a typical size $r_{\rm hl} < 35$ Mpc, densely spread in such a manner that locally the universe is nowhere described by the cheese metric, but globally remains FLRW. Another addition to subject to research, is to see the effect of virialisation of the mass shells, which, as pointed out in Ref. [21], may increase the effect on $d_{\rm A}$, and at the same time should decrease the Rees-Sciama effect, hence decreasing the potential trouble with the CMB.

General Conclusion

The common thread in this thesis is the use of observed cosmic perturbations to constrain theoretical models and parameters. The broad range of topics in this thesis is only emblematic for the essentially infinite possibilities that cosmic perturbations offer. The history of the universe is rich, and many effects play a role in the development of cosmic perturbations, yet different epochs and different effects have distinct imprints on the perturbations. By accurately mapping out the cosmic perturbations, we can test and constrain different cosmological models and their parameters.

In Part II, we explored constraints on the very early universe, in principle at the youngest state we can possibly probe today, the epoch of inflation. If the global Hubble factor for our Hubble volume is equal to the Hubble factor we observe in our nearby volume, then the CMB tells us that the universe is as good as spatially flat, as argued in Chapter 1. The spatial flatness and the observed perturbations that once have to have been super-Hubble, offer strong support for the paradigm of inflation. Taking inflation as a starting point, we constrained the shape of the, today still hypothetical, inflaton potential more consistent and more robust than before, in Chapters 3, 4 and 5. In Chapter 6, we emphasised that more data is needed in order to constrain the absolute scale of inflation. As such, this knowledge is not new, but we quantified the prior dependence of the scale of inflation, as well as the constraining power of the data today.

In Part III, our focus shifted to the secondary anisotropies in the CMB. We used the fact that the CMB anisotropy can gain a cross correlation with the large scale structure, to constrain the mass of the neutrinos in Chapter 7. Present data is not constraining enough to tighten the constraints on the neutrino mass using this effect, and we found that future data can possibly constrain the neutrino mass stricter without even taking into account the cross-correlation with the CMB. Nonetheless, the effect remains important, as it can distinguish between the effect of a genuine neutrino mass or an unknown effect that mimics neutrinos in the power spectrum, but fails to mimic neutrinos in the integrated Sachs-Wolfe effect. The effect represents an independent cross check.

Finally, in Chapter 8, we pointed out the importance of cosmic perturbations when constructing radically different models of the universe. We showed that if the lensing effect of voids and structures is the cause for the *apparent* acceleration of the expansion of the universe, the CMB would exhibit large secondary anisotropies. The absence of such anisotropies in the CMB, shows that at least the scenario

with large voids is ruled out.

Given the broad range of topics in this thesis, the finale is not just a single answer. It is a list of conclusions, as summarised here. If there is, however, a single conclusion we can draw from this bundle of topics, it is that its variety *per se* is a proof that cosmic perturbations are of utmost importance in the quest to understand the universe.

Acknowledgements

The thesis is over, here it is. My first word of gratitude goes to you, the reader, for making it all the way here.

As I wrote in the very first lines, this thesis is the result of close to three years of research at the Laboratoire d'Annecy-Le-Vieux de Physique Théorique, under supervision of Julien Lesgourgues, sometimes closely, sometimes distantly. Perhaps the 'sometimes closely, sometimes distantly' deserves an explanation. In my first year, here in Annecy, Julien closely guided me through a number of projects, rapidly leading to publications, rapidly allowing me to give seminars and short talks at conferences. But halfway the second year, Julien moved to Lausanne, and I stayed in Annecy. This was an excellent way to force me to learn to work more independently, still under supervision of Julien, but now distant. I would say that this was a good thing. Even though learning to work independently costs time, which may be precious during the process of writing a thesis, it is not a waste of time, but an invaluable moment of education. I am grateful to Julien for his support over all this time, full of energy, full of enthusiasm, full of humour, and sometimes full of wine or cider. Thank you for giving me this great opportunity and great stay in the French Alps! I sincerely enjoyed it.

This brings me to the next entity to thank. Namely all the French, simply for building a physics institute in a place so remote from large cities and close to a lot of wonders of nature. The time I spent on my thesis could not have been the same if it had not been in the mountains.

My life in Annecy was funded by the EU 6th Framework Marie Curie Research and Training network "UniverseNet" (MRTN-CT-2006-035863), for which I am grateful.

Another person that has played a great role in my being in Annecy is Tomislav Prokopec. It is to him that owe my gratitude for bringing me in contact with Julien, after successfully having guided me to my Masters diploma in Utrecht, inspiring me to continue in science in the first place.

I want to express my gratitude to all the friends that made life in Annecy a joy. I may forget people, since there were so many nice people. I thank everybody at LAPTH. In particular Nans, Gregory, Johannes, James, Jan, Timur, Daniel, Samuel, Walter, Nelly, Olivier, Julien M. thanks for the fun. I owe a special word of thanks to Laurent Gallot, for patiently telling me "don't go fast, learn to ski better first!" (in French, which I am sorry not to be able to flawlessly reproduce in written word here), every time he took me of an icy 45 degrees slope above any

canyon. In a first draft of some paper, Julien had to correct a misspelling. I wrote 'ski' in stead of 'sky'. I also thank Eric Pilon, for suggesting all the interesting trips by bike, like the devastating 'Signal de Bisanne'. Thanks Germano, for surviving a lone autumn with me in Chicago. Thanks Guillermo, for fun in many other places than Annecy.

I thank Glenn Starkman, for welcoming me warmly during a stay at CWRU.

Every time I returned to Utrecht, I was always surprised by the number of people that had not forgotten me yet. In principle I could do with a 'thanks to all the Juhluh-people', but let me mention: Martijn, Maarten, Sietze, Minne, Ties, Erik, Tristan, Manouk, Gijs, Gijs, Ron, Nici, Gerben, Ivo and Thomas. Of those *Utrechtenaren*, a special mention is on its place for Gijs, Tim and Erik, thanks for scraping me out of the 'vangrail' at the Forclaz in 2005, to get things glued together again.

And then, there are people how are not physicists. Even though with many of them, the contact was only little, it was worth while. Thank you Thomas Jaarsma, Tessa, Randy, Suzan.Thanks Theo, for always being there, even after periods of no attention.

And there are people who have a bigger influence in who I am than I can realise myself. My parents, Jan and Annette, usually in war, although improving over the years. Thanks for supporting me, even though I go away and do my thing, without contacting you much. Thanks for never giving up hope for me, and always stubbornly believing that all your children are miracles.

Thank you Govert and Jochem, brothers, for distracting me from work over Skype. I must say that our contact improved strongly when all three of us started writing a thesis, having to spent hours and hours at a desk, with only chat programs as distraction. Thank you for letting me brag every once in a while about any kind of trip in the mountains. Thanks for your interest, but also empathy whenever it was needed.

Floor, I could write a book of its own on my gratitude to you. When I left you in Utrecht to seek my glory in Annecy, we thought we had no future. And there you are, still my very best friend. Thank you for all your energy and joy. Things would not have been the same without you.

Appendix A

Vacuum states

This appendix previously appeared as section 3.4 in Ref [264].

A.1 Vacuum in Minkowsky space

For any canonically quantised field in Minkowsky space, the vacuum state is the state that is annihilated by any annihilation operator $a_{\vec{k}}$. That is,

$$a_{\vec{k}} |0\rangle = 0. \tag{A.1}$$

Let us for instance look at the massless scalar field in flat space, with the Lagrangian density,

$$\mathscr{L} = \tfrac{1}{2}\eta^{\mu\nu}\partial_\nu\phi\partial_\mu\phi, \tag{A.2}$$

where $\eta_{\mu\nu}$ is the Minkowski metric. The scalar field obeys the field equation,

$$\partial^2\phi(\eta, k) = 0. \tag{A.3}$$

One set of solutions is

$$u_{\vec{k}}(t, \vec{x}) = e^{i\vec{k}\cdot\vec{x}-ikt} \tag{A.4}$$

$$u^*_{\vec{k}}(t, \vec{x}) = e^{-i\vec{k}\cdot\vec{x}+ikt}. \tag{A.5}$$

The question then is, what combination of both solutions to choose as the vacuum state. To answer that question, I will make use of the concept of Killing vectors. For a given metric, a Killing vector points in a certain direction. For a given path in spacetime, the component of this path, which points in the direction of the Killing vector, is conserved. In other words, Killing vectors imply conserved quantities associated with the motion of free particles [41].

The vacuum state of a field should be the ground state of that field. Since the ground state is the state of lowest energy, the field will not evolve beyond that state without external influences and with a time independent Hamiltonian. This means that the ground state must be completely conserved in time. If the ground

state is not directed along the time-like Killing vector, then the components not directed along this vector will not be conserved in time. These extra components would radiate away in some manner, leading to a lower energy state. This is in contradiction with the definition of the ground state. If a state is directed along a Killing vector, it is an eigenfunction of that vector.

In flat space, ∂_t is the time-like Killing vector. To define the ground state, we demand that

$$\partial_t \phi(t, \vec{k}) = \sigma \phi(t, \vec{k}), \tag{A.6}$$

with σ being any constant.

Now we find, that for the ground state I can choose solely either $u_{\vec{k}}$ or $u^*_{\vec{k}}$.

The functions $u_{\vec{k}}$ and $u^*_{\vec{k}}$ are orthogonal, but also satisfy the equality

$$u^*_{-\vec{k}}(t, \vec{x}) = u_{\vec{k}}(t, \vec{x}). \tag{A.7}$$

Hence, all k-modes of u_k are covered when only one of both solutions is integrated over all k.

The field $\phi(t, \vec{x})$ may be expanded as

$$\begin{aligned} \phi(t, \vec{x}) &= \sum_{\vec{k}} \left[u_{\vec{k}}(t, \vec{x}) a_{\vec{k}} + \left(u_{\vec{k}}(t, \vec{x}) a_{\vec{k}} \right)^\dagger \right] \\ &= \sum_{\vec{k}} e^{i\vec{k}\cdot\vec{x}} \left[e^{ikt} a_{\vec{k}} + e^{-ikt} a^\dagger_{-\vec{k}} \right] \end{aligned} \tag{A.8}$$

Here $k = \left\| \vec{k} \right\|$. I have made the usual choice to define the modes (A.4) to have positive frequency when

$$\partial_t u_{\vec{k}}(t, \vec{x}) = -ik u_{\vec{k}}(t, \vec{x}), \tag{A.9}$$

with $k > 0$.

A.2 Ambiguity in curved space

Now moving back to curved space, we can recognise that the positive frequency choice is ambiguous in curved space. In flat space, ∂_t is a Killing vector, and we defined the positive frequency modes to be eigenfunctions of this Killing vector. In an arbitrary curved spacetime, ∂_t is not automatically a Killing vector, and there may not be a time-like Killing vector at all. This means one cannot by definition uniquely define a vacuum solution, in agreement with equation (A.6). Hence different bases may be chosen in which to express the solutions to the field equations. I.e., linear combinations of u_k and u^*_k can be used as a new basis. In that case, the new solutions $\overline{u}_k$ and $\overline{u}^*_k$ can be expressed in terms of the old solutions as

$$\overline{u}_{\vec{k}} = \alpha_{\vec{k}\vec{k}'} u_{\vec{k}'} + \beta_{\vec{k}\vec{k}'} u^*_{\vec{k}'}. \tag{A.10}$$

Likewise the new creation and annihilation operators can now be expressed in terms of the old ones as

$$\overline{a}_{\vec{k}} = \alpha_{\vec{k}\vec{k}'} a_{\vec{k}'} - \beta^*_{\vec{k}\vec{k}'} a^\dagger_{\vec{k}'}. \tag{A.11}$$

Equations (A.10) and (A.11) are known as the Bogoliubov transformations [19, 23].

With these new defined operators, a new vacuum is also defined, since

$$\overline{a}_{\vec{k}} \left|\overline{0}\right\rangle = 0. \tag{A.12}$$

That this is not the same vacuum as $|0\rangle$ follows from

$$\overline{a}_{\vec{k}} \left|0\right\rangle = -\beta^*_{\vec{k}\vec{k}'} a^\dagger_{\vec{k}'} \left|0\right\rangle = -\beta^*_{\vec{k}\vec{k}'} \left|1_{\vec{k}'}\right\rangle \neq 0. \tag{A.13}$$

A vacuum in one frame, contains particles in another frame. The vacua of both frames may not be conserved in time, as there may not be a timelike Killing vector. Only when a timelike Killing-vector field exists, the positive frequency modes (eigenfunctions of the timelike Killing vector with positive eigenvalues) can be defined as in equation (A.9). Then the ground state is uniquely defined.

A.3 Conformal vacuum

Special cases exist for which one can define a vacuum state in curved space. Let us for instance look at the massless conformally coupled scalar field, with the Lagrangian density,

$$\mathscr{L} = \tfrac{1}{2}\sqrt{-g}\partial^\mu\phi\partial_\mu\phi - \frac{1}{12}\sqrt{-g}R\phi^2, \tag{A.14}$$

where R denotes the Ricci scalar. The scalar field obeys the field equation,

$$\Box\phi(\eta, k) + \frac{1}{6}R\phi = 0. \tag{A.15}$$

A conformal transformation of the metric is defined as,

$$g_{\mu\nu} \rightarrow \tilde{g}_{\mu\nu} = \Omega(x)^2 g_{\mu\nu}. \tag{A.16}$$

Under such a transformation the Ricci scalar transforms as,

$$R \rightarrow \tilde{R} = \Omega(x)^2 R + 6\Omega(x)^{-3}\sqrt{-g}\Box\Omega(x), \tag{A.17}$$

and the field equation transforms as

$$\Box\phi(\eta, k) + \frac{1}{6}R\phi = 0 \rightarrow \tag{A.18}$$

$$\tilde{\Box}\tilde{\phi} + \frac{1}{6}\tilde{R}\tilde{\phi} = 0, \tag{A.19}$$

$$= \Omega(x)^{-3}\left[\Box + \frac{1}{6}R\right]\Omega(x)\tilde{\phi} = 0, \tag{A.20}$$

such that $\tilde{\phi} = \Omega(x)^{-1}\phi$ and the field equation is invariant under conformal transformations.

Now if we start in a FLRW-universe, with metric $g_{\mu\nu} = a(\eta)^2\eta_{\mu\nu}$, and choose the conformal transformation such that $\Omega(x)^2 = a(\eta)^{-2}$, we find in the conformal coordinate system

$$\Box\phi(\eta, k) + \frac{1}{6}R\phi = 0 \rightarrow \tag{A.21}$$

$$\partial^2\tilde{\phi} = 0, \tag{A.22}$$

since for the Minkowsky metric we have $\tilde{R} = 0$ and $\tilde{\Gamma}^{\rho}_{\mu\nu} = 0$.

In general for conformal spacetimes we can always perform a conformal transformation which takes us to the flat Minkowsky frame in which $\tilde{R} = 0$ and $\tilde{\Gamma}^{\rho}_{\mu\nu} = 0$.

Equation (A.22) shows that the field equation for the conformally coupled scalar reduces to that of a massless scalar in flat space, under a conformal transformation. As a consequence the modes of the conformally coupled field contain the flat space solution. We already know that in flat space we have the timelike Killing vector $\partial_{\tilde{t}}$, and have the well defined flat space vacuum state for the scalar field.

In that way is is natural to choose the vacuum state in the conformal spacetime in accordance with its flat space equivalent. We find that the vacuum state in the FLRW-metric must be given by,

$$\phi_{\text{vac}} = a(\eta)^{-1}\tilde{\phi}_{\text{vac}}. \tag{A.23}$$

In general we find that the Killing vector in flat spacetime is identified with a conformal Killing vector in curved (conformal) spacetime. A conformal Killing vector no longer implies a conserved quantity for any geodesic, but it still does for null geodesics [272]. A massless field evolves along null geodesics. Therefore the vacuum state in any frame can be defined to be the state that contains only positive-frequency modes in the comoving frame. For example, a field component ψ, not necessarily a scalar field, whose field equation under transformation (A.16) transforms to

$$\partial^2\left(a(\eta)\psi\right) = 0, \tag{A.24}$$

has in the flat frame the solutions given in equation (A.4) and its complex conjugate. Hence, in conformally flat space, that is $g_{\mu\nu} = a(\eta)^2\eta_{\mu\nu}$, its vacuum state can be written as

$$\psi(\eta, \vec{x}) = a(\eta)^{-1}\sum_k e^{i\vec{k}\cdot\vec{x}}\left[e^{ik\eta}a_{\vec{k}} + e^{-ikt}a^{\dagger}_{-\vec{k}}\right]. \tag{A.25}$$

The behaviour of the field under transformation (A.16) is of course defined by nature of the field, as it may be the component of a tensor or vector field.

A.4 Bunch-Davies vacuum

Now let us move on to a less simple example, the minimally coupled massless scalar field. The Lagrangian density is given by

$$\mathscr{L} = \tfrac{1}{2}\sqrt{-g}\partial^{\mu}\phi\partial_{\mu}\phi. \tag{A.26}$$

From this Lagrangian density we find the field equation,

$$\Box\phi = 0. \tag{A.27}$$

Apparently the minimally coupled massless scalar breaks conformal invariance.

If we quantise the field and transform to momentum space, the field equation becomes,

$$\left[\partial_0^2 + \frac{2a(\eta)'}{a(\eta)}\partial_0 + k^2\right]\phi_{\vec{k}}(\eta) = 0. \tag{A.28}$$

Now in the special case of a quasi-de Sitter universe, with the metric

$$g_{\mu\nu} = a(\eta)\eta_{\mu\nu}, \quad \text{with } a(\eta) = \tfrac{-1}{H_I\eta}, \tag{A.29}$$

where H_I is the Hubble constant during inflation and $-\infty < \eta < -1/H_I$, the field equation becomes,

$$\left[\partial_0^2 - \frac{2}{\eta}\partial_0 + k^2\right]a(\eta)\phi_{\vec{k}}(\eta) = 0. \tag{A.30}$$

The solution to this equation is given in terms of Hankel functions,

$$\phi_k(\eta) = \frac{a(\eta)^{-1}}{\sqrt{2k}}\left[\alpha\left(1 - \frac{i}{k\eta}\right)e^{-ik\eta} + \beta\left(1 + \frac{i}{k\eta}\right)e^{ik\eta}\right], \tag{A.31}$$

where $|\alpha| - |\beta| = 1$ satisfies the canonical commutation relations for this action.

For each mode with a comoving momentum $\vec{k}$, there exists a time η such that $k/a(\eta)$
ggH. In that case $k/(H_I a(\eta)) = k\eta \gg 1$. Hence for each a time exists when the solution is effectively reduced to

$$\phi_k(\eta) = \frac{a(\eta)^{-1}}{\sqrt{2k}}\left[\alpha e^{-ik\eta} + \beta e^{ik\eta}\right]. \tag{A.32}$$

If we compare this to the conformal vacuum, defined in the previous subsection in equation (A.25), we see that the observer must effectively observe the conformal vacuum. In that case the choice of parameters has to be $\alpha = 1$ and $\beta = 0$. This is what is called the Bunch-Davies vacuum[19, 34, 213]: a field reduces to the conformal vacuum in the asymptotic limit (early time) of the spacetime.

Appendix B

The Limber approximation

Let us consider some maps $X(\hat{n})$ expanded in spherical harmonics

$$X\left(\hat{n}\right) = \sum_{l=0}^{\infty} \sum_{-l}^{l} a_{lm}^{X} Y_{lm}(\hat{n}) \tag{B.1}$$

with

$$a_{lm}^{X} = \int d^2n \, Y_{lm}^{*}(\hat{n}) X(\hat{n}). \tag{B.2}$$

The two-point correlation function of any two statistically isotropic quantities X and Y can be expressed in terms of the power spectrum in multipole space

$$C_l^{XY} = \left\langle a_{lm}^{X} a_{lm}^{Y*} \right\rangle, \tag{B.3}$$

or in therms of the angular correlation function in a Legendre polynomial basis (p_l)

$$w^{XY}(\theta) = \sum_{l} \frac{2l+1}{4\pi} p_l(\cos\theta) C_l^{XY}. \tag{B.4}$$

In the frame of observations, a direction dependent quantity $X(\hat{n})$ is usually a quantity integrated over the line of sight, $X(\hat{n}) = \int dr \, X(\vec{x})$. The expression for a_{lm}^{X}, (B.2), can then easily be transformed to Fourier space. Subsequently expanding the plain wave in spherical harmonics and applying the completeness relation for spherical harmonics, one arrives at

$$a_{lm}^{X} = (-i)^l \int dr \, \frac{d^3k}{2\pi^2} X(\vec{k}) j_l(kr) Y_{lm}^{*}(\hat{k}), \tag{B.5}$$

where $X(\vec{k})$ is the Fourier transform of $X(\vec{x})$, $j_l(r)$ is the spherical Bessel function, and $k = |\vec{k}|$. This expression can be simplified using Limbers approximation, $\int dx \, f(x) j_l(x) \simeq \sqrt{\frac{\pi}{2l+1}} \int dx \, f(x) \delta(l + \frac{1}{2} - x)$, leading to

$$a_{lm}^{X} \simeq (-i)^l \sqrt{\frac{\pi}{2l+1}} \int \frac{dr}{r} \frac{k^2 d\Omega_k}{2\pi^2} X\left(\hat{k}, k\right) Y_{lm}^{*}(\hat{k}), \tag{B.6}$$

separating the $\vec{k}$ dependence of X in $\hat{k}$ and $k = \frac{l+\frac{1}{2}}{r}$.

Bibliography

[1] L. F. Abbott and M. B. Wise, *Constraints on Generalized Inflationary Cosmologies*, Nucl. Phys. **B244** (1984), 541–548. ↑38, 58, 68, 86

[2] N. Afshordi, Y.-T. Lin, D. Nagai, and A. J. R. Sanderson, *Missing Thermal Energy of the Intracluster Medium*, Mon. Not. Roy. Astron. Soc. **378** (2007), 293–300, available at astro-ph/0612700. ↑103

[3] N. Afshordi, Y.-S. Loh, and M. A. Strauss, *Cross-Correlation of the Cosmic Microwave Background with the 2MASS Galaxy Survey: Signatures of Dark Energy, Hot Gas, and Point Sources*, Phys. Rev. **D69** (2004), 083524, available at astro-ph/0308260. ↑103

[4] A. J. Albrecht and P. J. Steinhardt, *Cosmology for Grand Unified Theories with Radiatively Induced Symmetry Breaking*, Phys. Rev. Lett. **48** (1982), 1220–1223. ↑58, 68, 86

[5] S. Alexander, T. Biswas, A. Notari, and D. Vaid, *Local Void vs Dark Energy: Confrontation with WMAP and Type Ia Supernovae* (2007), available at 0712.0370. ↑120

[6] H. Alnes and M. Amarzguioui, *The supernova Hubble diagram for off-center observers in a spherically symmetric inhomogeneous universe*, Phys. Rev. **D75** (2007), 023506, available at astro-ph/0610331. ↑120

[7] H. Alnes, M. Amarzguioui, and O. Gron, *An inhomogeneous alternative to dark energy?*, Phys. Rev. **D73** (2006), 083519, available at astro-ph/0512006. ↑120

[8] M. Amarie, C. Hirata, and U. Seljak, *Detectability of tensor modes in the presence of foregrounds*, Phys. Rev. **D72** (2005), 123006, available at astro-ph/0508293. ↑86

[9] P. Astier et al., *The Supernova Legacy Survey: Measurement of* Ω_M, $\Omega_L ambda$ *and* w *from the First Year Data Set*, Astron. Astrophys. **447** (2006), 31–48, available at astro-ph/0510447. ↑120

[10] G. Ballesteros, J. A. Casas, and J. R. Espinosa, *Running spectral index as a probe of physics at high scales*, JCAP **0603** (2006), 001, available at hep-ph/0601134. ↑78

[11] J. M. Bardeen, *Gauge Invariant Cosmological Perturbations*, Phys. Rev. **D22** (1980), 1882–1905. ↑21

[12] J. M. Bardeen, P. J. Steinhardt, and M. S. Turner, *Spontaneous Creation of Almost Scale - Free Density Perturbations in an Inflationary Universe*, Phys. Rev. **D28** (1983), 679. ↑38, 58, 68, 86

[13] V. Barger, J. P. Kneller, H.-S. Lee, D. Marfatia, and G. Steigman, *Effective number of neutrinos and baryon asymmetry from BBN and WMAP*, Phys. Lett. **B566** (2003), 8–18, available at hep-ph/0305075. ↑103

[14] D. Baumann et al., *CMBPol Mission Concept Study: Probing Inflation with CMB Polarization* (2008), available at 0811.3919. ↑xi, 30, 31, 32

[15] M. Beltran, J. Garcia-Bellido, J. Lesgourgues, A. R Liddle, and A. Slosar, *Bayesian model selection and isocurvature perturbations*, Phys. Rev. **D71** (2005), 063532, available at astro-ph/0501477. ↑43, 89

[16] M. Beltran, J. Garcia-Bellido, J. Lesgourgues, and A. Riazuelo, *Bounds on CDM and neutrino isocurvature perturbations from CMB and LSS data*, Phys. Rev. **D70** (2004), 103530, available at astro-ph/0409326. ↑103

[17] M. Beltran, J. Garcia-Bellido, J. Lesgourgues, and M. Viel, *Squeezing the window on isocurvature modes with the Lyman- alpha forest*, Phys. Rev. **D72** (2005), 103515, available at astro-ph/0509209. ↑89

[18] F. Bernardeau, *Lens distortion effects on CMB maps*, Astron. Astrophys. **338** (1998), 767–776, available at astro-ph/9802243. ↑86

[19] N. D. Birrell and P. C. W. Davies, *Quantum fields in curved space*, Cambridge University Press, London, England, 1982. Cambridge, Uk: Univ. Pr. (1982) 340p. ↑147, 149

[20] T. Biswas, R. Mansouri, and A. Notari, *Nonlinear Structure Formation and Apparent Acceleration: an Investigation*, JCAP **0712** (2007), 017, available at astro-ph/0606703. ↑120

[21] T. Biswas and A. Notari, *Swiss-Cheese Inhomogeneous Cosmology & the Dark Energy Problem*, JCAP **0806** (2008), 021, available at astro-ph/0702555. ↑121, 122, 132, 133, 135, 139

[22] J. Bock et al., *Task Force on Cosmic Microwave Background Research* (2006), available at astro-ph/0604101. ↑87

[23] N. N. Bogoliubov, Sov. Phys. JETP **7** (1958), 51. ↑147

[24] K. Bolejko, *The Szekeres Swiss Cheese model and the CMB observations* (2008), available at 0804.1846. ↑121

[25] J. R. Bond, G. Efstathiou, and J. Silk, *Massive neutrinos and the large-scale structure of the universe*, Phys. Rev. Lett. **45** (1980), 1980–1984. ↑103

[26] J. R. Bond, C. R. Contaldi, Z. Huang, L. Kofman, and P. M. Vaudrevange, *Scanning inflation*. in preparation. ↑88

[27] S. Boughn and R. Crittenden, *A correlation of the cosmic microwave sky with large scale structure*, Nature **427** (2004), 45–47, available at astro-ph/0305001. ↑103

[28] R. H. Brandenberger, *Alternatives to Cosmological Inflation* (2009), available at 0902.4731. ↑20

[29] N. Brouzakis and N. Tetradis, *Analytical Estimate of the Effect of Spherical Inhomogeneities on Luminosity Distance and Redshift*, Phys. Lett. **B665** (2008), 344–348, available at 0802.0859. ↑121, 122, 133, 135

[30] N. Brouzakis, N. Tetradis, and E. Tzavara, *The Effect of Large-Scale Inhomogeneities on the Luminosity Distance*, JCAP **0702** (2007), 013, available at astro-ph/0612179. ↑121, 124, 126

[31] ———, *Light Propagation and Large-Scale Inhomogeneities*, JCAP **0804** (2008), 008, available at astro-ph/0703586. ↑121

[32] M. Bucher, J. Dunkley, P. G. Ferreira, K. Moodley, and C. Skordis, *The initial conditions of the universe: how much isocurvature is allowed?*, Phys. Rev. Lett. **93** (2004), 081301, available at astro-ph/0401417. ↑89

[33] T. Buchert, *Dark Energy from Structure - A Status Report*, Gen. Rel. Grav. **40** (2008), 467–527, available at 0707.2153. ↑121

[34] T. S. Bunch and P. C. W. Davies, *Quantum field theory in de sitter space: Renormalization by point splitting*, Proc. Roy. Soc. Lond. **A360** (1978), 117–134. ↑149

[35] A. Cabre, E. Gaztanaga, M. Manera, P. Fosalba, and F. Castander, *Cross-correlation of WMAP 3rd year and the SDSS DR4 galaxy survey: new evidence for Dark Energy*, Mon. Not. Roy. Astron. Soc. Lett. **372** (2006), L23–L27, available at astro-ph/0603690. ↑103

[36] A. Cabre, P. Fosalba, E. Gaztanaga, and M. Manera, *Error analysis in cross-correlation of sky maps: application to the ISW detection* (2007), available at astro-ph/0701393. ↑110

[37] A. Cabre, E. Gaztanaga, M. Manera, P. Fosalba, and F. Castander, *Evidence for dark energy: cross-correlating SDSS5 and WMAP3* (2006), available at astro-ph/0611046. ↑103

[38] R. R. Caldwell and A. Stebbins, *A Test of the Copernican Principle*, Phys. Rev. Lett. **100** (2008), 191302, available at 0711.3459. ↑120

[39] C. Caprini, S. H. Hansen, and M. Kunz, *Observational constraint on the fourth derivative of the inflaton potential*, Mon. Not. Roy. Astron. Soc. **339** (2003), 212–214, available at hep-ph/0210095. ↑39, 54

[40] A. Cardoso, *Constraining hybrid inflation models with WMAP three-year results*, Phys. Rev. **D75** (2007), 027302, available at astro-ph/0610074. ↑39, 59

[41] S. M. Carroll, *Lecture notes on general relativity* (1997), available at gr-qc/9712019. ↑145

[42] R. Casadio, F. Finelli, A. Kamenshchik, M. Luzzi, and G. Venturi, *Method of comparison equations for cosmological perturbations*, JCAP **0604** (2006), 011, available at gr-qc/0603026. ↑39

[43] M.-N. Celerier, *Do we really see a cosmological constant in the supernovae data ?*, Astron. Astrophys. **353** (2000), 63–71, available at astro-ph/9907206. ↑120

[44] J. Choe, J.-O. Gong, and E. D. Stewart, *Second order general slow-roll power spectrum*, JCAP **0407** (2004), 012, available at hep-ph/0405155. ↑39

[45] D. J. H. Chung and A. E. Romano, *Mapping Luminosity-Redshift Relationship to LTB Cosmology*, Phys. Rev. **D74** (2006), 103507, available at astro-ph/0608403. ↑120

[46] T. Clifton, P. G. Ferreira, and K. Land, *Living in a Void: Testing the Copernican Principle with Distant Supernovae*, Phys. Rev. Lett. **101** (2008), 131302, available at 0807.1443. ↑120

[47] T. Clifton, P. G. Ferreira, and J. Zuntz, *What the small angle CMB really tells us about the curvature of the Universe*, JCAP **0907** (2009), 029, available at 0902.1313. ↑121

[48] T. Clifton and J. Zuntz, *Hubble Diagram Dispersion From Large-Scale Structure* (2009), available at 0902.0726. ↑121

[49] J. M. Cline and L. Hoi, *Inflationary potential reconstruction for a WMAP running power spectrum*, JCAP **0606** (2006), 007, available at astro-ph/0603403. ↑39, 45, 63

[50] E. J. Copeland, E. W. Kolb, A. R. Liddle, and J. E. Lidsey, *Observing the inflaton potential*, Phys. Rev. Lett. **71** (1993), 219–222, available at hep-ph/9304228. ↑87

[51] ———, *Reconstructing the inflation potential, in principle and in practice*, Phys. Rev. **D48** (1993), 2529–2547, available at hep-ph/9303288. ↑87

[52] E. J. Copeland, A. R. Liddle, D. H. Lyth, E. D. Stewart, and D. Wands, *False vacuum inflation with Einstein gravity*, Phys. Rev. **D49** (1994), 6410–6433, available at astro-ph/9401011. ↑38

[53] C. Copi, D. Huterer, D. Schwarz, and G. Starkman, *The Uncorrelated Universe: Statistical Anisotropy and the Vanishing Angular Correlation Function in WMAP Years 1-3*, Phys. Rev. **D75** (2007), 023507, available at astro-ph/0605135. ↑20, 45

[54] C. J. Copi, D. Huterer, D. J. Schwarz, and G. D. Starkman, *On the large-angle anomalies of the microwave sky*, Mon. Not. Roy. Astron. Soc. **367** (2006), 79–102, available at astro-ph/0508047. ↑45

[55] C. J. Copi, D. Huterer, D. J. Schwarz, and G. D. Starkman, *No large-angle correlations on the non-Galactic microwave sky* (2008), available at 0808.3767. ↑45

[56] L. Covi, J. Hamann, A. Melchiorri, A. Slosar, and I. Sorbera, *Inflation and WMAP three year data: Features have a future!*, Phys. Rev. **D74** (2006), 083509, available at astro-ph/0606452. ↑39, 59, 70

[57] R. G. Crittenden and N. Turok, *Looking for Λ with the Rees-Sciama Effect*, Phys. Rev. Lett. **76** (1996), 575, available at astro-ph/9510072. ↑103

[58] P. Crotty, J. Garcia-Bellido, J. Lesgourgues, and A. Riazuelo, *Bounds on isocurvature perturbations from CMB and LSS data*, Phys. Rev. Lett. **91** (2003), 171301, available at astro-ph/0306286. ↑103

[59] P. Crotty, J. Lesgourgues, and S. Pastor, *Measuring the cosmological background of relativistic particles with WMAP*, Phys. Rev. **D67** (2003), 123005, available at astro-ph/0302337. ↑103

[60] A. Cuoco et al., *Present status of primordial nucleosynthesis after WMAP: results from a new BBN code*, Int. J. Mod. Phys. **A19** (2004), 4431–4454, available at astro-ph/0307213. ↑103

[61] F. de Bernardis, A. Melchiorri, L. Verde, and R. Jimenez, *The Cosmic Neutrino Background and the Age of the Universe*, JCAP **0803** (2008), 020, available at 0707.4170. ↑103

[62] H. P. de Oliveira and C. A. Terrero-Escalante, *Troubles for observing the inflaton potential*, JCAP **0601** (2006), 024, available at astro-ph/0511660. ↑39

[63] A. de Oliveira-Costa et al., *The large-scale polarization of the microwave background and foreground*, Phys. Rev. **D68** (2003), 083003, available at astro-ph/0212419. ↑86

[64] H. J. de Vega and N. G. Sanchez, *Single field inflation models allowed and ruled out by the three years WMAP data* (2006), available at astro-ph/0604136. ↑39, 59

[65] C. Destri, H. J. de Vega, and N. G. Sanchez, *MCMC analysis of WMAP3 and SDSS data points to broken symmetry inflaton potentials and provides a lower bound on the tensor to scalar ratio*, Phys. Rev. **D77** (2008), 043509, available at astro-ph/0703417. ↑39, 59, 87, 88

[66] S. Dodelson, *Modern cosmology* (S. Dodelson, ed.), 2003. ↑3, 21

[67] S. Dodelson and E. Stewart, *Scale dependent spectral index in slow roll inflation*, Phys. Rev. **D65** (2002), 101301, available at astro-ph/0109354. ↑39

[68] M. Doran, *Speeding Up Cosmological Boltzmann Codes*, JCAP **0506** (2005), 011, available at astro-ph/0503277. ↑107

[69] M. Doran and G. Robbers, *Early dark energy cosmologies*, JCAP **0606** (2006), 026, available at astro-ph/0601544. ↑107

[70] J. Dunkley et al., *Five-Year Wilkinson Microwave Anisotropy Probe (WMAP) Observations: Likelihoods and Parameters from the WMAP data* (2008), available at 0803.0586. ↑6, 92

[71] R. Durrer, *The Cosmic Microwave Background* (R. Durrer, ed.), 2008. ↑3, 21

[72] R. Easther and W. H. Kinney, *Monte Carlo reconstruction of the inflationary potential*, Phys. Rev. **D67** (2003), 043511, available at astro-ph/0210345. ↑71

[73] R. Easther and H. Peiris, *Implications of a running spectral index for slow roll inflation*, JCAP **0609** (2006), 010, available at astro-ph/0604214. ↑39, 55, 59, 60, 69, 70, 71, 78, 87

[74] G. Efstathiou et al., *Evidence for a non-zero Lambda and a low matter density from a combined analysis of the 2dF Galaxy Redshift Survey and Cosmic Microwave Background Anisotropies*, Mon. Not. Roy. Astron. Soc. **330** (2002), L29, available at astro-ph/0109152. ↑120

[75] A. Einstein and E. G. Straus, *The influence of the expansion of space on the gravitation fields surrounding the individual stars*, Rev. Mod. Phys. **17** (1945), 120–124. ↑121

[76] D. J. Eisenstein et al., *Detection of the Baryon Acoustic Peak in the Large-Scale Correlation Function of SDSS Luminous Red Galaxies*, Astrophys. J. **633** (2005), 560–574, available at astro-ph/0501171. ↑120

[77] G. F. R. Ellis and T. Buchert, *The universe seen at different scales*, Phys. Lett. **A347** (2005), 38–46, available at gr-qc/0506106. ↑121

[78] F. Finelli, M. Rianna, and N. Mandolesi, *Constraints on the Inflationary Expansion from Three Year WMAP, small scale CMB anisotropies and Large Scale Structure Data Sets*, JCAP **0612** (2006), 006, available at astro-ph/0608277. ↑39, 59

[79] G. L. Fogli, E. Lisi, A. Marrone, and A. Palazzo, *Global analysis of three-flavor neutrino masses and mixings*, Prog. Part. Nucl. Phys. **57** (2006), 742–795, available at hep-ph/0506083. ↑103

[80] P. Fosalba and E. Gaztanaga, *Measurement of the gravitational potential evolution from the cross-correlation between WMAP and the APM Galaxy survey*, Mon. Not. Roy. Astron. Soc. **350** (2004), L37–L41, available at astro-ph/0305468. ↑103

[81] P. Fosalba, E. Gaztanaga, and F. Castander, *Detection of the ISW and SZ effects from the CMB-Galaxy correlation*, Astrophys. J. **597** (2003), L89–92, available at astro-ph/0307249. ↑103

[82] W. L. Freedman et al., *Final Results from the Hubble Space Telescope Key Project to Measure the Hubble Constant*, Astrophys. J. **553** (2001), 47–72, available at astro-ph/0012376. ↑6, 120

[83] J. Garcia-Bellido and D. G. Figueroa, *A stochastic background of gravitational waves from hybrid preheating*, Phys. Rev. Lett. **98** (2007), 061302, available at astro-ph/0701014. ↑32

[84] J. Garcia-Bellido, D. G. Figueroa, and A. Sastre, *A Gravitational Wave Background from Reheating after Hybrid Inflation*, Phys. Rev. **D77** (2008), 043517, available at 0707.0839. ↑32

[85] J. Garcia-Bellido and T. Haugboelle, *Confronting Lemaitre-Tolman-Bondi models with Observational Cosmology*, JCAP **0804** (2008), 003, available at 0802.1523. ↑120

[86] ———, *Looking the void in the eyes - the kSZ effect in LTB models*, JCAP **0809** (2008), 016, available at 0807.1326. ↑120

[87] ———, *The radial BAO scale and Cosmic Shear, a new observable for Inhomogeneous Cosmologies* (2008), available at 0810.4939. ↑120

[88] J. Garcia-Bellido and D. Wands, *Metric perturbations in two-field inflation*, Phys. Rev. **D53** (1996), 5437–5445, available at astro-ph/9511029. ↑38

[89] D. Garfinkle, *Inhomogeneous spacetimes as a dark energy model*, Class. Quant. Grav. **23** (2006), 4811–4818, available at gr-qc/0605088. ↑120

[90] S. Ghassemi, S. K. Moghaddam, and R. Mansouri, *Lensing effects in inhomogeneous cosmological models* (2009), available at 0901.0340. ↑121

[91] T. Giannantonio et al., *A high redshift detection of the integrated Sachs-Wolfe effect*, Phys. Rev. **D74** (2006), 063520, available at astro-ph/0607572. ↑103

[92] J.-O. Gong and E. D. Stewart, *The density perturbation power spectrum to second-order corrections in the slow-roll expansion*, Phys. Lett. **B510** (2001), 1–9, available at astro-ph/0101225. ↑39

[93] K. M. Gorski et al., *HEALPix – a Framework for High Resolution Discretization, and Fast Analysis of Data Distributed on the Sphere*, Astrophys. J. **622** (2005), 759–771, available at astro-ph/0409513. ↑129

[94] B. R. Granett, M. C. Neyrinck, and I. Szapudi, *Dark Energy Detected with Supervoids and Superclusters* (2008), available at 0805.2974. ↑122

[95] I. J. Grivell and A. R. Liddle, *Inflaton potential reconstruction without slow-roll*, Phys. Rev. **D61** (2000), 081301, available at astro-ph/9906327. ↑39

[96] C. Grojean and G. Servant, *Gravitational Waves from Phase Transitions at the Electroweak Scale and Beyond*, Phys. Rev. **D75** (2007), 043507, available at hep-ph/0607107. ↑32

[97] V. G. Gurzadyan and A. A. Kocharyan, *Kolmogorov stochasticity parameter measuring the randomness in Cosmic Microwave Background* (2008), available at 0810.3289. ↑121

[98] ———, *Porosity criterion for hyperbolic voids and the cosmic microwave background*, Astron. Astrophys. **493** (2009), L61, available at 0807.1239. ↑121

[99] A. H. Guth, *The Inflationary Universe: A Possible Solution to the Horizon and Flatness Problems*, Phys. Rev. **D23** (1981), 347–356. ↑38, 58, 68, 86

[100] A. H. Guth and S. Y. Pi, *Fluctuations in the New Inflationary Universe*, Phys. Rev. Lett. **49** (1982), 1110–1113. ↑38, 58, 68, 86

[101] S. Habib, A. Heinen, K. Heitmann, and G. Jungman, *Inflationary perturbations and precision cosmology*, Phys. Rev. **D71** (2005), 043518, available at astro-ph/0501130. ↑39

[102] J. Hamann, S. Hannestad, G. G. Raffelt, and Y. Y. Y. Wong, *Observational bounds on the cosmic radiation density*, JCAP **0708** (2007), 021, available at 0705.0440. ↑103

[103] J. Hamann, J. Lesgourgues, and W. Valkenburg, *How to constrain inflationary parameter space with minimal priors*, JCAP **0804** (2008), 016, available at 0802.0505. ↑xi, 87, 92, 97

[104] S. Hannestad, *New constraint on the cosmological background of relativistic particles*, JCAP **0601** (2006), 001, available at astro-ph/0510582. ↑103

[105] ———, *Primordial Neutrinos*, Ann. Rev. Nucl. Part. Sci. **56** (2006), 137–161, available at hep-ph/0602058. ↑104

[106] ———, *Global neutrino parameter estimation using Markov Chain Monte Carlo* (2007), available at 0710.1952. ↑104

[107] S. Hannestad and G. G. Raffelt, *Neutrino masses and cosmic radiation density: Combined analysis*, JCAP **0611** (2006), 016, available at astro-ph/0607101. ↑103

[108] S. Hannestad, H. Tu, and Y. Y. Y. Wong, *Measuring neutrino masses and dark energy with weak lensing tomography*, JCAP **0606** (2006), 025, available at astro-ph/0603019. ↑104

[109] S. Hannestad and Y. Y. Y. Wong, *Neutrino mass from future high redshift galaxy surveys: Sensitivity and detection threshold*, JCAP **0707** (2007), 004, available at astro-ph/0703031. ↑104

[110] S. H. Hansen and M. Kunz, *Observational constraints on the inflaton potential*, Mon. Not. Roy. Astron. Soc. **336** (2002), 1007–1010, available at hep-ph/0109252. ↑39, 54

[111] S. W. Hawking, *The Development of Irregularities in a Single Bubble Inflationary Universe*, Phys. Lett. **B115** (1982), 295. ↑38, 58, 68, 86

[112] S. W. Hawking and I. G. Moss, *Supercooled Phase Transitions in the Very Early Universe*, Phys. Lett. **B110** (1982), 35. ↑38

[113] G. Hinshaw et al., *Three-year Wilkinson Microwave Anisotropy Probe (WMAP) observations: Temperature analysis*, Astrophys. J. Suppl. **170** (2007), 288, available at astro-ph/0603451. ↑38, 42, 44, 48, 64, 74

[114] W. Hu, N. Sugiyama, and J. Silk, *The Physics of microwave background anisotropies*, Nature **386** (1997), 37–43, available at astro-ph/9604166. ↑3, 21

[115] P. Hunt and S. Sarkar, *Constraints on large scale voids from WMAP-5 and SDSS* (2008), available at 0807.4508. ↑120, 121

[116] K. Ichikawa, M. Kawasaki, and F. Takahashi, *Constraint on the Effective Number of Neutrino Species from the WMAP and SDSS LRG Power Spectra*, JCAP **0705** (2007), 007, available at astro-ph/0611784. ↑103

[117] K. Ichikawa and T. Takahashi, *On the determination of neutrino masses and dark energy evolution from the cross-correlation of CMB and LSS*, JCAP **0802** (2008), 017, available at astro-ph/0510849. ↑104, 116

[118] H. Iguchi, T. Nakamura, and K.-i. Nakao, *Is dark energy the only solution to the apparent acceleration of the present universe?*, Prog. Theor. Phys. **108** (2002), 809–818, available at astro-ph/0112419. ↑120

[119] N. Jarosik et al., *Three-year Wilkinson Microwave Anisotropy Probe (WMAP) observations: Beam profiles, data processing, radiometer characterization and systematic error limits*, Astrophys. J. Suppl. **170** (2007), 263, available at astro-ph/0603452. ↑38, 42, 44, 48, 64

[120] W. C. Jones et al., *A Measurement of the Angular Power Spectrum of the CMB Temperature Anisotropy from the 2003 Flight of Boomerang*, Astrophys. J. **647** (2006), 823, available at astro-ph/0507494. ↑45, 46, 74

[121] K. Jones-Smith, L. M. Krauss, and H. Mathur, *A Nearly Scale Invariant Spectrum of Gravitational Radiation from Global Phase Transitions*, Phys. Rev. Lett. **100** (2008), 131302, available at 0712.0778. ↑86

[122] M. Joy, E. D. Stewart, J.-O. Gong, and H.-C. Lee, *From the Spectrum to Inflation : An Inverse Formula for the General Slow-Roll Spectrum*, JCAP **0504** (2005), 012, available at astro-ph/0501659. ↑39

[123] K. Kadota, S. Dodelson, W. Hu, and E. D. Stewart, *Precision of inflaton potential reconstruction from CMB using the general slow-roll approximation*, Phys. Rev. **D72** (2005), 023510, available at astro-ph/0505158. ↑39

[124] M. Kamionkowski, A. Kosowsky, and A. Stebbins, *A probe of primordial gravity waves and vorticity*, Phys. Rev. Lett. **78** (1997), 2058–2061, available at astro-ph/9609132. ↑86

[125] R Kantowski, *Corrections in the luminosity-redshift relations of the homogeneous friedmann models*, Astrophys. J **155** (1969), 89. ↑121

[126] A. Kiakotou, O. Elgaroy, and O. Lahav, *Neutrino Mass, Dark Energy, and the Linear Growth Factor*, Phys. Rev. **D77** (2008), 063005, available at 0709.0253. ↑104, 106, 107

[127] C. Kiefer, J. Lesgourgues, D. Polarski, and A. A. Starobinsky, *The coherence of primordial fluctuations produced during inflation*, Class. Quant. Grav. **15** (1998), L67–L72, available at gr-qc/9806066. ↑16, 17

[128] W. H. Kinney, *Inflation: Flow, fixed points and observables to arbitrary order in slow roll*, Phys. Rev. **D66** (2002), 083508, available at astro-ph/0206032. ↑71

[129] W. H. Kinney, E. W. Kolb, A. Melchiorri, and A. Riotto, *Inflation model constraints from the Wilkinson microwave anisotropy probe three-year data*, Phys. Rev. **D74** (2006), 023502, available at astro-ph/0605338. ↑39, 59

[130] A. Kogut et al., *PAPPA: Primordial Anisotropy Polarization Pathfinder Array*, New Astron. Rev. **50** (2006), 1009–1014, available at astro-ph/0609546. ↑87

[131] E. W. Kolb, V. Marra, and S. Matarrese, *On the description of our cosmological spacetime as a perturbed conformal Newtonian metric and implications for the backreaction proposal for the accelerating universe*, Phys. Rev. **D78** (2008), 103002, available at 0807.0401. ↑121

[132] ———, *Cosmological background solutions and cosmological backreactions* (2009), available at 0901.4566. ↑121

[133] E. W. Kolb and M. S. Turner, *The Early universe*, Front. Phys. **69** (1990), 1–547. ↑3, 21

[134] E. Komatsu et al., *Five-Year Wilkinson Microwave Anisotropy Probe (WMAP) Observations:Cosmological Interpretation*, Astrophys. J. Suppl. **180** (2009), 330–376, available at 0803.0547. ↑6, 32, 120

[135] A. Kosowsky, M. S. Turner, and R. Watkins, *Gravitational waves from first order cosmological phase transitions*, Phys. Rev. Lett. **69** (1992), 2026–2029. ↑32

[136] H. Kozaki and K.-i. Nakao, *Volume Expansion of Swiss-Cheese Universe*, Phys. Rev. **D66** (2002), 104008, available at gr-qc/0208091. ↑121

[137] L. M. Krauss, *Gravitational waves from global phase transitions*, Phys. Lett. **B284** (1992), 229–233. ↑86

[138] L. M. Krauss and M. S. Turner, *The cosmological constant is back*, Gen. Rel. Grav. **27** (1995), 1137–1144, available at astro-ph/9504003. ↑120

[139] W. Kundt, *Critical Thoughts on Cosmology* (2009), available at 0902.3151. ↑121

[140] M. Kunz, R. Trotta, and D. Parkinson, *Measuring the effective complexity of cosmological models*, Phys. Rev. **D74** (2006), 023503, available at astro-ph/0602378. ↑43, 96

[141] C.-l. Kuo et al., *High Resolution Observations of the CMB Power Spectrum with ACBAR*, Astrophys. J. **600** (2004), 32–51, available at astro-ph/0212289. ↑46, 120

[142] C. R. Lawrence et al., Millimeter and Submillimeter Detectors for Astronomy II, Proceedings of the SPIE **5498** (2004), 220–231. ↑87

[143] S. M. Leach, *Measuring the primordial power spectrum: Principal component analysis of the cosmic microwave background*, Mon. Not. Roy. Astron. Soc. **372** (2006), 646–654, available at astro-ph/0506390. ↑44

[144] S. M Leach and A. R Liddle, *Constraining slow-roll inflation with WMAP and 2dF*, Phys. Rev. **D68** (2003), 123508, available at astro-ph/0306305. ↑73

[145] S. M. Leach, A. R. Liddle, J. Martin, and D. J Schwarz, *Cosmological parameter estimation and the inflationary cosmology*, Phys. Rev. **D66** (2002), 023515, available at astro-ph/0202094. ↑17, 39, 48, 49, 73

[146] J. Lesgourgues and S. Pastor, *Massive neutrinos and cosmology*, Phys. Rept. **429** (2006), 307–379, available at astro-ph/0603494. ↑104, 106, 107, 116

[147] J. Lesgourgues, S. Pastor, and L. Perotto, *Probing neutrino masses with future galaxy redshift surveys*, Phys. Rev. **D70** (2004), 045016, available at hep-ph/0403296. ↑104, 116

[148] J. Lesgourgues, L. Perotto, S. Pastor, and M. Piat, *Probing neutrino masses with CMB lensing extraction*, Phys. Rev. **D73** (2006), 045021, available at astro-ph/0511735. ↑115

[149] J. Lesgourgues, A. A. Starobinsky, and W. Valkenburg, *What do WMAP and SDSS really tell about inflation?*, JCAP **0801** (2008), 010, available at 0710.1630. ↑xi, 69, 70, 71, 72, 74, 87, 92

[150] J. Lesgourgues and W. Valkenburg, *New constraints on the observable inflaton potential from WMAP and SDSS*, Phys. Rev. **D75** (2007), 123519, available at astro-ph/0703625. ↑xi, 59, 60, 61, 62, 64, 69, 87, 92, 96

[151] J. Lesgourgues, W. Valkenburg, and E. Gaztanaga, *Constraining neutrino masses with the ISW-galaxy correlation function*, Phys. Rev. **D77** (2008), 063505, available at 0710.5525. ↑xi

[152] A. Lewis and S. Bridle, *Cosmological parameters from CMB and other data: a Monte-Carlo approach*, Phys. Rev. **D66** (2002), 103511, available at astro-ph/0205436. ↑44, 48, 60, 70, 74, 92, 115

[153] A. Lewis, A. Challinor, and A. Lasenby, *Efficient Computation of CMB anisotropies in closed FRW models*, Astrophys. J. **538** (2000), 473–476, available at astro-ph/9911177. ↑70, 74

[154] A. R. Liddle and D. H. Lyth, *Cosmological Inflation and Large-Scale Structure* (A. R. Liddle and D. H. Lyth, eds.), 2000. ↑3, 13, 19, 21

[155] A. R Liddle, *On the inflationary flow equations*, Phys. Rev. **D68** (2003), 103504, available at astro-ph/0307286. ↑39

[156] ———, *Information criteria for astrophysical model selection*, Mon. Not. Roy. Astron. Soc. Lett. **377** (2007), L74–L78, available at astro-ph/0701113. ↑43

[157] A. R. Liddle, P. Mukherjee, and D. Parkinson, *Cosmological model selection*, Astron. Geophys. **47** (2006), 4.30–4.33, available at astro-ph/0608184. ↑43

[158] A. R. Liddle, P. Parsons, and J. D. Barrow, *Formalizing the slow roll approximation in inflation*, Phys. Rev. **D50** (1994), 7222–7232, available at astro-ph/9408015. ↑39, 71, 86

[159] J. E. Lidsey et al., *Reconstructing the inflaton potential: An overview*, Rev. Mod. Phys. **69** (1997), 373–410, available at astro-ph/9508078. ↑39

[160] E. Lifshitz, *On the gravitational stability of the expanding universe*, J. Phys.(USSR) **10** (1946), 116. ↑x

[161] A. D. Linde, *A New Inflationary Universe Scenario: A Possible Solution of the Horizon, Flatness, Homogeneity, Isotropy and Primordial Monopole Problems*, Phys. Lett. **B108** (1982), 389–393. ↑38, 58, 68, 86

[162] ———, *Scalar Field Fluctuations in Expanding Universe and the New Inflationary Universe Scenario*, Phys. Lett. **B116** (1982), 335. ↑38

[163] ———, *Chaotic Inflation*, Phys. Lett. **B129** (1983), 177–181. ↑38, 58, 68, 86

[164] ———, *Axions in inflationary cosmology*, Phys. Lett. **B259** (1991), 38–47. ↑38

[165] ———, *Hybrid inflation*, Phys. Rev. **D49** (1994), 748–754, available at astro-ph/9307002. ↑38

[166] L. Lorenz, J. Martin, and C. Ringeval, *Brane inflation and the WMAP data: a Bayesian analysis*, JCAP **0804** (2008), 001, available at 0709.3758. ↑59, 70

[167] M. LoVerde, L. Hui, and E. Gaztanaga, *Magnification-Temperature Correlation: the Dark Side of ISW Measurements*, Phys. Rev. **D75** (2007), 043519, available at astro-ph/0611539. ↑115

[168] D. H. Lyth, *What would we learn by detecting a gravitational wave signal in the cosmic microwave background anisotropy?*, Phys. Rev. Lett. **78** (1997), 1861–1863, available at hep-ph/9606387. ↑87

[169] C. J. MacTavish et al., *Spider Optimization: Probing the Systematics of a Large Scale B-Mode Experiment* (2007), available at 0710.0375. ↑87

[170] B. Maffei et al., *Proceedings of the workshop on dome c in toulouse*, Proceedings of the workshop on Dome C in Toulouse, EAS Publications Series **14** (2005), 251–256. ↑87

[171] A. Makarov, *On the accuracy of slow-roll inflation given current observational constraints*, Phys. Rev. **D72** (2005), 083517, available at astro-ph/0506326. ↑39, 41, 59, 78

[172] M. Malquarti, S. M. Leach, and A. R. Liddle, *From the production of primordial perturbations to the end of inflation*, Phys. Rev. **D69** (2004), 063505, available at astro-ph/0310498. ↑78

[173] M. Maltoni, T. Schwetz, M. A. Tortola, and J. W. F. Valle, *Status of global fits to neutrino oscillations*, New J. Phys. **6** (2004), 122, available at hep-ph/0405172. ↑103

[174] B B Mandelbrot, *The fractal geometry of nature*. ↑122

[175] G. Mangano, A. Melchiorri, O. Mena, G. Miele, and A. Slosar, *Present bounds on the relativistic energy density in the Universe from cosmological observables*, JCAP **0703** (2007), 006, available at astro-ph/0612150. ↑103

[176] R. Mansouri, *Structured FRW universe leads to acceleration: A non- perturbative approach* (2005), available at astro-ph/0512605. ↑120

[177] V. Marra, E. W. Kolb, and S. Matarrese, *Light-cone averages in a swiss-cheese universe*, Phys. Rev. **D77** (2008), 023003, available at 0710.5505. ↑121, 132

[178] V. Marra, E. W. Kolb, S. Matarrese, and A. Riotto, *On cosmological observables in a swiss-cheese universe*, Phys. Rev. **D76** (2007), 123004, available at 0708.3622. ↑121, 122, 123, 124, 125, 126, 132

[179] J. Martin and C. Ringeval, *Inflation after WMAP3: Confronting the slow-roll and exact power spectra to CMB data*, JCAP **0608** (2006), 009, available at astro-ph/0605367. ↑39, 41, 59, 62, 70

[180] P. Martineau and R. Brandenberger, *A Back-reaction Induced Lower Bound on the Tensor-to- Scalar Ratio* (2007), available at 0709.2671. ↑86

[181] I. Masina and A. Notari, *The Cold Spot as a Large Void: Rees-Sciama effect on CMB Power Spectrum and Bispectrum*, JCAP **0902** (2009), 019, available at 0808.1811. ↑122, 138

[182] B. S. Mason et al., *The Anisotropy of the Microwave Background to $l = 3500$: Deep Field Observations with the Cosmic Background Imager*, Astrophys. J. **591** (2003), 540–555, available at astro-ph/0205384. ↑120

[183] J. C. Mather et al., *Measurement of the Cosmic Microwave Background spectrum by the COBE FIRAS instrument*, Astrophys. J. **420** (1994), 439–444. ↑4

[184] J. C. Mather, D. J. Fixsen, R. A. Shafer, C. Mosier, and D. T. Wilkinson, *Calibrator Design for the COBE Far Infrared Absolute Spectrophotometer (FIRAS)*, Astrophys. J. **512** (1999), 511–520, available at astro-ph/9810373. ↑4

[185] J. D. McEwen, P. Vielva, M. P. Hobson, E. Martinez-Gonzalez, and A. N. Lasenby, *Detection of the ISW effect and corresponding dark energy constraints made with directional spherical wavelets*, Mon. Not. Roy. Astron. Soc. **373** (2007), 1211–1226, available at astro-ph/0602398. ↑103

[186] J. W. Moffat, *Cosmic Microwave Background, Accelerating Universe and Inhomogeneous Cosmology*, JCAP **0510** (2005), 012, available at astro-ph/0502110. ↑120

[187] ———, *Large scale cosmological inhomogeneities, inflation and acceleration without dark energy* (2005), available at astro-ph/0504004. ↑120

[188] ———, *Late-time inhomogeneity and acceleration without dark energy*, JCAP **0605** (2006), 001, available at astro-ph/0505326. ↑120

[189] T. E. Montroy et al., *A Measurement of the CMB Spectrum from the 2003 Flight of BOOMERANG*, Astrophys. J. **647** (2006), 813, available at astro-ph/0507514. ↑74

[190] M. J. Mortonson and W. Hu, *Impact of reionization on CMB polarization tests of slow-roll inflation*, Phys. Rev. **D77** (2008), 043506, available at 0710.4162. ↑86

[191] V. F. Mukhanov and G. V. Chibisov, *Quantum Fluctuation and Nonsingular Universe. (In Russian)*, JETP Lett. **33** (1981), 532–535. ↑58, 68, 86

[192] V. F. Mukhanov, H. A. Feldman, and R. H. Brandenberger, *Theory of cosmological perturbations. Part 1. Classical perturbations. Part 2. Quantum theory of perturbations. Part 3. Extensions*, Phys. Rept. **215** (1992), 203–333. ↑72

[193] P. Mukherjee, D. Parkinson, and A. R. Liddle, *A Nested Sampling Algorithm for Cosmological Model Selection*, Astrophys. J. **638** (2006), L51–L54, available at astro-ph/0508461. ↑97

[194] A. G. Muslimov, *ON THE SCALAR FIELD DYNAMICS IN A SPATIALLY FLAT FRIEDMAN UNIVERSE*, Class. Quant. Grav. **7** (1990), 231–237. ↑59

[195] Y. Nambu, *Quantum to classical transition of density fluctuations in the inflationary model*, Phys. Lett. **B276** (1992), 11–17. ↑17

[196] P. Oxley et al., *The EBEX Experiment*, Proc. SPIE Int. Soc. Opt. Eng. **5543** (2004), 320–331, available at astro-ph/0501111. ↑87

[197] N. Padmanabhan et al., *Correlating the CMB with Luminous Red Galaxies : The Integrated Sachs-Wolfe Effect*, Phys. Rev. **D72** (2005), 043525, available at astro-ph/0410360. ↑103

[198] L. Page et al., *Three year Wilkinson Microwave Anisotropy Probe (WMAP) observations: Polarization analysis*, Astrophys. J. Suppl. **170** (2007), 335, available at astro-ph/0603450. ↑38, 42, 44, 48, 64, 74

[199] C. Pahud, A. R Liddle, P. Mukherjee, and D. Parkinson, *Model selection forecasts for the spectral index from the Planck satellite*, Phys. Rev. **D73** (2006), 123524, available at astro-ph/0605004. ↑43

[200] D. Parkinson, P. Mukherjee, and A. R Liddle, *A Bayesian model selection analysis of WMAP3*, Phys. Rev. **D73** (2006), 123523, available at astro-ph/0605003. ↑43, 87

[201] H. Peiris and R. Easther, *Recovering the Inflationary Potential and Primordial Power Spectrum With a Slow Roll Prior: Methodology and Application to WMAP 3 Year Data*, JCAP **0607** (2006), 002, available at astro-ph/0603587. ↑39, 59, 69, 70, 71, 73, 87

[202] ———, *Slow Roll Reconstruction: Constraints on Inflation from the 3 Year WMAP Dataset*, JCAP **0610** (2006), 017, available at astro-ph/0609003. ↑39, 59, 62, 69, 70, 71, 73, 87

[203] W. J. Percival et al., *Measuring the Baryon Acoustic Oscillation scale using the SDSS and 2dFGRS*, Mon. Not. Roy. Astron. Soc. **381** (2007), 1053–1066, available at 0705.3323. ↑120

[204] S. Perlmutter et al., *Measurements of Omega and Lambda from 42 High-Redshift Supernovae*, Astrophys. J. **517** (1999), 565–586, available at astro-ph/9812133. ↑103

[205] L. Perotto, J. Lesgourgues, S. Hannestad, H. Tu, and Y. Y. Y. Wong, *Probing cosmological parameters with the CMB: Forecasts from full Monte Carlo simulations*, JCAP **0610** (2006), 013, available at astro-ph/0606227. ↑112

[206] F. Piacentini et al., *A measurement of the polarization-temperature angular cross power spectrum of the Cosmic Microwave Background from the 2003 flight of BOOMERANG*, Astrophys. J. **647** (2006), 833, available at astro-ph/0507507. ↑74

[207] E. Pierpaoli, *Constraints on the cosmic neutrino background*, Mon. Not. Roy. Astron. Soc. **342** (2003), L63, available at astro-ph/0302465. ↑103

[208] L. Pogosian, P. S. Corasaniti, C. Stephan-Otto, R. Crittenden, and R. Nichol, *Tracking Dark Energy with the ISW effect: short and long- term predictions*, Phys. Rev. **D72** (2005), 103519, available at astro-ph/0506396. ↑115

[209] D. Polarski and A. A. Starobinsky, *Semiclassicality and decoherence of cosmological perturbations*, Class. Quant. Grav. **13** (1996), 377–392, available at gr-qc/9504030. ↑17

[210] G. Polenta et al., New Astronomy Review **51** (2007), 256. ↑87

[211] B. A. Powell and W. H. Kinney, *Limits on primordial power spectrum resolution: An inflationary flow analysis*, JCAP **0708** (2007), 006, available at 0706.1982. ↑59, 62, 70

[212] J. R. Primack, *Whatever happened to hot dark matter?*, SLAC Beam Line **31N3** (2001), 50–57, available at astro-ph/0112336. ↑103

[213] T. Prokopec and W. Valkenburg, *The cosmology of the nonsymmetric theory of gravitation*, Phys. Lett. **B636** (2006), 1–4, available at astro-ph/0503289. ↑149

[214] N. Puchades, M. J. Fullana, J. V. Arnau, and D. Saez, *On the Rees-Sciama effect: maps and statistics*, Mon. Not. Roy. Astron. Soc. **370** (2006), 1849–1858, available at astro-ph/0605704. ↑103

[215] S. Rasanen, *Accelerated expansion from structure formation*, JCAP **0611** (2006), 003, available at astro-ph/0607626. ↑121

[216] ———, *Light propagation in statistically homogeneous and isotropic dust universes*, JCAP **0902** (2009), 011, available at 0812.2872. ↑120

[217] M. J. Rees and D. W. Sciama, *Large scale Density Inhomogeneities in the Universe*, Nature **217** (1968), 511–516. ↑122

[218] C. L. Reichardt et al., *High resolution CMB power spectrum from the complete ACBAR data set* (2008), available at 0801.1491. ↑74

[219] A. G. Riess et al., *Observational Evidence from Supernovae for an Accelerating Universe and a Cosmological Constant*, Astron. J. **116** (1998), 1009–1038, available at astro-ph/9805201. ↑103, 120

[220] C. Ringeval, *The exact numerical treatment of inflationary models*, Lect. Notes Phys. **738** (2008), 243–273, available at astro-ph/0703486. ↑39, 47, 59, 70

[221] A. Riotto, *Inflation and the theory of cosmological perturbations* (2002), available at hep-ph/0210162. ↑3, 21

[222] J. E. Ruhl et al., *The South Pole Telescope* (2004), available at astro-ph/0411122. ↑87

[223] R. K. Sachs, *Gravitational waves in general relativity. 6. The outgoing radiation condition*, Proc. Roy. Soc. Lond. **A264** (1961), 309–338. ↑126

[224] R. K. Sachs and A. M. Wolfe, *Perturbations of a cosmological model and angular variations of the microwave background*, Astrophys. J. **147** (1967), 73–90. ↑102

[225] D. S. Salopek and J. R. Bond, *Nonlinear evolution of long wavelength metric fluctuations in inflationary models*, Phys. Rev. **D42** (1990), 3936–3962. ↑39, 59, 86

[226] D. S. Salopek, J. R. Bond, and J. M. Bardeen, *Designing Density Fluctuation Spectra in Inflation*, Phys. Rev. **D40** (1989), 1753. ↑38

[227] A. Sandage et al., *The Hubble Constant: A Summary of the HST Program for the Luminosity Calibration of Type Ia Supernovae by Means of Cepheids*, Astrophys. J. **653** (2006), 843–860, available at astro-ph/0603647. ↑4

[228] K. Sato, *First Order Phase Transition of a Vacuum and Expansion of the Universe*, Mon. Not. Roy. Astron. Soc. **195** (1981), 467–479. ↑38, 58, 68, 86

[229] D. J. Schwarz, G. D. Starkman, D. Huterer, and C. J. Copi, *Is the low-l microwave background cosmic?*, Phys. Rev. Lett. **93** (2004), 221301, available at astro-ph/0403353. ↑45

[230] D. J. Schwarz, C. A. Terrero-Escalante, and A. A. Garcia, *Higher order corrections to primordial spectra from cosmological inflation*, Phys. Lett. **B517** (2001), 243–249, available at astro-ph/0106020. ↑39

[231] M. Seikel and D. J Schwarz, *How strong is the evidence for accelerated expansion?*, JCAP **0802** (2008), 007, available at 0711.3180. ↑120

[232] U. Seljak and M. Zaldarriaga, *Lensing-induced Cluster Signatures in the Cosmic Microwave Background*, Astrophys. J **538** (July 2000), 57–64, available at astro-ph/9907254. ↑103

[233] U. Seljak and M. Zaldarriaga, *Signature of gravity waves in polarization of the microwave background*, Phys. Rev. Lett. **78** (1997), 2054–2057, available at astro-ph/9609169. ↑86

[234] O. Seto, J. Yokoyama, and H. Kodama, *What happens when the inflaton stops during inflation*, Phys. Rev. **D61** (2000), 103504, available at astro-ph/9911119. ↑60

[235] J. L. Sievers et al., *Implications of the Cosmic Background Imager Polarization Data*, Astrophys. J. **660** (2007), 976–987, available at astro-ph/0509203. ↑46

[236] R. E. Smith et al., *Stable clustering, the halo model and nonlinear cosmological power spectra*, Mon. Not. Roy. Astron. Soc. **341** (2003), 1311, available at astro-ph/0207664. ↑109

[237] G. F. Smoot et al., *Structure in the COBE differential microwave radiometer first year maps*, Astrophys. J. **396** (1992), L1–L5. ↑120

[238] Y.-S. Song and L. Knox, *Dark energy tomography* (2003), available at astro-ph/0312175. ↑104

[239] D. N. Spergel et al., *First Year Wilkinson Microwave Anisotropy Probe (WMAP) Observations: Determination of Cosmological Parameters*, Astrophys. J. Suppl. **148** (2003), 175, available at astro-ph/0302209. ↑103

[240] ———, *Wilkinson Microwave Anisotropy Probe (WMAP) three year results: Implications for cosmology*, Astrophys. J. Suppl. **170** (2007), 377, available at astro-ph/0603449. ↑38, 39, 42, 44, 48, 59, 64, 103

[241] D. J. Spiegelhalter, N. G. Best, B. P. Carlin, and A. van der Linde, *Bayesian measures of model complexity and fit*, Journal of the Royal Statistical Society: Series B (Statistical Methodology) **64** (2002), no. 4, 583–639, available at http://www.blackwell-synergy.com/doi/pdf/10.1111/1467-9868.00353. ↑96

[242] G. D Starkman, R. Trotta, and P. M Vaudrevange, *Introducing doubt in Bayesian model comparison* (2008), available at 0811.2415. ↑43

[243] A. A. Starobinsky, *Spectrum of relict gravitational radiation and the early state of the universe*, JETP Lett. **30** (1979), 682–685. ↑38, 58, 68, 86

[244] ———, *A new type of isotropic cosmological models without singularity*, Phys. Lett. **B91** (1980), 99–102. ↑38, 58, 68, 86

[245] ———, *Dynamics of Phase Transition in the New Inflationary Universe Scenario and Generation of Perturbations*, Phys. Lett. **B117** (1982), 175–178. ↑38, 58, 68, 86

[246] ———, *Spectrum of initial perturbations in open and closed inflationary models* (1996), available at astro-ph/9603075. ↑60

[247] ———, *Inflaton field potential producing the exactly flat spectrum of adiabatic perturbations*, JETP Lett. **82** (2005), 169–173, available at astro-ph/0507193. ↑63

[248] G. Steigman, *Primordial nucleosynthesis: Successes and challenges*, Int. J. Mod. Phys. **E15** (2006), 1–36, available at astro-ph/0511534. ↑103

[249] P. J. Steinhardt and M. S. Turner, *A Prescription for Successful New Inflation*, Phys. Rev. **D29** (1984), 2162–2171. ↑39, 86

[250] E. D. Stewart, *The spectrum of density perturbations produced during inflation to leading order in a general slow-roll approximation*, Phys. Rev. **D65** (2002), 103508, available at astro-ph/0110322. ↑39

[251] E. D. Stewart and D. H. Lyth, *A more accurate analytic calculation of the spectrum of cosmological perturbations produced during inflation*, Phys. Lett. **B302** (1993), 171–175, available at gr-qc/9302019. ↑39, 73

[252] N. Sugiura, K.-i. Nakao, D. Ida, N. Sakai, and H. Ishihara, *How do nonlinear voids affect light propagation?*, Prog. Theor. Phys. **103** (2000), 73–89, available at astro-ph/9912414. ↑121

[253] R. A. Sunyaev and Y. B. Zeldovich, *Distortions of the Background Radiation Spectrum*, Nature **223** (August 1969), 721–+. ↑103

[254] J. Tauber et al., *Planck: The scientific programme* (2006), available at astro-ph/0604069. ↑87

[255] M. Tegmark et al., *Cosmological Constraints from the SDSS Luminous Red Galaxies*, Phys. Rev. **D74** (2006), 123507, available at astro-ph/0608632. ↑7, 42, 44, 48, 64, 74, 92, 95

[256] K. Tomita, *A Local Void and the Accelerating Universe*, Mon. Not. Roy. Astron. Soc. **326** (2001), 287, available at astro-ph/0011484. ↑120

[257] ———, *Analyses of Type Ia Supernova Data in Cosmological Models with a Local Void*, Prog. Theor. Phys. **106** (2001), 929–939, available at astro-ph/0104141. ↑120

[258] ———, *Anisotropy of the Hubble Constant in a Cosmological Model with a Local Void on Scales of 200 Mpc*, Prog. Theor. Phys. **105** (2001), 419, available at astro-ph/0005031. ↑120

[259] ———, *Dipole anisotropies of IRAS galaxies and the contribution of a large-scale local void*, Astrophys. J. **584** (2003), 580–584, available at astro-ph/0211137. ↑120

[260] R. Trotta, *Applications of Bayesian model selection to cosmological parameters*, Mon. Not. Roy. Astron. Soc. **378** (2007), 72–82, available at astro-ph/0504022. ↑43, 44

[261] ———, *Bayes in the sky: Bayesian inference and model selection in cosmology* (2008), available at 0803.4089. ↑88

[262] R. Trotta and A. Melchiorri, *Indication for primordial anisotropies in the neutrino background from WMAP and SDSS*, Phys. Rev. Lett. **95** (2005), 011305, available at astro-ph/0412066. ↑103

[263] M. S. Turner, *Recovering the inflationary potential*, Phys. Rev. **D48** (1993), 5539–5545, available at astro-ph/9307035. ↑87

[264] W. Valkenburg, *Nonsymmetric metric perturbations in cosmology, M.Sc. thesis* (2006). ↑145

[265] ———, *How much of the inflaton potential do we see?*, PoS **CARGESE2007** (2007), 018, available at 0708.3849. ↑xi

[266] ———, *Swiss Cheese and a Cheesy CMB*, JCAP **0906** (2009), 010, available at 0902.4698. ↑xi

[267] W. Valkenburg, L. M. Krauss, and J. Hamann, *Effects of Prior Assumptions on Bayesian Estimates of Inflation Parameters, and the expected Gravitational Waves Signal from Inflation*, Phys. Rev. **D78** (2008), 063521, available at 0804.3390. ↑xi

[268] R. A. Vanderveld, E. E. Flanagan, and I. Wasserman, *Mimicking Dark Energy with Lemaitre-Tolman-Bondi Models: Weak Central Singularities and Critical Points*, Phys. Rev. **D74** (2006), 023506, available at astro-ph/0602476. ↑120

[269] ———, *Luminosity distance in 'Swiss cheese' cosmology with randomized voids: I. Single void size*, Phys. Rev. **D78** (2008), 083511, available at 0808.1080. ↑121, 122, 133, 136, 137, 138

[270] P. M. Vaudrevange, *Inflationary trajectories*, Ph.D. Thesis, 2007. ↑88

[271] L. Verde, L.-M. Wang, A. Heavens, and M. Kamionkowski, *Large-scale structure, the cosmic microwave background, and primordial non-gaussianity*, Mon. Not. Roy. Astron. Soc. **313** (2000), L141–L147, available at astro-ph/9906301. ↑86

[272] R. M. Wald, *General relativity*, Chicago University Press, USA, 1984. ↑148

[273] S. Wang, Z. Haiman, W. Hu, J. Khoury, and M. May, *Weighing neutrinos with galaxy cluster surveys*, Phys. Rev. Lett. **95** (2005), 011302, available at astro-ph/0505390. ↑104

[274] S Weinberg, *Apparent luminosities in a locally inhomogeneous universe*, Astrophys. J **208** (1976), L1–L3. ↑121, 138

[275] K. W. Yoon et al., *The Robinson Gravitational Wave Background Telescope (BICEP): a bolometric large angular scale CMB polarimeter* (2006), available at astro-ph/0606278. ↑87

[276] M. Zaldarriaga and U. Seljak, *Reconstructing projected matter density from cosmic microwave background*, Phys. Rev. **D59** (1999), 123507, available at astro-ph/9810257. ↑86

Samenvatting

Dit proefschrift geeft een invulling aan de vele mogelijkheden die er zijn om kosmische storingen en theoretische modellen van het universum met elkaar te vergelijken. Met kosmische storingen bedoelen we kleine afwijkingen van het gemiddelde, in welke kosmologische quantiteit dan ook. Heden nemen wij kosmische storingen waar op verscheidene manieren. De twee manieren die ter sprake komen in dit proefschrift, zijn de anisotropie van kosmische achtergrondstraling en de distributie van materie in het universum, in de vorm van sterrenstelsels en clusters van sterrenstelsels.

Als het universum begon als een werkelijk homogeen en isotroop plasma van materie en straling, zoals we die kennen op aarde, dan zou het universum vandaag de dag nog steeds homogeen en isotroop zijn. In andere woorden, er zouden geen kosmische storingen zijn. En toch nemen we ze waar. De vooralsnog meest plausibele verklaring voor het bestaan en de oorsprong van deze storingen is het inflatieparadigma. In dit proefschrift demonstreren we nieuwe middelen om inflatie als theorie te testen. We zijn voorgaande analytische benaderingen voorbij gestreefd, en hebben de meest consistente, meest betrouwbare en meest onbevooroordeelde grenzen op parameters met betrekking tot de potentiaal van het inflaton verkregen.

Wanneer de kosmische storingen eenmaal bestaan, evolueren ze. De kosmische achtergrondstraling heeft bij haar ontstaan een afdruk van de kosmische storingen meegekregen, zoals deze geëvolueerd zijn tot op het moment van ontkoppeling van de achtergrondstraling. Vanaf dat moment bewegen de achtergrondfotonen vrijelijk door het universum, alhoewel ze nog steeds zwakjes interageren met de kosmische storingen waar ze doorheen reizen. We hebben aangetoond hoe dit secundaire effect gebruikt kan worden om de grenzen van de totale massa van de neutrino aan te scherpen. We hebben ook aangetoond dat dit secundaire effect een zwakheid aan het licht brengt van een bepaalde klasse van modellen, in welke de inhomogeneïteit van het universum in verband wordt gebracht met de ogenschijnlijke versnelling van de uitdijing van het heelal: het Gatenkaasuniversum. In dit proefschrift wordt het Gatenkaasuniversum uitgesloten in zijn huidige vorm.

Al met al zijn kosmische storingen een rijke bron van informatie over de fysica van het universum.

Trefwoorden: Kosmologie, Kosmische Achtergrondstraling, Kosmische Structuur, Inflatie, Neutrinomassa, Donkere Energie, Inhomogene Universum

Summary

This thesis exemplifies the many possibilities that are to be explored, relating cosmic perturbations to theoretical models of the universe. Today we observe cosmic perturbations in several ways. The two ways that are under consideration in this thesis, are the temperature anisotropies in the Cosmic Microwave Background (CMB) and distribution of matter in the universe, in the form of galaxies and clusters of galaxies.

If the universe started out as a truly homogeneous and isotropic plasma of matter and radiation, as we know it on earth, embedded in a space time described by general relativity, then the universe would still be homogeneous and isotropic today. In other words, cosmic perturbations would not exist. Yet we observe them. The, for now, most plausible explanation for the origin of these perturbations is the paradigm of inflation. In this thesis we demonstrate new tools for probing inflation. We have gone beyond previously developed analytical approximations, and obtained the most consistent, most reliable and most unprejudiced constraints on the inflaton potential to date.

Once the cosmic perturbations exist, their evolution continues. The CMB is created with an imprint of the cosmic perturbations as they evolved up to the time of decoupling of the CMB. Beyond that moment, the CMB photons freely travel through the universe, yet still weakly interact with the perturbations they travel through. We have shown that this secondary effect can be used to tighten constraints on the total mass of the neutrino. We have also shown that this secondary effect points out a weakness of a class of cosmologies in which the inhomogeneity of the universe is related to the apparent acceleration of the expansion of the universe: the Swiss-Cheese universe. In this thesis, the Swiss-Cheese model is ruled out in its present form.

Altogether, cosmic perturbations are a rich source of information on the physics of the universe.

Keywords: Cosmology, Cosmic Microwave Background, Large Scale Structure, Inflation, Neutrino mass, Dark Energy, Inhomogeneous Universe

Resumé

Cette thèse illustre les nombreuses possibilités permettant de relier les perturbations cosmologiques aux modèles théoriques décrivant l'univers. Aujourd'hui, nous observons ces perturbations cosmologiques sous des formes diverses. Les observations considérées dans cette thèse sont les anisotropies du rayonnement de fond cosmologique (CMB) et la distribution de matière dans l'univers (galaxies et amas de galaxies).

Si à un temps initial, l'univers consistait en un plasma homogène et isotrope de matière et de radiation plongé dans un espace-temps décrit par la relativité générale, il serait toujours homogène et isotrope aujourd'hui. Les perturbations cosmologiques n'existeraient pas. Cependant, nous les observons. Le mécanisme de génération des perturbations actuellement considéré comme le plus plausible repose sur le paradigme de l'inflation. Dans cette thèse, nous introduisons de nouveaux outils pour tester l'inflation. Nous sommes allés au-delà des approximations analytiques développées auparavant, et avons obtenu les contraintes sur le potentiel de l'inflaton les plus cohérentes, robustes et génériques publiées a ce jour.

Une fois les perturbations cosmologiques engendrées, elles continuent d'évoluer. Le CMB porte l'emprunte de ces perturbations telles qu'elles étaient au moment du découplage des photons. Par la suite, les photons ont voyagé librement à travers l'univers, en interagissant encore gravitationnellement avec les fluctuations de matière qu'ils traversaient. Nous avons montré que cet effet secondaire peut être utilisé pour améliorer les contraintes sur la masse totale des neutrinos. Nous avons aussi montré qu'il est à l'origine de plusieurs problèmes pour une classe de modèles cosmologiques dans lesquels les inhomogénéités de l'univers pourraient expliquer l'accélération apparente de son expansion: le modèle d'univers à bulles (swiss-cheese universe). Dans cette thèse, l'univers à bulle - tel qu'il a été définit dans la littérature - est infirmé.

En conclusion, les perturbations cosmologiques sont une source très riche d'informations sur l'évolution physique de notre univers.

Mots clé: Cosmologie, Fond Diffus Cosmologique, Structures aux Grandes Echelles, Inflation, masse du neutrino, Énergie Noire, Univers Inhomogène.